A Gravitational Lensing Analysis of Galaxy Clusters in the Southern Cosmology Survey

Rachel Natalie McInnes, MSci.

Doctor of Philosophy
University of Edinburgh
June 2010

Abstract

In this thesis I present the first gravitational lensing results from the Southern Cosmology Survey (SCS). I provide a preliminary study of an automated pipeline analysis of a large survey, in preparation for larger surveys. Future large-area sky surveys, such as Pan-STARRS-1 (PS1), have similar characteristics to the SCS data and will require full automation of the processing. Therefore, this data set provides an ideal test case to highlight the problems which will be faced by such surveys.

To analyse the large SCS dataset, I develop an automated weak lensing pipeline based on the KSB. This pipeline has been rigorously verified using simulations and data which I detail here. Results are shown from a weak lensing analysis of 152 optically-selected clusters in 56 square degrees. I fit universal Navarro, Frenk and White (NFW) profiles to measure cluster masses, and use the relatively large area of the survey to test the universal shape of cluster profiles using stacking of the tangential shears.

I present the first lensing mass measurements of Sunyaev-Zel'dovich (SZ) selected clusters. It has been long thought that SZ surveys would be a powerful way to detect galaxy clusters for cosmological studies. Simulations show that the SZ detection is independent of redshift and that the threshold corresponds very closely to a threshold in mass. It was, however, not guaranteed that the first blind SZ experiments would detect mass. Using optical imaging from the SCS, I present lensing masses for three clusters selected by their SZ emission in the South Pole Telescope survey (SPT). I confirm that the SZ selection procedure is successful in detecting mass concentrations and find that the SZ clusters have amongst the largest masses, as high as $15\times10^{14}M_{\odot}$. Consequently I can confirm that the first installment of SZ detections has detected large mass concentrations. Using the best fit masses for all the clusters, I analytically calculate the expected SZ integrated Y parameter.

Finally, the scaling relation of Reyes et al. (2008) of lensing M_{200}^{lens} against optical L_{200} is tested over the redshift range $z = 0.1 - 0.3$ and extended to $z = 0.3 - 0.8$. While there is some discrepancy in the lower redshift-range, we agree with Reyes et al (2008) in the higher-redshift sample if we assume no evolution of the scaling relation. To test the tangential shear profile of these clusters, 98 clusters are stacked. We find that by allowing the model to vary from an NFW, a very good fit can be found with a higher normalisation of the shears and a lower concentration. This study supports that of Mandelbaum et al. (2008) who show that that massive halos have a lower concentration than expected.

Like the SCS, new large area surveys such as PS1 are not very deep, and it is crucial to understand not only how to analyse this size of dataset, but also the sort of results one could expect to achieve. I show in this thesis that 2D mass reconstructions can be done on data of this quality, and large galaxy clusters successfully reconstructed. With a number density of $n \sim 9$ it is possible to detect the most massive clusters with lensing, but it is difficult. With the lower number density of $n \sim 6$ or lower expected from PS1 it will prove very difficult to detect individual clusters. However, PS1 will survey a massive area, and so the stacking analysis should work extremely well, and it should be possible to further test the shape of the cluster profiles with stacking as I demonstrated here with the smaller SCS dataset.

Declaration

I hereby declare that this thesis entitled A Gravitational Lensing Analysis of Galaxy Clusters in the Southern Cosmology Survey is not substantially the same as any that I have submitted for a degree or diploma or other qualification at any other University. I further state that no part of my thesis has already been or is being concurrently submitted for any such degree, diploma or other qualification.

Parts of the work contained in this thesis have been published in a refereed scientific journal.

> Sections of chapters 4 and 5 are based on work presented in the paper:
> "FIRST LENSING MEASUREMENTS OF SZ-DETECTED CLUSTERS"
> McInnes, R. N., Menanteau, F., Heavens, A. F., Hughes, J. P., Jimenez, R., Massey, R., Simon, P., Taylor, A., 2009, MNRAS, 399, L84

This thesis is the outcome of my own work except where specifically indicated in the text. Figures in the body of this thesis which are from the work of others have been credited as such in the associated caption.

Rachel N. McInnes, Msci
Edinburgh,
June 2010.

Acknowledgements

None of this would have been possible without the excellent supervision from my primary supervisor Alan Heavens. Thank you Alan for your endless help, support and encouragement. You have been an excellent supervisor to me and also a good friend, thank you.

I also want to express my gratitude to my second supervisors, Andy Taylor and Richard Massey who have played a huge role in my supervision. Thank you both for your expert help and advice. I would like to thank my thesis examiners Meghan Gray and Catherine Heymans for all their feedback and helpful suggestions.

Furthermore, I would like to thank Felipe Menanteau, Jack Hughes, Raul Jimenez for their help working on the Southern Cosmology Survey dataset, Patrick Simon for his help and work on mass reconstructions, Catherine Heymans for her help and many useful discussions, David Bacon for the time he spent teaching me KSB, and members of the DUEL network for including me in their meetings which were of invaluable help.

A huge thank you to John Barrow, who has given me hours and hours of computing support!

I am indebted to my many colleagues at the ROE who over the last three and a half years have provided support in many forms. And you've certainly made it more fun, so thanks to Jenny, Berian, Angela, Sarah, Alina, Hannah, Paula, Brendan, Fergus, Peder, Michele, Eric, Wing-Fai, Noelia, and all the other staff and students who have made my PhD such an enjoyable experience.

Thank you to all my friends for many much-needed distractions and fun! I want especially thank Sandie and Fi - you're amazing friends!

Craig, you've been an enormous help to me with this thesis in so many ways. Thank you my love! Thank you for always knowing how to make me laugh, for your encouragement, and your love.

Finally I would like to give a huge thanks to all of my family for supporting me every step of the way. Thank you for always being there for me. To my parents Alison and Tom, my brother Lewis and my grandparents Joan and Bill - you're fantastic people, thank you!

Contents

List of Figures

List of Tables

Abbreviations

ACT	—	Atacama Cosmology Telescope
BCG	—	Brightest Cluster Galaxy
CMB	—	Cosmic Microwave Background
CCD	—	Charge Coupled Device
CDM	—	Cold Dark Matter
CEA	—	Cylindrical Equal Area projection
CFHTLS	—	The Canada-France-Hawaii-Telescope Legacy Survey
CMB	—	Cosmic Microwave Background
DE	—	Dark Energy
DES	—	Dark Energy Survey
Dec.	—	Declination
FLRW	—	Friedmann-Lemaître-Robertson-Walker
FWHM	—	Full width half maximum
HALO	—	High Altitude Lensing Observatory
JDEM	—	Joint Dark Energy Mission
KSB	—	Kaiser, Squires and Broadhurst
LHC	—	Large Hadron Collider
LSST	—	Large Synoptic Survey Telescope
MBAC	—	Millimeter Bolometer Array Camera
NFW	—	Navarro, Frenk and White
Pan-STARRS	—	Panoramic Survey Telescope And Rapid Response System
PSF	—	Point Spread Function
PS1	—	Pan-STARRS 1
R.A.	—	Right Ascension
RW	—	Robertson Walker
SCS	—	Southern Cosmology Survey
SIS	—	Singular Isothermal Sphere
SPT	—	South Pole Telescope
STEP	—	Shear TEsting Programme
SZ	—	Sunyaev-Zel'dovich
TAN	—	Tangent plane projection
VST-KIDS	—	VLT Survey Telescope KIlo-Degree Survey
WCS	—	World Coordinate System
WIMP	—	Weakly Interacting Massive Particle
WMAP	—	Wilkinson Microwave Anisotropy Probe

Chapter 1

Introduction

This thesis concerns itself with estimating masses of galaxy clusters using gravitational lensing. Galaxy clusters are of great significance to cosmologists as they are the largest gravitationally bound structures in our Universe. By studying their properties, abundance, and evolution through their redshift distribution, we can constrain cosmology. Future full sky microwave and optical surveys will lead the way in this field. These enormous surveys will be orders of magnitude larger anything which has come before, and will have the power to discover new galaxy clusters, out to high redshifts. In this thesis I will discuss the theory of weak gravitational lensing needed for these cluster detections.

This thesis introduces a new automated lensing pipeline based on the Kaiser, Squires & Broadhurst (1995) KSB method. Using this pipeline, I present a gravitational lensing analyses of a new large survey, the Southern Cosmology Survey (SCS). The lensing results presented here are the first from this large SCS survey, and they provide a test bed for an automated pipeline on a large survey, in preparation for larger full-sky surveys in the future. The analyses presented here concern galaxy clusters, specifically measuring cluster masses using lensing, and testing the shape of their profiles by stacking the cluster signals. I combine cluster lensing results with optical and Sunyaev-Zel'dovich (SZ) data, and provide the first lensing mass measurements for SZ discovered clusters. This thesis provides a preliminary study - the results of which can be used to hone analyses techniques for even larger future surveys, such as Pan-STARRS.

The combination of SZ and lensing is very important in order to test the abundance and evolution of galaxy clusters, which in turn can constrain cosmological parameters. The SZ effect can be used to detect galaxy clusters out to high redshift, but in order to constrain cosmology, it is important to have reliable mass estimates for these clusters. Gravitational lensing can provide masses for these clusters. It is possible to find a relation between SZ signal and lensing mass, and with this relation, it will be possible to use the SZ to calculate a proxy for mass. The combination of microwave measurements in the form of the SZ effect, and gravitational lensing analyses of the optical imaging will lead to huge catalogues of galaxy cluster positions with accurate mass measurements. Using only one method (SZ or lensing) on its own has limited power, but combined these two complementary techniques are much more powerful. This important area of research is now emerging, because this work has only become possible with larger surveys. This initial study, providing the first lensing mass measurements for SZ detected clusters is the first step in testing the reliability of SZ clusters selection

technique.

In this first chapter I introduce background theories required for this thesis. To do this, I first examine the standard model of cosmology, and matter in the Universe. Next, I look at galaxy clusters, and how we can use observations and measurements of them to probe cosmology. I then look at one particular method of detecting galaxy clusters, which is the Sunyaev-Zel'dovich effect. I then review gravitational lensing observations which have led to constraints on cosmology.

1.1 The Standard Model of Cosmology

We now have a theory of cosmology which not only brings together Einstein's General Relativity, the Standard Model of particle physics, dark matter, dark energy, and inflation but also is supported by many observational surveys. We still have many questions which are unanswered, *what is the nature of dark matter? why is the vacuum energy non-zero? did inflation happen?*, and in our work we strive to get closer to answering such questions. Weak gravitational lensing not only allows us to test our theory of cosmology, but to probe dark matter, galaxy clusters and the geometry of the Universe. The results from gravitational lensing in the next few years should be exciting, as we start to get data from larger, and deeper, sky surveys.

The concordance model, or ΛCDM cosmology, is the simplest known cosmological model that is supported by our observations. In this model, our Universe is spatially flat, with an energy density dominated by Dark Energy (Λ, or DE) and Cold Dark Matter (CDM). Although we do not fully understand these components on a microscopic scale, the model successfully fits observations. Examples include those made of the Cosmic Microwave Background by the Wilkinson Microwave Anisotropy Probe (WMAP)[1] (see Spergel et al. (2003); Bennett et al. (2003); Komatsu et al. (2009) for details) and the Type 1A supernovae observations of the accelerating expansion of the Universe (see Riess et al. (2004)).

Λ is the cosmological constant (or DE) term which is causing the current accelerated expansion of the Universe. The cosmological constant is often described in terms of Ω_Λ, the fraction of energy density of a flat Universe in the form of the cosmological constant. Currently we believe $\Omega_\Lambda \simeq 0.73$. Cold Dark Matter is matter which is non-baryonic, possibly non-thermalised and collisionless. It is thought that this component makes up 22% of the energy density of the Universe at the present day . This leaves only 4% of the energy density of the Universe coming from Baryonic matter. The baryonic and dark matter energy density, Ω_m, makes up the rest of the energy density in the Universe ($\Omega_m \simeq 0.27$). There is still the question of what sort of elementary particle might make up dark matter. It is hoped that the answer to this might be found in the CERN Large Hadron Collider (LHC)[2] when it begins. If dark matter is the lightest supersymmetric particle then this could be detected by the LHC.

[1] Wilkinson Microwave Anisotropy Probe, http://map.gsfc.nasa.gov/ .

[2] LHC, http://lhc.web.cern.ch/lhc/ .

1.1.1 Cosmological Formalism

The ΛCDM model assumes that the *cosmological principle* holds. The cosmological principle states that, on large enough scales, the Universe follows two postulates:

1. The Universe is *isotropic*, i.e. the Universe's statistical properties are the same in all directions.

2. The mass distribution must be *homogeneous*, i.e. the Universe's statistical properties are the same at a given time. This means that there is no special position in the Universe, it looks the same from all points.

The Universe can be homogeneous without being isotropic, but if it is inhomogeneous then it necessarily anisotropic. The combination of isotropy and homogeneity (often referred to as *uniformity*) allows us to define a global cosmological time rather than just a local time. This is because the clocks can be synchronised if observers set their clocks to a standard time when the universal uniform density reaches a given value.

This section follows the approach taken in Peacock (1999). To describe spacetime in a homogeneous and isotropic Universe we use the expression for the line element. Locally, we know that this must reduce to the special relativistic case, $c^2 d\tau^2 = c^2 dt^2 - dx^2 - dy^2 - dz^2$. The relativistic line element can be written

$$c^2 d\tau^2 = g_{\mu\nu} dx^\mu dx^\nu \,, \tag{1.1}$$

where $g_{\mu\nu}$ is the *metric tensor*. Note that the term 'metric' is often used to mean 'line element' since they contain the same information. The metric is used to describe curved spacetime.

Using isotropy, we conclude that the metric can take the following form:

$$c^2 d\tau^2 = c^2 dt^2 - R^2(t)\left[f^2(r)dr^2 + g^2(r)d\beta^2\right] \,, \tag{1.2}$$

with the observer at the origin, and where in spherical polar coordinates $d\beta^2 = d\theta^2 + \sin^2 d\phi^2$, $R(t)$ is the time-dependent *scale factor*, and r is the time-independent *comoving coordinate*. The functions f and g can be chosen so that either $f = 1$ or $g = r^2$, to make conditions look similar to Euclidean space.

The Robertson Walker Metric

The Robertson-Walker metric (*RW metric*) describes a homogeneous and isotropic Universe and can be written in a number of different ways. The one used here is chosen such that the comoving coordinates are dimensionless, and such that $R(t)$ has dimensions of length. The RW metric is written as follows:

$$ds^2 = c^2 d\tau^2 = c^2 dt^2 - R^2(t)\left[dr^2 + S_k^2(r)d\beta^2\right] \,, \tag{1.3}$$

where

$$R_0 = \frac{c}{H_0}\left(\frac{k}{\Omega - 1}\right)^{1/2} \tag{1.4}$$

and where we define the function

$$S_k(r) = \begin{cases} \sin r & (k = 1) \\ \sinh r & (k = -1) \\ r & (k = 0)\,. \end{cases} \tag{1.5}$$

The value of k depends on the geometry of the Universe. When $k = +1$ the metric describes a *closed Universe* with positive curvature. The $k = -1$ case is that of an *open Universe* with negative curvature. Finally, the $k = 0$ case describes a *flat Universe* with zero curvature.

Expansion and the Freidmann Equation

To derive a metric which can describe a Universe which is expanding or contracting, we need to first introduce the Einstein Tensor, (See Peacock (1999) for more details of this)

$$G^{\mu\nu} = R^{\mu\nu} - \frac{1}{2} g^{\mu\nu} R \tag{1.6}$$

where $R^{\mu\nu}$ is the *Ricci tensor*, and R is the related curvature scalar such that $R = g_{\mu\nu}R^{\mu\nu}$. ${G^{\mu\nu}}_{;\nu} = 0$ and the stress-energy also has ${T^{\mu\nu}}_{;\nu} = 0$, so Einstein's field equations relating the Einstein tensor to the energy-momentum tensor $T^{\mu\nu}$ are written (in natural units[3]) as

$$G^{\mu\nu} = 8\pi T^{\mu\nu}\,. \tag{1.7}$$

Since ${g^{\mu\nu}}_{\nu} = 0$,[4] we can *add any constant multiple of the metric* to the Einstein tensor without disturbing the right hand side of Eq. (1.7). So we can write

$$G^{\mu\nu} + g^{\mu\nu}\Lambda = 8\pi T^{\mu\nu}\,. \tag{1.8}$$

Λ in Eq. (1.8) was originally added by Einstein to create a static Universe. This is now what we know as the cosmological constant and represents our acceleration term.

The field equations then simplify to the following two independent equations:

$$\left(\frac{\dot{a}}{a}\right)^2 = \frac{8\pi}{3}\rho - \frac{kc^2}{a^2} + \frac{\Lambda}{3}\,, \tag{1.9}$$

and

$$\frac{\ddot{a}}{a} = -\frac{4}{3}\pi\left(\rho + \frac{3P}{c^2}\right) + \frac{\Lambda}{3}\,. \tag{1.10}$$

Eq. (1.9) is known as Freidmann's Equation. If the RW metric in Eq. (1.3) has scale factor $a(t)$ which obeys Eq. (1.9) and Eq. (1.10) then it is called the Friedmann-Lemaître-Robertson-Walker (FLRW) metric.

A useful parameter to introduce at this point is the *Hubble Parameter*, $H(t)$. This is the relative expansion rate of the Universe, and it is defined as:

[3] $G = c = 1$

[4] This statement means that locally conditions obey special relativity

$$H(t) \equiv \frac{\dot{a}}{a} \,. \tag{1.11}$$

The present day value of the Hubble parameter (at $t = t_0$) is the *Hubble constant*, $H(t_0) = H_0$. Often in the literature the Hubble constant is expressed in terms of the *dimensionless Hubble parameter*, h,

$$H_0 \equiv 100h \text{ km/s/Mpc} \,. \tag{1.12}$$

Observations by Hubble Space Telescope (HST) Hubble Key Project (Freedman et al., 2001) suggest that $h \approx 0.73$.

From the Friedmann equation we discover that there is a relationship between the density of the Universe and its global geometry. For a given rate of expansion, the *critical density* of the Universe that will give $k = 0$ is:

$$\rho_c = \frac{3H^2}{8\pi G} \,, \tag{1.13}$$

this leads us to define a *density parameter* as the ratio of density (whether baryonic matter, dark matter or radiation density) to critical density,

$$\Omega_x \equiv \frac{\rho_x}{\rho_c} = \frac{8\pi G\rho_x}{3H^2} \,. \tag{1.14}$$

Since ρ and H change over time, this density parameter is epoch-dependent.

It is common to divide the energy content of the Universe into pressure-less matter, and radiation. Relations describing the varying number density of particles as the Universe expands are $\rho_m \propto a^{-3}$ and $\rho_r \propto a^{-4}$. The extra power of a^{-1} in the radiation term arises because of the energy reduction of photons due to redshifting. This allows us to write the density as

$$\frac{8\pi G\rho}{3} = H_0^2 \left(\Omega_{m,0}a^{-3} + \Omega_{r,0}a^{-4}\right) \tag{1.15}$$

where the subscript $_0$ denotes the density parameter value at the present time. The $\Lambda/3$ term of Eq. (1.9) can be considered to be an additional contribution to the density of the Universe. This is often referred to as a *vacuum energy*, and we define

$$\Omega_\Lambda \equiv \frac{\Lambda}{3H^2} \,. \tag{1.16}$$

Now we can re-write Eq. (1.15) to include the vacuum energy term:

$$\frac{8\pi G\rho}{3} = H_0^2 \left(\Omega_{m,0}a^{-3} + \Omega_{r,0}a^{-4} + \Omega_{\Lambda,0}\right) \,. \tag{1.17}$$

This allows us to write the first of Friedmann's equations as follows:

$$H^2(a) = H_0^2 \left[\Omega_{\Lambda,0} + \Omega_{m,0}a^{-3} + \Omega_{r,0}a^{-4} - (\Omega_{tot,0} - 1)\, a^{-2}\right] \,, \tag{1.18}$$

where Ω_{tot} is the sum of all the density parameters combined. A Universe which has zero curvature has $\Omega_{tot} = 1$ exactly at all times.

1.1.2 Redshift and Distance Measures

Redshift

On small scales, where conditions are Euclidean, the proper separation between two fundamental observers separated by comoving distance dr is $R(t)$dr. Hubble's law is given by $v = Hd$, with

$$H = \frac{\dot{R}}{R} \,. \tag{1.19}$$

At these small scales, the Doppler shift is given by the recessional velocity, v, and we define the redshift, z, in terms of the shift of spectral lines:

$$\frac{\nu_{emit}}{\nu_{obs}} \equiv 1 + z \simeq 1 + \frac{v}{c} \,. \tag{1.20}$$

At larger separations, where the effect of spatial curvature becomes important, we need a way to express redshift that does not involve measuring the radial velocity. From the metric, we see that the equation for a null geodesic is $r = \int_{t_{emit}}^{t_{obs}} cdt/R(t)$. The comoving distance is constant, but the domain of integration extends in time from when the photon is emitted, t_{emit}, to when it is observed, t_{obs}. Photons emitted at later times will be received at later times, but we know the comoving separation r is constant, so changes in t_{emit} and t_{obs} cannot alter the integral. This means that events at these large distances time-dilate according to how much the Universe has expanded since the photons we now recieve were emitted and leads us to the condition:

$$\frac{dt_{emit}}{dt_{obs}} = \frac{R(t_{emit})}{R(t_{obs})} \,, \tag{1.21}$$

and we can write the dilation in frequency as,

$$\frac{\nu_{emit}}{\nu_{obs}} \equiv 1 + z = \frac{R(t_{obs})}{R(t_{emit})} = \frac{1}{a(t)} \,, \tag{1.22}$$

where $a(t)$ is the normalized scale factor. Photon wavelengths therefore stretch with the Universe as they travel through it.

Distance Measures

In a curved spacetime, it is clear that the term *distance* no longer has a unique meaning. Unlike Euclidean space, different definitions of how to measure the distance between two points lead to different values. In the literature, it is common to find the use of four distances:

1. The proper distance
2. The comoving distance
3. The angular-diameter distance
4. The luminosity distance.

For gravitational lensing, it is the angular diameter distance which is most important as it relates the observed shear to the theoretical expectation. However, the comoving distance and the luminosity distance do also come in indirectly, because to a large extent they determine what the source population is. The luminosity distance is involved because the main criteria for sources being included, is that they are above the flux limit of the survey. Finally, the comoving distance comes in because for a given comoving number density of (sufficiently bright) sources, the distribution in redshift will depend on the comoving volume elements, which depend on both the comoving distance, and also the angluar diameter distance.

Distance measures relate two events, emission and observation. They are parameterised by the redshifts of the emitter and the observer, z_e and z_o,and we assume that the observer is taken to be at the origin of the coordinate system.

The *proper distance*, D_{prop}, is the actual radial distance you would measure with a ruler between two points separated by dr, at time t:

$$dD_{prop} = R(t)dr \, . \tag{1.23}$$

The *comoving distance*, D_{com}, is simply the distance r (in the comoving coordinates we have chosen) between the worldlines of an emitter and an observer both comoving with the cosmic expansion:

$$dD_{com} = dr \, . \tag{1.24}$$

From our metric in Eq. (1.3), the equation for a null geodesic is $cdt = -Rdr$ for a photon travelling radially towards the observer. Therefore we can write the following expression:

$$dD_{com} = -\frac{cdt}{a} = -\frac{cda}{\dot{a}a} = -\frac{cda}{a^2 H} \, . \tag{1.25}$$

Finally, using Eq. (1.18) and Eq. (1.22) and in the case where $\Omega_{r,0} \ll \Omega_{m,0}$, we reach the expression:

$$D_{com} = \int_{z_o}^{z_e} \frac{cdz}{H_0} \left\{ (1 - \Omega_{tot,0}) (1 + z)^2 + \Omega_{\Lambda,0} + \Omega_{m,0} (1 + z)^3 \right\}^{-\frac{1}{2}} \, . \tag{1.26}$$

The *angular-diameter distance*, D_{ang}, is defined in analogy to the relation in Euclidean space between the transverse size of an object and the angle it subtends at the observer. At cosmological distances, the *proper* transverse size of an object observed by us is its comoving size multiplied by the scale factor $a(t_e)$ at the time of emission:

$$dl_{trans} = \frac{1}{1 + z_e} S_k(r(z_o, z_e)) d\beta \, . \tag{1.27}$$

Therefore we can write the angular-diameter distance in terms of Eq. (1.26):

$$D_{ang} = \frac{1}{1 + z_e} S_k \left(D_{com}(z_e, z_o) \right) \, . \tag{1.28}$$

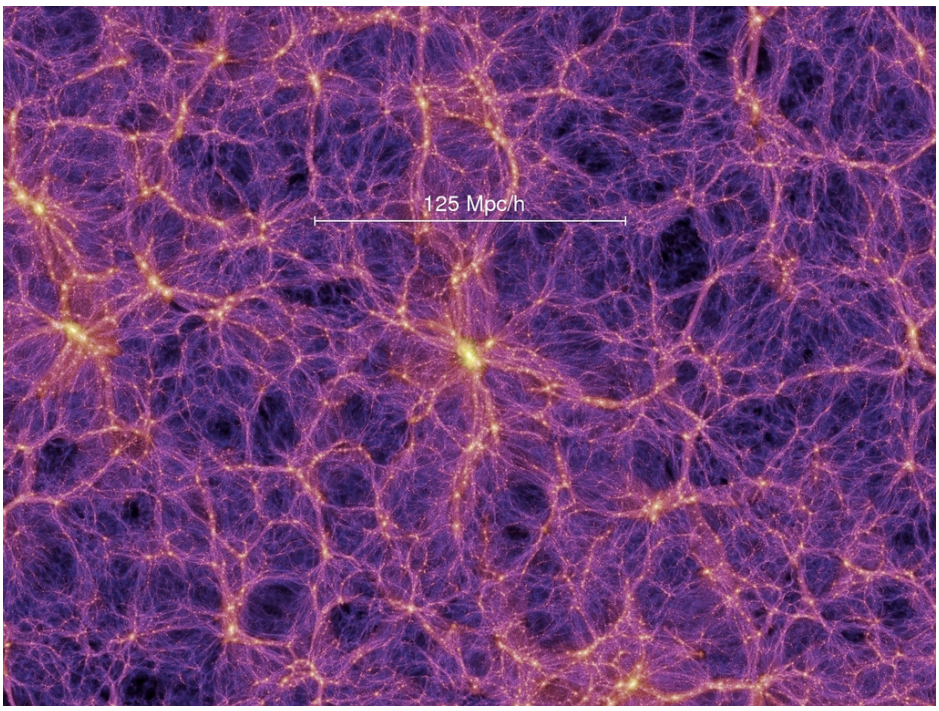

Figure 1.1: Image of the large scale structure of the Universe from the Millennium simulation. *Image credit:* Springel et al. (2005).

The received flux of a source of bolometric luminosity L is

$$\frac{L}{4\pi S_k^2(r)(1+z)^2}, \tag{1.29}$$

where the two factors of $(1 + z)$ arise from redshifting of photons and reduced arrival rate. This defines the *luminosity distance* as

$$D_L = (1+z)S_k. \tag{1.30}$$

1.2 Matter in the Universe

Observationally we see that our Universe is made up of stars which are grouped together in galaxies and that these galaxies are grouped together in clusters of galaxies. Clusters form in the regions of the Universe with the highest density of dark matter, and *voids* — areas devoid of matter — also exist. Though less apparent observationally, simulations indicate that these most dense regions are linked by *filaments* of dark matter, and this large scale structure is often known as a *cosmic web* because of its shape. The organisation of structure appears to follow as a hierarchical model up to the scale of superclusters and filaments. This is well illustrated in an image from a computer simulation of dark matter clustering is shown in Figure 1.1 (Springel et al., 2005).

Only on even larger scales, greater than hundreds of megaparsecs, the Universe

begins to appear smooth. Surveys do not find any continued structures of galaxies on scales greater than that of superclusters and voids. This agrees with the theory underpinning our cosmological models that the Universe is homogeneous on large scales (see § 1.1).

1.2.1 Contents of the Universe

Current measurements show that only 27% of our Universe is made up of matter, and that 73% of it is made up of the so-called dark energy (Komatsu et al., 2009). The matter contribution is made up of baryonic matter (4%) and cold dark matter (22%) (see § 1.2.4 for more detail).

Baryonic Matter

The particle physics definition of a baryon is a particle made up of three quarks. Protons are made of two up quarks and a down quark, and neutrons are made up of an up and two down quarks. Although electrons are not made of quarks, cosmologists use the term baryon to describe protons, neutrons and electrons. In the Universe, the baryonic matter takes the form of stars and gas.

Dark Matter

To fit observational evidence, it is believed that there is another type of fundamental particle which exists in our Universe. It is known as dark matter, and the details of its properties are unknown. What is known is that dark matter is not luminous, nor does it interact with other matter through the strong or nuclear forces. It does, however, interact gravitationally with other particles, and this is how its existence has been inferred.

Dark matter was postulated to account for the 'missing mass' measured with galactic rotation curves. Since then, its existence has been inferred with astrophysical evidence from orbital velocities of galaxies in clusters, and gravitational lensing (most notably the Bullet cluster: Clowe et al. (2006)). It is now understood that dark matter is the largest component of mass in galaxies and clusters of galaxies.

Because of its large contribution to the matter content of the Universe, dark matter is believed to play a key role in the formation of galaxies and structure, and in galaxy evolution. In spite of the importance of dark matter in our Universe and its formation, direct evidence of its existence has yet remained elusive.

Cold dark matter (or CDM) is the favoured model of the majority of dark matter in our Universe, and it is defined to be cold (meaning its velocity at the time of radiation-matter equality was non-relativistic), collisionless and non-baryonic.

When astronomers refer to dark matter, they often are also including neutrinos in this bracket. Neutrinos are extremely weakly interacting particles, who have a very small but non-zero rest mass. Neutrinos are created as the result of radioactive decay or nuclear reactions such as those that take place in stars, or when cosmic rays hit atoms. There are three types of neutrinos: the electron, tau, and muon, and their corresponding antiparticles. Electron neutrinos are produced during beta decay — whenever neutrons

change into protons (or protons into neutrons). Neutrinos, however, do interact via the weak interaction.

Radiation

We view our Universe through its interaction with electromagnetic radiation. This radiation fills our Universe at a large variety of frequencies. From the quantum mechanical viewpoint this radiation can be thought of as being made up of individual particles, called photons. Photons travel at the speed of light, and have zero rest mass.

Photons can interact with the baryons, for example a photon can scatter off a free electron (known as Thomson scattering or, in the relativistic case, Compton scattering). Also, a high-energy photon can ionize an atom by knocking an electron from the atom.

Cosmological Constant / Dark Energy

In the standard model of cosmology, ΛCDM, the Λ refers to the cosmological constant, or dark energy. Dark energy is a term which may account for the observations that the Universe is expanding at an accelerating rate. The nature of this term leading to the accelerated expansion of the Universe is unknown. It is known however that this ambiguous dark energy accounts for the largest component of the energy density of the present day Universe, at 73% (Komatsu et al., 2010).

1.2.2 Dark Matter Candidates

Although the consensus amongst scientists is that dark matter exists, the nature of this dark matter is unclear. There are many theories as to what it might be made up of. It is known that dark matter interacts with normal matter through the gravitational force. Particle physics provides a number of possible candidates which are Weakly Interacting Massive Particles (WIMPs). These candidates include heavy neutrinos or a supersymmetric particle. To understand the true nature of dark matter particles, particle physics experiments at accelerators such as the LHC[5] must produce them and study their quantum properties.

1.2.3 Structure Formation

From observations of the CMB we know that the Universe began in a hot, dense, nearly uniform state approximately 13.7Gyr ago. When we look at the Universe on small scales though, we see that it is inhomogeneous. We see structures on these small scales, from stars and planets, to galaxies, and up to scales of galaxy clusters and super clusters. From this nearly uniform early Universe, these structures have grown. Current structure formation models suggest that the Universe was formed as follows.

The very early Universe underwent a period of inflation, after which "initial" conditions of the Universe were set, including homogeneity and isotropy. At this stage, the Universe was radiation dominated, and big bang nucleosynthesis took place creating primordial elements, and the CMB was emitted. Once the Universe became dominated by matter, which is primarily dark matter, the sub-horizon areas of tiny

[5]Large Hadron Collider, http://lhc.web.cern.ch/lhc/

inhomogeneities started to undergo gravitational collapse, amplifying these small perturbations from uniformity. As dense regions became more dense, structures the size of galaxies and galaxy clusters began to form. Dark matter collapsed before recombination but baryons were supported by tight coupling to radiation, which exerted a high pressure. After recombination, pressure support of radiation was much reduced, and baryons fell into the dark matter potential wells. It was at this point that baryonic matter began to form stars and galaxies. In this model, structure forms hierarchically, with the smallest structures forming first, followed by groups, clusters and superclusters of galaxies.

In terms of galaxy formation, there is some evidence to suggest that this hierarchical model is incorrect. Studies of galaxies show "downsizing" rather than hierarchical formation. Examples of downsizing which have been observed are the fact that more massive galaxies form at higher redshift than low mass galaxies and that the stars in more massive galaxies are seen to have formed earlier and over a shorter timescale (See Neistein et al. (2006); Fontanot et al. (2009) and references therein).

1.2.4 Cosmological Parameters

The Hubble constant, H_0 measures the rate of expansion of the Universe, and is measured primarily from the expansion rate of the local Universe. It is currently thought that the value of this is $H_0 = 72 \pm 8\text{km s}^{-1}\text{Mpc}^{-1}$ (Freedman et al., 2001). The results from the fifth year data release of WMAP find that the value of the matter density $\Omega_m \sim 0.27$ (Komatsu et al., 2009). The value of the baryon density Ω_b can be found using $\Omega_b = 0.02h^{-2}$, which using the above value of the Hubble constant gives $\Omega_b = 0.04$. Supernovae observations tell us that the Universe is expanding at an accelerating rate (Riess et al., 1998; Perlmutter et al., 1999). Combining these results of a flat Universe obtained with CMB measurements, then this value can be calculated. Currently, $\Omega_\Lambda \sim 0.73$, implying 73% of the energy density of the present Universe is in this form (Komatsu et al., 2010). The dark energy equation of state, w, was proposed by Einstein to have a value of $w = -1$. Observations of CMB patterns, combined with observations of large scale structure are consistent with Einstein's cosmological constant of $w = -1$, and with no spatial curvature $\Omega_k = 0$.

Dark energy accounts for 73% of the energy density of the present Universe, and yet its existence and nature is not understood. Together, dark energy and dark matter pose some of the most important questions in fundamental physics today. Measuring accurately the equation of state of dark energy, w, is one of the biggest missions in observational cosmology today (see e.g. Refregier et al., 2010).

1.3 Galaxy Clusters

Galaxy clusters form in the densest part of the large scale structure of the Universe. Galaxy clusters are the largest gravitationally bound objects in the Universe and can be used as cosmological probes because their formation and evolution rate are sensitive to different cosmological parameters (e.g. Evrard, 1989; Haiman et al., 2001; Allen et al., 2004). The abundance of galaxy clusters as a function of mass $N(m, z)$ at high redshift z is particularly sensitive to different cosmological models. To probe cosmology and

dark energy we must observe galaxy clusters at high redshift and obtain mass estimates for them.

In this section I will discuss observational properties of galaxy clusters, look at how to measure the masses of clusters, and overview the current theory on galaxy cluster formation and evolution. For a comprehensive review of galaxy cluster properties and their evolution see Voit (2005).

1.3.1 Detecting Galaxy Clusters - Observable Properties

Galaxy clusters contain significantly more mass in the form of gas and dark matter than that from the stellar mass contained in galaxies. The large amount of gas in clusters allows them to be observed in X-ray and microwave bands, and these observations often tell us much more about the cluster than we can learn from optical observation. A cluster's total mass is made up of stars, hot gas and dark matter. Clusters typically have only 5% of their total mass in the form of baryonic matter from stars. A further 10% comes from the hot X-ray emitting gas, and the remainder is dark matter. Galaxy clusters contain $\sim 100-1000$ galaxies and have total masses in the region of $10^{14}-10^{15}M_{\odot}$, and have typical diameters of 2Mpc to 10Mpc. The velocities of individual galaxies in a cluster lie in the range $800 - 1000\text{kms}^{-1}$. Clusters typically have temperatures of $kT \gtrsim 2\text{keV}$.

In order to constrain cosmology through the cluster mass function, $N(m,z)$, there must be an unbiased sample of clusters with reliable mass estimates. In this section I will look at methods for detecting galaxy clusters. I will discuss each method's effectiveness at both cluster detection and cluster mass measurement.

Optical Observations

Although the stars in the galaxies contained in a galaxy cluster make up only a fraction of the total mass of a cluster, optical measurements have been long used to detect galaxy clusters. The Abell catalogue of clusters (Abell, 1958; Abell et al., 1989) was made from optical observations. It is made up of over 4000 clusters, and contains most of the known nearby clusters (up to redshift $z \simeq 0.2$). Cluster finding techniques today involve using either the luminosity distribution or optical richness to detect clusters. The luminosity distribution allows estimation of the total luminosity of the cluster. Optical richness is described as the number of cluster galaxies brighter than some characteristic luminosity. The brightest cluster galaxy (BCG) is then found, and distances and relative brightness of nearby galaxies are measured. Cluster membership can then be confirmed for individual galaxies using redshift or colour information, as clusters contain galaxies which are significantly redder as they often have less ongoing star formation.

A huge benefit of using optical data for cluster detection is that big data sets exist. There are many big surveys which cover large areas of the sky in optical imaging, and so optical cluster detection benefits from this data being available. Another advantage of using optical data to select clusters is that the data is high resolution - for example much higher resolution than a map obtained with weak lensing. Optical cluster detection is relatively cheap in observational terms as it can be done from the ground and cover large areas. The down side to detecting clusters optically, is that it only detects

the optical tracers, not the whole mass, as it cannot detect the gas or the dark matter. So the assumption which goes into detecting clusters using optical data, is that light traces mass. Also, clusters will often be selected using a matched filter technique, and so this might preferentially select clusters of a particular size or shape. Another possible problem of using optical data for cluster detection is in defining cluster membership, so as not to include foreground or background galaxies. This can be alleviated with colour information, by either applying colour cuts based on a colour-magnitude relationship for clusters, or using photometric redshift information.

Employing optical observations to measure cluster masses involves a number of assumptions. To estimate a mass, usually either a scaling relation between luminosity and mass is used, or else the virial theorem is applied if velocity dispersions are used. These either assume a relation between luminosity and mass (which has often been extrapolated from a small number of clusters, or a small redshift range) or it assumes virial equilibrium. The main value of obtaining mass measurements from optical data is the large area which can be covered, at a relatively low cost. The drawbacks, however, lie in the uncertainties in the scaling relations, and the fact that only the luminous baryonic matter is being observed, and a total mass extrapolated from there.

Optical data can be used to detect clusters down to small masses, for example groups of galaxies, but not out to particularly high redshift, unless very deep space based data is used.

Gravitational Lensing

Optical data can also be used with a gravitational lensing technique to detect clusters of galaxies. I will discuss in detail how this is done in Section 1.5 and Chapter 2. Here I provide an overview of using gravitational lensing for cluster detection and mass estimation for comparison with the other techniques discussed.

Gravitation lensing has the advantage that it does not only detect the luminous matter, but the whole projected mass distribution, including the large component from gas and dark matter. Because of this, cluster detections obtained using lensing are not dependent on the luminosity of optical tracers. Lensing is also sensitive to a range of mass ranges, and with deep enough data can be used to probe a higher redshift range than X-ray, although this deep lensing data is very expensive to obtain as it needs to be done from space. Even for lower redshift clusters, a drawback of using lensing for cluster detections is that to get good lensing data with a high enough number density of sources is expensive. Another drawback of using lensing for cluster detections lie in the fact that it is sensitive to line-of-sight contamination. This problem can be removed somewhat (as can the problem of Intrinsic Alignments, see Section 2.9.1), by using photometric redshift information, but this is also observationally expensive to get data in enough bands.

When it comes to methods of measuring masses of clusters, lensing is very effective. This is because, unlike optical, X-ray and SZ methods, it is measuring the projected mass distribution of the whole cluster, and is not reliant on assumptions such as hydrostatic equilibrium for the cluster gas. It is becoming increasingly apparent that we cannot fully model the complex gas physics in clusters within a simple framework, and lensing offers a solution to this. In order to turn the projected mass distribution into a mass, it is often necessary to fit the data to a mass profile. In doing this, there are

assumptions on the shape of the profile, e.g. Navarro, Frenk and White profile (NFW), or at least of circular symmetry. So, lensing mass measurements done in this way are not as accurate where there is substructure in the cluster or circular asymmetry. Also, as with using lensing for cluster detection, it is very expensive to measure masses in this way. This is particularly true for clusters at higher redshifts, as the lensing data needs to be deep enough to have enough galaxies behind the cluster in order to measure the lensing signal.

Lensing is expensive and technically demanding. It would be easier observationally to get proxies of mass from SZ or X-ray than to get masses from lensing.

X-ray Observations

In galaxy clusters, the total mass of the gas is greater than that of all stars. The deep potential wells of galaxy clusters compress and heat up the gas to X-ray emitting temperatures. The gas in galaxy clusters is between 10^7K and 10^8K, emitting X-rays in the form of bremsstrahlung and atomic line emission. The gas temperature can be inferred from a cluster's X-ray spectrum and therefore indicates the depth of the potential well, and the emission line strengths reveal the abundance of different chemical elements in the gas. Because X-ray emissivity depends on density squared, then clusters of galaxies strongly stand out against the lower density regions.

The benefits of using X-ray data for cluster detections are that by detecting the gas they are detecting more of the mass than optical tracers, and that clusters are prominent X-ray emitters. Compared to the optical bands — with many strong optical sources such as stars and galaxies — there is not much contamination from other X-ray sources. X-ray observations can be used to select lower redshift clusters, but will struggle to detect galaxy clusters beyond $z \sim 0.5$. X-ray observations are, however, less susceptible to projection effects. This is because the X-ray emissivity scales as the density squared, and so the signal coming from high density regions is stronger. Compared to optical observations, where the number counts of galaxies is more closely related to mass density, there are much less likely to be problems with projection along the line-of-sight of foreground and background objects with X-ray observations. The disadvantages to cluster detections using X-ray are that it is based on assumptions on the dynamical state of the cluster, and that the gas temperature traces mass. X-ray missions are also very expensive as they are space-based.

Mass measurements from X-ray data are based on gas temperature to mass scaling relations, and assume hydrostatic equilibrium. For this reason, the measurements of mass are less good if the dynamical state is disrupted or for example if the cluster has undergone recent merging.

Microwave Observations

Hot gas in clusters can also be observed through its effects on the Cosmic Microwave Background (CMB). The CMB is almost a perfect blackbody (Mather et al., 1990) and as the CMB photons pass through the hot gas in clusters, some of the photons are Compton scattered. This shifts the photons to higher energies. This effect is known as the Sunyaev-Zel'dovich or SZ effect and can be used to detect clusters of galaxies.

More information on the SZ effect is included in Section 1.4. The first clusters detected on the basis of their SZ signature were found by Staniszewski et al. (2008).

As a way to produce cluster catalogues, SZ has the potential to be a very powerful technique. SZ-detected clusters are in principle particularly powerful as they can be seen to high redshifts. They are also an unbiased way to detect clusters, as the SZ effect is not redshift dependent. However, the SZ effect measures the integral of pressure along line-of-sight, and so this technique is subject to projection effects (as in lensing) and the dynamical state of clusters (as in X-ray).

The intensity of the SZ effect summed over the entire cluster closely tracks the mass of the cluster (Motl et al., 2005), and so the mass can be estimated using SZ. As with X-ray and optical techniques however, this is dependent on a scaling relation relating the SZ observable to the total mass. The mass measured in this way is reliant on the accuracy of the scaling relation used. The SZ measurement is also susceptible to structure elongated along the line-of-sight, and to the cluster's dynamical state. A major advantage of SZ is that it is an unbiased detection of clusters out to high redshift, much higher redshift than lensing or X-ray measurements. It is also observationally less costly to get high redshift clusters' SZ measurements than lensing measurements.

It is clear therefore, that no one technique for cluster detection and measurement is perfect. Each method has flaws, whether it be assumptions on gas physics, or that it is observationally expensive, or that it is limited to lower redshifts. The most effective way is to combine a number of observational properties. The SZ effect can be used to detect galaxy clusters out to high redshift, but in order to constrain cosmology, it is important to have reliable mass estimates for these clusters. So, with gravitational lensing providing masses for these clusters, it is possible to find a relation between SZ signal and lensing mass. With this relation it will be possible to use the SZ to calculate a proxy for mass. By combining SZ and lensing, an unbiased catalogue of galaxy cluster positions with accurate mass measurements can be obtained.

1.3.2 Cluster Formation and Evolution

Galaxy clusters are the largest gravitationally bound objects, and they are the result of structure formation. Current structure formation theory is based around hierarchical formation, where small structures collapse first, and eventually build the largest bound structures - which today are clusters and superclusters of galaxies, filaments and sheets. Thus the growth and evolution of clusters directly traces the process of structure formation in the Universe.

Initial density perturbations in the density distribution of cold dark matter lead to small clumps of matter deviating from the Hubble flow and these collapse under gravity. This happens because the density perturbations have larger amplitudes on smaller scales. So the first pieces of a cluster to form are these small clumps, which grow through merging and then gravitationally collapse to form larger structures.

The Cluster Mass Function

The cluster mass function, $N(m, z)$ describes the number of clusters as a function of mass and redshift. We want to measure the number density of clusters as it is sensitive

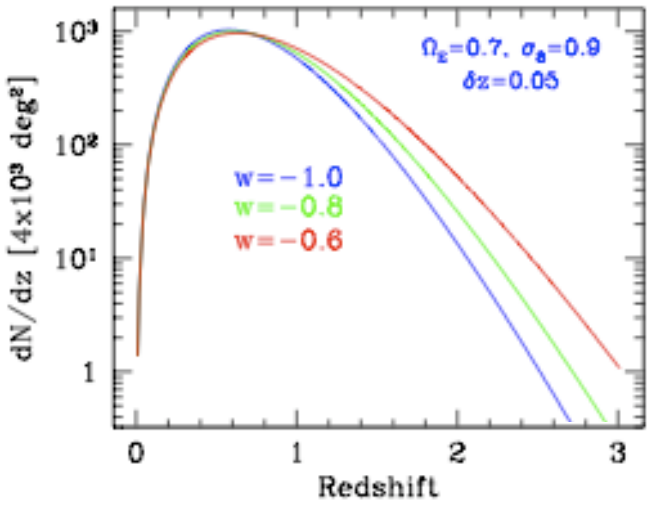

Figure 1.2: The cluster mass function for different values of w. It can be seen that, by measuring the abundance of clusters at different redshifts, these models with different dark energy equations of state can be tested. *Image credit:* Mohr (2005).

to σ_8 and the growth of density perturbations. The cluster mass function, $N(m, z)$, is also sensitive to Ω_Λ, Ω_m, H_0 and w. The cluster mass function's sensitivity to different cosmological models is well illustrated in the example shown in Figure 1.2. This figure shows a comparison of three different cosmological models, where only the dark energy equation of state w is varied as published in Mohr (2005). The three different values shown are for $w = -1$, $w = 0.8$, and $w = -0.6$, where all other cosmological parameters are kept the same. The cluster redshift distribution is sensitive to w, and it can be seen that by measuring the abundance of clusters at different redshifts, different cosmological models can be tested.

For example, if we look at Figure 1.2 in the region $z \sim 1.5$, the different models shown vary by about $10 - 20\%$. If we wanted to measure these to around 1% accuracy then we would need $N \sim 10^4$ $(1/\sqrt{N} = 0.01)$ galaxy clusters to distinguish between the models shown. However, in practice we also need to allow for the fact that other variables can change in the cosmological models (not only w), and so even more clusters would be needed to constrain w. Projects such as the Dark Energy Survey (DES)[6], will be able to test this given the large areas they can cover.

1.3.3 Measuring Cluster Mass

In order to measure $N(m, z)$ it is necessary to have mass estimates for galaxy clusters. This is usually done by defining a shape of a mass profile for the cluster, and estimating the mass within some defined radius. This section will look at how to define a cluster mass profile, and the definition of a commonly used profile, the Navarro, Frenk and White profile.

[6]DES, http://www.darkenergysurvey.org/

Cluster Mass Profiles

Observations of galaxy clusters reveal that the velocity dispersion of a cluster's galaxies is relatively constant with distance from the cluster centre. When modelling this effect, a useful model to start with is the simple isothermal model, where the density $\rho \propto r^{-2}$. The simplest analytical isothermal model is the Singular Isothermal Sphere (SIS) model which takes the form:

$$\rho(r) = \frac{\sigma_v^2}{2\pi G r^2}, \tag{1.31}$$

where σ_v is the velocity dispersion (see e.g. Binney & Tremaine, 1987). This model is unphysical, however, because of its singularity at $r = 0$, and the total mass diverges with radius and so the corresponding SIS mass is infinite.

Results from numerical simulations of galaxy cluster formation show that the dark matter halos have slopes which are shallower than isothermal at small radii, and steeper than isothermal at larger radii. Mass profiles of this sort can be expressed as:

$$\rho_M(r) \propto r^{-p}(r + r_s)^{p-q} \tag{1.32}$$

where p and q describe the inner and outer slopes of the power law, and r_s describes where the profile steepens.

There are a few examples of profiles which fit this prescription (including the Moore profile with $p = 1.5$, $q = 3$ (Moore et al., 1998), and the Rasia profile with $p = 1$, $q = 2.5$ (Rasia et al., 2004)) but the most widely used model for dark matter density profiles is the Navarro, Frenk and White profile, or NFW profile, with $p = 1$ and $q = 3$ (Navarro, Frenk & White, 1996).

The NFW profile is parameterised by a virial radius r_{200}, and a dimensionless concentration parameter c_s. Navarro, Frenk & White (1996) find that the density profile of the halo is

$$\rho(r) = \frac{\delta_c \rho_c}{(r/r_s)\,(1 + r/r_s)^2}\,. \tag{1.33}$$

where $\rho_c = \frac{3H^2(z)}{8\pi G}$ (see Section 1.1.1). The concentration parameter c_s is defined through r_{200} and the scale radius, r_s to be

$$c_s = \frac{r_{200}}{r_s} \tag{1.34}$$

where r_{200} is defined such that the mass density of the halo within r_{200} is 200 times the critical density of the Universe (at the redshift of the halo). The characteristic overdensity of the halo, δ_c, is

$$\delta_c = \frac{200}{3}\frac{c_s^3}{\ln(1 + c_s) + c_s/(1 + c_s)}\,. \tag{1.35}$$

Properties of the NFW profile used for lensing will be described in section 2.8.2.

Observationally, there is significant discussion about the type of universal profile which best fits galaxy clusters. NFW is by no means standard, and has the drawback that the simulations do not probe the inner slope well (due to the resolution of the

simulations) and that the simulations do not include the gravitational potential of the baryonic component (because of the computational time necessary for this), which is significant at the centre of clusters. One method to test the shape of profiles is to use strong or weak lensing. Cluster profiles are tested in Broadhurst et al. (2005); Limousin et al. (2008); Richard et al. (2009) who present results which are in good agreement with numerical simulations, however Sand et al. (2004, 2008) present evidence for shallower profiles. Using X-ray observations, different inner slopes of the profiles are also found (Ettori et al., 2002; Lewis et al., 2003; Zappacosta et al., 2006; Saha & Read, 2009). In the case of cluster profile investigations using lensing and X-ray, often only one or a few clusters are investigated, and so it is thus far difficult to test the universality of cluster profiles. For a recent summary of observational results testing cluster profiles see the introduction of Host & Hansen (2009). Host & Hansen (2009) also test the shape of cluster profiles using 11 galaxy clusters and find a strong indication for a non-universal profile. They acknowledge that because of the small sample size (although bigger than many others) is not sufficient to rule out the numerical predictions of a universal model.

The NFW profile assumes spherical symmetry. For halos which are very triaxial, Corless & King (2007) showed that neglecting halo triaxiality in parameterised NFW fits can lead to an overestimate of halo mass by up to 50% and an underestimate of concentration by a factor of 2. This should be particularly taken into account for strong lensing candidates as Corless & King (2007) show that these extremely triaxial halos are particularly efficient lenses (especially when elongated along the line-of-sight).

Concentration

The concentration parameter described above can be thought of as a way of expressing the transition of the density profile from shallow to steep. A more general form of the concentration parameter is $c_s = r_b/r_s$, where r_b is the bounding radius, and is most often chosen to be the virial radius, r_υ or r_{200}. Typical values of the concentration parameter from simulated clusters are $c_s \simeq 4 - 10$ (Voit, 2005). It has also been shown with simulations that lower mass clusters tend to have higher concentration values because they formed earlier when the density of the Universe was larger (Jing, 2000; Bullock et al., 2001; Jing et al., 2007).

Defining Cluster Mass

In order to define a cluster mass, a boundary for the edge of the cluster must be defined. It is common for a cluster mass to be defined with respect to the mean background matter density, or to the critical density, ρ_{cr}. If defined in the latter way, the cluster mass M_Δ is the amount of matter contained in a sphere of radius r_Δ whose mean density is $\Delta \times \rho_{cr}$. Often $\Delta = 200$ or $\Delta = 500$ is used by observers rather than the virial radius, as it is easier to observe properties of the cluster in outer regions where the density contrast is higher, and simulations show that the region within r_{500} is considerably more relaxed than within the virial radius r_υ. So a cluster mass defined as M_{200} is the mass within a region in which the density is 200 times the critical density ρ_{cr}. Do be careful to check in the literature as to to which definition is being used as sometimes it is not ρ_{cr} but the mean background matter density $\Omega_m \rho_{cr}$.

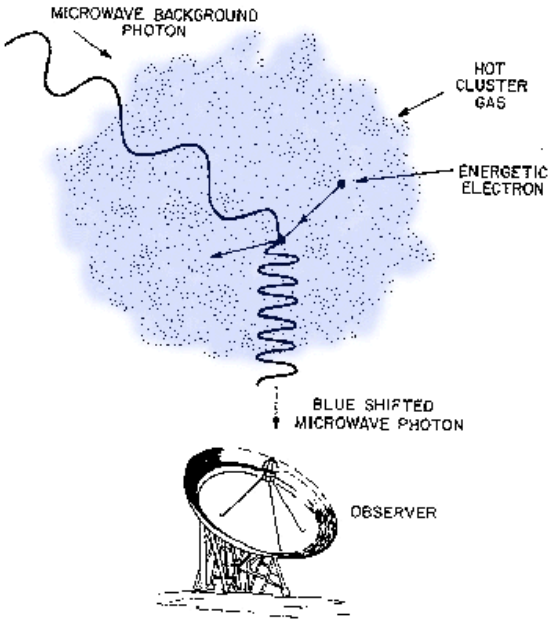

Figure 1.3: Schematic of the SZ effect. As a CMB photon passes through hot gas in a galaxy cluster, it is inverse Compton scattered and gains energy. This shift in frequency can be used to detect galaxy clusters. *Image credit:* http://astro.uchicago.edu/sza/ .

1.4 Sunyaev-Zel'dovich Effect

1.4.1 Introduction to SZ Theory

The Sunyaev-Zel'dovich, or SZ, effect is due to the inverse Compton scattering of the Cosmic Microwave Background (CMB) radiation (Sunyaev & Zel'dovich, 1981). The SZ effect occurs when high energy electrons in the hot gas of galaxy clusters inverse Compton scatter with photons from the CMB. After this process, the CMB photon gains a small amount of energy. An illustration of this process is shown in Figure 1.3. This interaction is most evident in the case of galaxy clusters because they are so massive. It is thought that about 1% of CMB photons are scattered in this way when they pass through cluster gas. When the CMB is observed in the direction of a galaxy cluster a deficit of CMB photons is seen (see, for example, Dawson et al. (2006)).

When the spectrum of the CMB is observed in the direction of a galaxy cluster, the SZ effect alters the intensity of the radiation. There are fewer low energy photons, and more photons with higher energy than one would expect from the CMB. The SZ effect has a unique spectral signature. It shows a decrease in CMB intensity at frequencies lower than 218GHz and increase at higher frequencies. Figure 1.4 shows the distortion of the CMB spectrum by the SZ effect (solid line) and that of the undistorted CMB (dashed line). This spectrum is for a fictional cluster which is 1000 times more massive than the average cluster, so that this effect is illustrated clearly. From this plot it can be seen that the intensity of photons below $\sim$ 218GHz is less than expected, and is higher at higher frequencies due to the SZ effect. For a real cluster, the distortion would be much smaller, of the order of mK. The $\sim$ 218GHz limit is the same for all clusters of all masses, and this value of the SZ limit arises because of the shape of the Black Body

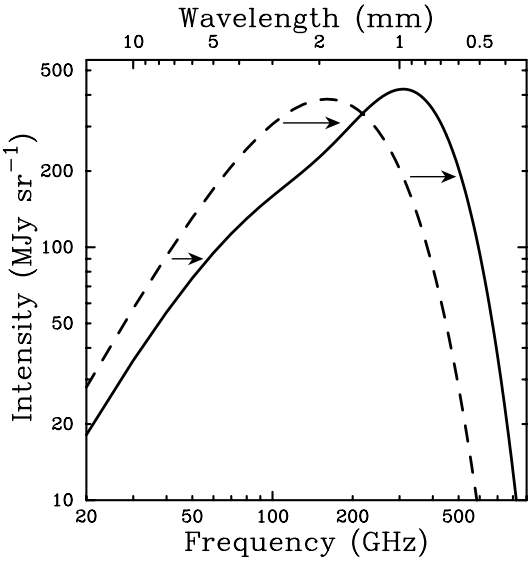

Figure 1.4: The result of the Sunyaev-Zel'dovich effect on the CMB spectrum. The spectrum of the undistorted CMB (dashed line), and the spectrum after SZ interactions (solid line). This distortion is what would be seen for a cluster 1000 times more massive than the average cluster, so that the effect can be seen clearly. Below ~ 218GHz the intensity of the CMB spectrum is decreased, and above ~ 218GHz the intensity is increased. *Image credit:* Carlstrom et al. (2002).

spectra. Because the scattering is increasing the energies of the photons, it changes the shape of the spectra we observe, with there being more high energy photons, and less with lower energies. As illustrated in Figure 1.4, the value of ~ 218GHz is where the undistorted and distorted spectra cross over.

Observers can use the SZ effect to find galaxy clusters. Due to the fact that the SZ effect is independent of redshift, it can be used to find galaxy clusters out to high redshift. This potentially allows observers to make a complete catalogue of clusters using the SZ effect.

1.4.2 Y parameter

The SZ Compton y parameter is a measure of how much the photons are up-scattered by hot electrons in a cluster. It characterises how much the CMB spectra is distorted by the cluster. The integrated Compton y paramater, Y, is a robust measure of the SZ signal since it is model-independent and simply sums the pixels in the observed maps (Benson et al., 2004). The value of $Y(\theta)$ (Y within some radius θ) is often quoted in SZ observations e.g. Hincks et al. (2009).

The SZ Compton y parameter is defined as

$$y = \frac{\sigma_T}{m_e c^2} \int \mathrm{d}l \, n_e k T_e = \frac{\sigma_T}{m_e c^2} \int \mathrm{d}l \, p_e \tag{1.36}$$

where σ_T is the Thompson cross section, c is the speed of light, k is Boltzmann's constant, n_e is the electron number density, T_e is the electron temperature, m_e is the

mass of the electron, and p_e is the electron pressure. The integrated Y parameter over solid angle is

$$Y = \int \mathrm{d}\Omega y(\Omega). \tag{1.37}$$

To compute Y we assume that gas follows dark matter and obtain an analytic result. It ignores the gas history (cf. Reid & Spergel (2006)[7]) but our simple model agrees, within 25%, with the empirical scaling relations of Motl et al. (2005) and Nagai (2006), and is supported by Atrio-Barandela et al. (2008) who show from stacked SZ clusters that the baryon profile is consistent with NFW. Y as a function of M_{200} is:

$$Y(M_{200}) = \frac{c_s \sigma_T \Omega_b (1+z)(GH_0)^{2/3} \delta_{200}^{1/3} M_{200}^{5/3}}{6 m_e c^2 D_A^2 \alpha \Omega_m [\ln(1+c_s) - c_s/(1+c_s)]^2}\,, \tag{1.38}$$

where c_s is the concentration (as introduced in Equation 1.34), D_A its angular diameter distance, M_{200} its mass within an overdensity $\delta_{200} = 200$, α is the total pressure divided by the electron pressure. For the derivation of this result see Appendix A.

The Compton Y parameter will be affected by the dynamical state of a cluster. For example if a cluster is undergoing merging or has significant or substructure then the simplified equations presented here, which assume hydrostatic equilibrium, will be in error.

1.4.3 The Power of Observing with SZ

Observations of the Sunyaev-Zel'dovich (SZ) effect (Sunyaev & Zel'dovich, 1981) are a powerful way to probe galaxy clusters by detecting the hot cluster gas (Birkinshaw, 1999). SZ-detected clusters are in principle particularly powerful as they can be seen to high redshifts. The intensity of the SZ effect summed over the entire cluster closely tracks the mass of the cluster (Motl et al., 2005) and so a lower mass cluster gives a weaker SZ signal than a higher mass cluster.

However it is the SZ decrement (Y) which is measured, not the mass, and — in order to use SZ observations to probe cluster properties and cosmological models — it is important to understand the mass - Y relationship. Although the Y measurement does give a rough mass estimate from the gas, without knowing about the other components of the cluster there are large uncertainties. By using projected mass measurements of clusters from gravitational lensing (which probes the whole cluster and not just the gas) it is possible to compare the SZ observables to these masses. Thus for low redshift clusters where lensing measurements are available, the calibration of the relationship between SZ and the cluster mass can be found (Lewis & King (2006), Sealfon et al. (2006)). To test the cluster mass function, we still need to obtain masses of high redshift clusters, and with the relationship between SZ and cluster mass at low z, the relation can be extrapolated to higher z to obtain accurate masses for all SZ detections.

[7] In the model of Reid & Spergel (2006), cluster asphericity, thermal conduction, intracluster magnetic fields, turbulent support and dynamical events such as mergers are ignored.

Current and Future SZ Surveys

SZ detections of previously known clusters have been made for tens of X-ray and optically selected clusters. What is particularly exciting now though is that the first clusters have been detected by their SZ signature.

A large area in the southern sky is currently being surveyed in SZ by the Atacama Cosmology Telescope (ACT) and the South Pole Telescope (SPT). The first clusters to be detected by their SZ decrement were found by Staniszewski et al. (2008) using the South Pole Telescope (SPT). These four clusters mark the start of using SZ surveys for cluster detection. Further SPT results have been published by Plagge et al. (2009) on clusters previously detected in X-ray. The first ACT results were published in (Hincks et al., 2009).

A new CMB mission called Planck[8] will survey the entire sky. Planck will be powerful at detecting the SZ effect because it has many frequency bands, both sides of 218GHz, and so the cross over between a decrement at lower frequencies, and increment at higher frequencies will be probed. This will allow the SZ signature to be distinguished from other effects or foreground contamination. Planck will be complemented by a full sky lensing analysis from the Pan-STARRS[9] survey. The relation between SZ and total cluster mass can be tested with the huge sample of clusters which will arise from these large area surveys.

1.5 Lensing and Cosmology

Many important cosmological results have been derived from the analysis of gravitational lensing effects. The theory of gravitational lensing will be introduced and discussed in Chapter 2 and is then used as an analysis technique throughout the rest of this thesis. Firstly, in this section, I will review some of the observational results of lensing, and describe how lensing can be used to constrain cosmology.

Gravitational lensing is dependent only on the projected mass distribution of the lens and so it is possible to study the mass distribution independent of its form, including the distribution of dark matter. It can be used to map the distribution of matter — including the elusive dark component — around galaxies, clusters of galaxies and on cosmological scales. Weak gravitational lensing causes small ($\sim$ a few %) changes to the shape of individual galaxies, which can be used to reconstruct the mass distribution in the region (Kaiser & Squires, 1993). Furthermore, the measurement of these lensing induced distortions of the shapes of distant galaxies is a powerful probe of dark energy and the geometry of the Universe. For recent reviews of weak lensing see Munshi et al. (2008) and Hoekstra & Jain (2008).

1.5.1 Cosmic Shear and Dark Energy

Light bundles propagating through the Universe are continually deflected by the large scale structure of the Universe. This lensing effect is known as *cosmic shear*. Cosmic

[8]Planck, http://www.esa.int/esaMI/Planck/

[9]Pan-STARRS, http://pan-starrs.ifa.hawaii.edu/public/

shear can be measured through correlation functions and aperture mass statistics. The cosmic shear signal depends on

- the cosmological model ($\Omega_m, \Omega_\Lambda, \Omega_v, w, H_0, ...$)
- the normalisation of σ_8 of the power spectrum
- the redshift distribution of the sources.

By measuring the correlation function over a significant range of angular scales, these parameters can be constrained. The measurement accuracy of the correlation function depends on the number density of galaxies (the number of galaxies per square arc minute), which is determined by the depth of the data and image quality, and the size of the area covered. Noise on this measurement is a combination of intrinsic ellipticity distribution and cosmic variance.

The Canada-France-Hawaii-Telescope Legacy Survey (CFHTLS) is the largest cosmic shear survey to date. CFHTLS is a 170 square degrees imaging survey in five optical bands. The results from the first year data from the CFHTLS survey were published in Hoekstra et al. (2006) and Semboloni et al. (2006).

1.5.2 Lensing by Galaxy Clusters - Observational Results

Reconstructing the mass distribution of galaxy clusters using weak lensing has now become routine. Reconstructions have shown that the mass distribution is quite similar to that of the projected galaxy distribution (Gray et al., 2002, 2009), and that of the X-ray emission for relaxed clusters. A cluster system which is not relaxed, is the Bullet Cluster (Clowe et al., 2006), and I discuss the results of lensing analysis, and the implications, of this in Section 2.2. Another cluster which has been found with gravitational lensing to be undergoing merging is MACS J0025.4-1222 (Bradač et al., 2008). Lensing is independent of the dynamical state of clusters and so lensing mass reconstructions do not rely on assumptions of gas physics as SZ and X-ray methods do.

Lensing can be used to provide mass estimates of clusters. However, there exists a degeneracy which means that obtaining the absolute value of κ from mass maps is not possible. This is called the *mass sheet degeneracy*. It means that although the relative convergence can be mapped, the absolute level of the convergence can have some constant added to it. It is not possible, without an independent measurement of the magnification or further assumptions, to break this degeneracy (Bradač et al., 2004). If the cluster surface mass density is found to be κ, then there exists a whole set of lens models with mass distribution

$$\kappa_\lambda = \lambda\kappa + (1 - \lambda) \tag{1.39}$$

which fit equally well (Schneider, 2006a). Here λ is an unknown constant, and the term $1 - \lambda = \kappa_c$ corresponds to adding a homogeneous surface mass density κ_c to the mass distribution.

The mass-sheet degeneracy means that model-free determination of cluster mass cannot be done, however by using fitting models (such as NFW), profile parameters can be determined. This means that masses are model-dependent, and so if the halo is triaxial, or has significant substructure, a lensing mass measurement will be less

accurate. Clusters which have triaxial halos will have underestimated concentrations if spherical symmetry has been assumed (see Section 1.3.3).

As well as providing masses for known clusters, lensing can be used as a way to find clusters. A lensing mass reconstruction of Abell 1705 by Dahle et al. (2002) showed a mass peak south west of the cluster. This has now been confirmed optically, and shows that lensing maps can be used to detect clusters of mass. Wittman et al. (2006) were the first to present a sample of galaxy clusters selected blind by their weak gravitational lensing shear signal in the Deep Lens Survey, showing the potential of shear-selected cluster catalogues.

Gravitational lensing is a very powerful method to search for dark matter halos because it is independent of baryonic properties (which determine luminosities). The method has the potential to be able to detect dark clumps of matter too. Dietrich et al. (2005) present a mass reconstruction of the double cluster Abell 222 and Abell 223, and they show evidence for a possible dark filament between this close pair of clusters.

3D Maps and Tomography

Given distance information for each of the sources, it is possible to build a 3D map of the mass density. The technique used to calculate distance to each source is called photometric redshift. The photometric redshift is calculated using photometry with standard filters to determine the redshift of the object. The filters used are quite broad, so the technique depends on the source having strong features which can be easily recognised. This technique differs from spectroscopic redshifts, where spectroscopy (rather than photometry) is used to calculate redshift.

3D lensing reconstructions require deep data, and accurate photometric redshifts. The COSMOS survey used Hubble Space Telescope data with extensive follow up data to map the three-dimensional large scale structure (Massey et al., 2007a). Figure 1.5 is from Massey et al. (2007a) and shows this three dimensional lensing reconstruction. A 3D mapping, or *tomography*, technique is also shown in Simon et al. (2009).

1.5.3 Future Lensing Surveys

The next generation of large-area lensing surveys include Pan-STARRS[10] , Dark Energy Survey (DES)[11], Euclid[12], Joint Dark Energy Mission (JDEM)[13], VLT Survey Telescope - Kilo-Degree Survey (VST-KIDS)[14], the Large Synoptic Survey Telescope (LSST)[15] and High Altitude Lensing Observatory (HALO). Of the ground based surveys, VST-KIDS will cover 1500 square degrees, Pan-STARRS will carry out a 3π survey, DES 5,000 square degrees and LSST, 20,000 square degrees. HALO, is a 1,500 sq deg balloon based survey that will fly above 99% of the Earths atmosphere to observe gravitational lensing. JDEM and Euclid are space based surveys, and Euclid is designed to span 20,000 square degrees.

[10]Pan-STARRS, http://pan-starrs.ifa.hawaii.edu/public/
[11]DES, http://www.darkenergysurvey.org/
[12]Euclid, http://sci.esa.int/euclid
[13]JDEM, http://jdem.gsfc.nasa.gov/
[14]VST-KIDS, http://www.astro-wise.org/projects/KIDS/
[15]LSST, http://www.lsst.org/lsst

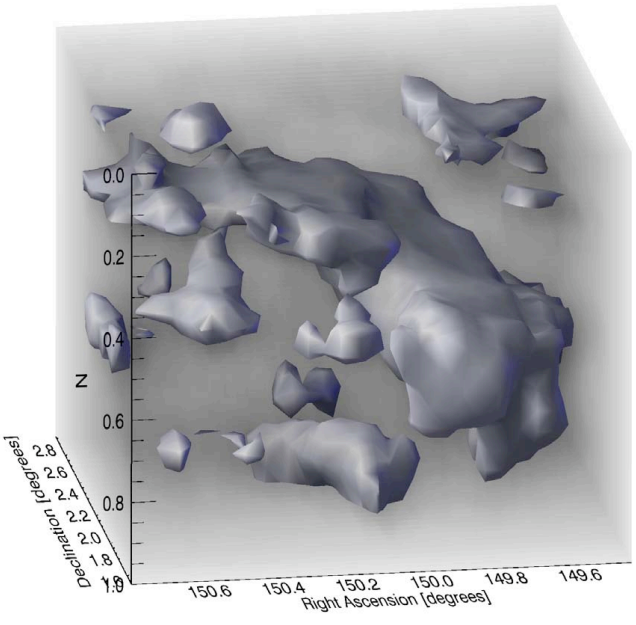

Figure 1.5: 3D lensing reconstruction of large scale structure from the COSMOS survey. *Image credit:* Massey et al. (2007a).

These large-area surveys will allow lensing measurements of nearly the whole sky, and will be able to measure masses for the many new galaxy clusters which could be found with the new large-area SZ surveys.

1.6 Outline of Thesis

We have now been introduced to the concordance model of cosmology which is the model underpinning our understanding of the Universe. We have seen the relevance of galaxy clusters to cosmology, and seen that SZ and gravitational lensing can be powerful probes of these clusters. Now that we have been introduced to the necessary background of the thesis, I will outline the following chapters.

- In **Chapter 2** I go through in detail the theory of weak gravitational lensing, introducing and deriving key equations which will be used in the research detailed in the following chapters.

- In the **3**rd **Chapter** I detail a new weak lensing pipeline and discuss the results of testing it on simulations. I then introduce the data set which has been used in this research, the Southern Cosmology Survey (SCS), and report on the results of using the pipeline to test these data.

- In **Chapter 4** I report on results of comparing the results of the SCS gravitational lensing analysis to Sunyaev-Zel'dovich data, and present the first lensing measurements of Sunyaev-Zel'dovich detected galaxy clusters.

- In the **5th Chapter** I examine the comparison of gravitational lensing masses of galaxy clusters to optical observables, test a weak lensing - luminosity scaling relation, and stack the clusters to test the shape of the mass profile.
- Finally, **Chapter 6** contains a summary of the work contained in this thesis, and makes suggestions towards future work to lead on from the results presented here.

Chapter 2

Weak Gravitational Lensing Theory

When light passes close to a massive object, its path is bent by the object's gravitational field. The term used to describe light deflection by massive bodies, and the resulting observational effect, is 'gravitational lensing'. The object bending the light ray is known as a 'gravitational lens' because it acts in a similar way to an optical lens.

Gravitational lensing is independent of the luminosity of the lens, and thus it provides a way to study the dark universe — which we cannot observe directly — including the distribution of dark matter. Gravitational lensing is an invaluable technique to map mass distributions and to measure masses of objects, such as galaxy clusters, because it does not depend on detecting luminous matter or rely on assumptions of hydrostatic equilibrium or other gas physics. It allows us to measure the entire mass distribution, not only the baryons or the gas, but also the dark matter. Gravitational lensing is also a very useful tool for cosmology and can be used to constrain cosmological parameters which tell us about the construction of our universe. For comprehensive reviews of gravitational lensing see Narayan & Bartelmann (1996); Bartelmann & Schneider (2001); Schneider (2006a,b); Hoekstra & Jain (2008); Munshi et al. (2008).

In this chapter I present the gravitational lensing theory necessary for the work in this thesis, starting with basic weak gravitational lensing theory. Weak gravitational lensing typically causes small ($\sim$ a few %) changes to the shape of individual galaxies. By measuring the shapes and orientations of galaxies over a large area of sky, the average *shear* can be measured, and these distortions can be used to reconstruct the mass distribution in the region (Kaiser & Squires, 1993). I will describe how to measure the shear of individual galaxies, and how these shear measurements can be used to reconstruct the mass distribution. I will then discuss how to use shear measurements to estimate masses of galaxy clusters.

2.1 Lensing régimes

Tidal gravitational fields cause differential deflection of light rays. This means that the size and shape of their projection on the sky are changed. In some cases the deflection can be so strong that luminous 'arcs' or *Einstein rings* are observed (see Figure 2.1 for an example of arcs). In some cases light rays passing close to a sufficiently massive body can be bent so strongly that multiple rays can reach the observer. This means that multiple images of the same object are observed, each in the direction that a ray has

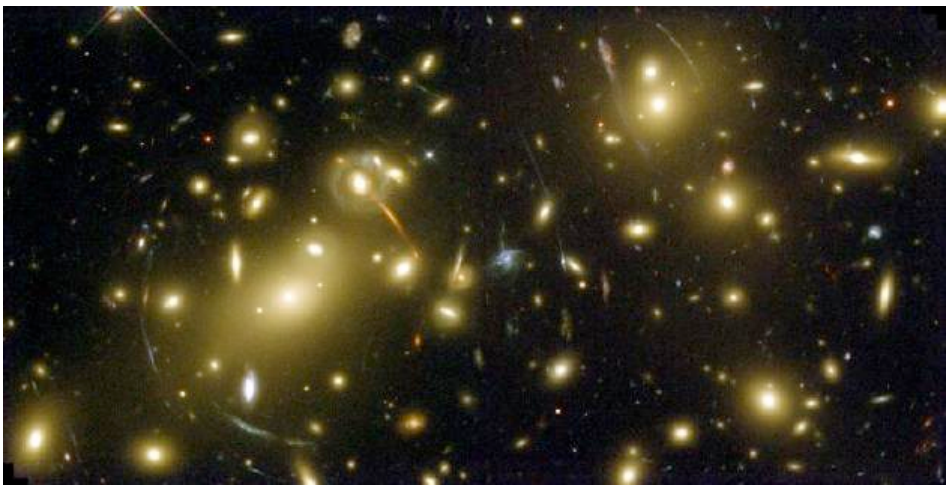

Figure 2.1: Arcs caused by Gravitational Lensing. *Image credit:* Bartelmann (2006).

arrived. Also, large galaxy clusters can magnify distant sources. This magnification effect is sometimes referred to as a *cosmic telescope* or *gravitational telescope*. This is because it allows us observe objects which would otherwise be too faint or distant to observe. This gravitational effect occurs because gravitational lenses concentrate light from distant objects (Kneib et al., 1996; Santos et al., 2004; Kneib et al., 2004), and thus we can study instrinsically faint sources using the lens as a gravitational telescope. See Kochanek (2004) for a full review of strong lensing.

Einstein rings, arcs, and multiple images are all effects classed as *strong* gravitational lensing. Weaker gravitational effects occur more often, however. Although these weak distortions are small and can hardly be noticed in an individual image, the net distortion averaged over an area of sky can be detected. These distortion effects due to *weak* lensing can be used to give us statistical properties of the matter distribution between us and the lensed source.

In a third lensing régime —micro-lensing — magnification of a distant source can occur. Micro-lensing can be thought of as a version of strong lensing where the image separation is too small to be resolved. Multiple images are formed but their separations are below the limiting resolution of our observations and this causes the source to appear magnified. Micro-lensing occurs for sufficiently small lens masses (such as a star), and for sufficiently distant sources and lenses. See Wambsganss (2006) for a review of micro-lensing.

Whether strong, weak or micro-lensing effects are seen depends on the the size of the *lensing potential*, which we will meet shortly. The work in this thesis is based on the theories of weak lensing, and so many of the derivations in the following sections are those for a weak gravitational field.

2.2 Applications of Gravitational Lensing

Gravitational lensing is a tool which is used by observational cosmologists. There are two main areas which this tool can be applied: 1) probing dark matter and 2) probing

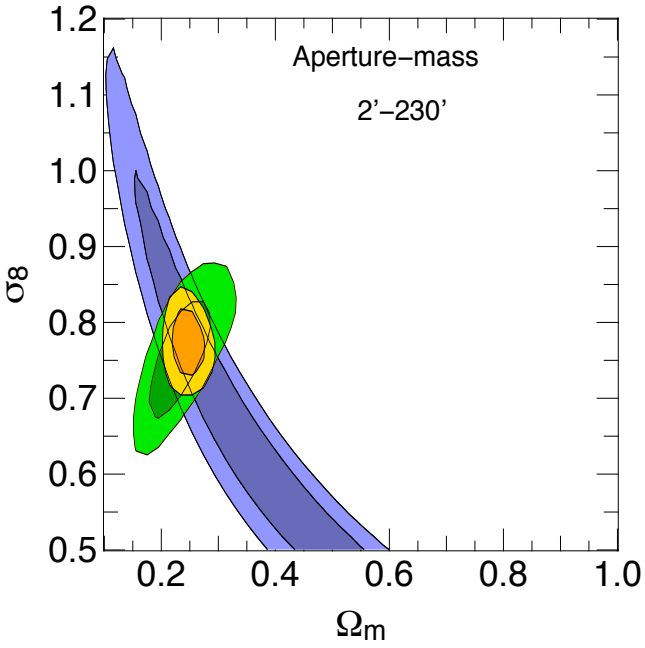

Figure 2.2: Cosmological parameter constraints from CFHTLS results from Fu et al. (2008) in blue and WMAP3 results from Spergel et al. (2007) in green. Contours levels are at 1 and 2σ. The combined contours of WMAP3 and CFHTLS are shown in orange. *Image credit:* Fu et al. (2008).

the geometry of the universe.

1. Gravitational lensing depends only on the projected 2D mass distribution of the lens and not on whether the matter is baryonic matter or dark matter. Dark matter can thus be investigated using this method as the lens is independent of luminosity and composition.

2. Gravitational lensing not only tells us about the lensing object, but about the space that the light ray has travelled through to reach us from its source. Cosmological parameters including σ_8 and Ω_m can be constrained through lensing (Bacon et al., 2000; Hoekstra et al., 2002; Benjamin et al., 2007; Fu et al., 2008; Kilbinger et al., 2009; Schrabback et al., 2009).

Lensing results can constrain a combination of Ω_m and σ_8. This is clearly demonstrated in Figure 2.2 (from Fu et al. (2008)) which shows lensing results from the CFHTLS (Fu et al., 2008) in blue. Cosmic shear analyses can be combined with other methods, such as CMB measurements, to further constrain the parameters Ω_m and σ_8. The WMAP3 CMB results are shown in green (Spergel et al., 2007), and the combined WMAP3 and CFHTLS contours are shown in orange. This joint analysis of CFHTLS and WMAP3 provides the result $\Omega_m = 0.248 \pm 0.019$ and $\sigma_8 = 0.771 \pm 0.029$ (Fu et al., 2008).

A good example of gravitational lensing being used to detect dark matter is the Bullet Cluster (Clowe et al., 2006). The Bullet Cluster is in fact two clusters which have collided, and they provide evidence for dark matter. Its name comes from the

Figure 2.3: Image of the Bullet Cluster. *Image credit:* NASA and Markevitch et al. (2002); Clowe et al. (2006). The mass map (dark matter) is shown in blue, and the X-ray is shown in pink, both on top of the optical image. The dark matter map has been made using gravitational lensing mass reconstruction - a unique way to probe dark matter. You can see that the X-ray gas has interacted when the two clusters have passed through each other, while the majority of the mass of the two clusters has not interacted, and have passed without a collision. This is evidence for collisionless dark matter.

shape of the shock front formed by the gas. Figure 2.3 shows an image of the Bullet Cluster made by NASA using an X-ray map from Markevitch et al. (2002) and an optical image and lensing map from Clowe et al. (2006). In a galaxy cluster, baryonic matter is mostly contained in the gas (5 times as much baryonic matter in the gas than in the stars). The lensing mass map is in blue and it shows where the mass lies. The X-ray map is shown in pink, and these are both on top of the optical image. It can be seen that the X-ray map and the lensing map do not coincide. The mass concentration is where the galaxies are, not where the X-ray gas is. This is direct proof that the majority of the mass in these clusters is not made up from the X-ray gas. It also tells us that this matter detected in the lensing maps is collisionless matter. We know this because from the X-ray map we can see that the gas has interacted when the two clusters passed through each other, while the majority of mass has not interacted, and has passed without a collision. This provides strong evidence for the existence of collisionless dark matter.

2.3 The Principles of Weak Gravitational Lensing

To understand how lensing — specifically weak gravitational lensing — actually works I begin this section with light deflection and derive the equations for the deflection angle followed by the lens equation. The lens equation is the key to deriving imaging properties of the lens, and I discuss these. I then consider how, in practice, measurements of individual galaxies' shapes are made and examine the Kaiser-Squires method for mass reconstruction.

2.3.1 Light Deflection

This section and section 2.3.2 follow the approach taken in Bartelmann (2006) to derive the deflection angle of light by a point mass. To convince myself of this result, I also derived it from the geodesic equation, and then secondly with the Euler-Lagrange equation. I have included these derivations in Appendices B and C.

Using Effective Refractive Index

Fermat's principle states that light takes the path along which the travel time is extremal. This can be expressed as shown below in Eq. (2.1).

$$\delta \int_A^B n\left[n\boldsymbol{x}(l)\right] \frac{dl}{c} = 0 \,, \tag{2.1}$$

where n is the index of refraction, $\boldsymbol{x}$ is the trajectory of the photon, and we assume that the gravitational field is weak, and that the lens is small compared to cosmological distances.

For gravitational lensing, Eq. (1.3) needs to include the potential, Φ. In the weak lensing limit we can write the metric as

$$ds^2 = \left(1 + \frac{2\Phi}{c^2}\right) c^2 dt^2 - \left(1 - \frac{2\Phi}{c^2}\right) R^2(t) \left[dr^2 + S_k^2(r) d\beta^2\right] \,, \tag{2.2}$$

where Φ is the peculiar gravitational potential and the requirement for a weak field is that $|\Phi| \ll c^2$.

We know that photons travel along null geodesics and so they have $ds = 0$. Along the radial path, and taking the observer to be the origin, we can write the following:

$$\left(1 + \frac{2\Phi}{c^2}\right) c^2 dt^2 = \left(1 - \frac{2\Phi}{c^2}\right) R^2(t) dr^2 \,, \tag{2.3}$$

and so, taking $dx = R(t)dr$, c' can be thought of as the effective speed of light, in a weak gravitational field:

$$c' = \frac{|d\boldsymbol{x}|}{dt} \approx c\left(1 + \frac{2\Phi}{c^2}\right) \,. \tag{2.4}$$

This leads us to an equation for the index of refraction:

$$n \equiv \frac{c}{c'} \approx 1 - \frac{2\Phi}{c^2} \,. \tag{2.5}$$

Since $\Phi \leq 0$ and $n \geq 1$, we can see that $c' \leq c$. We have to be careful about the interpretation of writing an index of refraction for light. The speed of light in a gravitational field is reduced *as seen by an outside observer*, but of course, light as measured locally has to travel at vacuum speed c. The interpretation of this observed reduction, as seen from outside the frame, is that the clocks run slow in a gravitational field. This is an important point: light rays in a gravitational field take a longer time than they would in a vacuum. This time delay between the perturbed and the unperturbed ray is called the *Shapiro delay* and is given by

$$\Delta t = \int \frac{dl}{c'} - \int \frac{dl}{c} = \int (n-1)\frac{dl}{c} = -\frac{2}{c^3}\int \Phi dl \,. \tag{2.6}$$

We now want to apply Fermat's principle to find out the deflection angle between the perturbed and unperturbed ray. To do this, we first introduce the (so far arbitrary) curve parameter λ, such that

$$dl = \left|\frac{d\boldsymbol{x}}{d\lambda}\right| d\lambda \equiv |\dot{\boldsymbol{x}}| d\lambda \,. \tag{2.7}$$

Using the *Lagrangian* $\mathcal{L}(\boldsymbol{x}, \dot{\boldsymbol{x}}) \equiv n[\boldsymbol{x}(\lambda)]\,|\dot{\boldsymbol{x}}| = n[\boldsymbol{x}(\lambda)]\left(\dot{\boldsymbol{x}}^2\right)^{\frac{1}{2}}$, Fermat's principle can be re-expressed using the Euler-Lagrange equation

$$\frac{d}{d\lambda}\frac{\partial \mathcal{L}}{\partial \dot{\boldsymbol{x}}} = \frac{\partial \mathcal{L}}{\partial \boldsymbol{x}} \,, \tag{2.8}$$

and becomes

$$n\dot{\boldsymbol{e}} = \boldsymbol{\nabla} n - \boldsymbol{e}\cdot(\boldsymbol{\nabla}\cdot\boldsymbol{e}) \,, \tag{2.9}$$

with $\boldsymbol{e} \equiv \dot{\boldsymbol{x}}$, the tangent vector to the light ray. Eq. (2.9) gives us the *perpendicular* gradient of n, so this allows us to write

$$\dot{\boldsymbol{e}} = \frac{1}{n}\boldsymbol{\nabla}_\perp n = \boldsymbol{\nabla}_\perp \ln n = \boldsymbol{\nabla}_\perp \ln\left(1 - \frac{2\Phi}{c^2}\right) \approx -\frac{2}{c^2}\nabla_\perp \Phi \,. \tag{2.10}$$

The integral of $-\dot{\boldsymbol{e}}$ along the path gives us the *total deflection angle*,

$$\hat{\boldsymbol{\alpha}} = \frac{2}{c^2}\int_A^B \boldsymbol{\nabla}_\perp \Phi d\lambda \,. \tag{2.11}$$

Using Euler-Lagrange Equation

For weak fields we use Eq. (2.2) as our metric and define *conformal time*, in place of the usual time coordinate. Conformal time is defined by

$$d\eta = \frac{cdt}{R(t)} \,. \tag{2.12}$$

This allows us to re-write Eq. (2.2) more simply:

$$ds^2 = R^2(t)\left\{\left(1 + \frac{2\Phi}{c^2}\right)d\eta^2 - \left(1 - \frac{2\Phi}{c^2}\right)\left[dr^2 + S_k^2(r)\left(d\theta_x^2 + d\theta_y^2\right)\right]\right\} \,. \tag{2.13}$$

We can now write the metric tensor for the weakly perturbed flat FLRW metric as

$$R^2(t)\begin{pmatrix} 1+2\Phi/c^2 & 0 & 0 & 0 \\ 0 & -(1-2\Phi/c^2) & 0 & 0 \\ 0 & 0 & -r^2(1-2\Phi/c^2) & 0 \\ 0 & 0 & 0 & -r^2(1-2\Phi/c^2) \end{pmatrix} . \tag{2.14}$$

A derivation of the deflection angle using the geodesic equations is shown in Appendix B, but the most compact way to derive the deflection angle is using the Euler-

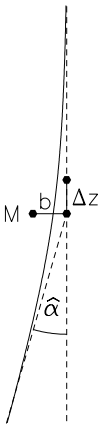

Figure 2.4: Light deflection by a point mass. The unperturbed ray passes the mass M at impact parameter b and is deflected by angle $\hat{\boldsymbol{\alpha}}$. *Image credit:* Narayan & Bartelmann (1996).

Lagrange equation. You will often see this result expressed in terms of the comoving transverse distance, $X = S_k\theta_x$. Please see Appendix C for the full derivation. This allows us to write the result:

$$\frac{d^2\boldsymbol{X}}{d\eta^2} = -\frac{2}{c^2}\boldsymbol{\nabla}_\perp\Phi \, . \tag{2.15}$$

where $\boldsymbol{\nabla}_\perp = \left(\frac{d}{dX}, \frac{d}{dY}\right)$. The integral of $-\frac{d^2X}{d\eta^2}$ along the path gives us the *total deflection angle*,

$$\hat{\boldsymbol{\alpha}} = \frac{2}{c^2}\int_A^B \boldsymbol{\nabla}_\perp\Phi d\lambda \, . \tag{2.16}$$

This is the same as we derived with the previous method (see Eq 2.11). In the cases we are interested in, the deflection angle is very small. So we can make a small angle approximation (known as Born's approximation), that the deflection angle is the same if we integrated not along the deflected ray, but along the *unperturbed* ray. For cosmological lensing, the Born approximation is very accurate (Kaiser, 1992; Bernardeau et al., 1997; Jain et al., 2000).

2.3.2 Deflection Angle of a Point Mass

To illustrate the above situation, we will now consider the deflection angle of a point mass M along the z axis (See Figure 2.4). The impact parameter, b, is the closest approach distance, and most of the deflection occurs within $\Delta z \sim \pm b$ of the closest approach. The (Newtonian) gravitational potential of the lens is

$$\Phi = -\frac{GM}{r} = -\frac{GM}{(b^2 + z^2)^{\frac{1}{2}}} \, . \tag{2.17}$$

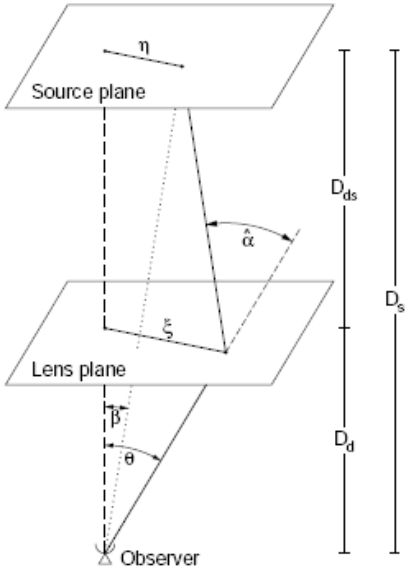

Figure 2.5: Diagram showing the angles and distances between the observer, lens plane, and source plane. *Image credit:* Bartelmann & Schneider (2001).

We now calculate an expression for $\boldsymbol{\nabla}_\perp \Phi$

$$\boldsymbol{\nabla}_\perp \Phi(b, z) = \frac{GM\boldsymbol{b}}{(b^2 + z^2)^{\frac{3}{2}}} \,, \tag{2.18}$$

and substitute this into Eq. (2.11) to give us another expression for the deflection angle

$$\hat{\boldsymbol{\alpha}} = \frac{2}{c^2} \int \boldsymbol{\nabla}_\perp \Phi dz = \frac{4GM}{c^2 b} = \frac{2}{b} R_s \,, \tag{2.19}$$

where R_s is the Schwarzschild radius of the point mass. This allows us to say that the deflection angle is just twice the inverse of the impact parameter in units of the Schwarzschild radius. Note that this deflection angle calculated using General Relativity is exactly twice the value of the angle calculated with Newtonian physics.

2.3.3 The Lens Equation and Thin Screen Approximation

Figures 2.5 and 2.6 show the source plane and the image plane of the gravitational lens system. (Here, and for the following section, please now refer to Narayan & Bartelmann (1996)). $\boldsymbol{\theta}$ is used as coordinates for the image(s) and $\boldsymbol{\beta}$ for the source(s). It can be seen from Figure 2.6 that $\boldsymbol{\theta}$ and $\boldsymbol{\beta}$ are related by Eq. (2.20)

$$D_s \boldsymbol{\beta} = D_s \boldsymbol{\theta} - D_{ds} \hat{\boldsymbol{\alpha}} \,, \tag{2.20}$$

where D_d, D_{ds} and D_s are the angular diameter distances between the observer and

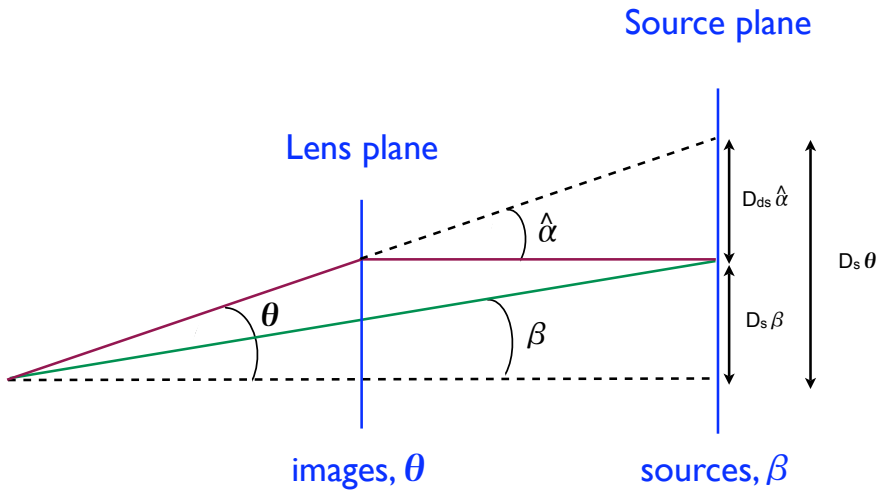

Figure 2.6: Sketch of the lens plane and source plane with angles marked. The lens equation (Eq. 2.22) can be derived from this diagram.

lens, lens and source, and observer and source respectively.[1]

We now define the *reduced deflection angle*, $\boldsymbol{\alpha}$ and define it to be

$$\boldsymbol{\alpha} \equiv \frac{D_{ds}}{D_s}\hat{\boldsymbol{\alpha}} \,. \tag{2.21}$$

This allows us to write the simple *lens equation* (or ray-tracing equation):

$$\boldsymbol{\beta} = \boldsymbol{\theta} - \boldsymbol{\alpha} \,. \tag{2.22}$$

As was said in Section 2.3.2 and illustrated in Figure 2.4, most of the light deflection occurs within $\Delta z \sim \pm b$ of the closest approach. Here Δz is usually very much smaller than the distances between both the lens and the source and the observer and the lens. If this is the case, then we can make an assumption about the lens — namely that it is a thin lens compared to the light path— and we call this the *thin screen approximation*. This approximation allows us to project the mass distribution of the lens along the line-of-sight and replace it with a mass sheet perpendicular to the line-of-sight. This allows us to define the *surface mass density* of the mass sheet

$$\Sigma(\boldsymbol{\xi}) = \int_{-\infty}^{+\infty} \rho(\boldsymbol{\xi}, z)\, dz \,, \tag{2.23}$$

where $\boldsymbol{\xi}$ is the 2 Dimensional position vector of the light ray as it hits the lens plane. The deflection angle at position $\boldsymbol{\xi}$ is then the sum of all the individual deflections due

[1]Note that, in general, $D_{ds} \neq D_s - D_d$ because these are angular diameter distances. The angular diameter distance is given in Equation 1.28.

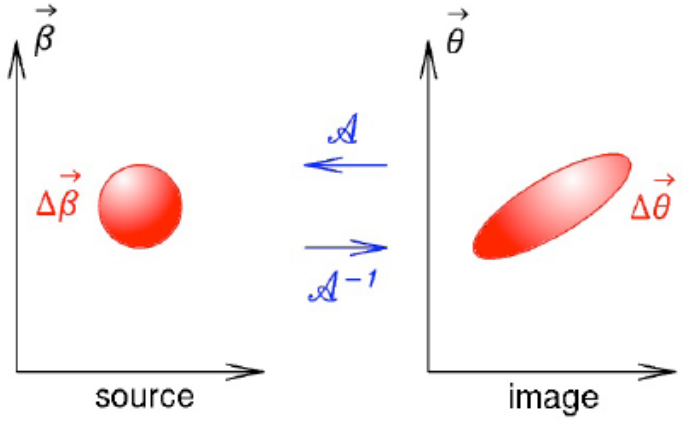

Figure 2.7: Illustration of how the Jacobian relates the source and the image. *Image credit:* Bartelmann (2006)

to all the point masses in the plane:

$$\hat{\boldsymbol{\alpha}}(\boldsymbol{\xi}) = \frac{4G}{c^2}\int \frac{(\boldsymbol{\xi}-\boldsymbol{\xi}')\,\Sigma(\boldsymbol{\xi}')}{|\boldsymbol{\xi}-\boldsymbol{\xi}'|^2} d^2\xi' \ . \tag{2.24}$$

Note that the deflection angle is linear in mass.

2.4 Mapping Between the Source and the Image Plane

The *local* imaging properties of the lens mapping between the source and the image plane are described by the Jacobian matrix, $\mathcal{A}$. (See Figure 2.7). We define the Jacobian in terms of the source and image position vectors:

$$\Delta\boldsymbol{\beta}_i = \left(\frac{\partial\boldsymbol{\beta}_i}{\partial\boldsymbol{\theta}_j}\right)\Delta\boldsymbol{\theta}_j \tag{2.25}$$

$$\Delta\boldsymbol{\beta}_i = \mathcal{A}_{ij}\Delta\boldsymbol{\theta}_j \tag{2.26}$$

where

$$\mathcal{A}_{ij} \equiv \frac{\partial\boldsymbol{\beta}_i}{\partial\boldsymbol{\theta}_j} = \delta_{ij} - \frac{\partial\boldsymbol{\alpha}_i}{\partial\boldsymbol{\theta}_j} \tag{2.27}$$

where δ_{ij} is the kronecker delta. From this point forward we will use the notation:

$$\partial_i = \frac{\partial}{\partial\boldsymbol{\theta}_i} \ . \tag{2.28}$$

This allows us to write Eq. 2.27 as

$$\mathcal{A}_{ij} = \delta_{ij} - \partial_j\boldsymbol{\alpha}_i \tag{2.29}$$

and because we know $\alpha_i = \partial_i\varphi$

$$\mathcal{A}_{ij} = \delta_{ij} - \partial_i\partial_j\varphi \ . \tag{2.30}$$

$\mathcal{A}$ is also known as the *amplification matrix*. $\mathcal{A}$ is symmetric and we can decompose it into an isotropic and an anisotropic term as follows.

$$\mathcal{A}_{ij} = \delta_{ij} - \left(\frac{1}{2}\partial^2\varphi\delta_{ij} + \left(\partial_i\partial_j\varphi - \frac{1}{2}\partial^2\varphi\delta_{ij}\right)\right) \tag{2.31}$$

which we can write as

$$\mathcal{A}_{ij} = \delta_{ij} - \kappa - \gamma_{ij} \,. \tag{2.32}$$

where the local convergence term is

$$\kappa = \frac{1}{2}\partial^2\varphi \,, \tag{2.33}$$

and the non-local shear term is (e.g. Brown et al., 2003):

$$\gamma_{ij} = \partial_i\partial_j\varphi - \frac{1}{2}\partial^2\varphi\delta_{ij} \,. \tag{2.34}$$

From Eq. 2.32 we can write γ_{ij} as

$$\gamma_{ij} = \begin{bmatrix} \partial_1^2\varphi - \frac{1}{2}\left(\partial_1^2 + \partial_2^2\right)\varphi & \partial_1\partial_2\varphi - 0 \\ \partial_2\partial_1\varphi - 0 & \partial_2^2\varphi - \frac{1}{2}\left(\partial_1^2 + \partial_2^2\right)\varphi \end{bmatrix} \tag{2.35}$$

$$\gamma_{ij} = \begin{bmatrix} \frac{1}{2}\left(\partial_1^2 - \partial_2^2\right)\varphi & \partial_1\partial_2\varphi \\ \partial_2\partial_1\varphi & -\frac{1}{2}\left(\partial_1^2 - \partial_2^2\right)\varphi \end{bmatrix} \equiv \begin{bmatrix} \gamma_1 & \gamma_2 \\ \gamma_2 & -\gamma_1 \end{bmatrix} \,, \tag{2.36}$$

and so we can write $\mathcal{A}_{ij}$ as:

$$\mathcal{A}_{ij} = \begin{bmatrix} 1-\kappa & 0 \\ 0 & 1-\kappa \end{bmatrix} + \begin{bmatrix} -\gamma_1 & -\gamma_2 \\ -\gamma_2 & \gamma_1 \end{bmatrix} \,. \tag{2.37}$$

The first term is the isotropic expansion term (this is the convergence[2] that we met earlier in the section) and the second term is the *shear* term. An illustration of the effects of each of these is shown in Figure 2.8.

Using the trace of $\mathcal{A}$ and equating Eqs. (2.37) and (2.30) lead us to the following:

$$\gamma_1 = \frac{1}{2}\left(\partial_1^2\varphi - \partial_2^2\varphi\right), \tag{2.38}$$

$$\gamma_2 = \partial_1\partial_2\varphi = \partial_2\partial_1\varphi \,, \tag{2.39}$$

$$\kappa = \frac{1}{2}\left(\partial_1^2\varphi + \partial_2^2\varphi\right) \,. \tag{2.40}$$

The effects of gravitational lensing on a circular source are shown in Figure 2.8. A circular source with radius r is distorted into an ellipse with semi-major and semi-minor axes

$$a = \frac{r}{1-\kappa-\gamma} \,, \quad b = \frac{r}{1-\kappa+\gamma} \,. \tag{2.41}$$

[2] The term *convergence* comes from light deflection in empty space. Do remember that, in practice, this can often be an expansion term.

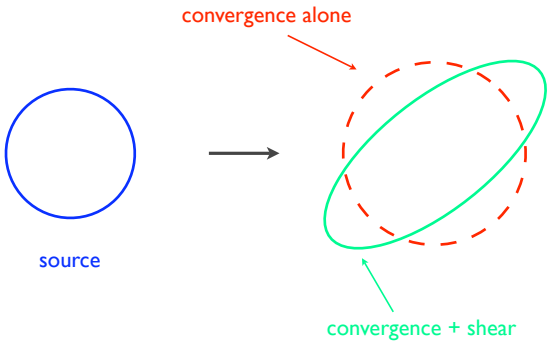

Figure 2.8: There are two basic types of distortion in gravitational lensing. The convergence which is isotropic, and the shear which is anisotropic

2.5 Measurements of Shapes and Shear

The key to observing weak gravitational lensing involves the careful measurement of shapes of many individual galaxies. There are different ways to measure the shape of an object. The method described here is the one set out in Kaiser, Squires & Broadhurst (1995) and Schneider (2006b).

In order to define the shape of an object, we must first define the centre of the image, $\overline{\theta}$,

$$\overline{\boldsymbol{\theta}} \equiv \frac{\int d^2\theta\, I(\boldsymbol{\theta}) q_I[I(\boldsymbol{\theta})]\boldsymbol{\theta}}{\int d^2\boldsymbol{\theta}\, I(\boldsymbol{\theta}) q_I[I(\boldsymbol{\theta})]} \tag{2.42}$$

where $I(\boldsymbol{\theta})$ is the brightness distribution (surface brightness) of the image, and $q_I(I)$ is a weight function. Note that in lensing the surface brightness is invariant: $I^s(\beta) = I(\theta)$.

In general, galaxies are not 'elliptical', i.e. the isophotes are not typically ellipses. So how do we define an ellipticity for an arbitrary image shape? We do so in terms of brightness moments. We next define the tensor of *second brightness moments*,

$$Q_{ij} = \frac{\int d^2\theta\, I(\boldsymbol{\theta}) q_I[I(\boldsymbol{\theta})](\theta_i - \overline{\theta}_i)(\theta_j - \overline{\theta}_j)}{\int d^2\boldsymbol{\theta}\, I(\boldsymbol{\theta}) q_I[I(\boldsymbol{\theta})]}\,, \quad i,j \in \{1,2\}\,. \tag{2.43}$$

The trace of Q describes the size of the image, and the traceless part gives us the ellipticity information. From Eq. (2.43), two alternative complex ellipticities can be defined:

$$\chi \equiv \frac{Q_{11} - Q_{22} + 2iQ_{12}}{Q_{11} + Q_{22}}\,; \quad \epsilon \equiv \frac{Q_{11} - Q_{22} + 2iQ_{12}}{Q_{11} + Q_{22} + 2\left(Q_{11}Q_{22} - Q_{12}^2\right)^{\frac{1}{2}}} \tag{2.44}$$

Figure 2.9 shows the shape of image ellipses for a circular source, in terms of their two ellipticity components, χ_1 and χ_2.

Now that we know how to define the ellipticity of a source, we need a way to transform between image ellipticities and source ellipticities. The second moment brightness tensor $Q_{ij}^{(s)}$ (or Quadrupole moments), the complex ellipticities $\chi^{(s)}$ and $\epsilon^{(s)}$

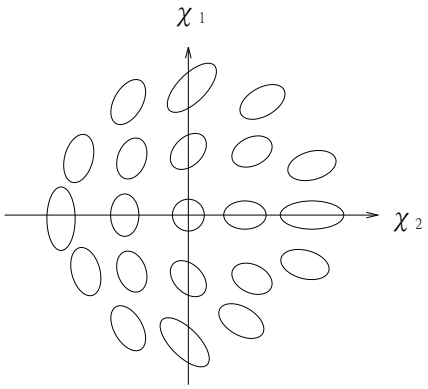

Figure 2.9: Shape of image ellipses for a circular source, in terms of χ_1 against χ_2. A plot of e_1 against e_2 would look quite similar. *Image credit:* Schneider (2006b)

for the unlensed source are defined in the same way:

$$Q_{ij}^{(s)} = \frac{\int d^2\beta\, I^{(s)}(\boldsymbol{\theta}) q_I[I^{(s)}(\boldsymbol{\beta})](\beta_i - \overline{\beta}_i)(\beta_j - \overline{\beta}_j)}{\int d^2\boldsymbol{\beta}\, I^{(s)}(\boldsymbol{\theta}) q_I[I^{(s)}(\boldsymbol{\beta})]} \;, \quad i,j \in \{1,2\} \;. \tag{2.45}$$

We find that with $d^2\beta = \det \mathcal{A} d^2\theta$, $\boldsymbol{\beta} - \overline{\boldsymbol{\beta}} = \mathcal{A}(\boldsymbol{\theta} - \overline{\boldsymbol{\theta}})$, we can write

$$Q^s = \mathcal{A} Q \mathcal{A}^T = \mathcal{A} Q \mathcal{A} \quad \text{where } \mathcal{A} = \mathcal{A}(\overline{\boldsymbol{\theta}}) \;. \tag{2.46}$$

To transform between the source and image ellipticities, the following relation can be used (Seitz & Schneider, 1997)

$$\chi^{(s)} = \frac{\chi - 2g + g^2\chi^*}{1 + |g|^2 - 2\mathcal{R}e(g\chi^*)} \;; \quad \epsilon^{(s)} = \begin{cases} \frac{\epsilon - g}{1 - g^*\epsilon} & \text{if } |g| \le 1 \;; \\ \\ \frac{1 - g\epsilon^*}{\epsilon^* - g^*} & \text{if } |g| > 1 \;. \end{cases} \tag{2.47}$$

where $g = g(z) = \frac{\gamma(z)}{1-\kappa(z)}$ is called the *reduced shear*. Note that $g \approx \gamma$ for weak lensing.

In the weak lensing régime ($\kappa \ll 1, |\gamma| \ll 1$) , the reduced shear $|g| \ll 1$ and Eq. 2.47 reduces to (where e is ellipticity defined as χ)

$$e' = e^s + 2g \;. \tag{2.48}$$

Note that if the ellipticity is defined as ϵ then $e' = e^s + g$.

If we assume that the sources are randomly orientated then the expectation value of the source ellipticities will vanish and we can write:

$$\langle e^s \rangle = 0 \;. \tag{2.49}$$

Taking the average of Eq. 2.48 we see that:

$$\langle e' \rangle = 0 + 2\langle g \rangle \;, \tag{2.50}$$

and if these sources are in small enough area of sky, we can assume that the light from each of these galaxies experiences the same shear , and so we now can write

$$\gamma \approx g \approx \langle g \rangle = \frac{\langle e' \rangle}{2} \,. \tag{2.51}$$

So now we have an equation to calculate the shear γ from the measured observables of galaxies, $\langle e' \rangle$. Note the factor of 2 here for this definition of ellipticity. [3]

It is important to note however, that because of the telescope optics, and atmospheric turbulence (seeing) that there is a blurring effect called The Point Spread Function. This effect makes practical implementations of this much more complicated. See Section 3.2.4 and Section 3.4.2 for information on how to correct for the Point Spread Function.

The KSB shape measurement method described here is the one used in this work. Alternative methods for shape measurement include Shapelets and Lensfit. Shapelets is a method which decomposes a galaxy's shape into orthogonal basis functions (Refregier, 2003). Lensfit (Miller et al., 2007; Kitching et al., 2008) treats shape measurement as a model fitting problem and tries to fit a model to the galaxy shape, using a χ^2 goodness of fit. This method is a lot slower than KSB, but uses individual exposures and so avoids the problem of co-adding individual frames. KSB is often used for cluster lensing, as the systematics are quite small, and it is a quick method.

2.5.1 Lensing Potential, Shear and Convergence

The equations in this section are presented in Schneider (2006a). We define a scalar potential, the *effective lensing potential* as

$$\psi(\boldsymbol{\theta}) = \frac{D_{ds}}{D_d D_s} \frac{2}{c^2} \int \Phi(\boldsymbol{\theta}, z)\, dz \,. \tag{2.52}$$

The critical surface-mass density is defined as

$$\Sigma_{cr} \equiv \left(\frac{c^2}{4\pi G} \frac{D_s}{D_l D_{ds}} \right) , \tag{2.53}$$

and this allows us to define the *convergence*, κ,

$$\kappa = \frac{\Sigma}{\Sigma_{cr}} \,. \tag{2.54}$$

We now write the lensing potential in terms of the convergence:

$$\psi(\boldsymbol{\theta}) = \frac{1}{\pi} \int \kappa(\boldsymbol{\theta}) \ln |\boldsymbol{\theta} - \boldsymbol{\theta}'| d^2\theta' \,, \tag{2.55}$$

The derivatives of ψ with respect to $\boldsymbol{\theta}$ have well chosen properties. Firstly, the gradient of ψ is equal to the deflection angle, $\boldsymbol{\alpha}$. Secondly, the Laplacian of ψ is equal to twice the convergence:

$$\kappa = \frac{1}{2} \nabla^2 \psi \,. \tag{2.56}$$

[3] Depending on how ellipticity has been defined, you will see in the literature that sometimes $\gamma \approx \langle e' \rangle$ is used.

2.6 From Shear to Convergence - Making 2D Mass Maps

The relations for shear and convergence given in Eq. 2.38 - Eq. 2.40 can be written compactly in complex notation in terms of ∂, defined by $\partial = \partial_1 + i\partial_2$. From this we can define $\partial^2 = \partial\partial^*$, $\partial^2 = \partial_1^2 + \partial_2^2$ and $\partial\partial = (\partial_1 + i\partial_2)(\partial_1 + i\partial_2) = \left(\partial_1^2 - \partial_2^2\right) + 2i\partial_1\partial_2$. We will also use $\partial^2\partial^{-2} = 1$, and it is useful to note the realtions in Fourier space: $\partial_i = -il_i$, $\partial^2 = -|l|^2$, and $\partial^{-2} = -\frac{1}{l^2}$.

Using this complex notation, we derive the Kaiser-Squires relation (Kaiser & Squires, 1993) between the convergence and the shear. In this notation, we can express κ and γ as follows (see Eqs. 2.33 and 2.34)

$$\kappa = \frac{1}{2}\partial^2\psi \,, \tag{2.57}$$

$$\gamma_{ij} = \begin{bmatrix} -\gamma_1 & -\gamma_2 \\ -\gamma_2 & \gamma_1 \end{bmatrix} = \partial_i\partial_j\psi - \frac{1}{2}\partial^2\psi\delta_{ij} \,. \tag{2.58}$$

Using this equation, we perform the operation $\partial_i\partial_j$ to Eq. (2.58):

$$\partial_i\partial_j\gamma_{ij} = \partial^2\partial^2\psi - \frac{1}{2}\partial^2\psi = \frac{1}{2}\partial^2\partial^2\psi = \partial^2\kappa \tag{2.59}$$

so we can write the following relation for κ:

$$\kappa = \partial^{-2}\partial_i\partial_j\gamma_{ij} + c \,, \tag{2.60}$$

where c is a constant of integration. Alternatively, if we express γ as:

$$\gamma = \frac{1}{2}\left(\partial_1^2 - \partial_2^2\right)\psi + i\partial_1\partial_2\psi \,, \tag{2.61}$$

We can write the convergence-shear relation in a different way:

$$\partial^*\partial^*\gamma = \frac{1}{2}\partial^*\partial\partial^*\partial\psi = \frac{1}{2}\partial^2\partial^2\psi = \partial^2\kappa \,, \tag{2.62}$$

and finally

$$\kappa = \partial^{-2}\partial^*\partial^*\gamma \,. \tag{2.63}$$

Using the Fast Fourier Transform relations stated above, an expression for the convergence in Fourier space, $\kappa_{\boldsymbol{l}}$, can be written

$$\begin{aligned} \kappa_{\boldsymbol{l}} &= -\tfrac{1}{l^2}(-il_i)\left(-il_j\right)\gamma_{\boldsymbol{l}\,ij} \\ &= \hat{l}_i\hat{l}_j\gamma_{\boldsymbol{l}\,ij} \,, \end{aligned} \tag{2.64}$$

where $\hat{l}_i = \frac{l_i}{|\boldsymbol{l}|}$. Now we substitute the values of γ_{ij} from the matrix in Eq. (2.58) to get the Kaiser-Squires relation,

$$\begin{aligned}\kappa_{\boldsymbol{l}} &= \hat{l}_1\left(\hat{l}_1\gamma_{\boldsymbol{l}11} + \hat{l}_2\gamma_{\boldsymbol{l}12}\right) + \hat{l}_2\left(\hat{l}_1\gamma_{\boldsymbol{l}21} + \hat{l}_2\gamma_{\boldsymbol{l}22}\right)\\ &= \hat{l}_1\left(\hat{l}_1\gamma_{\boldsymbol{l}1} + \hat{l}_2\gamma_{\boldsymbol{l}2}\right) + \hat{l}_2\left(\hat{l}_1\gamma_{\boldsymbol{l}2} - \hat{l}_2\gamma_{\boldsymbol{l}1}\right)\\ &= \hat{l}_1\hat{l}_1\gamma_{\boldsymbol{l}1} + \hat{l}_1\hat{l}_2\gamma_{\boldsymbol{l}2} + \hat{l}_2\hat{l}_1\gamma_{\boldsymbol{l}2} - \hat{l}_2\hat{l}_2\gamma_{\boldsymbol{l}1}\\ &= \left(\hat{l}_1^2 - \hat{l}_2^2\right)\gamma_{\boldsymbol{l}1} + 2\hat{l}_1\hat{l}_2\gamma_{\boldsymbol{l}2}\,.\end{aligned} \tag{2.65}$$

Another way of expressing this equation is with circular coordinates. In polar coordinates, we define $l_1 = l\cos\varphi_l$ and $l_2 = l\sin\varphi_l$. This leads us to an expression for the coefficients of γ_1 and γ_2 in Eq. (2.65):

$$\frac{l_1^2 - l_2^2}{l_1^2 + l_2^2} = \frac{l^2\cos^2\varphi_l - l^2\sin^2\varphi_l}{l^2\cos^2\varphi_l + l^2\sin^2\varphi_l} = \cos^2\varphi_l - \sin^2\varphi_l = \cos 2\varphi_l\,, \tag{2.66}$$

$$\frac{l_1 l_2}{l_1^2 + l_2^2} = \frac{l^2\cos\varphi_l\sin\varphi_l}{l^2\cos^2\varphi_l + l^2\sin^2\varphi_l} = \cos\varphi_l\sin\varphi_l = \frac{1}{2}\sin 2\varphi_l\,. \tag{2.67}$$

So writing Eq. (2.65) in this notation we get

$$\kappa_{\boldsymbol{l}} = \cos 2\varphi_l\gamma_{\boldsymbol{l}1} + \sin 2\varphi_l\gamma_{\boldsymbol{l}2}\,. \tag{2.68}$$

Now that we have this expression, we have a very quick way to compute the κ field from individual shears. More details on the map making using this equation appears in Section 3.2.6.

2.7 Lensing E and B modes

The scalar gravitational potential should only produce a curl-free shear signal. The existence of any significant curl component should be treated as a systematic shear error. We can split the shear (or the convergence) into two modes, one which measures the divergence, and one which measures the curl. We call this *E and B mode decomposition*, with the E mode being the allowed curl-free component and the B mode being the systematic curl component. Figure 2.10 shows the E modes generated by over-densities (top left) and under-densities (top right). The bottom panels show the two curl modes which are not created by gravitational lensing.

We define the E modes and B modes of the lensing potential ψ_E and ψ_B by

$$\psi = \psi_E + i\psi_B \tag{2.69}$$

where ψ_E and ψ_B are both real.

This allows us to write expressions for complex γ and κ,

$$\gamma = \left[\frac{1}{2}\left(\partial_x^2 - \partial_y^2\right) + i\partial_x\partial_y\right]\psi \;\text{ and }\; \kappa = \frac{1}{2}\left(\partial_x^2 + \partial_y^2\right)\psi\,, \tag{2.70}$$

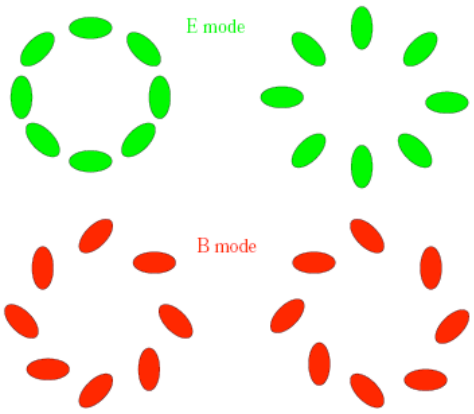

Figure 2.10: The top panel shows allowed E modes created by gravitational lensing. The bottom panel shows B modes which are not allowed by a scalar gravitational potential. *Image credit:* Van Waerbeke & Mellier (2003).

which we can then Fourier transform:

$$\gamma_{\boldsymbol{l}} = \left[-\frac{1}{2}\left(l_x^2 - l_y^2\right) - il_x l_y\right]\psi_{\boldsymbol{l}} \text{ and } \kappa_{\boldsymbol{l}} = -\frac{1}{2}\left(l_x^2 + l_y^2\right)\psi_{\boldsymbol{l}}\,, \tag{2.71}$$

where $\psi_{\boldsymbol{l}}(r) \equiv \int d^2\boldsymbol{\theta}\psi(\boldsymbol{\theta}, r)e^{i\boldsymbol{l}\cdot\boldsymbol{\theta}}$.

The recovered $\kappa(\boldsymbol{\theta})$ should be real, but due to random and systematic errors with real data it often has a significant imaginary part. We call this imaginary part the B mode.

We want to extract the E and B mode shear fields and convergences. To do this we firstly write

$$\kappa(\boldsymbol{\theta}) = \kappa_E(\boldsymbol{\theta}) + i\kappa_B(\boldsymbol{\theta}) \tag{2.72}$$

where κ_E is real and due to lensing (and errors), and κ_B is real and due only to errors. Written in Fourier space, this becomes

$$\kappa_{\boldsymbol{l}} = \kappa_{E,\boldsymbol{l}} + i\kappa_{B,\boldsymbol{l}}\,. \tag{2.73}$$

Since κ_E and κ_B are real, $\kappa^*_{E,\boldsymbol{l}} = \kappa_{E,-\boldsymbol{l}}$ and $\kappa^*_{B,\boldsymbol{l}} = \kappa_{B,-\boldsymbol{l}}$. Using this fact and Eq. (2.73), we get the following relation:

$$\kappa^*_{\boldsymbol{l}} = \kappa^*_{E,\boldsymbol{l}} - i\kappa^*_{B,\boldsymbol{l}} = \kappa_{E,-\boldsymbol{l}} - i\kappa_{B,-\boldsymbol{l}} \tag{2.74}$$

and so

$$\kappa^*_{-\boldsymbol{l}} = \kappa_{E,\boldsymbol{l}} - i\kappa_{B,\boldsymbol{l}}\,. \tag{2.75}$$

From Eq. (2.73) and Eq. (2.75) we can now write the following:

$$\begin{aligned} \kappa_{E,\boldsymbol{l}} &= \tfrac{1}{2}\left(\kappa_{\boldsymbol{l}} + \kappa^*_{-\boldsymbol{l}}\right) \\ \kappa_{B,\boldsymbol{l}} &= \tfrac{1}{2i}\left(\kappa_{\boldsymbol{l}} - \kappa^*_{-\boldsymbol{l}}\right) \end{aligned} \tag{2.76}$$

The $\kappa_{\boldsymbol{l}}$ are extracted from the transform of γ by

$$\kappa_{\boldsymbol{l}} = \frac{\left[\left(l_x^2 - l_y^2\right) - 2il_xl_y\right]}{\left(l_x^2 + l_y^2\right)}\gamma_{\boldsymbol{l}}\,. \tag{2.77}$$

Finally, we can obtain the B mode shear pattern from

$$\gamma_{B,\boldsymbol{l}} = \frac{\left[\left(l_x^2 - l_y^2\right) + 2il_xl_y\right]}{|\boldsymbol{l}|^2}\kappa_{B,\boldsymbol{l}}\,. \tag{2.78}$$

You will notice that the B modes are a 45° rotation of the E modes. So another way to test for systematics (B modes) is to rotate the data by 45° and repeat the E mode analysis. Anything which was a B mode will now show up as a signal. This is carried out in Chapter 4 when the tangential shear is calculated.

2.8 Mass Estimation

In this thesis, in order to obtain mass estimates for galaxy clusters, I have calculated the tangential shear, and fitted this to Navarro, Frenk & White (1996) (NFW) profiles. This section defines tangential shear, and the NFW profile.

2.8.1 Tangential Shear

The shear components γ_1 and γ_2 are defined relative to a reference cartesian co-ordinate frame; often it is useful to measure them with respect to a different direction. Arcs in a cluster are tangentially aligned and so this tangential direction is useful. We then want to measure shear with respect to a certain direction - i.e. the centre of the cluster. If ϕ species a direction, the tangential and radial components of the shear relative to this direction are defined as:

$$\gamma_t = -\Re\left[\gamma \exp^{-2i\phi}\right] \tag{2.79}$$

$$\gamma_r = -\Im\left[\gamma \exp^{-2i\phi}\right] \tag{2.80}$$

In order to measure the mass of an object, such as a galaxy cluster, we can use the *tangential shear*. To calculate this we define a centre, in this case the galaxy cluster centre, and calculate the tangential shear in radial bins around it. In the same way that B modes gave us a measure of systematics in our mass maps, calculating the radial shear gives us the B mode signal here. The mean tangential shear at different radii can then be compared to models (e.g. NFW profiles) to produce mass estimates for the cluster.

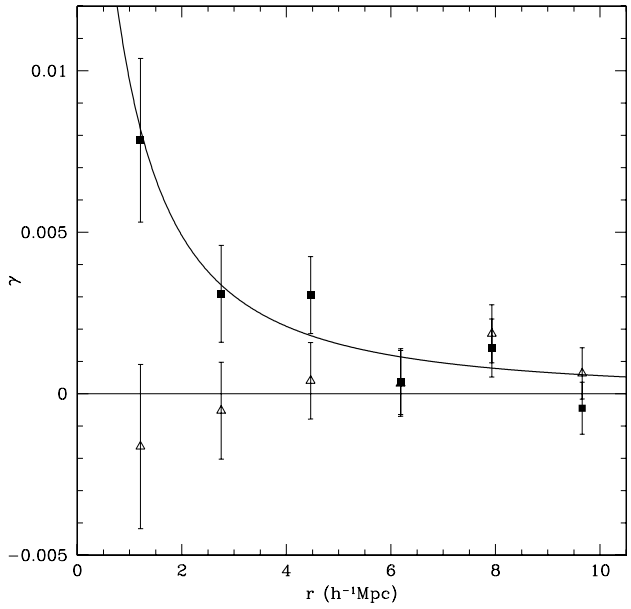

Figure 2.11: Tangential shear profile of the Coma Cluster in the SDSS, with best-fit NFW profile. The filled squares show the measured shear, and the empty triangles the B mode. The solid line shows the best-fit NFW model. *Image credit:* Kubo et al. (2007).

2.8.2 Lensing by NFW

We met the Navarro, Frenk & White (1996), NFW profile in Section 1.3.3. It is a widely used model for dark matter denisity profiles, and is parameterised by a virial radius r_{200}, and a dimensionless concentration parameter c_s. The density profile of the halo was given in Equation 1.33, and the concentration parameter c_s is defined through r_{200} and the scale radius, r_s to be $c_s = \frac{r_{200}}{r_s}$ (Equation 1.34). The parameter r_{200} is defined such that the mass density of the halo within r_{200} is 200 times the critical density of the Universe (at the redshift of the halo). The characteristic overdensity of the halo, δ_c, is that given by Equation 1.35.

A plot of the tangential shear profile, from distance r from the centre of the Coma Cluster along with the best fitting NFW profile is shown in Figure 2.8.2 from SDSS data (Kubo et al., 2007). The tangential shear measurements are shown with solid squares, and the empty triangles denote the B mode signal, and the solid line gives the best-fitting NFW profile. In this thesis I will be measuring the tangential shear profiles of clusters, and fitting them to the NFW profile to constrain the mass of the cluster.

For an NFW, the mean dimensionless surface mass density inside radius x is (King et al., 2001):

$$\bar{\kappa}(x) = \kappa_k h(x) \,, \tag{2.81}$$

where

$$\kappa_k = \frac{2 r_s \delta_c \rho_c}{\Sigma_{cr}} \,, \tag{2.82}$$

where the critical mass density, Σ_{cr}, is that given in Equation 2.53, and

$$\begin{aligned} h(x<1) &= \frac{2}{x^2}\left(\frac{2\,\mathrm{atanh}\sqrt{\frac{1-x}{1+x}}}{\sqrt{1-x^2}} + \ln\left(\frac{x}{2}\right)\right), \\ h(x=1) &= 2 + 2\ln\left(\frac{1}{2}\right), \\ h(x>1) &= \frac{2}{x^2}\left(\frac{2\,\mathrm{atan}\sqrt{\frac{x-1}{1+x}}}{\sqrt{x^2-1}} + \ln\left(\frac{x}{2}\right)\right). \end{aligned} \tag{2.83}$$

The equations for the surface mass density of an NFW lens can be found in Bartelmann (1996); Oaxaca Wright & Brainerd (1999).

From King et al. (2001), the shear of an NFW profile can be expressed as

$$\gamma(x) = \kappa_k j(x)\,, \tag{2.84}$$

where κ_k is that given in Eq. 2.82, and the scaled gamma, $j(x)$, is as follows:

$$\begin{aligned} j(x<1) &= \frac{4\,\mathrm{atanh}\sqrt{\frac{1-x}{1+x}}}{x^2\sqrt{1-x^2}} + \frac{2\ln\left(\frac{x}{2}\right)}{x^2} - \frac{1}{x^2-1} + \frac{2\,\mathrm{atanh}\sqrt{\frac{1-x}{1+x}}}{(x^2-1)\sqrt{1-x^2}}, \\ j(x=1) &= 2\ln\left(\frac{1}{2}\right) + \frac{5}{3}, \\ j(x>1) &= \frac{4\,\mathrm{atan}\sqrt{\frac{x-1}{1+x}}}{x^2\sqrt{x^2-1}} + \frac{2\ln\left(\frac{x}{2}\right)}{x^2} - \frac{1}{x^2-1} + \frac{2\,\mathrm{atan}\sqrt{\frac{x-1}{1+x}}}{(x^2-1)^{\frac{3}{2}}}, \end{aligned} \tag{2.85}$$

where $x = r/r_s$. These equations for the shear of an NFW profile and $j(x)$ will be used in Chapter 5 when cluster shear profiles are stacked to test the shape of their profile.

2.9 Systematic Errors

In weak lensing, the signal that needs to be measured is very small. From the shape measurement of an individual galaxy there is no way to be certain that the measurement was unbiased. So how can we test whether the lensing analysis was biased? There are two, complementary, options. The first is to test the results using simulated data (see Section 3.3 and Heymans et al. (2006); Massey et al. (2007b)) and the second is to carry out tests based on real data. Weak lensing is rather unique in the sense that the systematics can be studied very well. Using E and B mode decomposition (see Section 2.7 for more details), the systematic error can be quantified. There are other tests of systematics which can be done (see Section 3.4), which help understand each dataset. Although it is worth noting that knowing that systematics are present does not necessarily mean that it is clear how to deal with them, or how they have arisen.

The main sources of systematic error in a lensing analysis can be described as:

- knowledge of the Point Spread Function (PSF)

- correction of the PSF and shear calibration
- errors on photometric redshift and
- intrinsic alignments of galaxies.

I will address the first two of these items in Sections 3.2.4 and 3.4.2, but to briefly explain, there should be no correlation between corrected galaxy shape and PSF anisotropy. So if there is a correlation then this is a definite sign that improvements are needed.

Bridle & King (2007) showed that it is important to have accurate photometric redshift information for each galaxy, and that uncertainties in these, or a systematic error in photometric redshifts contribute to systematic errors on lensing results.

2.9.1 Intrinsic Alignments

A key assumption for weak lensing is that all background galaxies are randomly orientated on the sky, so that any observed correlation of galaxy orientation is caused by gravitational lensing. This assumption, however, neglects the fact that during galaxy formation, tidal interactions can correlate the ellipticities of galaxies. Intrinsic alignments in the galaxy shapes contaminate the lensing signal, so it is important to understand these effects.

Two types of intrinsic alignments have been identified, and these are often referred to as 'II' and 'GI' terms. The II term is the *intrinsic-intrinsic* alignment, and it affects galaxies which are physically close together (Heavens et al., 2000; Croft & Metzler, 2000; Crittenden et al., 2001; Catelan et al., 2001). When nearby galaxies form, their halos are forming in the same tidal field, and so they can become aligned in the same direction. This term can be reduced by removing galaxies pairs which are both close together on the sky, and have similar photometric redshifts (King & Schneider, 2002; Heymans & Heavens, 2003; Takada & White, 2004), or by fitting parameterized models (King & Schneider, 2003).

The second alignment effect is a harder concept to visualise. It is the GI, or the *gravitational-intrinsic* term and was first recognised by Hirata & Seljak (2004). This term is the correlation between the shape of a foreground galaxy, and the sheared shape of the background galaxy being lensed by the foreground galaxy. This effect causes an anti-correlation between the shapes of galaxies which are at different redshifts, so are physically very far apart, and this anti-correlation suppresses the lensing signal. Further work on this has been done by Mandelbaum et al. (2006); Bridle & Abdalla (2007); Hirata et al. (2007); Joachimi & Bridle (2009) . Bridle & King (2007) discuss the photometric redshift requirements for reducing the effect of intrinsic alignments.

Intrinsic alignments do affect cluster masses, but the clusters looked at in this thesis have $\gamma \sim 0.05$, and so any signal from intrinsic alignments is likely to be lower than this. Also, the statistical errors on the clusters mass measurements in this thesis are so large, that any affect from intrinsic alignments would be much smaller than the statistical error.

2.10 Summary

In this chapter we have been introduced to the theory of weak gravitational lensing. We have seen how the deflection angle of light bent around massive objects is derived and

how coordinates in the image plane and source plane are related by the lens equation. The Jacobian describes how to map between the source plane and the image plane, and from this we get expressions for shear and convergence. The shear and convergence are the lensing properties we are trying to measure in this thesis. In Section 2.5 we were introduced to how the shape and shear of objects are measured, and how the shear is estimated from the ellipticity of an object. We then discussed how to go from shear to convergence using the Kaiser-Squires method involving Fast Fourier Transforms. This is done in order to build up maps of the surface density. Lensing E and B mode decomposition was defined. B modes are a very important test of systematic errors, and will be used throughout this thesis. To measure masses of clusters in this thesis, I measure tangential shear and fit to NFW profiles and in Section 2.8 this theory was set out.

Chapter 3

Southern Cosmology Survey Analysis with Automated Lensing Pipeline

The large data set used in this thesis is from the Southern Cosmology Survey (SCS) and it remains one of the largest lensing data sets to date. Because of its enormous size, the task of performing a weak lensing analysis on this data using an existing manual lensing pipeline was unfeasible. The only realistic way to process this vast volume of data was to automate the pipeline. Unlike the existing pipeline, it was required that the automated pipeline would run without constant user consultation and input.

I have written an automated lensing pipeline, capable of handling large data sets, and it was written such that it could be used for future surveys (which would only get larger in size). The new pipeline needed to be able to handle the large data set quickly and accurately, and so I tested the pipeline thoroughly on simulations and data. The result is an automated lensing pipeline which runs faster while performing consistently and accurately.

Using my new automated pipeline I have analysed the SCS data. The pipeline successfully ran on the SCS data without any manual interaction, thus saving a huge amount of time. I then used the lensing results to write a series of tests to probe the quality and characteristics of the SCS data. These successfully highlighted issues with both the data and the pipeline, and I was able to resolve these problems.

3.1 Southern Cosmology Survey Dataset

The data set which I have used is public data from the Blanco Cosmology Survey (BCS). This is a National Optical Astronomy Observatory (NOAO) Large Survey Project observing 45 nights over 3 years on the Blanco 4m telescope at the Cerro Tololo InterAmerican Observatory (CTIO) in Chile. The Mosaic II camera is being used for a deep, four band optical (*griz*), photometric survey of two 50 deg^2 patches of the southern sky. This survey will be complemented with Sunyaev-Zel'dovich (SZ) information for the fields (see Ch. 1.4) by the ACT and SPT.

3.1.1 The MOSAIC II Camera

The dataset for this project has been taken with the MOSAIC II camera. This camera offers a 36" x 36" field, with 0.27" per pixel in an 8192 x 8192 mosaic of 2048 x 4096 CCDs. The layout of the CCDs is shown on the left in Figure 3.1. There are gaps between the CCDs of ~0.7 mm (~50 pixels ≈13.5") in rows; ~0.5 mm (~35 pixels ≈9.5") in columns. The *griz* filters for the MOSAIC II camera are shown on the right of Figure 3.1.

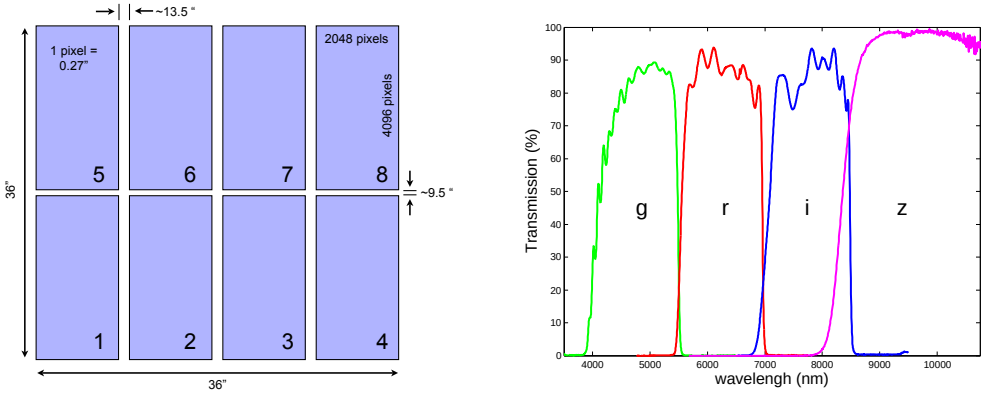

Figure 3.1: *Left:* The CCD layout of the MOSAIC II camera (not to scale). *Right:* The filter response of the MOSAIC II camera in *g*, *r*, *i* and *z* bands. *Image credit:* Menanteau et al. (2009)

3.1.2 Characteristics of the Southern Cosmology Survey

The survey aims to attain a sensitivity about an order of magnitude deeper than SDSS. Two areas of southern sky have been targeted: centred on 23h00m, -55°12m and 05h30m, -52°47m. These fields lie within a larger area of the southern sky which the Atacama Cosmology Telescope (ACT) and the South Pole Telescope (SPT) plan to survey. The NOAO survey began in 2005 and took 3 years of data.

There are 144 tiles for each field, the 23 hour field is a long, thin strip of 4x36 tiles while the 5 hour field is a 12x12 tile square (see Fig. 3.2). Each tile is around 42 arc minutes across, and I have 19 tiles in the 23hr field, and 100 tiles in the 5hr field (in all bands).

We utilize the *r* and *i* band data for our shear analysis. We have not included the *z* band data because it is subject to significant fringing [1]. Likewise, we omit the *g* band data as at this wavelength we are imaging the younger populations which are often associated with HII regions and spiral arms. This means that the galaxy images in the *g* band are messier which makes it much harder to define the galaxy shape. Galaxies are usually more regular in the redder bands, as you see the old populations and the shapes are more regular, and so the shape noise is lower in *r* and *i*.

We saw in Figure 3.1 the CCD layout for a single exposure using the MOSAIC II camera. However, 2 or 3 individual exposures have been added together to create the

[1] Fringe patterns often occur at the red end of the optical spectrum. Fringes are Newton's Rings which are formed when long wavelength light passes through the CCD and reflects back into the detector causing an interference pattern.

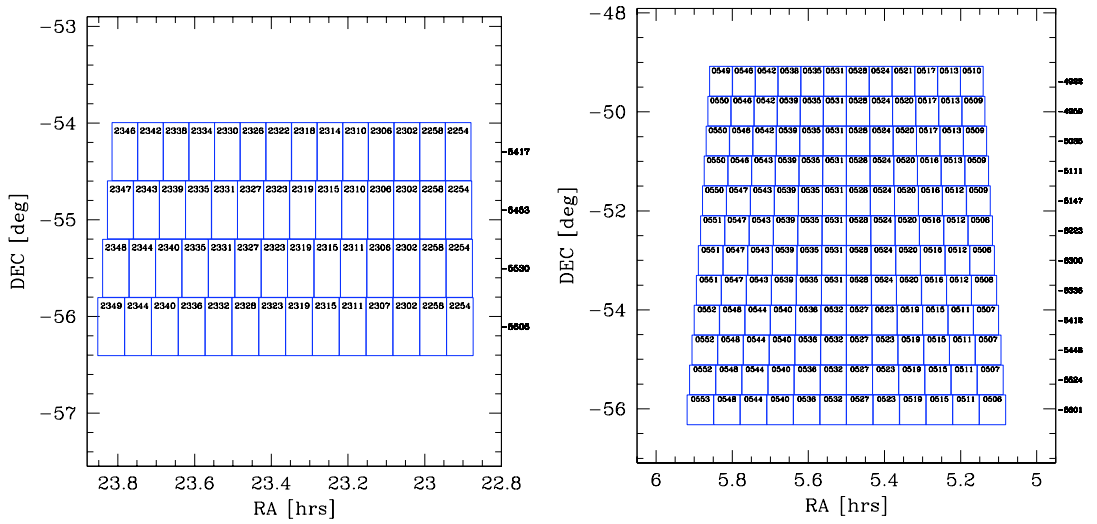

Figure 3.2: *Left:* Sketch of the tiles in the 23^{hr} field and *Right:* Tiles in the 5^{hr} field.

final images which I have used. This adding is called co-addition, and the process not only gives deeper data, but also can be used to fill in gaps not covered in the first exposure. The exposures are *dithered* which means they are shifted slightly in position on the sky. This dithering process allows the gaps between the CCDs to be filled, thus maximising the area of sky which is covered by the image.

The BCS *i* band images are made from 3 co-added exposures and the *r* band data have 2 exposures per image. The typical exposure strategy was 2x125s, 2x300s, 3x450s and 3x235s in the *g, r, i* and *z* bands respectively. The dither steps were roughly 2.304 arcminutes in the North-South direction, and 4.608 arcminutes in the East-West direction. The resulting dither pattern for the *r* and *i* band images can be seen in the *weightmaps* shown in Figure 3.3. A weightmap is a way of showing how deep different parts of an image are: they show you how many exposures each part of a co-added image has. These weightmaps have the value 0 in areas which has never been observed; the value 1 for areas with one exposure; 2 in double exposure regions etc. You can see in Figure 3.3 that the gaps between the CCDs create a distinctive *tramline* pattern when the images are co-added.

The image reduction was carried out by Felipe Menanteau and Jack Hughes using The Rutgers Southern Cosmology Pipeline. The reduction included flat field correction, CCD calibration, removal of saturated star bleed-trails, and generation of bad pixel masks. The images were astrometrically recalibrated and WCS solution found by matching stars to known sources in the US Naval Observatory Catalog. Next the images were aligned, stacked and median combined using SWarp (Bertin, 2006) and a source catalogue with photometric redshifts was produced using SExtractor (Bertin & Arnouts, 1996). For more information on the image reduction pipeline see Menanteau et al. (2009).

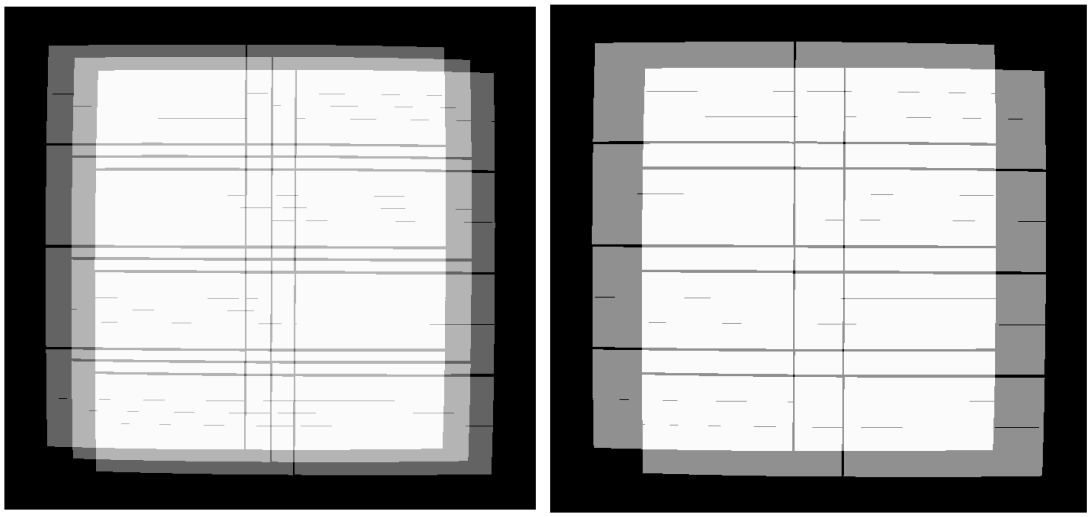

Figure 3.3: *Left:* Typical weightmap for a 3-exposure *i* band image and *Right:* Weightmap for a 2-exposure *r* band image.

Median Redshift of Survey

Using the median *i* band magnitude of ∼22.6, I calculated the corresponding median photometric redshift of this sample using Brown et al. (2003). This calculation was done as follows.

I wrote a code which uses Eq. 29 from Brown et al. (2003) to re-create their Figure 7. Unfortunately (I confirmed this at the time with Andy Taylor) the fit quoted in the paper is incorrect, as I found out when I plotted Eq. 29 - it does not re-create Figure 7. So I used the values of median z and median *r* band magnitude from Table 2 in their paper to recreate Figure 7 and re-fitted this to get the correct coefficients (to replace coefficients in Eq 29). I then estimated the median *r* band magnitude using *r*-*i* ∼0.3, (Blanton et al., 2003), and found it to be ∼22.9. Then, using the plot of Figure 7, I translated median *r* to median photometric redshift. This lead to a corresponding median photometric redshift of $z = 0.65$.

For work on future surveys, such as Pan-STARRS1, I would recommend estimating the median redshift using a newer, bigger sample from CFHTLS (Ilbert et al., 2006). I have tested the effect of using Ilbert et al. (2006) to calculate the median magnitude, and it leads to an increase in the value of median redshift from $z = 0.65$ to $z = 0.7-0.75$ for a given magnitude. The median redshift is used when calculating cluster masses (see Chapter 4 and Chapter 5) and this change in z_{median} will affect the resulting mass estimate. I have tested the NFW mass fitting routine on one cluster, at redshift $z = 0.18$, and have calculated the differences between the masses received based on the three different values of median redshift. The result is a small reduction in the masses (5% per 0.05 in z, which is 0.1 σ of the mass estimate). The change in the resulting mass estimate is much less than the statistical error. Estimating the redshift distribution using Ilbert et al. (2006) would be preferable for future lensing surveys, and using Brown et al. (2003) has lead to slightly higher mass estimates by around 5-10%.

69% of galaxies in our catalogue also had photo-zs, and these measured values lead to a consistent redshift distribution (Menanteau et al., 2009). The median magnitude of

all sources in my lensing catalogue was ~22.6, the median magnitude of those sources in this catalogue which had photo-zs was ~22.2. The median magnitude of sources in this catalogue *without* photoz was ~23.5. Note that when it came to cutting the foreground sources in the catalogues when looking at specific clusters, objects without photo-z were assumed to be at higher redshift than the cluster, and they have been left in all catalogues.

3.2 Automated Lensing Pipeline

Previous lensing surveys (such as COMBO-17, CFHT deep and COSMOS) have been a few square degrees in size, and have had $\sim 10^5$ galaxies. With these surveys there has been time to manually look at and clean up each image to remove systematics. Current surveys (e.g. CFHTLS wide and SCS) are reaching 100 sq. deg. and previous analysis techniques begin to struggle with this amount of data. Future surveys (such as Pan-Starrs 1 and EUCLID) are going to cover over 20,000 square degrees, imaging over 1 billion galaxies, and the only way to analyse this data is with an automated pipeline.

I have developed and tested a new automated lensing pipeline which is capable of handling large data sets. This pipeline is based on that described in Bacon et al. (2000) which was further developed in Brown et al. (2003). Time and accuracy are key to this pipeline and so testing was very important (see section 3.3). The pipeline takes co-added *r* or *i* band images and outputs object catalogues with shear measurements as well as producing a 2-D mass reconstruction for each field. My pipeline successfully runs on both simulated (see Sec 3.3) and real data (McInnes et al., 2009) without any manual intervention, and produces consistent results, while running faster than the old pipeline.

The stages in the pipeline are:

- source selection
- shape measurement
- star/galaxy separation
- fitting the Point Spread Function
- shear calculation, and
- mass reconstruction.

The following section takes these stages in turn, explaining the methods used. The pipeline contains many different codes written in MATLAB, IDL, C, FORTRAN and TC SHELL . The new sections of code which I have written are in MATLAB, IDL or TC SHELL , and I have edited in the other languages and adapted the outputs of these codes so that the output is in the correct format to be used as the input to the next code.

A flow diagram showing the processes in this pipeline is shown in Figure 3.4. The necessary inputs and the outputs of each stages are illustrated here. The quantities in red are values which are added to the source catalogue at each stage for each source. The values x and y are the source positions, ν is signal-to-noise, and r_g is the gaussian radius. The magnitude is denoted *mag* and the half-light radius, r_h. The components of the ellipticity of the source are denoted $e1$ and $e2$, while P_{sm} and P_{sh} are the smear polarizability and shear polarizability tensors respectively, given in Eqs. 3.7 and 3.11.

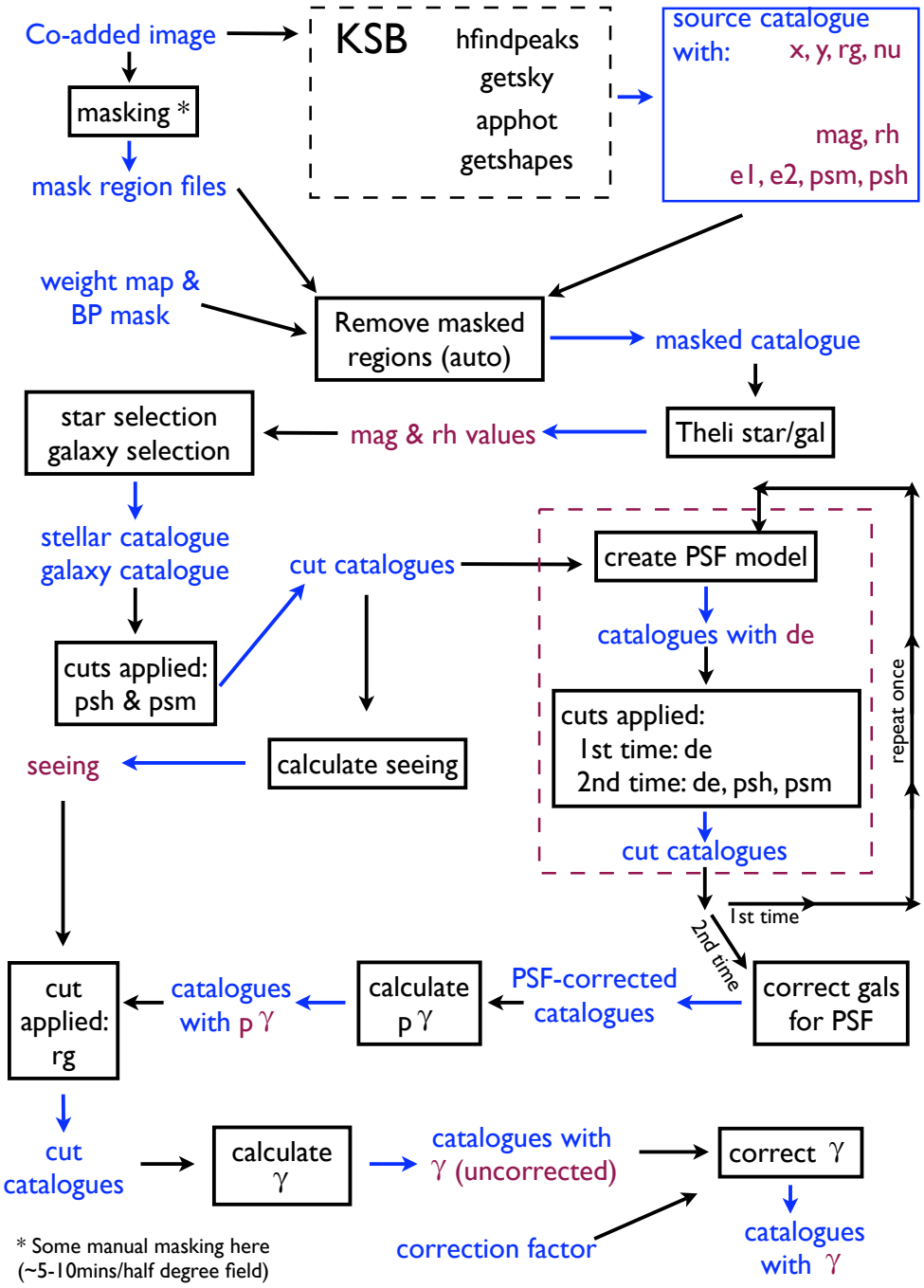

Figure 3.4: Flow diagram showing stages in the lensing pipeline and the inputs and outputs of each step. Note that the only part of this pipeline which needs manual interaction is part of the masking, as discussed in Section 3.2.1. The quantities in red are values which are added to the source catalogue at each stage for each source. The values x and y are the source positions, ν is signal-to-noise, and r_g is the gaussian radius. The magnitude is denoted *mag* and the half-light radius, r_h. The components of the ellipticity of the source are denoted $e1$ and $e2$, while P_{sm} and P_{sh} are the smear polarizability and shear polarizability tensors respectively, given in Eqs. 3.7 and 3.11. During the PSF fitting, the value of the $e - e_{model}$ for the stellar sources is given by de. The value P_γ is defined in Eq. 3.15, and γ is the shear (Eq. 3.16).

During the PSF fitting, the value of the $e - e_{model}$ for the stellar sources is given by de. The value P_γ is defined in Eq. 3.15, and γ is the shear (Eq. 3.16).

The pipeline runs automatically except from one piece of masking (see Section 3.2.1) which requires user interaction. This manual masking can be carried out first however, and then the full pipeline will run automatically. So, all fields can be masked at one time, and then the pipeline can be run on all fields automatically so it is not disruptive. I will now describe each of these stages in turn.

3.2.1 Masking Data

Before the automated pipeline can be run, the data need to have areas masked out. This process is not fully automated but I have included a discussion of the steps needed to do *masking* as it is a very important first step. Masking is the process which involves removing areas of data which cannot be used, these include saturated stars and diffraction spikes, satellite trails and other artefacts which need to be removed - due to optical effects such as flaring [2]. Figure 3.5 shows examples of areas which need to be masked.

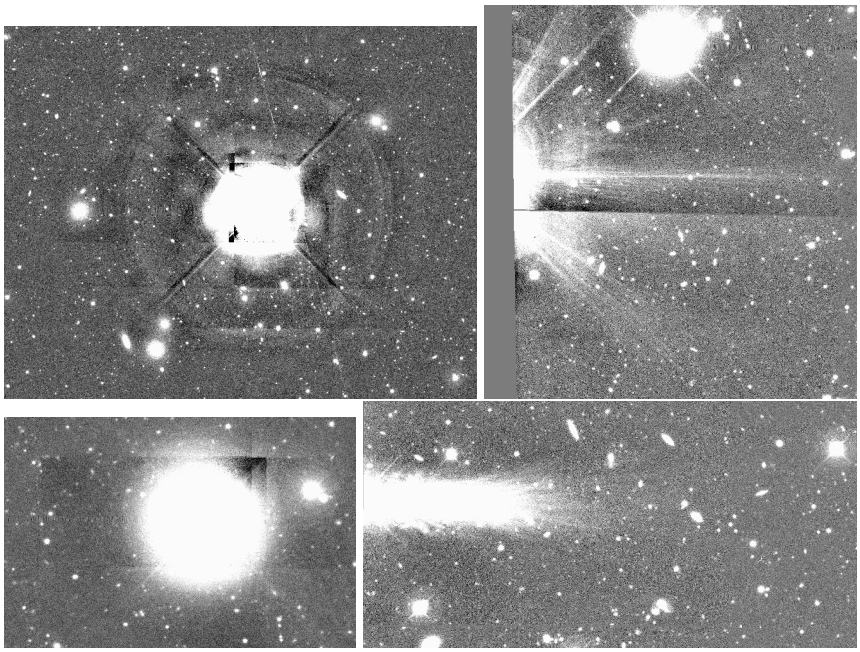

Figure 3.5: Examples of regions which need to be masked from data. *Top Left:* A large saturated star with diffraction spikes, bleed trails and a satellite trail passing through. *Top Right:* A saturated star at the edge of a field causing flaring and other distortions. *Bottom Left:* Another example of a saturated star with bleed trails and *Bottom Right* flaring at the edge of CCD chip.

The reason for ensuring that these regions are removed, is that the *source selection* stage of the pipeline can falsely detect sources in these regions, and it leads to a catalogue which contains spurious sources which are actually noise. This is particularly dangerous in lensing analyses because the shapes of these spurious sources can

[2]Flaring is an effect caused where light from a very bright object is reflected at the edge of a CCD chip back into the CCD and causes the light to be detected in surrounding pixels. It causes bright patterns which look like flares, and can be found around the edge of the images.

affect the lensing signal. This effect is particularly prominent if the spurious sources are aligned along satellite trails or diffraction spikes - where they have large ellipticities in the same direction. As well as distorting the E mode signal, the effects without masking can also be seen in the B mode signal, around large stars and other artefacts. Figure 3.6 shows an example of a mass reconstruction and signal-to-noise (S/N) map with and without masking. It can be seen in the maps made using the unmasked data, that the E modes are higher, and also the B modes have higher signal-to-noise in some areas. The mass reconstruction from masked data has a lower E mode signal-to-noise. An image of the mask used is shown in Figure 3.7. Areas within the green circles are removed during masking, as are areas in the white horizontal stripes, which are at the location of bad pixels.

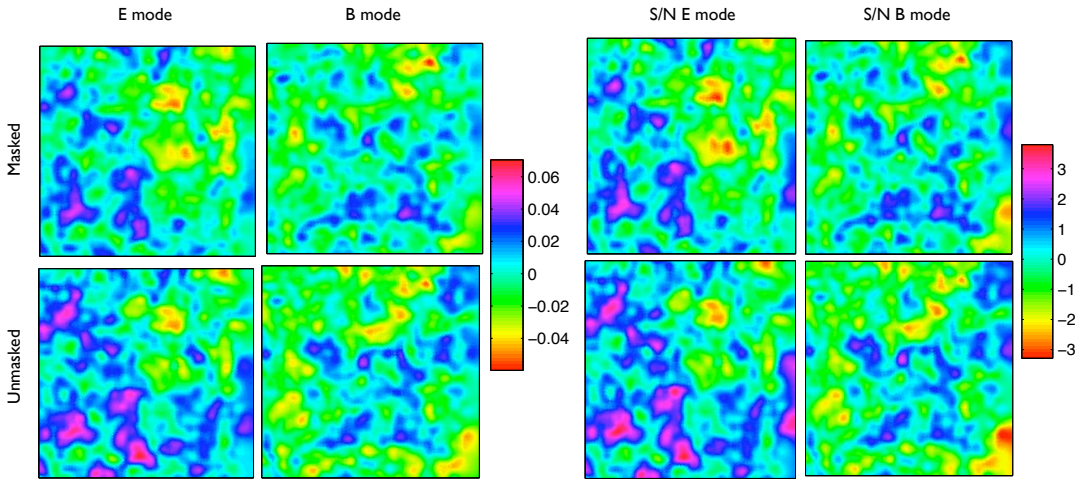

Figure 3.6: Comparison of mass reconstruction and S/N maps with and without masking. *Top row:* E mode and B mode mass reconstructions, and signal-to-noise maps for a field which has been masked (width ∼ 42′) and *Bottom row:* as above row but for the unmasked data. You can see that in the unmasked data, the B mode maps have higher signal-to-noise in some areas, and that the E modes are higher than in the masked data. Also the E mode signal-to-noise is lower after masking.

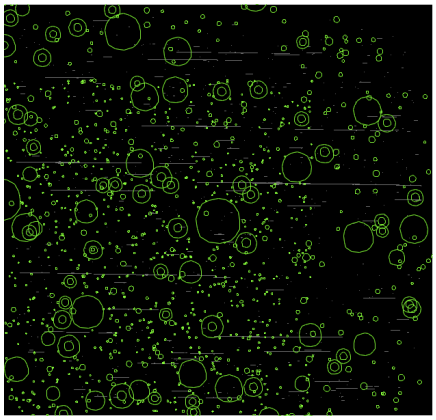

Figure 3.7: The mask used for the field in Figure 3.6. Areas within green circles are removed during masking, as well as bad pixels which lie within the white stripes in the background.

Masks are therefore created and masking of the initial source catalogue is carried out before any further stages of the analysis pipeline are run. There are three different stages of masking:

- tramlines and bad-pixels - *(automatically)*
- saturated stars - *(either manually or automatically)*
- satellite trails and image checking - *(manually)*.

Tramline and Bad-Pixel Masks

Tramline regions — areas of lower exposure due to the dithering process (see Sec. 3.1.2) — need to be removed as the source selection method used cannot successfully deal with the varying depth of the image. It calculates an average background noise level over the whole image, and if the image includes different depths, then the routine picks out many more (spurious) sources in the lower-exposure regions, as it allocates these regions the same background noise level. To get around this problem, the single and double exposure areas are removed from around the edges and the tramline regions using a code which I wrote. The code masks these regions by finding the positions of these lower exposure areas using information from the weight-map (as shown in Fig. 3.3 and removing from the catalogue, any sources which lie within these regions or less than 10 pixels away. This process was carried out on each individual tile, as the dither distance varied slightly for each tile.

I would suggest that for future surveys, such as Pan-STARRS, that rather than throwing away regions with lower-exposures, that the weight map was incorporated along with the source selection in a statistical way. This would be important for other surveys, like the Southern Cosmology Survey, which have large dither steps, or with data which had more than 3 exposures, so that data is not lost in these lower-exposure regions. Another option would be to use a lensing analysis pipeline such as LENSFIT. LENSFIT has the benefit that it uses individual tiles rather than co-added images, and so areas would not be lost which had fewer exposures.

There are small regions of the images (largely around stars) which appear striped. These are regions of interpolated star bleed trails and in a few cases bad columns. The raw images are plagued by heavily saturated stars that bleed into the field, and as part of the image reduction, the diffraction spike bleeds were masked and the gaps were filled by interpolation of surrounding pixels. This means that the image is more aesthetically pleasing, but for lensing, areas with stripy patterns would cause similar problems to the diffraction spikes or satellite trails discussed above. For this reason, these must also be removed. A bad-pixel weightmap was provided for each image, showing the positions where bad pixels were, pixel bleed trails and where star diffraction spikes had been removed. This weightmap was then used in the same way as described above to remove sources from these regions.

The top two plots of Figure 3.8 show the spurious source detection in the tramline regions (left) and the catalogue once the tramline masking has been carried out (right). It can be seen in this right-hand plot that areas remain which have a higher density of sources, these are due to large stars. The next step in the masking is to remove these stars.

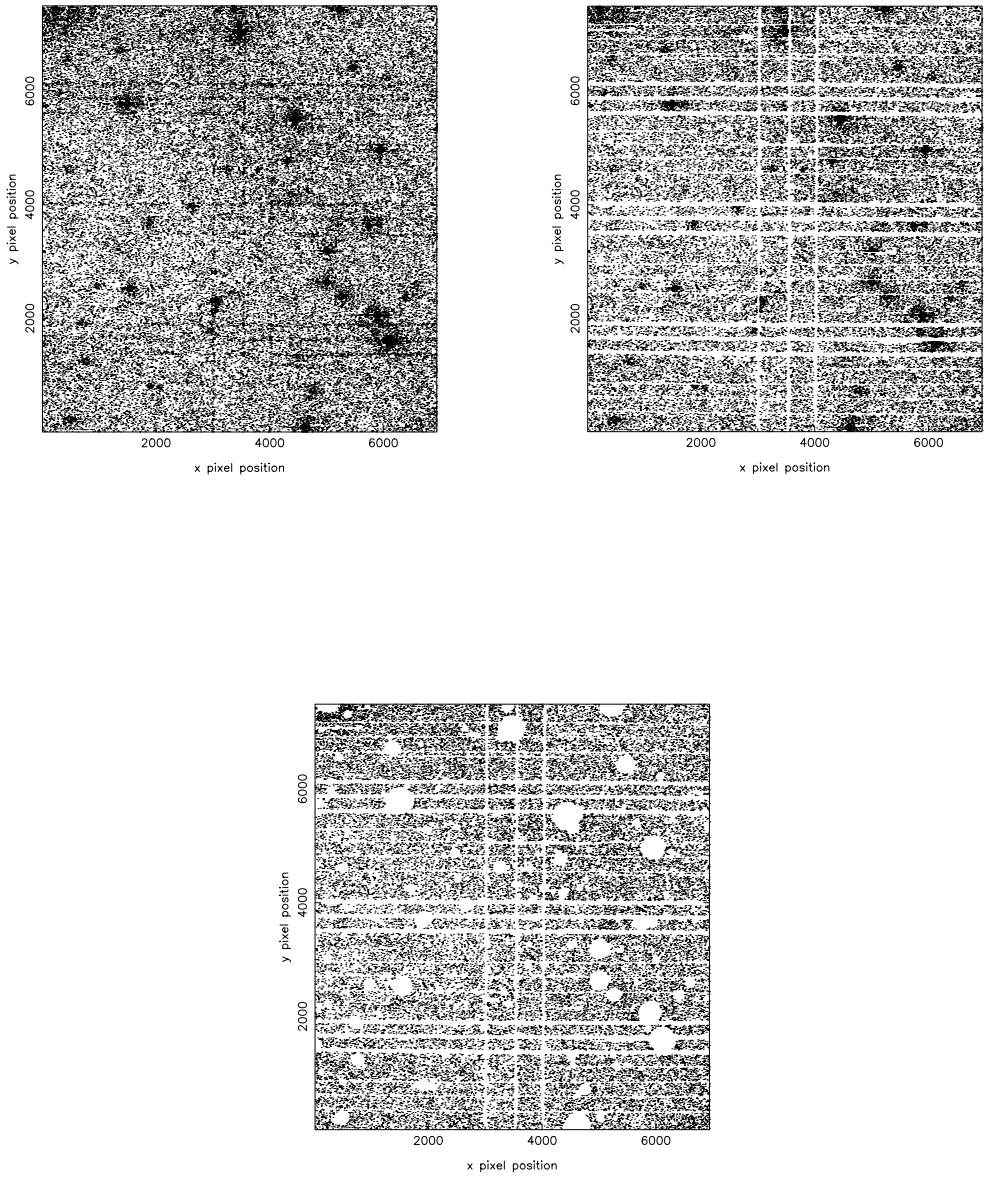

Figure 3.8: *Top Left:* Source catalogue after initial source selection, note that spurious sources are detected in the gap between CCD chips, creating a tramline patter. *Top Right:* Source catalogue after the automated tramline removal. Overdensities of sources still remain where bright stars are, and *Bottom Left* the final source catalogue after masking.

Manual Star Masks

Star masks can be made manually in SAO IMAGE DS9 (which from now will be referred to as DS9). To do this, the image was viewed in DS9 and *polygons* were drawn around the saturated stars. The polygons were then written out as DS9 *region files*. I masked

the SCS 23^{hr} field manually using this technique, and 5 tiles in the 5^{hr} field (24 tiles in total). The bottom plot of Figure 3.8 shows the catalogue after a manual star mask has been applied.

Automated Star Masks

Although the manual star masks are effective, creating them is an extremely slow process[3], with each mask taking over 1 hour to make. So, when tasked with masking the 100 tiles of the 5^{hr} field I found an attractive alternative thanks to Thomas Erben. Using the automated star masking routine from his THELI algorithm (Erben et al., 2005), creating these masks became a computational task rather than a manual one.

The automated star masks are created by using the World Coordinate System (WCS) information from the header of each image, and comparing to known star catalogues. Known stars from GSC1 catalogue were used to mask bright stars, and from GSC2.2 were used to mask faint stars. The result was a *region file* of positions of the masks. I masked the SCS 5^{hr} field automatically using this technique (100 tiles). Fig. 3.9 shows the difference between the manually produced and automated masks.

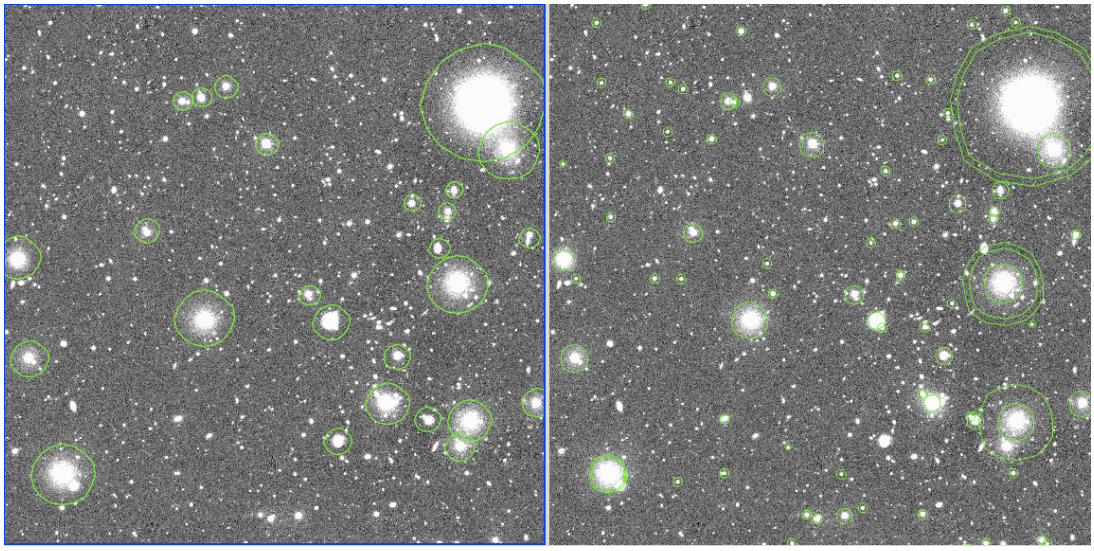

Figure 3.9: Comparison of manual and automated star masks. *Left:* Star mask created manually, and *Right:* automated star mask.

Satellite Trails and Other Artefacts

The final stage of the masking is to remove satellite trails and any other remaining artefacts which cause concern. This was done by viewing each tile in DS9 and creating masks for each satellite trail or artefact by creating a polygon of the right shape around the areas which need to be removed. The polygons were then written out as DS9 *region files*. I strongly recommend that even for very large surveys that it is necessary to eyeball each field at some point. It was clear from this data that there will always be the chance of some defects or problem with the field that might not be detected by

[3] and as anyone who has ever had to make star masks will know, very tedious!

the automatic checks or masking, and so I believe it is always necessary to view each field by eye. This manual intervention would not necessary take long, roughly 5 – 10 minutes per half degree field, depending on the number of satellite trails etc.

Both the region files of the star masks and the satellite trails and artefact mask were then used by another code (used by kind permission from Richard Massey) which took the region file and catalogue and removed any sources lying within a polygon region.

3.2.2 Source Selection and Shape Measurement

I measured galaxy shapes using the Kaiser et al. (1995) (KSB) method. Several variants of KSB have been developed; my pipeline is based on that originally described in Bacon et al. (2000) and developed in Brown et al. (2003) (and hence labelled "MB" in Heymans et al. (2006)), but has been automated to process rapidly the large SCS data set. I independently tested my method's performance on simulated images containing a known shear signal, from the Shear TEsting Programme (STEP) (see Heymans et al., 2006; Massey et al., 2007b). The method deviates from "MB" in automated star/galaxy separation and in Point Spread Function (PSF) interpolation (see Section 3.2.3 and 3.2.4).

This pipeline locates individual galaxies via the IMCAT[4] HFINDPEAKS algorithm. As illustrated in Figure 3.4, HFINDPEAKS outputs a catalogue of sources with the following information: x, y, ν, and guassian radii r_g. HFINDPEAKS is a *hierarchical peak finder* which essentially smooths the image and finds the peaks which remain. It uses gaussian filters with progressively larger smoothing scale to find significant peaks. Objects are defined to have the point of highest significance in these smoothed fields. HFINDPEAKS assumes a flat sky background across the field (c.f. SEXTRACTOR where a weight map can be supplied). Objects are defined to have a size r_g equal to the size of the (best matched) gaussian smoothing kernel that left them the greatest detection significance, and are assigned that detection significance.

Shape measurement is carried out by GETSHAPES. The shape parameters are defined in terms of weighted quadrupole moments:

$$Q_{ij} = \int \mathrm{d}^2\theta W(\theta)\theta_i\theta_j f(\theta) \tag{3.1}$$

where angles, θ are measured with respect to the object position as defined by HFINDPEAKS. $W(\theta)$ is the gaussian with scale length equal to some multiple of the object size determined by HFINDPEAKS. I use a factor of $4r_g$ in this thesis. The ellipticity or polarisation parameters are then defined as:

$$e_\alpha = Q_\alpha/T, \tag{3.2}$$

with

$$Q \equiv Q_{11} - Q_{22}, \tag{3.3}$$
$$Q_2 \equiv 2Q_{21}, \tag{3.4}$$
$$T \equiv Q_{11} + Q_{22}. \tag{3.5}$$

[4] http://www.ifa.hawaii.edu/~kaiser/imcat

The smear polarisability tensor and the shear polarisability tensor are also calculated by GETSHAPES. These are the response to ellipticity under convolution with a PSF, and under gravitational lensing shear. So, at this stage, e_1, e_2, P_{sm} and P_{sh} are added to the catalogue as shown in Figure 3.4.

Smear polarisability

A galaxy's smear polarisability depends mostly on its size. Kaiser et al. (1995) show that the ellipticity of a PSF corrected galaxy can be described as

$$e_\alpha^{\rm cor} = e_\alpha^{\rm obs} - P_{\alpha\beta}^{\rm sm} p_\beta. \tag{3.6}$$

where p_β is a measure of the PSF anisotropy and

$$P_{\alpha\beta}^{sm} = X_{\alpha\beta}^{sm} - e_\alpha e_\beta^s, \tag{3.7}$$

where

$$X_{\alpha\beta}^{sm} = \frac{1}{T}\int {\rm d}^2\theta \times \begin{bmatrix} 2W + 4W'\theta^2 + 2W''(\theta_1^2-\theta_2^2)^2 & 4W''(\theta_1^2\theta_2^2)\theta_1\theta_2 \\ 4W''(\theta_1^2\theta_2^2)\theta_1\theta_2 & 2W + 4W'\theta^2 + 8W''\theta_1^2\theta_2^2 \end{bmatrix} f(\theta), \tag{3.8}$$

$$e_\alpha^s \equiv \frac{1}{T}\int {\rm d}^2\theta \begin{pmatrix} \theta_1^2-\theta_2^2 \\ 2\theta_1\theta 2 \end{pmatrix} (6W' + 2W''\theta^2) f(\theta), \tag{3.9}$$

where primes denotes differentiation with respect to θ^2. $P_{\alpha\beta}^{sm}$ depends only on the image shape after seeing.

Shear polarisability

A galaxy's shear polarisability P^{sh} depends mostly its intrinsic shape. It describes the change in that shape during shearing, such as that produced by gravitational lensing

$$\delta e_\alpha = P_{\alpha\beta}^{sh}\gamma_\beta, \tag{3.10}$$

with

$$P_{\alpha\beta}^{sh} = X_{\alpha\beta}^{sh} - e_\alpha e_\beta^{sh}, \tag{3.11}$$

where

$$X_{\alpha\beta}^{sh} = \frac{1}{T}\int {\rm d}^2\theta \times \begin{bmatrix} 2W\theta^2 + 2W'(\theta_1^2-\theta_2^2)^2 & 4W'(\theta_1^2-\theta_2^2)\theta_1\theta_2 \\ 4W'(\theta_1^2-\theta_2^2)\theta_1\theta_2 & 2W\theta^2 + 8W'\theta_1^2\theta_2^2 \end{bmatrix} f(\theta), \tag{3.12}$$

$$e_\alpha^{sh} = 4e_\alpha + \frac{2}{T}\int {\rm d}^2\theta \begin{pmatrix} \theta_1^2-\theta_2^2 \\ 2\theta_1\theta 2 \end{pmatrix} \theta^2 W' f(\theta), \tag{3.13}$$

where primes denotes differentiation with respect to θ^2.

3.2.3 Star/Galaxy Separation

Departing from the "MB" pipeline, I performed star/galaxy separation via the automated THELI algorithm (Erben et al., 2005). The THELI program selects stars by examining the distribution of objects in a size-magnitude diagram, where stellar objects show up in a prominent locus. The program automatically determines the stellar locus from a size versus magnitude plot. In this case, the size used was the half-light radii, r_h. The algorithm works by dividing the sources into bins of size s, where s is the size co-ordinate which can be chosen. It then calculates the gradient and the change of number of objects for all of the bins. The best solution for stellar size ('best size') is found when the gradient changes after two consecutive positive values and where the number of objects is highest. The range in size is taken as two times the 'step size', s, centred on the 'best size'. The magnitude range is calculated from all objects falling within the size range of stars. An offset, o, is added to the lower magnitude limit in order to avoid saturated stars. Additionally, the algorithm uses objects with a signal-to-noise range above a specified cut value. The values used in this work were $s = 0.17$, $o = 1.1$, and signal-to-noise cut of 65. These values were tuned to this particular dataset, and future users of this algorithm would need to fine-tune the values of these parameters to best select the stellar locus for different datasets. For further details on this algorithm see Erben et al. (2005).

Figure 3.10 shows size-magnitude diagrams which illustrate the result of star/galaxy classification by the automated pipeline for one of the SCS fields. The top plot of Fig 3.10 shows in red the sources selected as stars, and the bottom plot shows in cyan the sources which have been selected as galaxies. The branch to the above left of the stellar locus contains large bright objects which are likely to be saturated stars. Sources which appear in the bottom right hand corner of the plot, are very small and likely to be spurious detections from noise or cosmic rays. The central curved branch of galaxies illustrates the detection threshold of the survey. All remaining sources — which were neither classified as stars or galaxies — are discarded at this point. These discarded objects will be a combination of saturated sources (both galaxies and stars), cosmic rays, very faint galaxies and spurious detections from noise.

Figure 3.11 shows details of star selection for four different fields (the Top Left plot is the same as that shown in Figure 3.10). The red points are sources which have been selected as stars by the automated THELI routine. Here you can see more clearly the stellar locus which has been selected. It can be seen that the use of $o = 1.1$ leads to quite a conservative use of the stars, to ensure that the saturated stars are not used. If sources are selected at this stage which are not stars, but galaxies, then this contaminates the PSF measurement. If stars are discarded at this stage, then it means that less stars can be used to characterise the PSF. For these reasons it is important to carefully select stars and galaxies for lensing analyses. A decision has to be made as to where to cut the stellar locus on the right hand side of these diagrams, and I believe that these plots show that the sources selected as stars do not go too far into the dense region of sources, where it is unclear what is a star and what is a galaxy. These four plots are typical of the SCS fields, and show that there is some variation field-to-field in the size-magnitude diagrams, but that the automatic star/galaxy separation successfully isolates the stellar locus.

I also automated the removal of galaxies with abnormally large values of shear

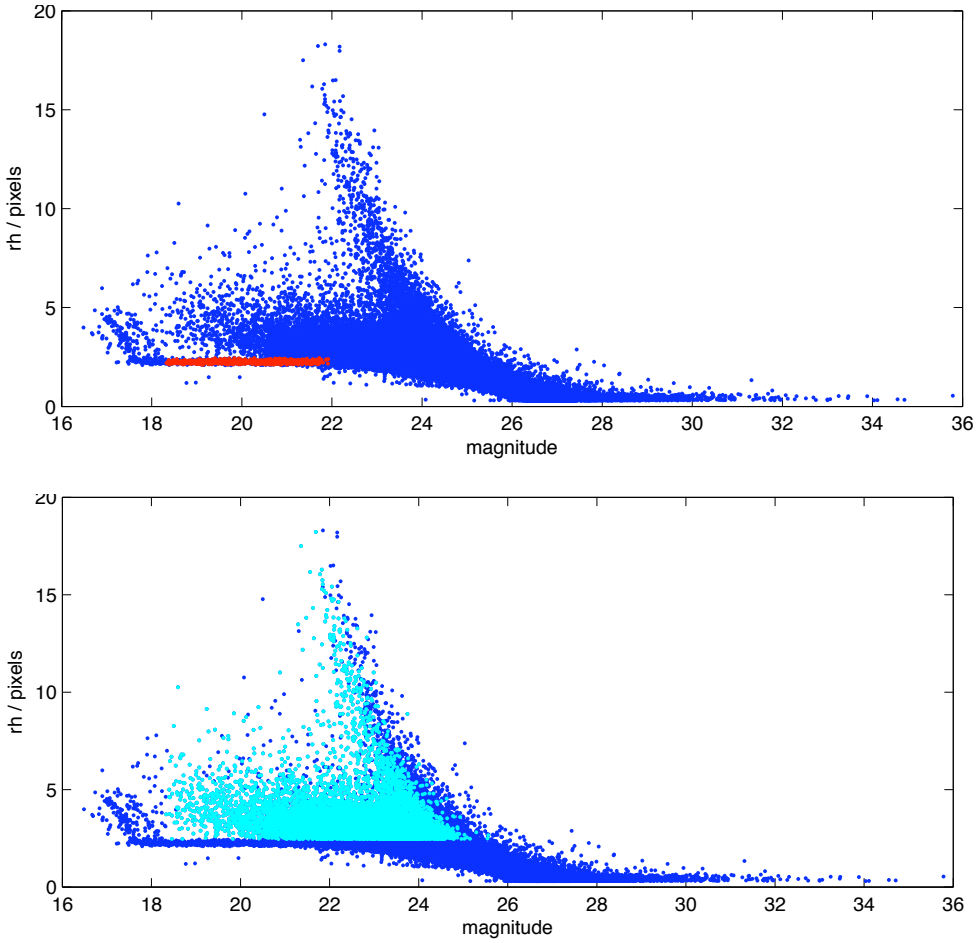

Figure 3.10: Size-magnitude diagrams illustrating star/galaxy separation in an SCS field. *Top:* Dark blue points show the full catalogue and red points are those selected as stars by the automated pipeline. *Bottom:* As above, but here the sources selected are galaxies (shown in cyan). All remaining sources which were neither classified as stars or galaxies were discarded at this point.

polarizability, P_{sh}, or smear polarizability, P_{sm}, which was present in the "MB" method but labour intensive and slow. These cuts were done by fitting a straight line through all the values of P_{sh} and calculating the standard deviation σ of the points. Sources were removed which were more than 2σ from the median value. The P_{sm} cut was then carried out in the same way. Galaxies with a signal to noise ratio, $\nu < 5$ were also excluded.

3.2.4 Fitting the Point Spread Function

The observed shapes of galaxies were then corrected for the blurring effect of the Point Spread Function (PSF). I measured the PSF from the shapes of the 0.5 unsaturated stars per square arcminute between magnitudes 22.0 and 18.1 (signal-to-noise 55 to 1670). The PSF typically has an ellipticity of 0.035 ± 0.019, where the error is the standard deviation throughout the survey. Optical effects and temporal variation of the atmosphere and telescope between dithered exposures produce complex patterns

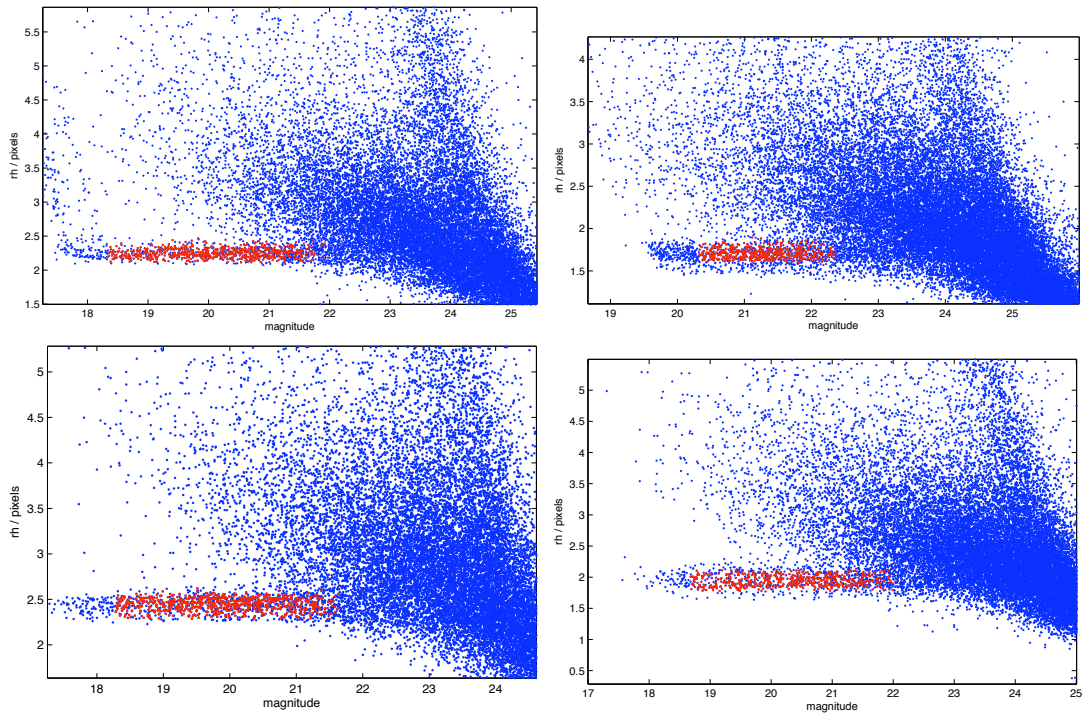

Figure 3.11: Detail of size-magnitude diagrams to illustrate star selection for four different fields. Red points are those selected as stars by the automated routine.

in PSF size and ellipticity within each field. This variation was fitted as a sum of polynomials (of order 4 in the x and y directions) plus sums of sines and cosines (of orders up to 4 in x and 8 in y). These choices give a small r.m.s. residual $|e|$ of 0.0092. The motivation for including sines and cosines in the PSF model was because of the oscillatory behaviour observed, as illustrated in Figure 3.12. Figure 3.12 shows stellar residuals e_1 and e_2 plotted against x for one field of SCS data. When the sines and cosines are included in the model, this oscillatory behaviour in the residuals is not seen as strongly (see Section 3.4.2).

At this stage, further cuts were carried out on the catalogues. Cuts on P_{sh} and P_{sm} were carried out in the same way as before, but this time any outliers beyond 2.5σ were excluded. Finally, a cut on $de = e - e_{model}$ was carried out, with a 3.5σ cut employed.

3.2.5 Shear Estimate

As illustrated in the flow diagram in Figure 3.4, after galaxies had been corrected for the Point Spread Function, P_γ and the shear, γ were calculated. The shear polarizability factor $\frac{1}{2}\mathrm{Tr}(P^\gamma)$ was fitted as a function of galaxy size. One final cut was applied at this stage too, on the gaussian radius, r_g. Galaxies with a value of r_g smaller than 1.1 times the seeing were removed from the catalogue. The shear estimator is related to the ellipticity, P^{sh} and P^{sm} as follows

$$e_\alpha^{\mathrm{cor}} = e_\alpha^s + P^\gamma_{\alpha\beta}\gamma_\beta\,, \tag{3.14}$$

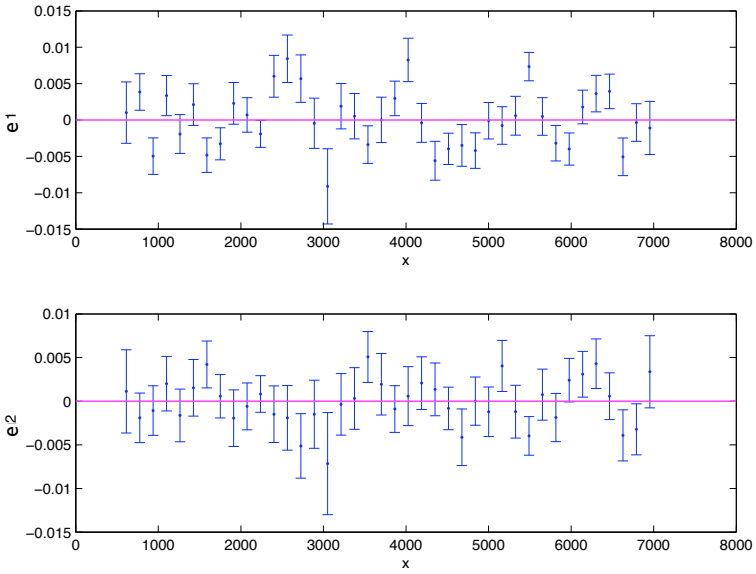

Figure 3.12: The oscillatory behaviour of the PSF is illustrated here in this plot of stellar residuals e_1 and e_2 against x position for one of the SCS fields. This plot is typical of the other fields before the full PSF correction was done including sines and cosines.

where e^s is the intrinsic source ellipticity and γ is the pre-seeing gravitational shear. Luppino & Kaiser (1997) show that

$$P^{\gamma}_{\alpha\beta} = P^{\rm sh}_{\alpha\beta} - P^{\rm sm}_{\alpha\mu}\,(P^{\rm sm*})^{-1}_{\mu\delta}\,P^{\rm sh*}_{\delta\beta}\,, \tag{3.15}$$

where $P^{\rm sm*}$ and $P^{\rm sh*}$ are the stellar smear and shear polarisability tensors respectively. Combining the PSF correction, equation (3.6), and the P^{γ} seeing correction, the final KSB shear estimator $\hat{\gamma}$ is given by

$$\hat{\gamma}_{\alpha} = (P^{\gamma})^{-1}_{\alpha\beta}\left[e^{\rm obs}_{\beta} - P^{\rm sm}_{\beta\mu}p_{\mu}\right]. \tag{3.16}$$

My method underestimates shear, but consistently throughout a wide range of observing conditions, which is henceforth compensated for in our shear measurements by applying a calibration factor of $1/(0.82 \pm 0.05)$ (see Sec 3.3). This is a known feature of the MB pipeline, which performs well when the shear is corrected by this factor. Now, for each tile, there exists a catalogue containing, amongst many other parameters, shear and galaxy position. This lead to a number density $n = 9$ galaxies per square arcminute, and a median magnitude of $i{\sim}23$. The shear catalogues can then be used to build mass reconstructions of the field (see Section 3.2.6), or calculate the tangential shear around a cluster to measure cluster masses (see Section 4.2.1).

3.2.6 2-D Mass Reconstruction

Kaiser-Squires Reconstruction

I have written a code which reconstructs the 2D mass surface density and separates the E and B modes. This is done by binning the shear values in a fine grid and using the Kaiser-Squires relation (Kaiser & Squires, 1993) as set out in Ch. 2.6. The convergence

fields were then gaussian smoothed. Figure 3.13 shows mass reconstructions of an SCS field of size 42' by 42'. The E-mode map is shown on the left, and the B mode lensing map on the right hand side. Three known clusters are marked with an X on the E mode maps.

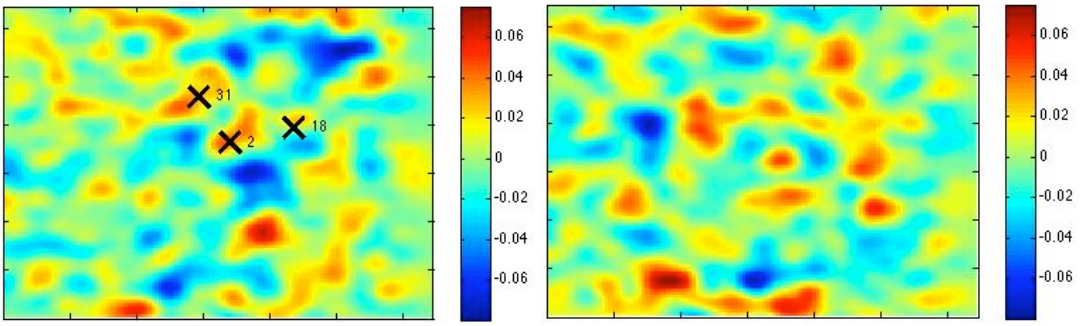

Figure 3.13: Mass reconstruction using Kaiser-Squires relation of an SCS field 42' by 42'. *Left:* E-mode and *Right:* B mode lensing maps. The Xs on the E mode map mark the positions of three known clusters.

Reconstructing the mass distribution using this method is computationally very fast, but it has the limitation that the fast fourier transform (FFT) method does not deal well with holes in the field or boundary effects. To avoid problems at the edges of each field, I padded each image with zero shear regions. This still leaves problems when there are holes in the field, which occur when stars and defects are masked.

Wiener-Filter Reconstruction

For a robust treatment of missing regions of data I used a Wiener-filtered mass reconstruction method developed by Patrick Simon (Hu & Keeton (2002, section II), Simon et al. (2009)) to reconstruct the surface mass density. To address the mass-sheet degeneracy the average surface mass density is set to zero when averaged over the whole field of view (half a square degree). This is done by setting all the $l = 0$ Fourier space modes to zero, which is equivalent to saying that the mean density contrast on each lens plane is exactly zero. For large enough fields of view this should be a reasonable assumption and this lifts the mass-sheet degeneracy (Simon et al., 2009). The reconstruction method takes into account the number of sources in each area and weights them accordingly. An outline of the code is given here, but for further details of the code see Simon et al. (2009).

The two-point correlation function of the lensing convergence, used as prior for the Wiener reconstruction, was estimated from the shear-shear correlation (Bartelmann & Schneider, 2001) $\xi_+(\theta)$ in the data itself. In order to have a smooth prior, I fitted the measured ξ_+ with $\xi_+(\theta) = a/(1 + b\,\theta)$ where a and b are constants determined by the fit. To obtain signal-to-noise maps of the lensing maps I divided the maps by the r.m.s.-variance between 200 noise realisations, which were generated by randomly rotating the ellipticities of the sources followed by a Wiener reconstruction. Figure 3.14 compares the reconstruction of an SCS field (of size 42 by 42 arc minutes) using Kaiser-Squires method and Wiener-filter method. The top row of reconstructions were made with my Kaiser-Squires routine but in this case the bottom row shows reconstructions

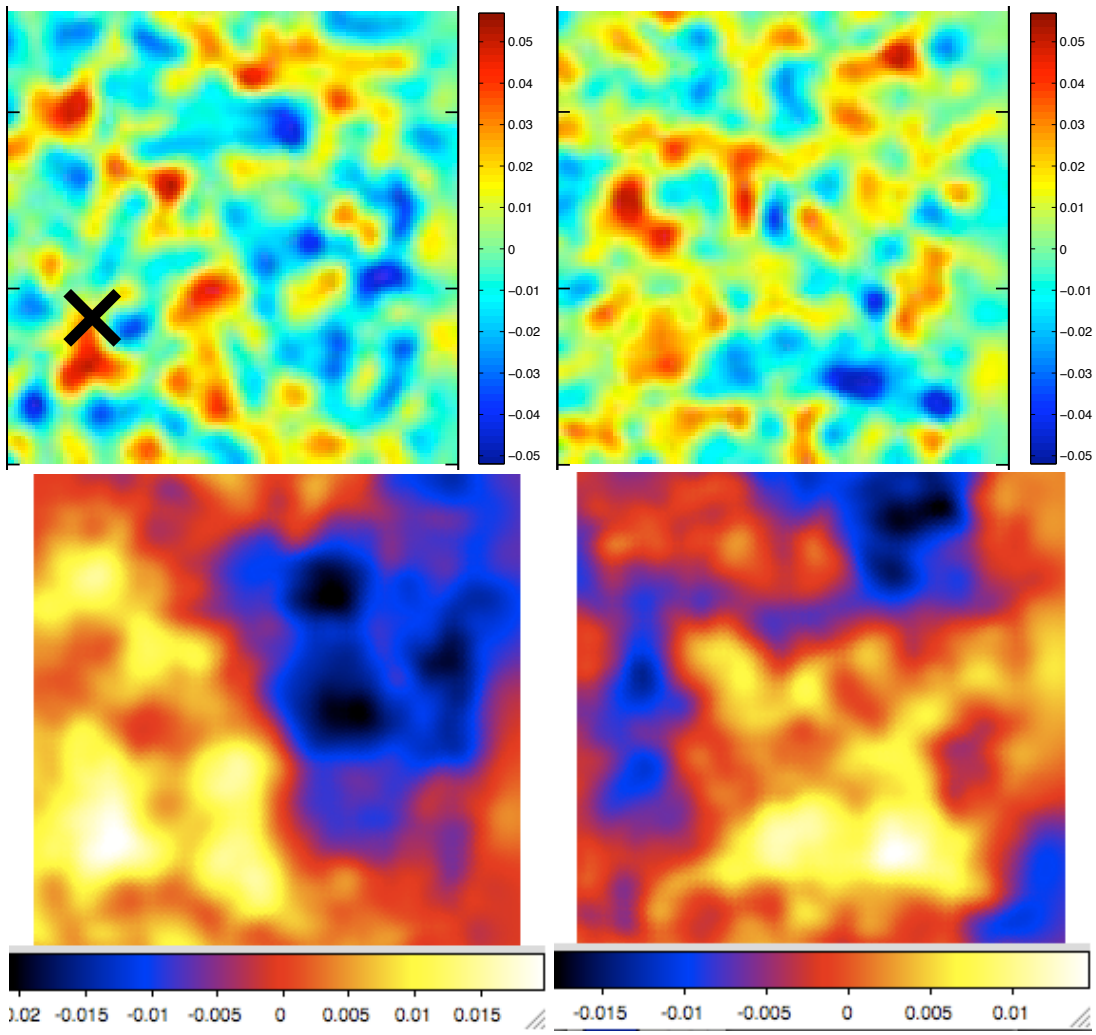

Figure 3.14: Mass reconstruction comparing Kaiser-Squires method to Wiener-filter reconstruction of an SCS field of size 42' by 42'. *Top Row:* reconstructions made with my map making routine and *Bottom Row:* reconstructions of the same field using Wiener-filter routine. *Left:* E-mode and *Right:* B mode lensing maps. The X on the E mode map marks the position of a known cluster. Note that the B mode of the wiener reconstruction is defined such that $B_w = -B_{KS}$

of the same field using Wiener-filter routine. Again, the E-mode maps are on the left, and B mode maps on right. The X on the E mode map marks the position of a known cluster. The first thing that is apparent from these different reconstructions is that the smoothing scale is different. The Wiener-filter has more smoothing and so smaller structures are not seen. Comparing the E-mode maps, the same features can be made out. The known cluster can be seen in both maps, but it is of higher significance in the Wiener-filter map. In the Wiener-filter map the cluster has the highest value kappa of the field, which is not the case in my Kaiser-Squires reconstruction. The B mode maps have been defined differently in the Wiener filter method from the previous two methods, such that $B_w = -B_{KS}$ and so the colour map is flipped.

This Wiener-filter method involved manually fitting ξ_+ and entering the constants of the fit, and so it was slow to compute many fields. Also the S/N maps, although

automated, computationally take around 12 hours to run per field. For this reason, these Wiener filter reconstructions were only done for fields containing clusters of particular interest, and I used my Kaiser-Squires method for all other fields (which took 2 seconds per field).

3.3 Testing the Automated Pipeline on Simulations

3.3.1 STEP

The Shear TEsting Programme, STEP is a project which uses collaboration to compare different methods of shear measurement for weak lensing (See Heymans et al. (2006) and Massey et al. (2007b)). STEP1 contains simulated data for testing weak lensing analysis of ground-based observations (Heymans et al., 2006). Simulated survey images were made using the *SkyMaker* programme. A series of five different shears were then applied to the galaxy catalogues by modifying the observed intrinsic source ellipticity to create sheared galaxies where

$$e = \frac{e^s + g}{1 + g \times e^s}\,, \tag{3.17}$$

and g is the complex reduced shear. For this set of simulations, the convergence $\kappa = 0$, and so the reduced shear is

$$g = \frac{\gamma}{1 - \kappa} = \gamma. \tag{3.18}$$

There are 64 images of each combination of 5*6 PSF and lens combinations making 1920 images in total. I have run the pipeline on all of the 1920 STEP1 images and I have measured the average shear per image. I then calculated the mean shear for each different lens and PSF combination. The input shears are shown in Table 3.1, along with the size and nature of the PSF distortions. Diagrams of the PSF models are shown in Figure 3.15. These 6 different PSF models were designed to be realistic models of the different types of PSF distortions occurring in ground based surveys. The typical ellipticity of a PSF from real data is of order 5%, and so PSF1 most closely matches most data (and indeed the data in this thesis). PSF2 features a tracking error, and is very elliptical in comparison. The other PSF models are non-Gaussian, but not elliptical.

Michael Brown and David Bacon used a correction factor of $\gamma_{corr} = \gamma/0.85$ to calibrate their results for STEP1 (Bacon et al., 2001). I have calculated the calibration correction factor needed for this pipeline to produce the correct results for STEP, and Table 3.2 shows the correction needed for each PSF/Lens combination. You can see that, when the shear signal is small, the pipeline cannot cope with PSF2 well, which is the most elliptical of the PSFs. Note that for PSF2 (the most elliptical) the pipeline does not perform consistently. For this reason PSF2 was excluded from the measurement of the mean calibration factor, and we note that we would not use our pipeline for images with such elliptical PSFs. Note that, as reported in Section 3.2.4, the typical PSF of the SCS data was 0.035 ± 0.019 which is much less than PSF2. The STEP PSF which most closely matched the SCS images is PSF1. I recommend that for future lensing

Shear ID	γ_1	γ_2	PSF ID	PSF type	Ellipticity
0	0.0	0.0	0	no anisotropy	0.00
1	0.005	0.0	1	coma	~ 0.04
2	0.01	0.0	2	jitter, tracking error	~ 0.08
3	0.05	0.0	3	defocus	~ 0.00
4	0.1	0.0	4	astigmatism	~ 0.00
			5	triangular (trefoil)	0.00

Table 3.1: Information on the different STEP simulation properties including input shear values for the fields, and the nature of the PSF distortions

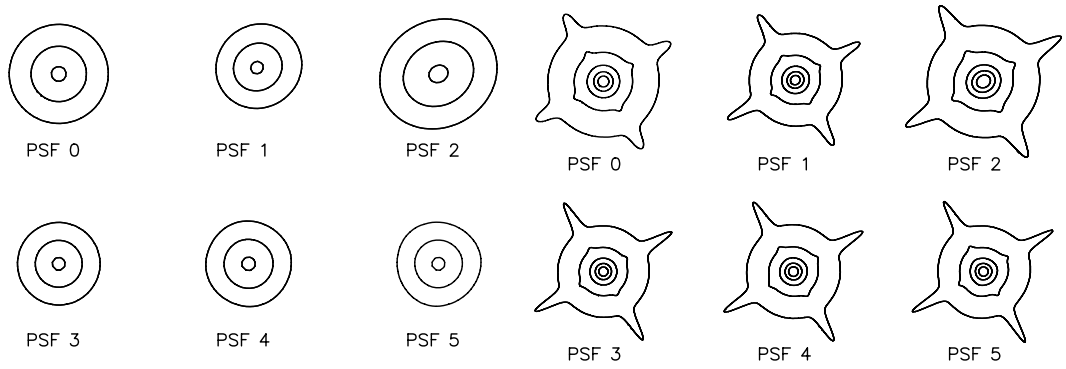

Figure 3.15: *SkyMaker* PSF models, as described in Table 3.1. The left panel shows the PSF core distortion, with contours marking 3%, 25% and 90% of the peak intensity. The right panel shows the extended diffraction spikes, with contours marking 0.003%, 0.03%, 0.3%, 3% and 25% of the peak intensity (Heymans et al., 2006).

surveys, that this flag is built into the pipeline to highlight large PSFs.

The results of the STEP analysis are plotted in Figure 3.16, where the true γ_1 against the measured γ_1 for the 6 different STEP PSFs are shown. The measurements of γ_1 are shown with blue crosses and the cyan line is the best fit line to these data. The red line (the upper line in all cases) shows a one-to-one correspondence for γ_1 true to guide the eye. Error bars are included, and it can be seen that for PSF2, the scatter on the measurements is much larger. As already mentioned, the pipeline was not successful in performing consistently for such an elliptical PSF. The error bar on the highest shear for PSF0 is also much larger.

These plots illustrate the fact that In each case this pipeline systematically underestimates the shear. A correction factor was calculated from these STEP tests. The calibration factor calculated from these results is $\gamma_{corr} = \gamma/(0.82 \pm 0.05)$. This correction factor is now included in our pipeline and is used for all data.

Lens \ PSF	0	1	2	3	4	5
1	0.807790	0.839264	-2.922317	0.823395	0.679695	0.899775
2	0.737738	0.832972	-0.127410	0.906818	0.823662	0.775540
3	0.790321	0.811933	0.951306	0.814837	0.807446	0.807729
4	0.999087	0.802821	0.689770	0.812676	0.805756	0.813826

Table 3.2: STEP calibration results ($\langle\gamma_{measured}\rangle$ /γ_{true}) for each different lens and PSF combination. Note that for PSF2 (the most elliptical) the pipeline does not perform consistently. For this reason PSF2 was excluded from the measurement of the mean calibration factor, and we note that we would not use our pipeline for images with such elliptical PSFs. Note that, as reported in Section 3.2.4, the typical PSF of the SCS data was 0.035 ± 0.019 which is much less than PSF2.

3.4 Systematic Tests on the Southern Cosmology Survey

There are various systematic tests which can be carried out on weak lensing data. These are routinely done in lensing analyses to understand systematic problems with new data sets. Tests can outline problems with the reduction or telescope or an analysis pipeline. After running the automated pipeline on the SCS data, I carried out a series of tests to understand the data. These tests were successful as they raised issues with the reduction and our pipeline.

All of these tests are done in a code which I have written which can easily be extended to new data or other data sets - such as Pan-STARRS. I would suggest for Pan-STARRS analysis that these tests were included in the initial pipeline (which would be a simple addition of calling this code at the end of the existing pipeline), and that flags were written in to highlight if any of these systematic tests raise any concerns. This would ensure that any fields which may cause concern are looked at, and that any errors in the tracking or bad seeing conditions could also be monitored. Any fields flagged up could be looked at in more detail individually and tested further or excluded if need be.

3.4.1 Testing Astrometric Accuracy

Astrometric accuracy — the precision of the World Co-ordinate System (WCS) information — is important for gravitational lensing. In order to test the accuracy of the astrometry of the SCS images, I compared the positional information of sources from regions in different images which overlapped. I did this for 5 pairs of overlapping regions, from different areas of the survey. After matching sources from two different images of the same part of the sky, I calculated the offset on the sky in Right Ascension and declination for each source. Because the only regions which overlapped were single-exposure regions, the source selection had produced many spurious sources, so a cut in magnitude, removing the faintest detections, reduced the number of sources which were not matched successfully. The number of sources which were matched was 2348 over the 5 different areas. The median offset in Right Ascension was found to be 0.044″ and median offset in declination 0.036″, with the scatter of the distribu-

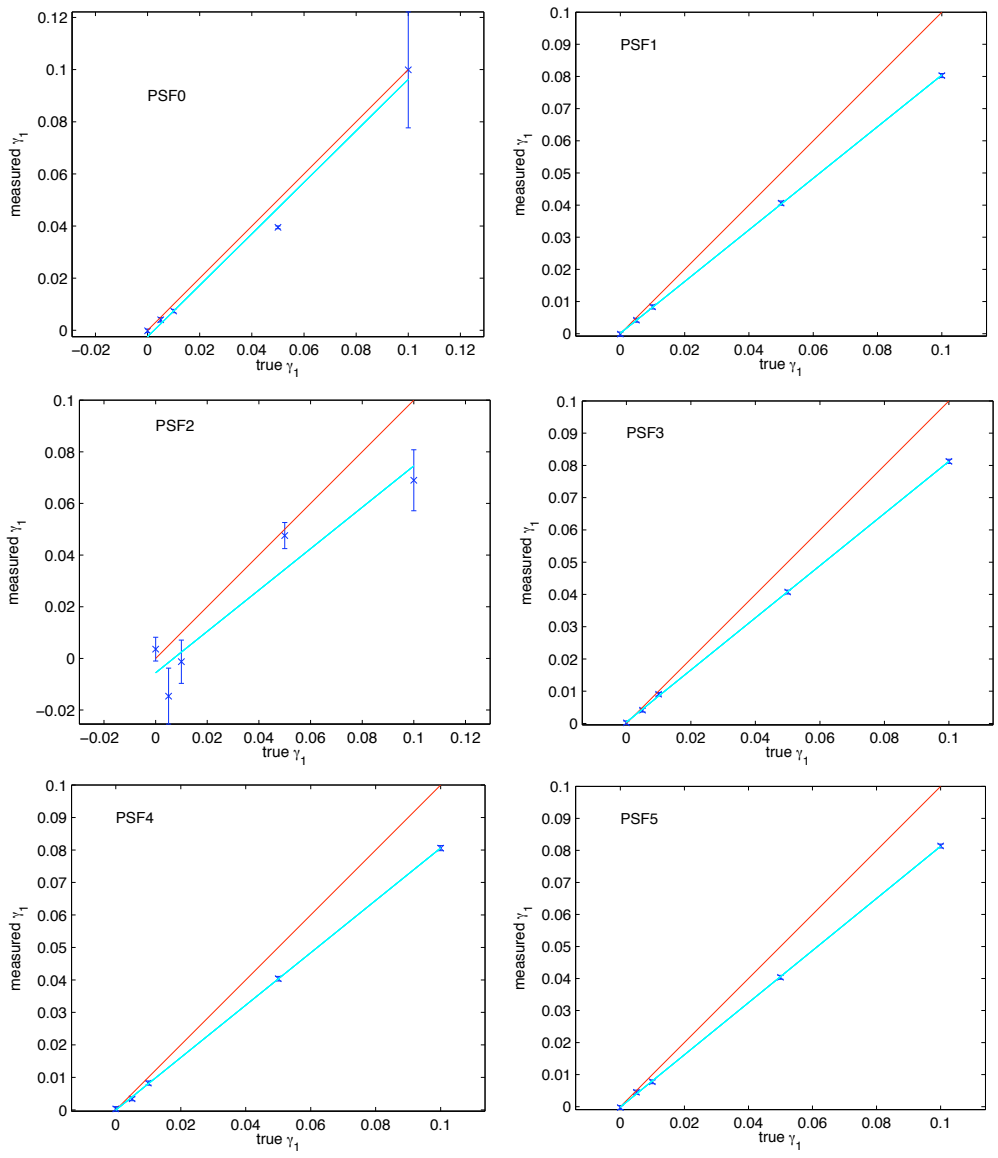

Figure 3.16: STEP results showing the true γ_1 against the measured γ_1 for the 6 different STEP PSFs. The red line (the upper line in all cases) shows a one-to-one correspondence for γ_1 true to guide the eye. The measurements of γ_1 are shown with blue crosses and the cyan line is the best fit line to these data. In each case this pipeline systematically underestimates the shear, and a correction factor was calculated from these STEP tests.

tion (equivalent width) equal to 0.180″ and 0.165″ in Right Ascension and declination respectively. The pixel scale is 0.27″, and 71% of the sources have an offset which is less than the pixel scale. The scatter was calculated via 1.48× the median of the absolute deviations. Figure 3.17 shows the distribution of offsets in R.A. and declination in arcseconds. Because the outcome of this analyses is to produce mass reconstructions, and the smoothing of these maps is $\sim 1'$, then astrometric distortions of $< 1''$ will not affect the resulting maps.

For gravitational lensing analyses, not only the field-to-field pixel registration is important, but also the sub-pixel registration from the co-addition of multiple exposures. Any shift when co-adding exposures will affect the shape measurement of galaxies.

It is important for lensing that this is done very accurately (Bacon et al., 2000). For future work I would stress the importance of testing the accuracy of the astrometric solution for sub-pixel registration.

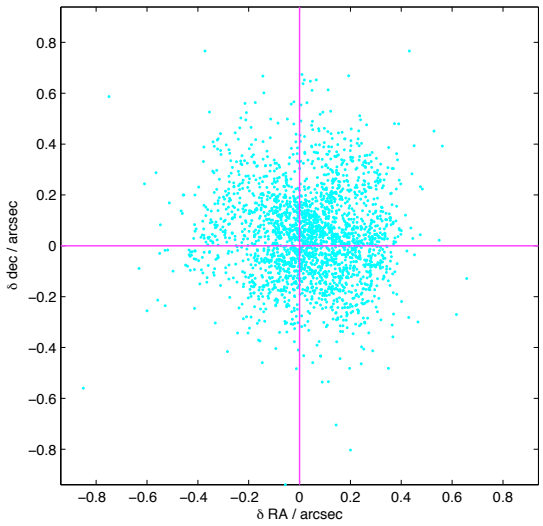

Figure 3.17: Testing astrometric accuracy: the difference in astrometric information for sources matched from different images of the same regions. δR.A. and δ declination are shown in arcseconds for $\sim$ 2300 sources.

3.4.2 Systematic Tests on 23^{hr} field

To better understand the quality of the SCS data and the effectiveness of my lensing analysis on this data, I ran a series of tests. These tests proved very successful and as a result of them I was able to better understand the data - in particular the performance of the automated pipeline, and properties of the telescope optics.

The 3 crucial results of this work are that

- A problem with the Point Spread Function fitting was singled out and then fixed
- *r* band data rejected on account that it performed noticeably worse than *i* band data in these tests, and
- no other correlations were seen so we assume that the pipeline and data are of satisfactory quality for lensing analyses.

The SCS *r* and *i* band data were both used initially, and these tests highlighted that the *r* band was subject to more systematics. This is likely to be because the *r* band images have only 2 exposures, and so the complex PSF patterns over each chip create a complicated PSF which is difficult to model precisely. In comparison the *i* band has 3 exposures, and so some of the patterns at the chip edges are averaged out, and so the overall pattern is smoother and easier to model. For this reason, the *i* band data were used.

The SCS data used in this section has had masking carried out by hand (see Sec. 3.2.1) and the plots in this section are the result of 17 tiles (each 42′ across).

Correcting for the Point Spread Function

There should be no correlation between the shear of a galaxy and stellar ellipticity in that region. The observed shapes of galaxies were corrected for the blurring effect of the Point Spread Function (PSF). Because I measured the PSF from the shapes of the unsaturated stars, any residual correlation between stellar ellipticity and galaxy shear would be the result of the galaxy shapes not being corrected enough. Similarly an anti-correlation between stellar ellipticity and galaxy shear would arise from an over-correction of the galaxy shapes. Figure 3.18 shows the correlation of stellar ellipticity components e_1 and e_2 with the galaxy shear components, γ_1 and γ_2. The binning was done as follows: all the sources from 17 images in the 23^{hr} field were taken, and binned onto a 20×20 grid using their x and y pixel positions. This gave on average 21.5 galaxies and 1.8 stars per bin. Therefore, each point on this plot represents the average galaxy shear and average stellar ellipticity in a small area. A linear fit to the points is shown for each correlation, and the coefficients of the fit given for each plot (the gradient and offset of the line). I have also calculated the mean values of e_1, e_2, γ_1, and γ_2 and they are all consistent with zero, as this also plot suggests. The results for the means were $e_1 = -0.008 \pm 0.010$, $e_2 = -0.007 \pm 0.014$, $\gamma_1 = 0.011 \pm 0.074$, and $\gamma_2 = 0.007 \pm 0.068$.

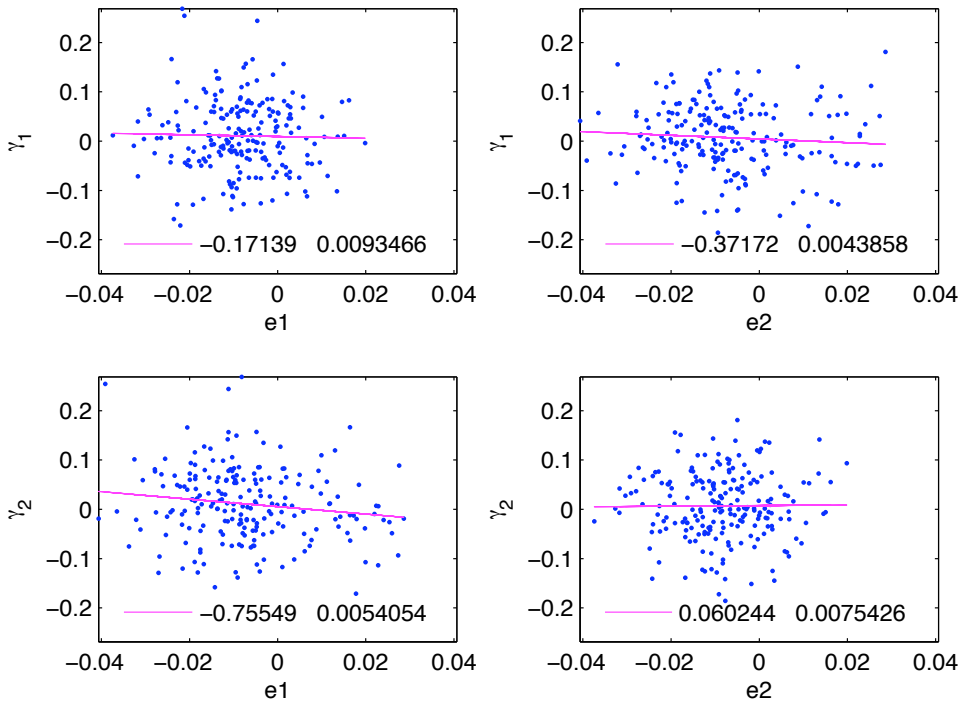

Figure 3.18: Galaxy shear components γ_1 (*top*) and γ_2 (*bottom*) as functions of stellar ellipticity components e_1 (*left*) and e_2 (*right*). The best-fit line is plotted and the coefficients of this linear fit are given on each plot.

Fitting the Point Spread Function

I have written a code which compares the model stellar ellipticity and the measured stellar ellipticity, both for each field and over the whole set of images. This tells us how well the Point Spread Function (PSF) is being fitted. It was clear that there were problems with the PSF fitting, which is likely to be due to the differences and discontinuities at the edges of CCD chips. The reason for the CCDs causing a problem is that each chip could be slightly differently orientated or misaligned. This would cause the ellipticity of sources to be biased within each chip. Optical effects and temporal variation of the atmosphere and telescope between dithered exposures produce complex patterns in PSF size and ellipticity within each field. This variation was fitted as a sum of polynomials (of order 4 in the x and y directions) plus sums of sines and cosines (of orders up to 4 in x and 8 in y) (see Section 3.2.4).

Figures 3.19 and 3.20 show measured, model and residual stellar ellipticity for 8 different tiles. These plots show that the new PSF fitting routine successfully fits the complicated PSF which are often very elliptical and which vary considerably over the different tiles. Note that, as reported in Section 3.2.4, the typical PSF of the SCS data was 0.035 ± 0.019 which is much smaller than the very elliptical STEP PSF2 of ~ 0.08 on which our pipeline failed. We would not use our pipeline on data which had a PSF as high as ~ 0.08, and, as discussed in Section 3.3.1 would suggest that a test and flag were built into this pipeline for use on future datasets such as Pan-STARRS in case such an elliptical PSF was present.

Checking for other correlations

The other tests which I carried out were correlations between galaxy shear and

- stellar ellipticity
- x position (along field)
- y position
- magnitude
- signal to noise
- size, and
- seeing.

The reason for comparing shear to these other galaxy properties was that shear should *not* be correlated to any of these, and if it was then this would highlight a problem with the data analysis or the pipeline. Initial tests of comparisons of shear and x and y pixel position showed worrying correlations, which highlighted that the PSF fitting was not accurate enough. This lead me to change the PSF fitting routine, and it has now been adapted to be able to fit the PSF from this telescope and now does so sufficiently well that plots of x and y position and shear now show no significant correlations. Figure 3.21 shows the galaxy γ_1, γ_2 and stellar e_1, e_2 plotted against x and y pixel position.

In Figure 3.22 galaxy shear components γ_1 and γ_2 are plotted against each other. This plot shows that there is no correlation between γ_1 and γ_2 because the cluster of points are centred on $0, 0$ and the distribution is evenly distributed circularly.

Property	γ_1/e_1	χ^2 (ν = 15)	γ_2 / e_2	χ^2 (ν = 15)
x	γ_1	10.8	γ_2	12.4
y	γ_1	15.3	γ_2	17.4
x	e_1	6.4	e_2	14.1
y	e_1	17.6	e_2	15.9
ν	γ_1	14.6	γ_2	12.0
mag	γ_1	20.2	γ_2	16.8
r_g	γ_1	11.1	γ_2	13.0

Table 3.3: χ^2 values for systematic tests shown in Figures 3.21, 3.23, 3.24, and Figure 3.25. There were $\nu = 15$ degrees of freedom, and so these χ^2 values confirm that there are no significant correlation between the shear and these properties, as one would expect $\chi^2 = \nu \pm \sqrt{2\nu} = 15 \pm 5.5$ for this distribution.

The following plots also show that there is no significant correlation between the remaining properties: Figure 3.23 galaxy shear components γ_1 and γ_2 are plotted against signal-to-noise ratio ν; Figure 3.24 galaxy shear components γ_1 and γ_2 are plotted against AB magnitude; Figure 3.25 galaxy shear components γ_1 and γ_2 are plotted against gaussian radius, r_g. I calculated the χ^2 value for each of these combinations, and the results are shown in Table 3.3, for 15 degrees of freedom. These χ^2 values confirm that there are no significant correlation between the shear and these properties, as one would expect $\chi^2 = \nu \pm \sqrt{2\nu} = 15 \pm 5.5$ for this distribution.

Summary of SCS properties

Properties of i-band fields in the 23^{hr} field of SCS including the gaussian radii of stars, r_g, stellar and galaxy densities, and photo$z$ coverage are shown in Table 3.4.

3.5 Conclusions

Until recently, lensing surveys have been a few square degrees in size. With these surveys there has been time to manually look at and clean up each image to remove systematics. Previous analysis techniques begin to struggle with the amount of data produced in current surveys. Future surveys are going to cover nearly the full sky, and the amount of data produced from these will be orders of magnitude larger than anything before. With this amount of data, a fully automated lensing pipeline is needed. I have developed such a pipeline, and rigourously tested in on STEP simulations. Like the pipeline it is based on (Bacon et al., 2000; Brown et al., 2003), it consistently underestimates shear by a factor 0.82 ± 0.05.

The pipeline takes co-added r or i band images and outputs object catalogues with shear measurements as well as producing a 2-D mass reconstruction for each field. My pipeline successfully runs on both simulated (see Sec 3.3) and real data (McInnes et al., 2009) without any manual intervention, and produces consistent results, while running faster than the old pipeline.

I have introduced the Southern Cosmology Survey data set, which has a number density $n = 9$ galaxies per square arcminute, and a median magnitude of i~23. This

Table 3.4: Properties of *i*-band fields in the 23^{hr} field of SCS including gaussian radius of stars (r_g), stellar and galaxy densities, and photo$z$ coverage.

Field ID	r_g (/pixel)	r_g (/")	gals	stars density	gal density (/'^{2})	stellar photoz (/'^{2})	%
BCS2322-5417	2.51	0.68	8668	775	8.2	0.73	74.8
BCS2323-5453	2.31	0.62	10352	545	9.8	0.52	70.6
BCS2323-5530	2.04	0.55	8239	514	7.7	0.48	67.3
BCS2323-5606	2.11	0.57	8732	618	8.1	0.57	64.7
BCS2327-5453	1.87	0.50	9884	417	8.9	0.37	66.7
BCS2327-5530	2.32	0.63	7501	413	6.9	0.38	63.0
BCS2328-5606	2.19	0.59	8677	569	8.1	0.53	64.4
BCS2330-5417	2.34	0.63	8161	487	7.5	0.45	70.2
BCS2331-5453	2.13	0.58	11064	634	10.3	0.59	72.8
BCS2331-5530	2.20	0.59	12306	662	11.2	0.60	73.7
BCS2332-5606	2.31	0.62	9714	542	8.8	0.49	73.5
BCS2334-5417	2.17	0.59	10423	533	9.6	0.49	70.7
BCS2335-5453	2.42	0.65	8313	612	7.7	0.56	69.8
BCS2335-5530	2.86	0.77	7848	521	7.2	0.48	70.4
BCS2336-5606	2.08	0.56	11320	610	10.4	0.56	69.9
BCS2338-5417	2.04	0.55	9068	432	8.3	0.40	67.6
BCS2339-5453	1.92	0.52	10073	532	9.2	0.49	66.4
Mean	2.10 ±0.57	0.57 ±0.15	9430 ±1350	554 ±93	8.7 ±1.2	0.51 ±0.09	69.2 ±3.5

corresponds to a median photometric redshift of $z = 0.65$ (Brown et al., 2003). Photometric redshifts are available for 69% of galaxies in our catalogue, and these measured values lead to a consistent redshift distribution (Menanteau et al., 2009).

Using the new automated pipeline, I have tested the quality of this new dataset. As a result of this testing, we conclude that the *r* band data — which is less deep — is too noisy to use for these analyses, and we proceed with the deeper *i* band data. We also test correlations between the galaxy shear and stellar ellipticity, x and y position, magnitude, signal-to-noise, size and seeing, and see no large residuals. The SCS data has a complex PSF arising from the alignment of CCD chips, and co-addition of the images from the Mosaic II camera. This has been minimised by modelling the PSF variation as a sum of polynomials (of order 4 in the x and y directions) plus sums of sines and cosines (of orders up to 4 in x and 8 in y). These choices give a small r.m.s. residual $|e|$ of 0.0092.

I recommend that for future large sky surveys that such a pipeline is implemented. I recommend that each field is viewed by eye at the start of the process, and that automatic systematic tests and flags are implemented to ensure that the data quality is monitored.

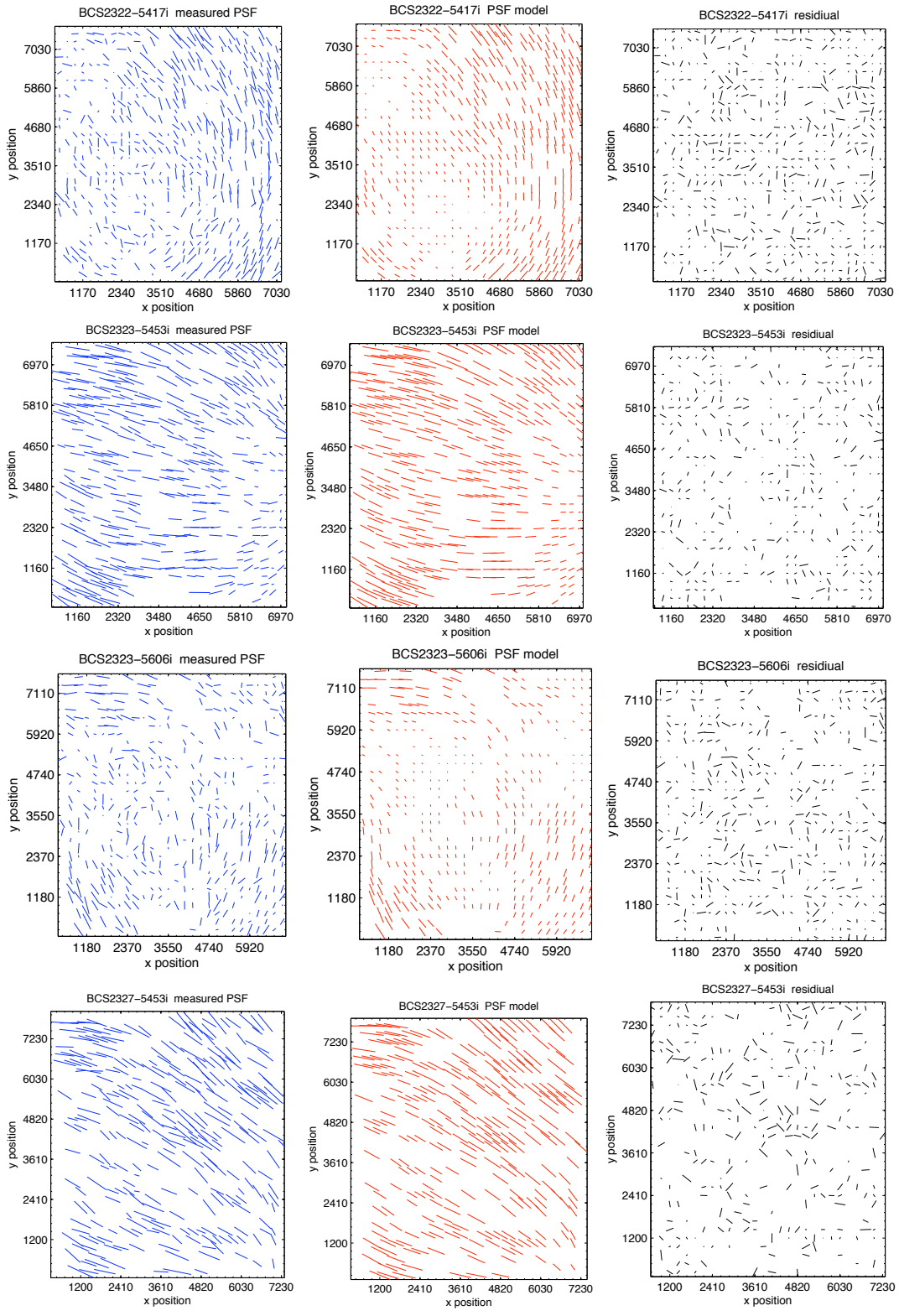

Figure 3.19: PSF plots showing measured stellar ellipticity (*left column, in blue*), the model fit to the stellar ellipticity (*central column, in red*) and residual between the measured and the model fit (*right column, in black*) for four different fields (*one per row*).

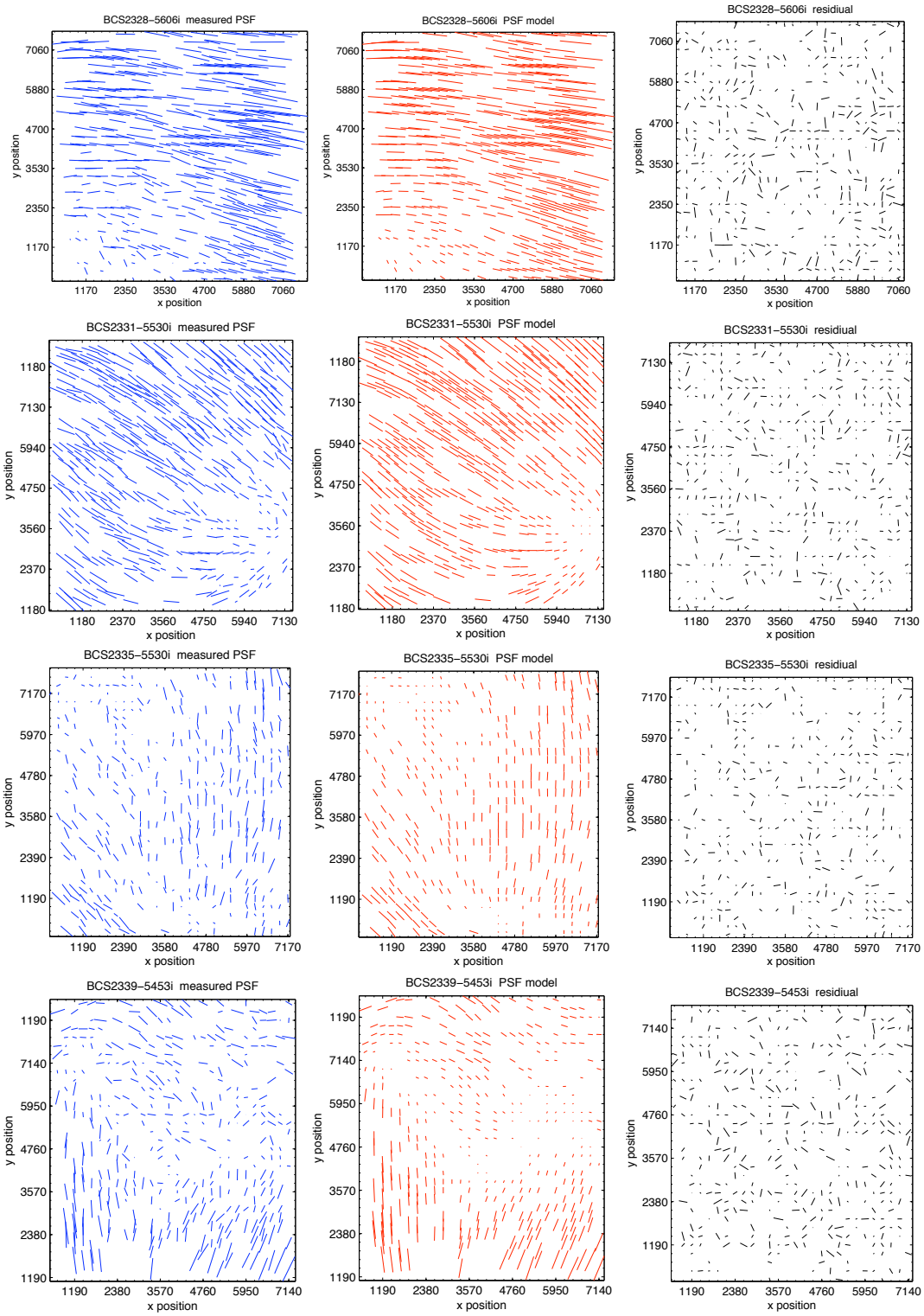

Figure 3.20: PSF plots showing measured stellar ellipticity (*left column, in blue*), the model fit to the stellar ellipticity (*central column, in red*) and residual between the measured and the model fit (*right column, in black*) for four different fields (*one per row*).

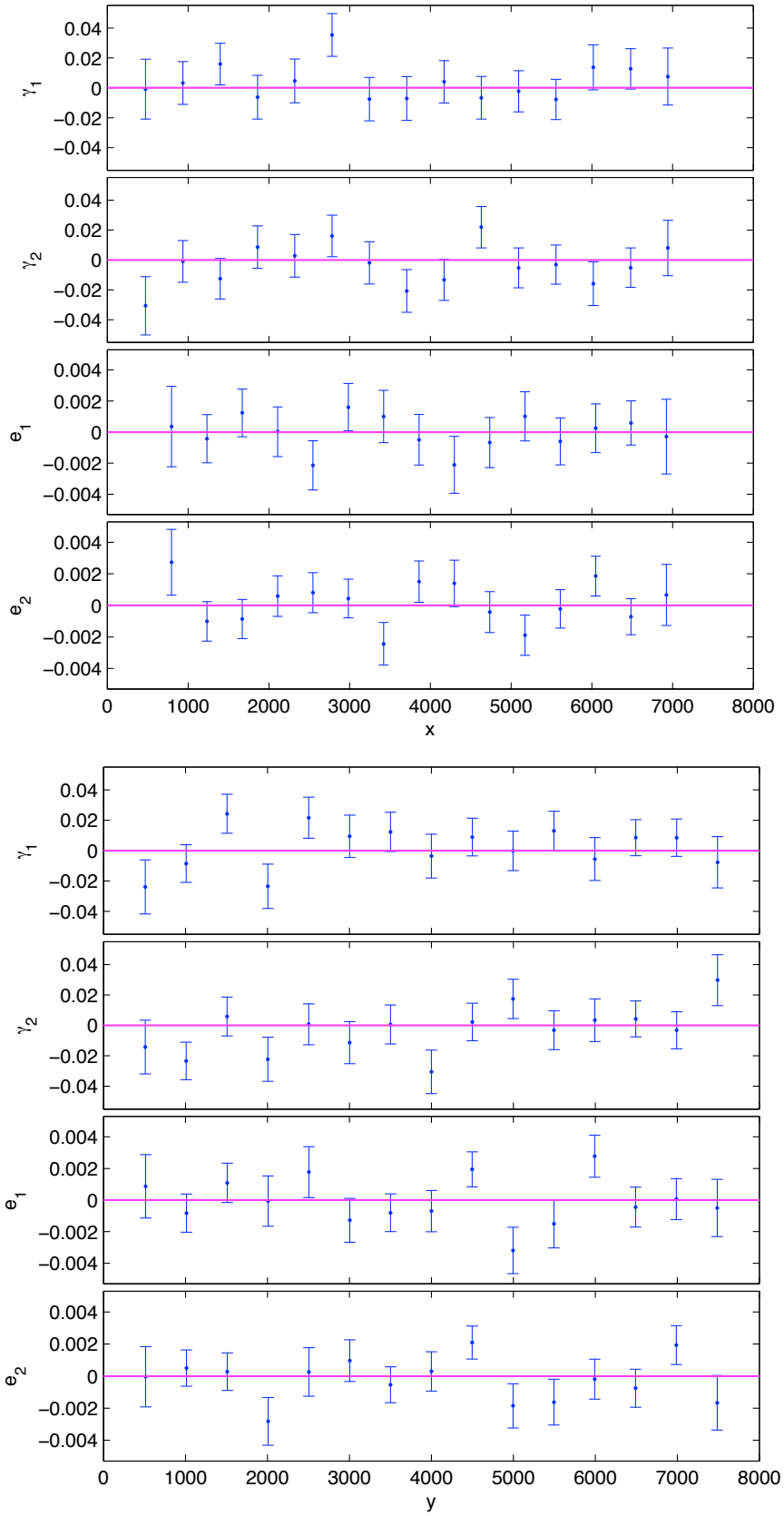

Figure 3.21: *Top*: Galaxy γ_1, γ_2 and stellar e_1, e_2 against y pixel position. *Bottom*: Galaxy γ_1, γ_2 and stellar e_1, e_2 against y pixel position.

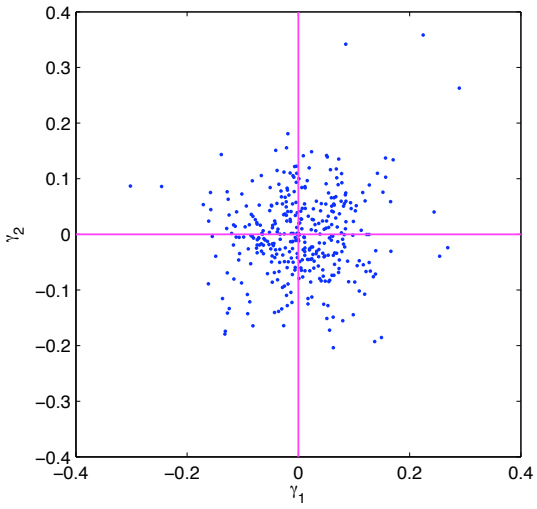

Figure 3.22: Galaxy shear component γ_1 against γ_2.

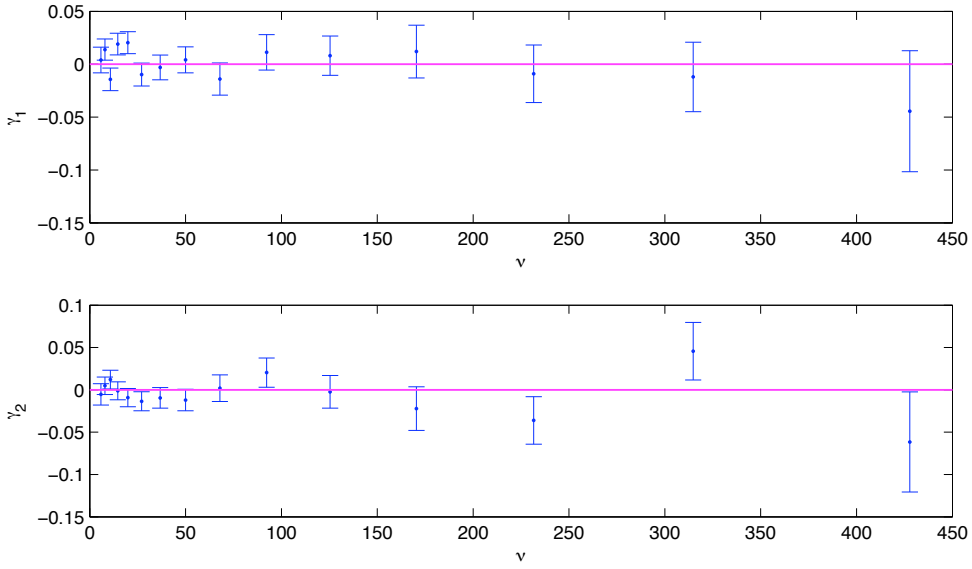

Figure 3.23: Galaxy shear components γ_1 and γ_2 as a function of signal-to-noise ratio, ν.

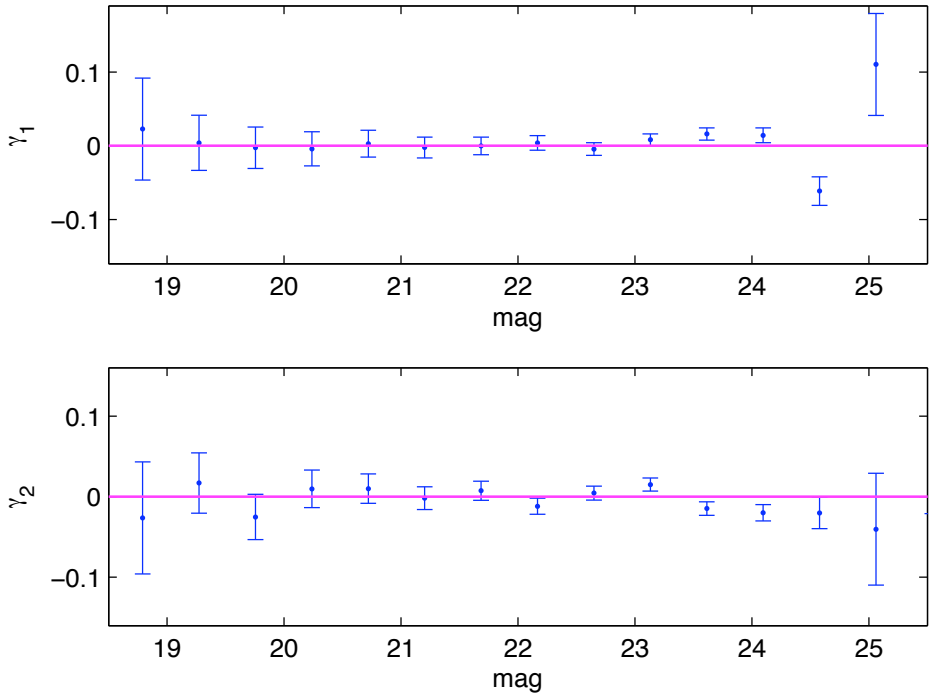

Figure 3.24: Galaxy γ_1 and γ_2 against AB magnitude.

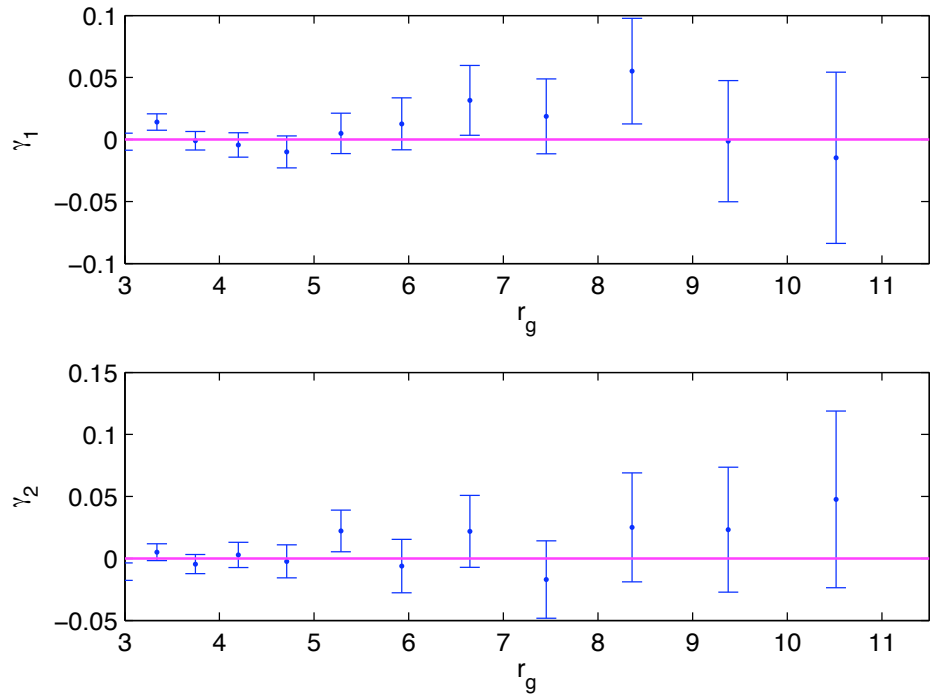

Figure 3.25: Galaxy γ_1 and γ_2 against gaussian radius, r_g.

Chapter 4

Combining Lensing Measurements with SZ Data

Galaxy clusters are the largest gravitationally bound objects in the Universe and can be used as cosmological probes because their formation and evolution rate are sensitive to different cosmological parameters (e.g. Evrard, 1989; Haiman et al., 2001; Allen et al., 2004). The abundance of galaxy clusters as a function of mass $N(m, z)$ at high redshift z is particularly sensitive to different cosmological models. To probe cosmology and dark energy we must observe galaxy clusters at high redshift and obtain mass estimates for them. By doing this, different cosmological models can be tested, as illustrated in Figure 1.2.

Observations of the Sunyaev-Zel'dovich (SZ) effect (Sunyaev & Zel'dovich, 1981) are a powerful way to probe galaxy clusters by detecting the hot cluster gas (Birkinshaw, 1999). SZ-detected clusters are in principle particularly powerful as they can be seen out to high redshifts. The intensity of the SZ effect summed over the entire cluster closely tracks the mass of the cluster (Motl et al., 2005). X-ray or SZ effect mass estimates are based on simplified assumptions such as a hydrostatic equilibrium for the cluster gas. It is becoming increasingly apparent, however, that we cannot fully model the complex gas physics in clusters within a simple framework. Nonetheless, it will be very challenging to calibrate cluster masses at high redshift, so in order to use SZ observations to probe cluster properties and cosmological models it is important to understand the relationship between mass and SZ observables in lower redshift systems. Gravitational lensing facilitates the calibration of the SZ observables to obtain accurate masses for SZ detections (Lewis & King, 2006; Sealfon et al., 2006). A large area in the southern sky is currently being surveyed in SZ by the Atacama Cosmology Telescope (ACT) and the South Pole Telescope (SPT).

Gravitational lensing is dependent only on the projected mass distribution of the lens and so it is possible to study the mass distribution independent of its form, including the distribution of dark matter. Gravitational lensing typically causes small ($\sim$ a few %) changes to the shape of individual galaxies, and the correlation of these distortions can be used to reconstruct the mass distribution in the region (Kaiser & Squires, 1993); for a review see Munshi et al. (2008).

In this chapter I present measurements of weak lensing masses for clusters which were, for the first time, detected blind by their SZ decrement (Staniszewski et al., 2008). This chapter is structured as follows: in Section 4.2 I present the data and

discuss the image processing; The mass measurements are presented in Section 4.3 and I compare these with measurements from other techniques and calculate the Y parameters.

Parts of the work contained in this chapter have been published in a refereed scientic journal, and appear in the paper:

> "FIRST LENSING MEASUREMENTS OF SZ-DETECTED CLUSTERS"
> McInnes, R. N., Menanteau, F., Heavens, A. F., Hughes, J. P., Jimenez, R., Massey, R., Simon, P., Taylor, A., 2009, MNRAS, 399, L84

Throughout this thesis I assume a flat cosmology with $\Omega_m = 0.27$, $\Omega_\Lambda = 0.73$ and $H_0 = 100h$ km s^{-1}Mpc^{-1} with $h = 0.71$.

4.1 First SZ-detected Clusters

The first galaxy clusters to be discovered with an SZ survey were found by Staniszewski et al. (2008). These were detected blindly by their SZ signals, not preselected with optical or X-ray measurements. Four clusters were found, three of which were previously undetected, and a fourth which had been previously identified as a cluster by X-ray measurements from the ROSAT all sky survey. For further information see Staniszewski et al. (2008). The survey used was the South Pole Telescope (SPT), which was designed to coincide with the area surveyed by the Blanco telescope for the Southern Cosmology Survey.

This work is exciting as it marks the beginning of surveys which will detect galaxy clusters directly from SZ, and this is very important as the SZ is unbiased in cluster selection and can detect clusters up to high redshift. An important step is to calibrate the SZ measurements with lensing mass measurements so as to constrain the cluster mass function (see Section 1.4), and so it is of great interest to further examine these four clusters.

The SZ measurements of the four SPT clusters from Staniszewski et al. (2008) are shown in Figure 4.1. Measurements are shown at three different frequencies: 150GHz, 95GHz and 225GHz. In this colour scale, decrements are shown in red. As discussed in Section 1.4, the Sunyaev-Zel'dovich effect is such that a decrement will appear at frequencies lower than 218GHz, but not at frequencies higher than 218GHz. For the four SPT clusters, this characteristic can be seen clearly.

4.1.1 Optical Cluster Measurements

The four clusters were further examined in optical and X-ray by Menanteau & Hughes (2009) and Figure 4.2 contains composite colour images from g r i bands of the four clusters. The position of the SZ decrement found by SPT is marked with a green cross, and red ellipses show the position of the brightest cluster galaxy (BCG) as found by Menanteau & Hughes (2009). X-ray contours are also shown for SPT 0517-5430. For further information on optical and X-ray properties of these clusters see Menanteau & Hughes (2009).

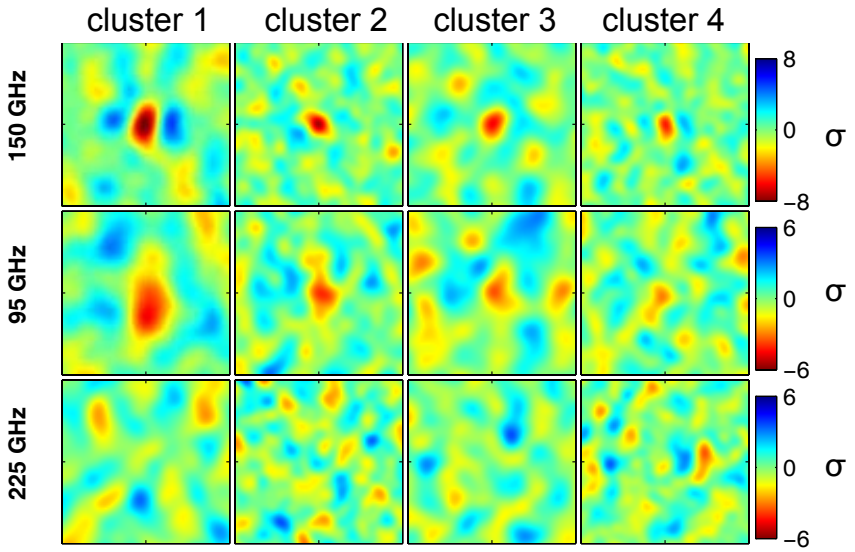

Figure 4.1: Sunyaev-Zel'dovich measurements of the 4 clusters detected by SPT. The scale gives detection significance in σ. The size of each map is 20×20 arcminutes. The SZ decrements are shown in red, and each plot is centred on the cluster. Three wavebands are shown for each of the 4 clusters. The Sunyaev-Zel'dovich signature is that a decrement will appear at frequencies lower than 218GHz, but not at higher frequencies. For each of these clusters we can see that the decrement does not appear at 225GHz which substantiates that the decrements at the lower frequencies are clusters. *Image credit:* (Staniszewski et al., 2008).

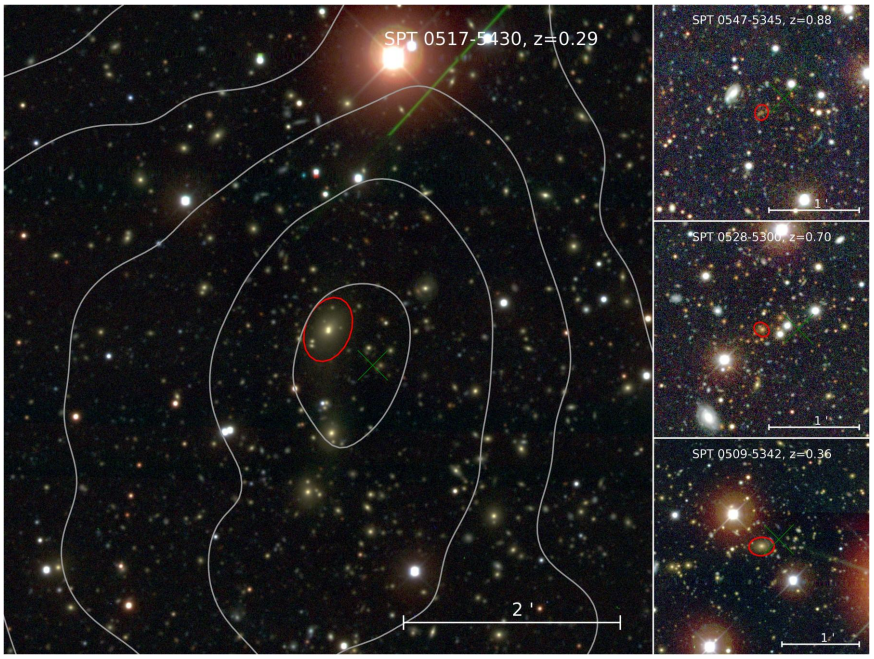

Figure 4.2: The four SPT SZ clusters shown in a composite *g r i* colour image from SCS data by Menanteau & Hughes (2009). Green crosses show the position of the SZ decrement found by SPT, and red ellipses show the position of the BCG as found by Menanteau & Hughes (2009). X-ray contours are also shown for SPT 0517-5430. *Image credit:* Menanteau & Hughes (2009).

Table 4.1 shows the cluster IDs and redshifts, which link the numbering used in some figures to the cluster IDs. Also shown in this table is the cluster richness, N_{200}^{gal}, as published in Menanteau & Hughes (2009).

Cluster	Cluster ID	z_{photo}	N_{200}^{gal}
Cluster 1	SPT 0517-5430	z = 0.27	168.9 ± 15.3
Cluster 2	SPT 0528-5300	z = 0.70	69.3±9.8
Cluster 3	SPT 0509-5342	z = 0.36	76.1 ± 9.2
Cluster 4	SPT 0547-5345	z = 0.88	12.7 ± 3.7

Table 4.1: The four SZ clusters: IDs, redshifts and cluster richness (Menanteau & Hughes, 2009).

Optical Cluster Detection and Defining Cluster Membership

In Section 1.3.1, a comparison of cluster detection techniques using different wavelength observations was presented. The cluster catalogues used in this thesis were optically selected, and in this section I will describe how this optical cluster selection was carried out by Menanteau et al. (2009). In addition to the four SPT clusters, the same selection process was used for the data introduced in the following sections.

The work described in this section was carried out by Felipe Menanteau. Clusters were selected using a matched filter and photometric redshift cluster detection technique, where peaks over 2σ were selected. Photometric redshifts (photo-zs) were calculated using multi-band SExtractor (Bertin & Arnouts, 1996) *g,r,i,z* isophotal magnitudes and the redshift probability distributions of each object were found using the BPZ code (Benítez, 2000). Cluster membership and richness were defined using the MaxBCG prescription (Koester et al., 2007). Only galaxies defined as E/S0 by BPZ were used. Cluster members were also assigned based on the estimated cluster size r_{200}. The radius r_{200} was defined as the radius in which the number density is estimated to be $200/\Omega_m$ times the average galaxy number density. The value of r_{200} was estimated from the cluster richness using a scaling relation by Hansen et al. (2005) derived from SDSS data, and was extrapolated beyond $z \sim 0.3$ for the higher redshift clusters. The cluster richness, N_{200}^{gal}, is the number of E/S0 galaxies within r_{200} with colours and luminosities that satisfy specific conditions for cluster membership (see Table 4.1). The false positive cluster detection fraction was found to be 1% at $z = 0.6$ and 20% at $z = 0.7$, although Olsen et al. (2007) used a similar method and found 30% contamination at 3.5σ and Milkeraitis et al. (2010) found contamination to be 23% at 3.5σ. Also, because the analysis is based on a magnitude-limited sample, there will be some fraction of lower luminosity galaxies which will fall below the detection limit. The fraction of the cluster luminosity missing is estimated to be 4%, 13%, 29% and 38%, at $z = 0.4, 0.5, 0.6$ and 0.7 respectively. This will lead to an underestimate in cluster masses by roughly these factors. For further detail on cluster membership and selection, please see Menanteau et al. (2009).

More information on the measured optical properties of these clusters, including how optical mass estimates were calculated, will follow in Section 4.3.2 and Section 5.1.3.

4.2 Observations

I used publicly available data from the Blanco Cosmology Survey - a National Optical Astronomy Observatory Large Survey Project observing 60 nights over 4 years on the Blanco 4m telescope at the Cerro Tololo InterAmerican Observatory in Chile. The Mosaic II camera is being used for a deep, four-band optical (*griz*) survey of two 50 deg^2 patches of the southern sky. Two areas of southern sky have been targeted, centred on 23^h00^m, $-55^\circ12^m$ and 05^h30^m, $-52^\circ47^m$. These fields lie within a larger area of the southern sky which ACT and SPT plan to survey. The chapter is based on observations taken in 2005, with the exception of 2 clusters from 2006 data. The seeing varies between 0.81″ and 1.09″ with a mean of 0.89″. The image reduction was carried out by Felipe Menanteau using the Rutgers Southern Cosmology Pipeline (flat field correction, CCD calibration, removal of saturated star bleed-trails, and bad pixel masks). Next the images were aligned, stacked and median combined using SWarp (Bertin, 2006); an astrometric solution was found by matching stars to sources in the US Naval Observatory Catalog. Additional masks were made to remove saturated stars, satellite trails and other blemishes in the image, removing 8% in total. For more information see Menanteau et al. (2009). Note that I use AB magnitudes throughout. To calculate photometric redshifts (photo-zs), multi-band SExtractor (Bertin & Arnouts, 1996) *g,r,i,z* isophotal magnitudes were used to find redshift probability distributions of each object. This was done by Felipe Menanteau using the BPZ code (Benítez, 2000), see also Menanteau et al. (2009). I utilized the *i* band data, 3 co-added exposures of 450s each, for this shear analysis. I focused on the 4 clusters found in SZ (Staniszewski et al., 2008).

4.2.1 Mass Estimates Method

In order to obtain a mass estimate for each cluster, the following steps were carried out:

- foreground galaxies were removed,
- a cluster centre was found using either Wiener mass reconstruction or luminosity-weighted centre, and
- the shear was fitted to an NFW model to give mass estimate.

This section explains each of these processes in turn.

Removal of Foreground Galaxies

For individual cluster measurements, each catalogue was cut at the redshift of the cluster, to remove foreground galaxies. The reason for doing this is that we only wanted to use source galaxies behind the clusters to make lensing measurements of the clusters. Galaxies in front of the cluster have not been lensed by the cluster, and so if they were included in the catalogues, then the lensing signal would be diluted by these unlensed galaxies. These cuts were made using the photo-z information for each galaxy. Galaxies which had a photo-z value equal to or less than the photo-z of the cluster were removed. When cutting the foreground sources in the catalogues, objects without

photo-z were assumed to be at higher redshift than the cluster, and they have been left in all catalogues.

Cluster Centres

The centre of each cluster was chosen to be the luminosity-weighted centre, the exception to this being three SPT clusters (those at redshifts $z = 0.27$, $z = 0.36$ and $z = 0.70$). I will explain shortly how these clusters were centred. The fourth SPT cluster, at redshift $z = 0.88$ was also centred on its luminosity weighted centre. The luminosity-weighted centre was calculated by Felipe Menanteau using the r-band luminosities of all of the galaxies classified as cluster members according to their photo-z.

The three SPT clusters at redshifts $z = 0.27$, $z = 0.36$ and $z = 0.70$ were centred using their Wiener mass reconstructions. Mass reconstructions were carried out for these three SPT clusters using a Wiener-filtered mass reconstruction method developed by Patrick Simon (Hu & Keeton (2002, section II) Simon et al. (2009)) to reconstruct the surface mass density (described in Section 3.2.6). The centre of each of these clusters was chosen to be the peak of the mass map. These centres are not the same as the luminosity-weighted centres, but should more closely match the centre of the dark matter halo.

The fourth SPT cluster, at redshift 0.88, was also centred on its luminosity-weighted centre. This was done because we would not expect to be able to map this cluster with gravitational lensing, because the data is not deep enough to have enough sources behind this cluster.

The Wiener-filtered maps were used solely to find the centre of the cluster, then the NFW model was fitted to the tangential shear data (not the Wiener reconstructed maps).

Fitting NFW Profiles

The IMCAT ETPROFILE routine was used to calculate the tangential shear, γ_T, and the average convergence within an aperture of size θ, $\bar{\kappa}(< \theta)$ in radial bins around the cluster centre. The same ETPROFILE code was used to calculate the B modes - radial shear, γ_r, and the B mode convergence, $\bar{\kappa}_B(< \theta)$ by rotating the E mode shear data by 45° (see Section 2.7).

In order to obtain mass estimates, the binned output from IMCAT'S ETPROFILE routine was used to carry out a χ^2-fit of the reduced shear to the universal Navarro, Frenk & White (1996), NFW profile. The concentration index of the halo was taken as a function of mass and cluster redshift (Dolag et al., 2004) so we had a one-parameter system. As a result of this process, a mass estimate, M_{200}^{Lens}, was obtained for each cluster (given by the most likely mass) and asymmetric one-sigma errors are given for that estimate. As introduced in Section 1.3.3, M_{200} is the mass within a region in which the density is 200 times the mean background matter density $\Omega_m \rho_{cr}$. In the NFW fit, r_{200} was also calculated. This is the radius where the density enclosed is 200 times the critical density.

4.3 First lensing measurements of SZ-detected clusters

The Wiener-filtered mass reconstructions for three of the SPT SZ-detected clusters are shown in Figures 4.3, 4.4 and 4.5. We would not expect to detect the fourth SZ cluster at redshift $z \sim 0.88$ with this lensing data, as it is not deep enough and there are not enough sources at higher redshift than the cluster in order to measure the lensing signal. Our mass maps of clusters SPT0517-5430, SPT0509-5342, and SPT0528-5300 have peak S/N=2.9, 3.2 and 1.9 respectively. The reconstruction of SPT0528-5300 is not a strong detection in the map, with a lower signal-to-noise of only 1.9. The position of the peak of each mass map is shown in these plots with a blue asterisk. The r_{200} measurement (obtained from the NFW fit) is also plotted here with a blue circle centred on the mass peak. A circle indicates the BCG in each optically selected cluster, an $\times$ indicates a peak in X-ray emission, and a + denotes the SZ peak. In the cases of the two lower redshift clusters, SPT0517-5430 and SPT0509-5342, the r_{200} measurements centred on the mass peak enclose the BCG as well as the SZ peak and X-ray peak. In the case of the $z = 0.7$ cluster, SPT0528-5300, the BCG and SZ peak are just outside the r_{200} radius as centred on the mass peak. This suggests that perhaps the mass peak found is not close enough to be part of the same cluster which was found with SZ, or that the cluster has extended substructure and is not a uniform NFW shape. The other possibility is that the mass peak found with lensing is the result of some false lensing signal. False lensing signals can arise for a number of reasons, such as intrinsic alignments, an incorrect PSF model correction, insufficient masking which can lead to false detections which mimic a lensing signal, or structure along the line of sight. These maps have been reconstructed from catalogues which have the foreground galaxies cut, and so this effect should be minimised in front of the cluster. However, extended filamentary structure along the line of sight behind the cluster could still cause lensing peaks when the mass is looked at in 2D. The possible effects of masks needs to be considered too, particularly in the cases of the reconstructions of SPT0517-5430 and SPT0509-5342, both of which have large stars close to the peaks. The area surrounding each star has been masked, and so there is no shear information in that area. This means that the reconstruction in this area has less information, and so this may have affected the shape of the contours in these regions.

To test the likelihood of finding peaks of this size in randomised noise fields, a peak statistics analysis was carried out by Patrick Simon. For each of the 3 fields containing the SPT clusters, he created 1000 random noise realisations. Using these, he calculated peak statistics, and the probability of finding peaks of different signal-to-noises. A peak was defined as a pixel larger than any of its direct neighbours. The resulting cumulative statistics show that for the field containing cluster SPT0517-5430 (with peak S/N = 2.9), there was a probability of 0.02% of finding a peak with S/N = 2.9 in pure noise in a field of size 42×42 arcmin. In this same field, a S/N peak of 2 had a 1.2% chance of being from random noise. In the field containing cluster SPT0509-5342 (S/N = 3.2), a peak with S/N=3.2 had a probability 0.1% of being found in a pure noise field (of size 42×42 arcmin). For this same field, a S/N peak of 2 had a 6% chance of finding a peak of this size in a random noise field. Finally, for the lowest S/N detection of these three clusters, SPT0528-5300 (with peak S/N=1.9), there is a 6% probability that a peak with S/N = 1.9 is from pure noise (again, in a field of size 42×42 arcmin). These statistics show that, for the case of the two lower

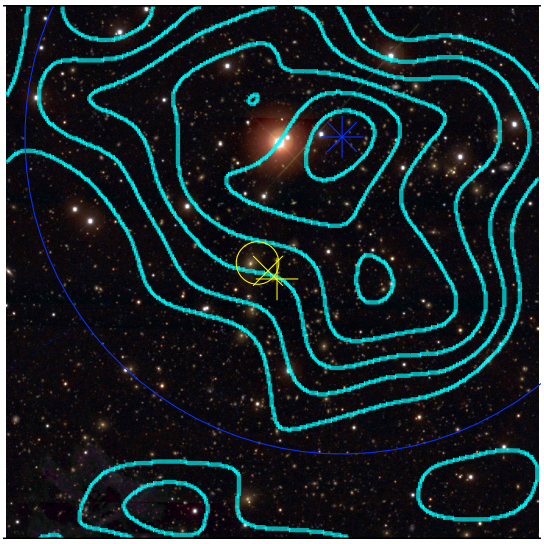

Figure 4.3: Lensing mass reconstructions for SZ-detected cluster SPT 0517-5430 ($z = 0.27$). Contours show the projected lensing convergence (mass distribution), at 1%, 1.5%, 2%, ... 4%. The field is 11.25 arcminutes by 11.25 arcminutes. A circle indicates the BCG in each optically selected cluster, an × indicates a peak in X-ray emission, and a + denotes the SZ peak. A blue asterisk marks the position of the mass peak, and the r_{200} measurement from the NFW fit is plotted with a blue circle. This reconstruction has peak SN = 2.9 at the position of the cluster.

redshift clusters, that these detections are very unlikely to have come from noise. For the $z = 0.7$ cluster, there is a 6% chance of finding a peak such as this in random noise.

4.3.1 Convergence Results

Figure 4.6 shows the average convergence within an aperture of size θ, $\bar{\kappa}(< \theta)$, for the three detected SPT clusters. In red (empty circle) I show the B-mode. It can be seen for SPT 0517-5430 (Figure 4.6, *Top*) that the convergence E mode is much higher than the B mode. Also, the convergence and B mode results for SPT 0528-5300 (Figure 4.6, *Bottom*) suggests that the shear catalogue is reasonably free of systematics. The B modes in the inner region of SPT 0509-5342 (Figure 4.6, *Middle*) are lower than the E modes, but in the outer radii (> 200arcsec), the B modes are higher than the E mode convergence, suggesting that there may be systematic problems with this NFW fit.

Figure 4.7 shows the reduced tangential shear, for the three detected SPT clusters. In magenta, the NFW fit is shown, and the one sigma errors on the fit is shown in dashed magenta lines. The dashed error bars show the B modes added in quadrature. The chi-squared fit uses these errors (given by statistical errors added in quadrature to the B mode). The NFW fit of reduced shear for SPT 0517-5430 has a goodness of fit reduced $\chi^2 = 0.72$, SPT 0509-5342 has reduced $\chi^2 = 1.13$, and SPT 0528-5300 has reduced $\chi^2 = 0.81$. The values of reduced χ^2 for clusters SPT 0517-5430 and SPT 0528-5300 show that the NFW is well fitted to the data because they are less than 1. The NFW fit to cluster SPT 0509-5342, with reduced $\chi^2 = 1.13$, is a less good fit. This can also be seen by the data (Figure 4.7 *Top Right*), that the data is less well fit by an NFW. This cluster also had higher B modes in the average convergence plots (see

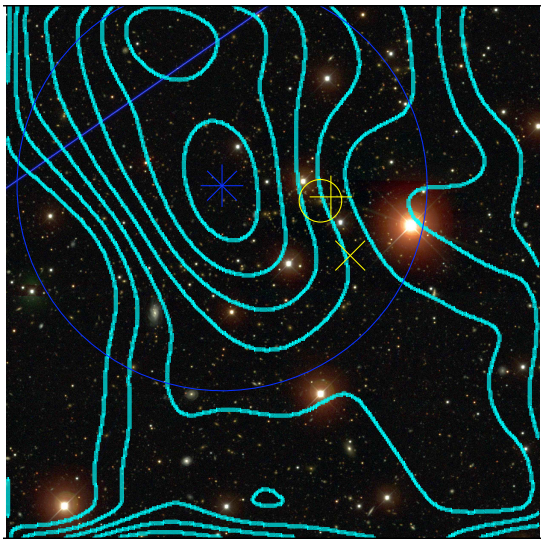

Figure 4.4: Lensing mass reconstructions for SZ-detected cluster SPT 0509-5342 ($z = 0.36$). Contours show the projected lensing convergence (mass distribution), at 1%, 1.5%, 2%, ... 4%. The field is 11.25 arcminutes by 11.25 arcminutes. A circle indicates the BCG in each optically selected cluster, an × indicates a peak in X-ray emission, and a + denotes the SZ peak. A blue asterisk marks the position of the mass peak, and the r_{200} measurement from the NFW fit is plotted with a blue circle. This reconstruction has peak SN = 3.2 at the position of the cluster.

Figure 4.6). Despite being a poorer fit, an NFW is, however, a satisfactory fit to these data, as we would expect the reduced $\chi^2 = 1 \pm \frac{\sqrt{2\nu}}{\nu}$, where ν is the number of degrees of freedom of the fit. For this fit $\nu = 8$ and so we would expect $\chi^2 = 1 \pm 0.5$. Therefore, a fit of $\chi^2 = 1.13$ is sufficiently good.

Calculating $\bar{\kappa}$ constant

In Figure 4.6 the average convergence within an aperture of size θ, $\bar{\kappa}(< \theta)$ were presented. These $\bar{\kappa}$ values are defined from infinity inwards towards the clutser centre, in radial bins centred on the cluster. The values calculated in the KSB ETPROFILE code start at the outside edge of the cluster at $r = r_{max}$. Beyond $r = r_{max}$ ETPROFILE assumes the contribution to $\bar{\kappa}$ is zero. Because of the mass sheet degeneracy (see Section 1.5.2), the value of $\bar{\kappa}$ outside the maximum radius is unknown. We choose to fix it by assuming a profile for the density and calculating the outer surface mass density theoretically rather than assuming zero. I have calculated the theoretical value of kappa from infinity to r_{max}, for each cluster (this value is dependent on cluster mass). This constant value is then added to the kappa bar values in each bin. I find this to be a very small correction in each case, and so find that the assumption in the KSB ETPROFILE code that the contribution beyond r_{max} is negligible is valid.

The following calculation was carried out to calculate the value of $\bar{\kappa}$ constant. The $\bar{\kappa}$ output for each cluster from KSB ETPROFILE is (Clowe et al., 2000):

$$\bar{\kappa}(r) = 2 \int_0^r \gamma_t(r') \, \mathrm{d} \ln r' \, . \tag{4.1}$$

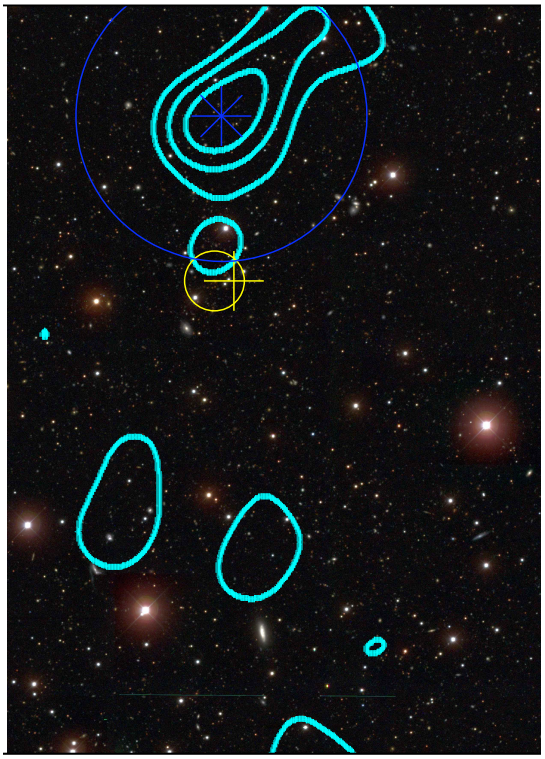

Figure 4.5: Lensing mass reconstructions for SZ-detected cluster SPT 0528-5300 ($z = 0.7$). Contours show the projected lensing convergence (mass distribution), at 1%, 1.5%, 2%, ... 4%. The field is 11.25 arcminutes by 15.75 arcminutes. A circle indicates the BCG in each optically selected cluster, an × indicates a peak in X-ray emission, and a + denotes the SZ peak. A blue asterisk marks the position of the mass peak, and the r_{200} measurement from the NFW fit is plotted with a blue circle. This reconstruction has peak SN = 1.9 at the position of the cluster.

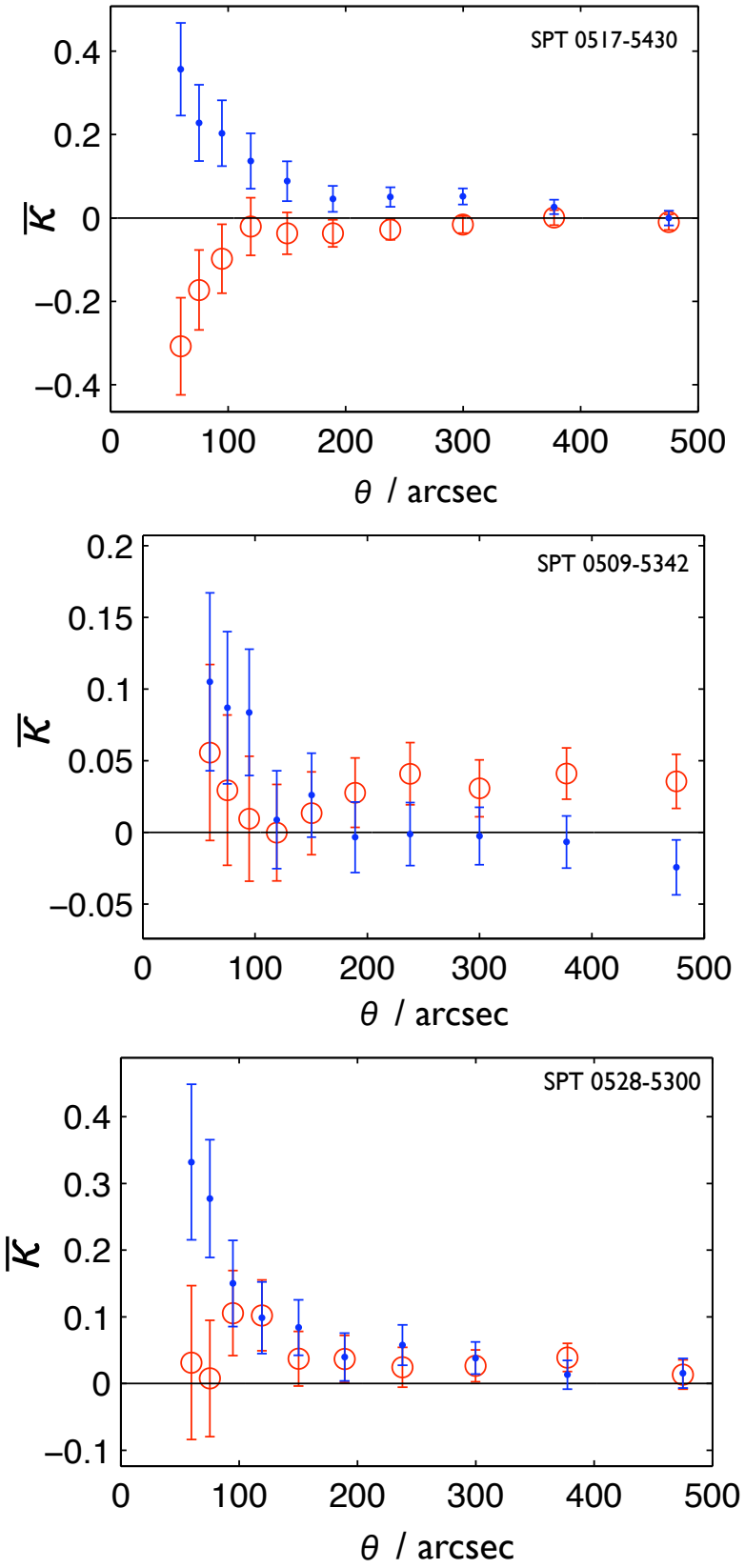

Figure 4.6: Average convergence within an aperture of size θ, $\bar{\kappa}(< \theta)$ for the three detected SPT clusters. The red (empty circle) shows the B-mode systematic error.

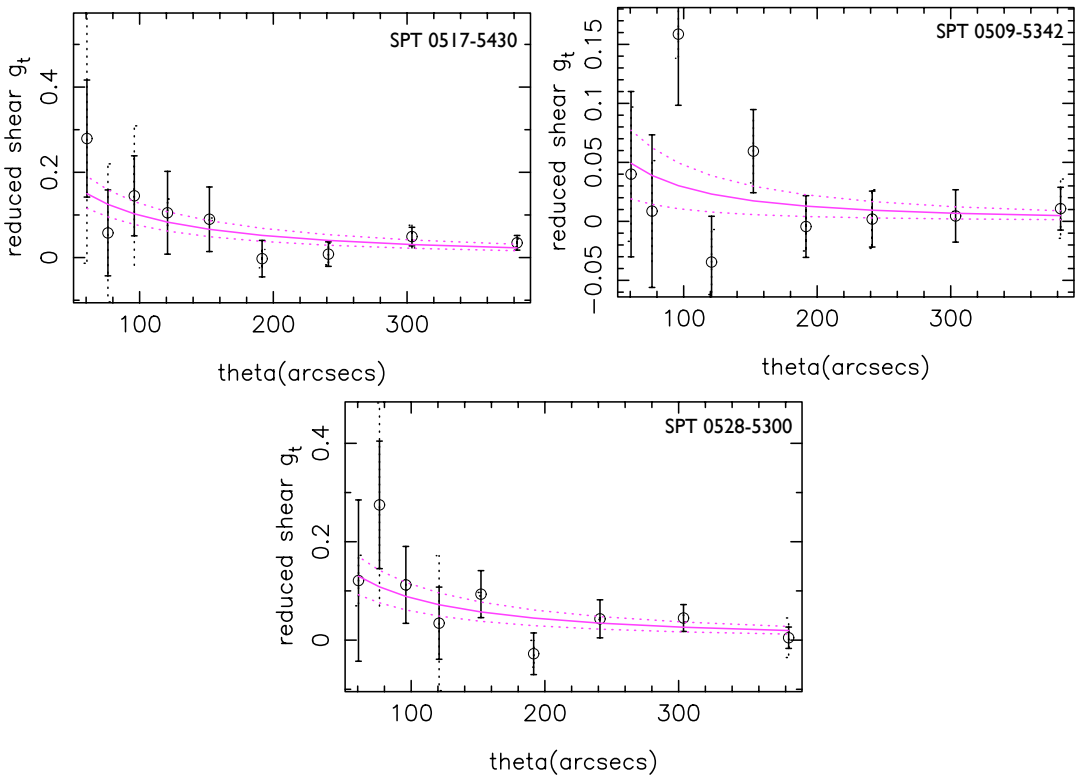

Figure 4.7: Reduced tangential shear for the three detected SPT clusters. The dashed error bars show the B mode added in quadrature. The NFW fit for each cluster is shown in magenta, with the one sigma errors on the fit shown in dashed magenta lines. The NFW fit of reduced shear for SPT 0517-5430 has a goodness of fit reduced $\chi^2 = 0.72$, SPT 0509-5342 has reduced $\chi^2 = 1.13$, and SPT 0528-5300 has reduced $\chi^2 = 0.81$.

And this is calculated out to $r = r_{max}$. Beyond $r = r_{max}$ ETPROFILE assumes the contribution to $\bar{\kappa}$ is zero. However we want to know what the whole integral is from zero to infinity so we need to also calculate the integral from r_{max} to infinity

$$\bar{\kappa}_{\rm const} = 2 \int_{r_{max}}^{\infty} \gamma_t(r)\, {\rm d} \ln r \,, \tag{4.2}$$

and add this constant to the result from Eq. 4.1. To do this I used the equations from King et al. (2001) which were shown in Section 2.8.2. I calculated this theoretical value of $\bar{\kappa}$ from r_{max} to infinity for each cluster to add to the output of $\bar{\kappa}$ from KSB. The results of this calculation of $\bar{\kappa}_{\rm const}$ are negligible and are shown in Table 4.3.

4.3.2 *Y* Parameter Results

As introduced in Section 1.4, the SZ effect occurs when high energy electrons in the hot gas of galaxy clusters inverse Compton scatter with photons from the CMB. After this process, the CMB photon gains a small amount of energy. The SZ effect has a unique spectral signature: a decrease in CMB intensity at frequencies lower than 218GHz and increase at higher frequencies. The Compton y parameter, and integrated Compton Y parameter are measures of this SZ effect (see Eqs. 1.36 and 1.37). The Y parameter is a measure of how much the photons are upscattered by hot electrons in a cluster.

I have also calculated the expected Compton y parameter and its integral over solid angle, $Y \equiv \int {\rm d}\Omega\, y(\Omega)$ for the clusters. In Table 4.2 I show the expected temperature decrement in the Rayleigh-Jeans limit $\langle -\Delta T_{RJ} \rangle = 2 T_{CMB} \langle y \rangle$, averaged within r_{200}, where T_{RJ} is the temperature in the Rayleigh-Jeans limit and T_{CMB} is the temperature of the Cosmic Microwave Background (CMB). As was shown in Figure 1.3, there is a cross over at around 218GHz between the increment at higher frequencies and decrement and lower frequencies. The amount of decrement though depends on where in the lower frequency range is observed. The values quoted are for the Rayleigh-Jeans limit. At 150GHz, however, the actual decrement is smaller by a factor 0.29 (Carlstrom et al., 2002, Fig. 2).

To compute Y we assume that gas follows dark matter and obtain an analytic result. It ignores the gas history (cf. Reid & Spergel (2006))[1] but our simple model agrees, within 25%, with the empirical scaling relations of Motl et al. (2005) and Nagai (2006), and is supported by Atrio-Barandela et al. (2008) who show from stacked SZ clusters that the baryon profile is consistent with NFW. Eq. 1.38 gives Y as a function of M_{200}. We assume that ions and electrons are in thermal equilibrium with a Helium mass fraction of 0.24, $\alpha = 1.93$. See Appendix A for a full derivation of Eq. 1.38. We also assume the concentration index

$$c_s(M_{200}) = 9.59(1+z)^{-1} (M_{200}/10^{14} h^{-1} M_\odot)^{-0.102} \,, \tag{4.3}$$

(Dolag et al., 2004), but note that this is for a $\sigma_8 = 0.9$ cosmology, higher than current estimates (Komatsu et al., 2009). Different studies at $\sigma_8 = 0.9$ and $\sigma_8 = 1$ show differences of the order of 15% on $c_s(M)$ (Dolag et al., 2004; Bullock et al., 2001), but

[1] In the model of Reid & Spergel (2006), cluster asphericity, thermal conduction, intracluster magnetic fields, turbulent support and dynamical events such as mergers are ignored.

the trend is in an unexpected direction (increasing with decreasing σ_8), so extrapolation to the current WMAP7 value of $\sigma_8 = 0.8$ is not straightforward. One might expect it to go the other way, since $c_s(M)$ tends to increase with time (hence with σ_8). We take the $\sigma_8 = 0.9$ concentration, but note that with the expected evolution, it may overestimate c_s by around 10%. This is small in comparison with the mass errors.

Values of Y were predicted for clusters with mass detections, with statistical errors which are dominated by the error in M_{200}^{Lens}.

Mass Estimates

With a uniform prior on masses, I record in Table 4.2 the most likely masses and asymmetric one-sigma errors for the SPT SZ clusters. X-ray masses from soft X-ray luminosity using the correlations in Reiprich & Böhringer (2002) are shown in Table 4.2. Also included here are mass estimates $M_{L_{200}}$ and M_{L_X} which are published in Menanteau & Hughes (2009). $M_{L_{200}}$ is an estimate of the mass, calibrated by weak lensing measurements for SDSS clusters (Reyes et al., 2008), within a radius r_{200} in which the number density is estimated to be $200/\Omega_m$ times the average galaxy number density. This is discussed in further detail in Section 5.1.3. Predicted Y and average y within r_{200} are also shown here, along with the cluster centre used. Recent ACT SZ measurements (Hincks et al., 2009) are in agreement with our predictions for the two low-redshift clusters which we can compare. Observations of SPT0517-5430 with XMM-Newton yield an X-ray mass within r_{500} of $6.4 \times 10^{14} M_\odot$ (Zhang et al., 2006).

Looking at the recent ACT paper by Hincks et al. (2009) we can see that they detect clusters with Y per steradian down to $Y \sim 0.1$. This translates into Y_{200} in the units used here ($/10^{-5} arcmin^2$) of $\sim$ 10. So, I would predict that clusters with $Y_{200} \sim 10$ should be detected by ACT. It is surprising therefore that they do not detect cluster SPT 0528-5300.

4.3.3 Further properties of the SPT clusters

Table 4.3 shows further properties of these clusters obtained when fitting NFW profiles to the tangential shear measurements of each cluster. Values of the concentration parameter c, the scale radius r_s for the NFW fit are given here. For information on $\bar{\kappa}$ constant see Section 4.3.1. The value of median source redshift for each cluster is also shown here. The median z of sources was calculated with a given n(z) $\propto z^2 exp{-}(z/z_0)^{1.5}$, for which the median is $1.41 z_0$. From this, the fraction of sources with redshift greater than the cluster redshift was calculated by integrating $n(z)$ from the cluster redshift to infinity. The concentration is given by Equation 4.3 and it is not a free parameter in the fit.

4.4 Conclusions

There has been longstanding optimism that SZ selection would be among the most favourable ways of detecting clusters for cosmological studies, since simulations show

Table 4.2. Cluster Weak Lensing, Optical, X-ray Mass Estimates & Predicted SZ

ID	R.A. Dec. Center of NFW fit		Center	$z_{\rm photo}$	$M_{L_{200}}$ ($10^{14}M_\odot$)	$M_{L_{\rm X}}$ ($10^{14}M_\odot$)	M_{200}^{Lens} ($10^{14}M_\odot$)	$2T_{CMB}\langle y\rangle$ (μK)	Y_{200} (10^{-5} $arcmin^2$)
SPT 0517-5430	05:16:27.3	−54:27:39.4	map	$0.27^{+0.02}_{-0.02}$	17	8	$6.74^{+3.46}_{-2.49}$	338^{+520}_{-210}	413^{+423}_{-225}
SPT 0509-5342	05:09:24.4	−53:43:34.4	map	$0.36^{+0.02}_{-0.02}$	4	6	$1.28^{+1.40}_{-0.97}$	77^{+164}_{-18}	23^{+57}_{-20}
SPT 0528-5300	05:28:04.8	−52:58:55.6	map	$0.70^{+0.03}_{-0.02}$	≥ 21	< 11	$15.44^{+9.03}_{-6.96}$	2138^{+3443}_{-1150}	1082^{+1309}_{-696}
SPT 0547-5345	05:46:41.1	−53:44:52.1	lum.	$0.88^{+0.08}_{-0.04}$	≥ 4	10	< 2.56	-	-

Note. — Physical properties of SZ selected clusters in the SCS regions. Redshifts are the photometric redshift of the BCG, with $\pm 1\sigma$ limits. The ID is based on the position of the BCG. The NFW fit is centred at either the peak in the mass map (map) where available, or the luminosity-weighted centre (lum.). The values of $M_{L_{200}}$ and $M_{L_{\rm X}}$ are those published in Menanteau & Hughes (2009). The uncertainty in $M_{L_{200}}$ is estimated to be a factor of two (Menanteau et al., 2009). Values of $2T_{CMB}\langle y\rangle$ and Y are predicted from M_{200}^{Lens} using Eq. 1.38. Note that ΔT_{SZ} at 150GHz is 0.29 of the penultimate column value.

Table 4.3. Cluster properties of NFW fits including concentration c_s, r_{200} and the correction to KSB ETPROFILE value of $\bar{\kappa}$.

Cluster ID	z_{lens}	z_{source}	r_{200} (h^{-1} Mpc)	c_s	$\bar{\kappa}_{const}$	M_{200}^{Lens} ($10^{14}M_\odot$)
SPT 0517-5430	$0.27^{+0.02}_{-0.02}$	0.79	$1.17^{+0.17}_{-0.17}$	$6.4^{+0.3}_{-0.3}$	0.0059	$6.74^{+3.46}_{-2.49}$
SPT 0509-5342	$0.36^{+0.02}_{-0.02}$	0.84	$0.65^{+0.18}_{-0.25}$	$7.1^{+0.5}_{-1.1}$	0.0014	$1.28^{+1.40}_{-0.97}$
SPT 0528-5300	$0.70^{+0.03}_{-0.02}$	1.09	$1.32^{+0.22}_{-0.24}$	$4.4^{+0.2}_{-0.3}$	0.0062	$15.44^{+9.03}_{-6.96}$

Note. — z_{source} is the median source redshift of galaxies behind each cluster.

that the SZ detection threshold corresponds very nearly to a threshold in mass and is redshift-independent. Despite this, it was not guaranteed that the first SZ experiments could trace mass. In order to demonstrate this I have measured, for the first time, weak lensing masses of clusters detected by their Sunyaev-Zel'dovich signature. Of the four clusters detected by the SPT and published recently by Staniszewski et al. (2008), I have detected three of them, using optical imaging data from the Southern Cosmology Survey. The fourth cluster, at redshift of 0.88, is too distant to be detected with these optical data. By fitting NFW profiles I have established that the published SZ peaks correspond to mass regions, and so I can confirm that the first installment of SZ selected clusters trace the most massive clusters.

I have also presented weak lensing mass estimates for other clusters detected optically in the SCS. As one might expect the published SZ clusters have masses at the upper end of the sample $10^{14} - 10^{15} M_{\odot}$. Furthermore, I have presented analytic predictions for the integrated Compton Y parameter for the all clusters in the sample for future comparison with SZ observations. The predictions presented here will be invaluable as the new SZ measurements are gradually made for these clusters.

The Southern Cosmology Survey was designed such that it surveyed a large area of the southern sky, a common area also being survey in SZ with the Atacama Cosmology Survey (ACT). Unfortunately, the ACT data was not available in the time frame of this thesis and so I was unable to test how well lensing mass peaks correlated with SZ decrements. However, when this ACT data is available, it will be of great interest to this community.

The Atacama Cosmology Telescope (ACT) is currently observing the southern sky in submillimetre wavelengths. It is looking at the cosmic microwave background in 3 frequencies, 148GHz, 218GHz and 277GHz. These frequencies enable it to detect the Sunyaev-Zel'dovich (SZ) effect — which manifests itself as a deficit at 148GHz and which is not present at the other two higher frequencies — and therefore to detect large galaxy clusters (see Section 1.4). The first results from ACT were published by Hincks et al. (2009) where they successfully detected 8 previously detected clusters and 2 new cluster candidates using this SZ data.

As discussed earlier in this chapter (see Section 4) the SZ effect is a powerful way to detect and probe galaxy clusters. It has been shown that the intensity of the SZ effect summed over the entire cluster closely tracks the mass of the cluster (Motl et al., 2005) and in order to calibrate this relation between SZ and mass, we need to utilise gravitational lensing mass measurements. Comparison of ACT and SPT data with SCS data is an important step in calibrating the relation between lensing mass and SZ measurement, which can be done more fully with the larger sky surveys of Pan-STARRS and Planck.

The South Pole Telescope (SPT) is another SZ survey which overlaps with some of the SCS field, and has the advantage that it is placed at the South Pole, where the atmospheric conditions are much better. It does, however, suffer because of its latitude in the way in which it can scan the sky, and cannot scan the sky in different directions the way ACT can, which is a way to reduce systematics Hincks et al. (2009).

A new CMB mission called Planck will survey the entire sky. Planck will be powerful at measuring the SZ effect because it has many frequency bands, both sides of 218GHz, and so the cross over between a decrement at lower frequencies, and increment at higher frequencies will be probed. This will allow the SZ signature to be

distinguished from other effects or foreground contamination. Planck will be complemented by a full sky lensing analysis from the Pan-STARRS survey. In order for Pan-STARRS to be used for such analysis, there will probably need to be improvements to the image quality. It is currently thought that the PS1 3π survey will have a number density of $n \sim 6$ galaxies per square arcminute, and so this dataset is likely to have very similar properties, and problems, that have been encountered with this SCS dataset.

The relation between SZ and total cluster mass can be tested with the huge sample of clusters which will arise from these large area surveys. Future Pan-STARRS surveys, and surveys such as EUCLID, or DES are likely to have the power to provide a calibration between lensing mass and SZ when combined with Planck.

Chapter 5

Comparing Lensing with Optical Measurements

As discussed in Section 1.3 and in Section 4, galaxy clusters are effective probes of cosmology because the number of clusters as a function of mass $N(m,z)$ at high redshift z is particularly sensitive to different cosmological models. Galaxy clusters can be selected by many different methods, including gravitational lensing, X-ray, Sunyaev-Zel'divich effect and optical richness. But in order to exploit these clusters as probes to test $N(m,z)$ we need to know how their observable properties relate to their masses. Gravitational lensing measurements of galaxy clusters provide mass measurements which are not dependent on gas assumptions like hydrostatic equilibrium (as X-ray measurements do), and do not rely on only measuring the optical tracers (as luminosity measurements do). Dynamical measurements can also be made of cluster masses, from velocity dispersions of galaxies, but with the caveat that relaxation of the cluster must be assumed. Note that although lensing masses do not require assumptions about equilibrium, the clusters in this thesis are measured by NFW profile fitting which carries its own assumptions (see Section 1.3.3).

The relation between the true total mass of a cluster, and an optical or X-ray observable property of the cluster is called a *scaling relation*. Scaling relations between galaxy cluster masses obtained by lensing, and X-ray, SZ or optical tracers will allow measurement of $N(m,z)$ for the largest number of clusters. Scaling relations are useful because there is no way that lensing masses will be obtained for all clusters, and so a proxy is needed. A caveat is that the scaling relations may be calculated at lower redshifts than the high redshift clusters which will be found with SZ, so some assumption will need to be made about the scaling relation evolution with redshift. One plausible assumption is that the scaling relations do not change with redshift at all. It is possible however, that there is some range of redshifts over which evolution could be tested (up to $z \sim 0.5$ perhaps), but one would need to extrapolate beyond that, inevitably leading to some uncertainty.

Work on the scaling relations between lensing mass measurements and X-ray properties have been carried out by Hoekstra (2007), Bardeau et al. (2007), Pedersen & Dahle (2007), Zhang et al. (2008). Scaling relations between optical tracers and lensing measurements have been measured by Johnston et al. (2007) and Reyes et al. (2008). For this study, I utilise a large optically selected cluster catalogue provided by Felipe Menanteau and compare my lensing data to optical tracers, as was done in Reyes et al.

(2008).

In this chapter I present measurements of weak lensing masses for 152 clusters from the 23^{hr} and 5^{hr} fields from the Southern Cosmology Survey, discuss scaling relations relating lensing masses to optical observables, and stack clusters to test mass profiles. The data in the two fields are analysed separately in this thesis. The 23^{hr} field was the first field available to me, and as well as presenting mass estimates for clusters in this field, I predicted SZ Y parameters for the clusters in this field. Over a year later, the 5^{hr} field data became available. This field is much larger — over 6 times the size of the 23^{hr} field — and so has a much larger number of clusters. With this larger field I carried out the stacking and scaling relations work on only this field. The results of these two fields are presented separately: in Section 5.1 I present the 23^{hr} field results; and in Sections 5.2 - 5.4 the 5^{hr} data. This chapter is structured as follows: in Section 5.1 I present lensing mass measurements for 38 optically selected clusters from the 23^{hr} data and describe centering methods; in Section 5.2 I present lensing masses for 114 clusters in the 5^{hr} field. Section 5.3 describes the comparison of lensing mass with optical measurements, constraining the L_{200} scaling relation of Reyes et al. (2008) to higher redshift. In the final part of this study, in Section 5.4, I describe the results of stacking the clusters to test the mass profile.

The measurements from optical imaging of L_{200}, $L_{\rm BCG}$, $M_{L_{200}}$ and the photometric redshifts in this chapter were all provided by Felipe Menanteau. Section 5.1.2 of this chapter has been published in a refereed scientic journal, and appears in the paper:

> "First lensing measurements of SZ-detected clusters"
> McInnes, R. N., Menanteau, F. , Heavens, A. F., Hughes, J. P., Jimenez, R., Massey, R., Simon, P., Taylor, A., 2009, MNRAS, 399, L84

Throughout this thesis I assume a flat cosmology with $\Omega_m = 0.27$, $\Omega_\Lambda = 0.73$ and $H_0 = 100h$ km s^{-1}Mpc^{-1} with $h = 0.71$.

5.1 Clusters in the Southern Cosmology Survey 23hr field

The 23^{hr} field of the Southern Cosmology Survey (SCS) is $\simeq$ 8 square degrees, and includes 43 clusters detected optically by Menanteau et al. (2009). Concentrating on these 43 clusters, I measured lensing masses for them using exactly the same technique described in Chapter 4 for the SZ-selected clusters. Because the SZ clusters were very massive clusters, then the signal to noise of the mass reconstructions was higher, and it was possible to use the centre of the mass reconstruction as the centre of the NFW fit. For these 23^{hr} clusters, I looked at a range of centre-finding techniques described below.

5.1.1 The Cluster Centre

In the literature there are examples of different cluster centres being used for cluster mass measurements. A commonly used centre is the Brightest Cluster Galaxy (BCG) (e.g. used by Hoekstra (2007)). Another possibility is to use the X-ray centre and this

is used by Abate et al. (2009), where they find that the X-ray peak is a good proxy for cluster centre. I have looked at a few centre finding techniques for lensing mass measurements.

In the analysis pipeline, the NFW fit uses the binned output from IMCAT'S ETPROFILE routine and fitted the best NFW profile to it, giving a mass estimate and chi squared goodness of fit. It became apparent that using the BCG as the cluster centre was not always giving a strong signal in the central bins of our data. My hypothesis was that perhaps the result of an NFW fit at different centres could be used to give an improved cluster centre. I wanted to test whether the best fitting (minimum χ^2) NFW would provide the best centre of the cluster.

Taking the existing routine (which required one centre position per cluster), I adapted the routine so that it calculated an NFW fit for each cluster at many different central positions. These different centres were equally spaced centred on the BCG. This code was designed such that the size of the grid and also the spacing between the grid points could be easily chosen. The code operates as follows:

- A grid of possible centres is made
  and then for each possible centre
  - Data is binned radially around that centre
  - Tangential shear is calculated using IMCAT'S ETPROFILE
  - The NFW fitting code is called
  - The NFW outputs are created and saved

- These outputs for all centres are collated
- Three grids are formed: cluster mass estimates; χ^2; and signal-to-noise.

The result of this is shown for three clusters (SPT 0517-5430, SPT 0528-5300 and SPT 0509-5342 which were introduced in Chapter 4) in Figure 5.1. The left hand column shows the results of χ^2 at different central positions, the middle column shows the mass measurements for those different centres, and the final column the signal-to-noise of the mass estimate at each central position. The three rows contain results for the three different clusters: the top row is for SPT 0517-5430, the middle row is SPT 0528-5300, and the bottom row is SPT 0509-5342. The size of the area covered for cluster SPT 0517-5430 is $\simeq$ 3.6 arcmin square, and for the other two clusters, a larger area of $\simeq$ 9 arcmin square has been computed. In each case, the BCG position is marked with a purple + sign. The purple $\times$ indicates the position of the minimum χ^2 value. Unfortunately it is possible (and indeed this is the case in these three examples) for the lowest χ^2 value to be the fit of an NFW having a zero mass. The lowest χ^2 value is often far away from the BCG, and does not help us to find a good fitting non-zero mass for the cluster. The resulting mass 'maps' (middle column) are effectively mass reconstructions with a small smoothing scale, and so one cannot use this information to pick the centre without biasing the result. Finally, if we look at the signal-to-noise results, we see that these are very similar to the mass results. The noise across this region must be almost constant, but again, we would be biased if we selected our cluster centre by using the largest signal-to-noise.

To conclude, searching for the cluster centre using the best fitting NFW, or its mass estimate is not a viable way forward. I believe that this technique has not worked because the best-fitting (lowest χ^2 value) NFW can be one which has zero mass. Perhaps another reason why this technique is not picking out the massive regions is that either the clusters are not best fitted by an NFW profile (See Section 5.4), or that the lensing data are too noisy because of the data quality. I have resumed centering the clusters on their luminosity-weighted centre, which, as discussed in Section 4.2.1, was calculated using the r-band luminosities of all of the galaxies classified as cluster members according to their photo-z. In the cases where I had a Wiener mass reconstruction for a cluster, the luminosity-weighted centre was closer to the peak of the mass reconstruction than the BCG centre was. Therefore, it seems that using the luminosity-weighted centres should more closely match the mass distribution than using the BCG. As already said, when using the BCG as the cluster centre was not always giving a strong signal in the central bins of our data. Using fits centred like this will reduce the mass of the cluster, because the NFW fit will be brought down by the lower central bins. These mass profiles were improved by centering on the luminosity-weighted centre or mass reconstruction. Possibly by centering on the luminosity-weighted centre, and therefore by more closely matching the centre of the mass distribution, the tangential shear signal, and hence mass, will be higher than if the BCG was used.

5.1.2 Cluster Lensing Mass Results

I present the measurements of weak lensing masses for 38 optical clusters selected from $\simeq$ 8 square degrees (Menanteau et al., 2009). Of the 43 clusters detected by Menanteau et al. (2009), I found non-zero mass estimates for 24 clusters, and upper limits for the remaining clusters. I do not consider 5 of the clusters as they are in regions only observed in a single exposure. All clusters discussed in this chapter are centred on their luminosity-weighted centre. The weak lensing masses, M_{200}^{Lens} are shown in Table 5.1. In Table 5.1, I also show the expected temperature decrement in the Rayleigh-Jeans limit $\langle -\Delta T_{RJ} \rangle = 2T_{CMB}\langle y \rangle$, averaged within r_{200}. Both of these have been calculated in the same way as for the SZ-selected clusters as described in Section 4.3.2. Table 5.1 also contains other properties of these optically selected clusters, including the co-ordinates of the luminosity-weighted centre, the photometric redshifts of the BCG with $\pm 1\sigma$ limits, and the optical mass estimate $M_{L_{200}}$, where the uncertainty in this is estimated to be a factor of two (Menanteau et al., 2009). It should be noted that ΔT_{SZ} at 150GHz is 0.29 of the value of $2T_{CMB}\langle y \rangle$ (see Section 4.3.2). Based on the results in Hincks et al. (2009), I would estimate that the clusters with $Y_{200} > 10$ should be detected by ACT (as discussed in Section 4.3.2).

5.1.3 $M_{L_{200}}$

The method for this optical cluster selection was described in Section 4.1.1. In this selection method, E/S0 galaxies were used. The value of r_{200} was estimated from the cluster richness using a scaling relation by Hansen et al. (2005) derived from SDSS data, and was extrapolated beyond $z \sim 0.3$ for the higher redshift clusters. In this section I will compare my lensing measurements to $M_{L_{200}}$, obtained from Felipe

Table 5.1. Cluster Weak Lensing, Optical & Predicted SZ

ID	R.A. Centre of NFW fit	Dec.	$z_{\rm photo}$	$M_{L_{200}}$ ($10^{14}M_\odot$)	M_{200}^{Lens} ($10^{14}M_\odot$)	$2T_{CMB}\langle y\rangle$ (μK)	Y_{200} (10^{-5} $arcmin^2$)
SCSO J232540.2-544430.9	23:25:32.2	−54:44:21.5	0.10±0.02	2.10	$0.23^{+0.89}_{-0.23}$	7^{+88}_{-7}	6^{+75}_{-6}
SCSO J232230.9-541608.3	23:22:27.2	−54:16:26.9	0.12±0.02	1.62	$0.85^{+0.92}_{-0.59}$	27^{+64}_{-23}	39^{+93}_{-33}
SCSO J233000.4-543707.7	n/a		0.14±0.02	1.19	-	-	-
SCSO J232419.6-552548.9	23:24:33.6	−55:26:14.4	0.18±0.04	1.19	< 0.26	-	-
SCSO J233106.9-555119.5	23:31:08.2	−55:50:56.4	0.19±0.04	0.55	$0.20^{+0.69}_{-0.20}$	8^{+83}_{-8}	2^{+19}_{-2}
SCSO J233252.9-561454.1	23:32:51.4	−56:15:29.8	0.20±0.03	1.17	< 0.09	-	-
SCSO J233215.5-544211.6	23:32:17.1	−54:42:43.1	0.20±0.04	1.69	$1.02^{+0.84}_{-0.61}$	40^{+70}_{-32}	25^{+42}_{-19}
SCSO J233037.1-554338.8	23:30:34.8	−55:43:41.5	0.20±0.04	0.99	$1.62^{+1.07}_{-0.77}$	65^{+44}_{-31}	68^{+50}_{-24}
SCSO J233550.6-552820.4	23:35:46.4	−55:29:21.3	0.22±0.04	0.67	$0.03^{+0.71}_{-0.03}$	1^{+250}_{-1}	$0.1^{+21}_{-0.1}$
SCSO J232200.4-544459.7	23:22:01.8	−54:45:38.8	0.27±0.04	1.73	$0.26^{+0.86}_{-0.26}$	12^{+125}_{-12}	2^{+18}_{-2}
SCSO J233522.6-553237.0	23:35:20.0	− 55:32:30.9	0.29±0.04	2.19	$0.85^{+1.60}_{-0.85}$	42^{+205}_{-42}	11^{+55}_{-11}
SCSO J233807.5-560304.9	23:38:07.7	−56:02:55.0	0.30±0.04	2.60	< 0.64	-	-
SCSO J232956.0-560808.3	23:29:55.8	−56:08:28.2	0.32±0.04	1.99	$2.13^{+2.75}_{-1.73}$	117^{+350}_{-110}	49^{+75}_{-46}
SCSO J232839.5-551353.8	23:28:41.0	−55:13:25.2	0.32±0.05	1.00	$1.69^{+2.01}_{-1.32}$	92^{+249}_{-85}	33^{+88}_{-30}
SCSO J232633.6-550111.5	23:26:31.1	−55:01:26.9	0.32±0.05	2.81	< 0.48	-	-
SCSO J233753.8-561147.6	23:37:57.1	−56:12:05.8	0.33±0.04	2.94	$0.15^{+0.74}_{-0.15}$	8^{+148}_{-8}	1^{+9}_{-1}
SCSO J232156.4-541428.8	23:21:55.5	−54:14:20.0	0.33±0.04	1.25	< 0.71	-	-
SCSO J233003.6-541426.7	23:30:06.3	−54:13:58.9	0.33±0.04	0.88	$2.81^{+2.07}_{-1.47}$	160^{+241}_{-113}	75^{+114}_{-53}
SCSO J233231.4-540135.8	n/a		0.33±0.04	1.67	-	-	-
SCSO J233430.2-543647.5	n/a		0.35±0.05	3.59	-	-	-
SCSO J233110.6-555213.5	23:31:08.4	−55:51:38.3	0.39±0.05	1.04	< 0.56	-	-
SCSO J233618.3-555440.3	23:32:13.8	−55:54:16.4	0.49±0.03	0.94	$0.97^{+1.59}_{-0.97}$	78^{+314}_{-78}	9^{+36}_{-9}
SCSO J233706.3-541903.8	23:37:11.3	−54:18:57.5	0.51±0.04	1.58	$0.85^{+3.03}_{-0.85}$	71^{+820}_{-71}	7^{+80}_{-7}
SCSO J233816.9-555331.1	23:38:12.7	−55:53:12.5	0.52±0.03	1.29	$0.35^{+2.09}_{-0.35}$	29^{+711}_{-29}	2^{+37}_{-2}
SCSO J233556.8-560602.3	23:35:55.6	−56:05:50.5	0.52±0.03	7.15	$1.35^{+2.03}_{-1.22}$	117^{+423}_{-114}	15^{+54}_{-15}
SCSO J232619.8-552308.8	23:26:14.5	−55:23:22.9	0.52±0.03	1.25	$2.81^{+3.34}_{-2.22}$	250^{+672}_{-231}	52^{+140}_{-48}
SCSO J233425.6-542718.0	23:34:26.9	−54:27:32.5	0.53±0.04	3.41	< 0.37	-	-
SCSO J232215.9-555045.6	23:22:17.0	−55:50:07.1	0.56±0.04	2.40	$0.32^{+4.13}_{-0.32}$	29^{+2303}_{-29}	1^{+103}_{-1}
SCSO J232247.6-541110.1	23:22:53.0	−54:10:54.8	0.58±0.04	1.16	$5.11^{+5.57}_{-4.09}$	532^{+1286}_{-495}	138^{+333}_{-129}
SCSO J232211.0-561847.4	23:22:13.6	−56:18:35.7	0.61±0.05	5.65	$0.47^{+2.61}_{-0.47}$	48^{+1045}_{-48}	2^{+50}_{-2}
SCSO J233731.7-560427.9	23:37:30.0	−56:04:01.2	0.61±0.05	3.05	$2.56^{+3.87}_{-2.56}$	276^{+1005}_{-276}	41^{+149}_{-41}
SCSO J234012.6-541907.2	23:40:08.8	−54:19:02.9	0.62±0.04	5.23	< 2.56		
SCSO J234004.9-544444.8	23:40:02.9	−54:44:21.0	0.66±0.05	4.20	$6.74^{+4.45}_{-3.36}$	843^{+1118}_{-575}	212^{+281}_{-145}
SCSO J232342.3-551915.1	23:23:45.5	−55:19:08.9	0.67±0.04	2.72	< 0.51	-	-
SCSO J232829.7-544255.4	23:28:27.5	−54:42:19.3	0.68±0.04	8.34	$0.59^{+3.12}_{-0.59}$	69^{+1409}_{-69}	3^{+67}_{-3}
SCSO J233403.7-555250.7	n/a		0.71±0.04	0.88	-	-	-
SCSO J233951.1-551331.3	n/a		0.73±0.04	1.3	-	-	-
SCSO J233720.2-562115.1	23:37:22.4	−56:20:44.8	0.75±0.03	0.70	$5.61^{+7.24}_{-4.87}$	835^{+2488}_{-806}	151^{+450}_{-145}

Note. — Physical properties of optically selected clusters in the SCS 23^{hr} region. Redshifts are the photometric redshift of the BCG, with $\pm 1\sigma$ limits. The ID is based on the position of the BCG. The NFW fit is centred at the luminosity-weighted centre (lum.). $M_{L_{200}}$ is published in Menanteau et al. (2009) and the uncertainty in $M_{L_{200}}$ is estimated to be a factor of two (Menanteau et al., 2009). Values of $2T_{CMB}\langle y\rangle$ and Y are predicted from M_{200}^{Lens} using Eq. 1.38. Note that ΔT_{SZ} at 150GHz is 0.29 of the penultimate column value.

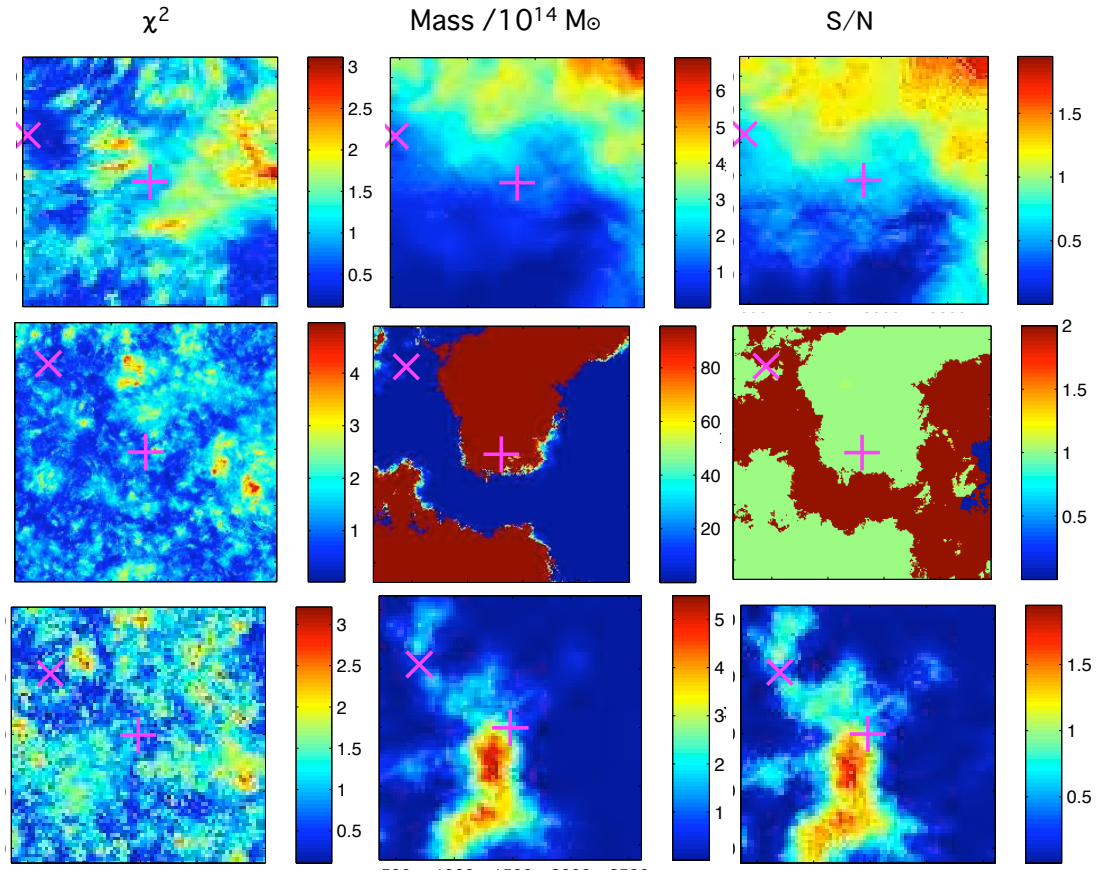

Figure 5.1: Fitting NFW profiles to different centres of three clusters. The *Top Row:* shows results for the cluster SPT 0517-5430 ($\simeq$ 3.6 arcmin square), *Middle Row:* cluster SPT 0528-5300 ($\simeq$ 9 arcmin square), and *Bottom Row:* cluster SPT 0509-5342 ($\simeq$ 9 arcmin square). *Left Column:* The χ^2 of each NFW fit at each centre position. *Middle Column:* The resulting cluster mass at each centre, in $10^{14} M_{\odot}$, and *Right Column:* Signal-to-noise (S/N) of the mass estimate at each centre position. The purple + signs mark the BCG position, and the purple $\times$ mark the position of the lowest χ^2 value.

Menanteau. $M_{L_{200}}$ is an estimate of the mass derived from the optical luminosity of the cluser, calibrated by weak lensing measurements for SDSS clusters (Reyes et al., 2008), within a radius r_{200} in which the number density is estimated to be $200/\Omega_m$ times the average galaxy number density. This is subject to uncertainties in bias, but is claimed to be an unbiased (to 5%) estimate of the radius where the mass density is 200 times the critical density (Johnston et al., 2007). The uncertainty in $M_{L_{200}}$ is estimated to be a factor of two (Menanteau et al., 2009) due to the uncertainty in extrapolating the scaling relation to higher redshifts and uncertainty in cluster membership.

Both Menanteau et al. (2009) and Reyes et al. (2008) select galaxies to be cluster members which are inside r_{200}, as calculated from the empirical relation by Hansen et al. (2005). In both cases, galaxies have to to have luminosities dimmer than that of the BCG and brighter than $0.4L^*$.

$M_{L_{200}}$ is calculated from Equations 16b and 17b of Reyes et al. (2008). They parametrize the scaling of mass as a power law in L_{200} with an additional scaling with L_{BCG} at fixed L_{200}:

$$M_{14}(L_{200}, L_{\rm BCG}) = M_L^0 (L_{200,10}/40)^{\alpha_L} (L_{\rm BCG}/\bar{L}_{\rm BCG}^{(L)})^{\gamma_L} \quad (5.1)$$

where M_{14} is $M_{200\bar{\rho}}$ in units of $10^{14}h^{-1}M_\odot$, $L_{200,10}$ is the cluster luminosity in units of $10^{10}h^{-2}L_\odot$, and the BCG luminosity dependence is pivoted at the mean L_{BCG} at the given L_{200}. They parametrize this relation of mean L_{BCG} as:

$$\bar{L}_{\rm BCG}^{(L)} \equiv \bar{L}_{\rm BCG}(L_{200}) = a_L L_{200,10}^{b_L} \quad (5.2)$$

where $a_L = (7.77, 7.92) \times 10^{10}h^{-2}L_\odot$, $b_L = (0.67, 0.66)$ for the two redshift ranges $(0.10 < z < 0.23, 0.23 < z < 0.30)$. Using Eqs. 5.1 and 5.2 a cluster mass estimate can be made for any cluster with using measurements of L_{200} and L_{BCG}.

Best-fitting coefficients, derived by Reyes et al. (2008), for the scaling of cluster masses with L_{200} and L_{BCG} are shown in Table. 5.3. Later in this analysis I will attempt to measure these same coefficients to see if I obtain consistent results (see Section 5.3).

Figure 5.1.3 compares lensing and optical mass estimates, $M_{L_{200}}$ for the SPT clusters and for the 24 optically selected clusters with non-zero lensing mass measurements. We see that the SZ-discovered detections are amongst the most massive of the clusters, with masses generally exceeding $3 \times 10^{14}M_\odot$. The red dashed line shows a one-to-one correspondence between $M_{L_{200}}$ and M_{200}^{lens} and is there as a guide to the eye. Lower error bars marked with a triangle signify that the lower error reaches zero. Error bars were set at $\Delta\chi^2 = 1$. I tested the fit of these data to a one-to-one correspondence between $M_{L_{200}}$ and M_{200}^{Lens}, and also to a flat line of zero gradient. I calculated the χ^2 of each fit, to give an indication as to whether there was any correlation between $M_{L_{200}}$ and M_{200}^{lens} . The results were reduced $\chi^2 = 48$ for $M_{200}^{lens} = M_{L_{200}}$ and reduced $\chi^2 = 231$ for the flat line $M_{200}^{Lens} =< M_{200}^{Lens} >$. The χ^2 fit uses the (in this case incorrect) assumption that the error bars are symmetric. I used the (larger) lower error bars for these results. Although such high reduced χ^2 values show that neither are very well fitted, I have not tried to find the best fit line here, I was trying to show whether or not the lensing masses are showing any correlation with the optical masses. These χ^2 results show that the data are more closely fitted to a line of gradient equal to one than to a flat line of zero gradient.

The correlation between the optical masses (Menanteau et al., 2009; Menanteau & Hughes, 2009) and the weak lensing masses gives some justification for using the optical luminosity as a mass proxy. Interestingly, one of the SZ clusters has conflicting optical and X-ray mass estimates, suggesting that $M_{L_{200}}$ may be overestimated.

5.2 Clusters in the Southern Cosmology Survey 5hr field

The second area of Southern sky in the Southern Cosmology Survey is the 5^{hr} field centred on 05^h30^m, $-52°47^m$. I have run the new lensing pipeline on 48 square degrees of this field - which is 6 times larger than the area covered by the 23^{hr} field. In this large field, I have a list of 121 optically-selected clusters from Felipe Menanteau. Because of the much larger size of this 5^{hr} fields compared to the previous 23^{hr} field, I used only this larger field (and hence larger cluster list) for the following work.

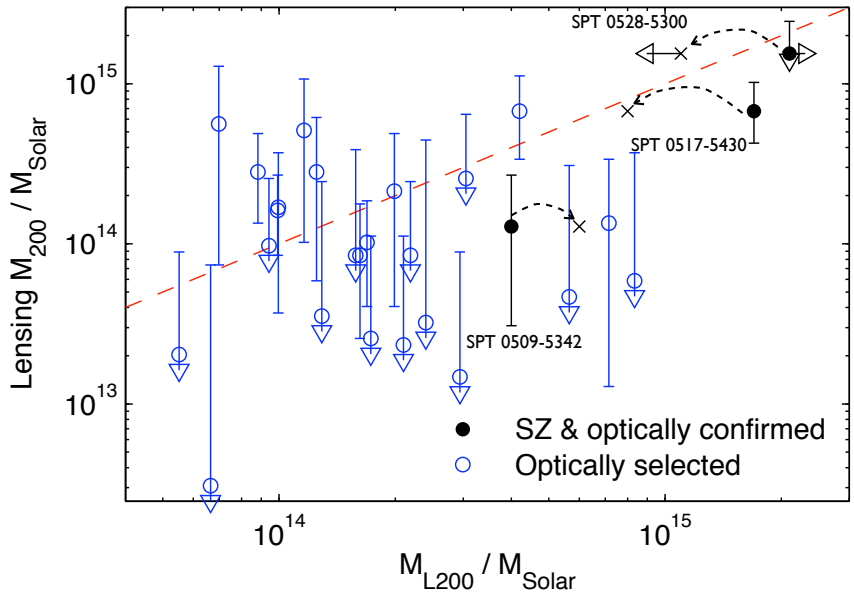

Figure 5.2: Lensing mass M_{200}^{Lens} measurement against optical mass $M_{L_{200}}$ for SZ and optically selected clusters. Filled circles show the SZ-selected and optically confirmed clusters, while empty circles denote clusters observed optically. Lower error bars marked with a triangle signify that the lower error reaches zero. X-ray mass estimates are shown as an $\times$ on this plot for the 3 SZ-detected clusters, joined by an arc to the optical estimate. The dashed line is $M_{L_{200}} = M_{200}^{Lens}$ to guide the eye. The uncertainty in $M_{L_{200}}$ is estimated to be a factor 2 (Menanteau et al., 2009).

5.2.1 B Mode Systematics

As described in Section 3.2.6, mass reconstructions were produced for each tile using the Kaiser-Squires method. The E and B mode maps for each of the 98 tiles are shown in Figure 5.3. This figure shows that there are some fields where the B mode signal is particularly large, and in some cases also larger than the E mode signal for that field. The B mode is a measure of the systematic errors in the field, and so the fields with large B modes highlight a problem with the analysis or data quality. For this reason, I have compared the B mode maps to pure noise maps, and removed those fields where the B modes are too high. The fields that have been removed will not be used for further analysis in this work. I will describe below how I have applied this cut on the fields with the worst B modes.

I created 1000 random noise maps using the shear catalogues from 10 different images. The x and y positions and value of $|\gamma|$ were taken from the real data, but the orientation of the galaxies was randomised. One hundred random shear fields were created from each of 10 different shear catalogues. The standard deviation of the kappa values over all these realisations was calculated and found to be $\sigma = 0.009$. I then defined a 'peak' in the map to be a value above 3σ. I considered counting the number of peaks that could be seen in each map (noise and B mode), but realised that the size of the peak was also important (i.e. one peak covering a larger area was just as bad as two small peaks in the map). For this reason, I calculated the fraction of each map which belonged to a peak, where values above 3σ were defined as being in a peak. Figure 5.4 compares the fraction of each map which contains peaks between pure noise maps (left) and B mode data (right). It can be seen that the B modes from the data, have a much higher fraction containing peaks than the pure noise maps. The mean fraction of B modes containing peaks is 0.097 ± 0.042, whereas from the noise maps it is much lower at 0.005 ± 0.004. Ideally, one would want the B modes to only contain random noise and therefore have the same properties as the pure noise maps. In the ideal case, one would want to remove any fields which had B modes which were much higher than pure noise. With the current dataset this would lead to all the fields being removed. The quality of this data (including it having a number density of $n \sim 9$ galaxies per square arc minute, and the elliptical PSF) means that it is far from ideal lensing data. It is important, however, to be able to use this data, but still to remove the worst B mode fields where the analysis has clearly failed. I would recommend for future surveys, such as Pan-STARRS that they employ a similar cut of fields with the worst B modes, and in surveys further ahead, where the number density is much larger (around $n > 30$), I would recommend using more stringent cuts, to remove and fields with B modes not consistent with pure noise maps.

For this data, however, it is important to remove the fields in which the B modes are highest, highlighting a problem with the analysis and/or the data. Using Figure 5.4, I have applied a cut of 0.18 to the fraction of B modes containing peak values, as these points are outliers and lie above the main trend of points. The outlying points from Figure 5.4 are then plotted in Figure 5.5, this time along with their E mode data. Here we can see the fraction of E mode which is peaks shown in black, and the fraction of B mode which is peaks shown in red. In four out of five cases the B mode is also larger than the E mode signal in this field. One field, however, has a larger E mode in this field, and so I will leave this field in the analysis. The remaining four fields, are now

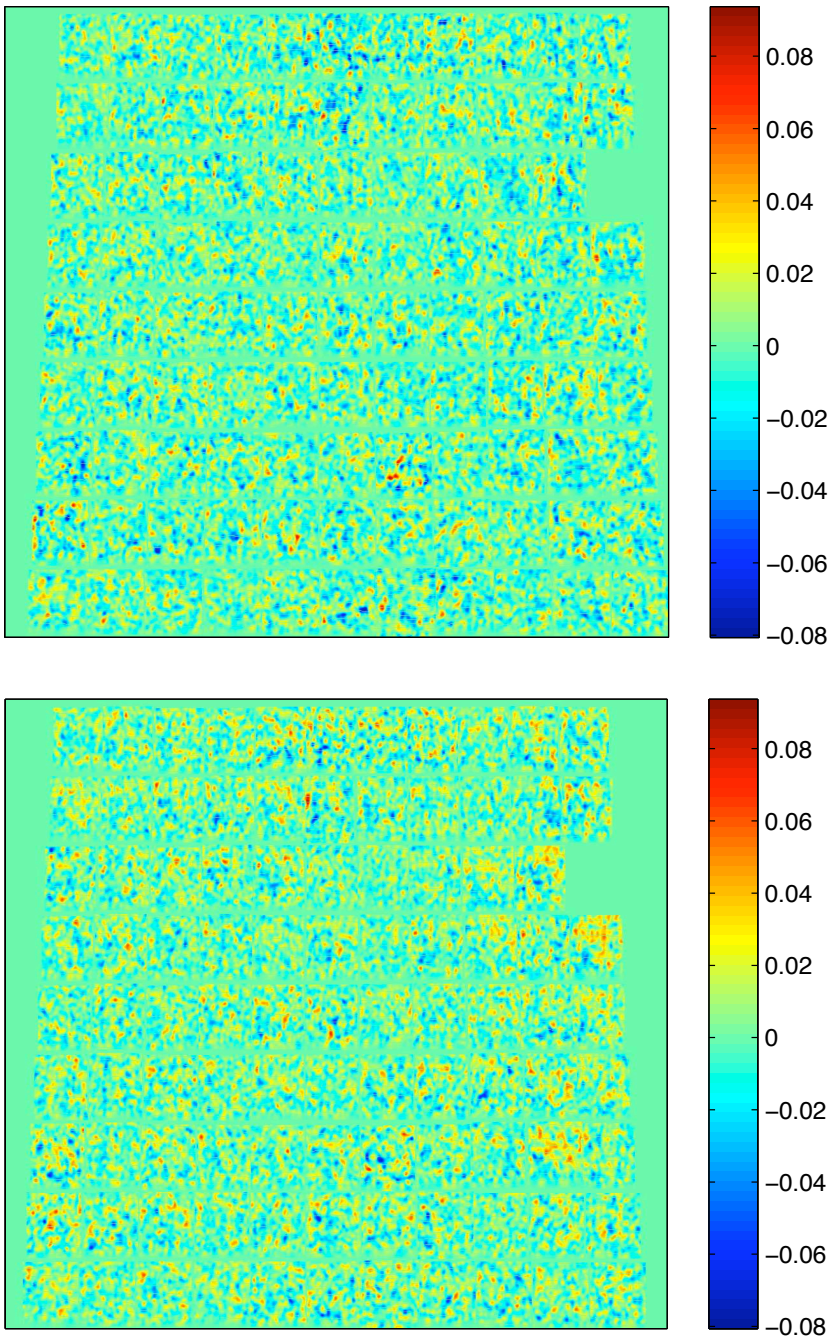

Figure 5.3: *Top:* The tiled E mode reconstructions for the 98 tiles from the full SCS 05^{hr} field and *Bottom:* the lensing B mode reconstructions. Each of the 98 tiles is 42' × 42'.

removed from further analysis. The fields which have been removed are highlighted in Figure 5.6.

5.2.2 Cluster Lensing Mass Results

Of the 121 optically-selected clusters, 6 lay in single exposure regions, where the data are not deep enough for a lensing analysis and 1 lay in a field which was removed

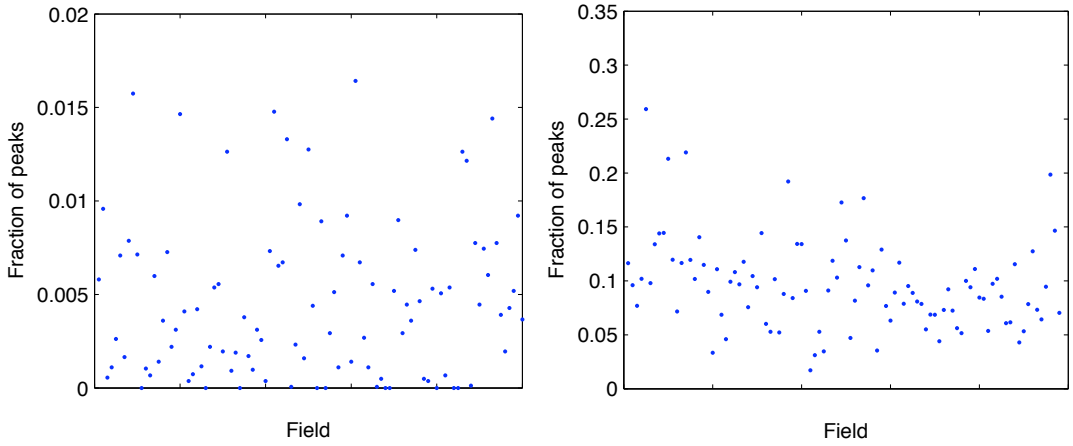

Figure 5.4: *Left:* The fraction of each field which contains peaks in pure noise maps and *Right:* the fraction of each field which contains peaks in B mode (data) maps.

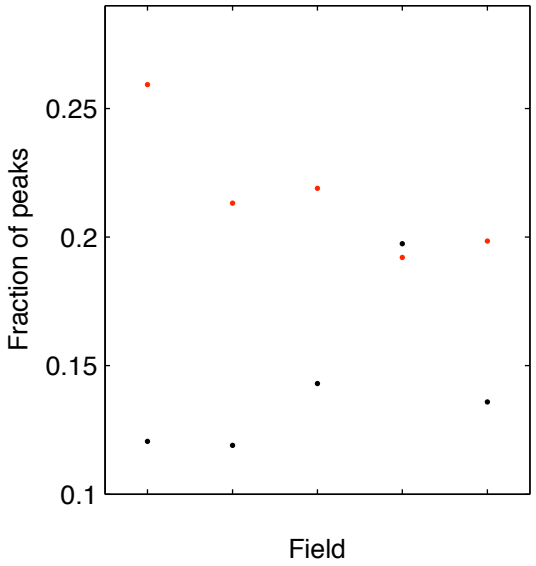

Figure 5.5: Comparison of the fraction of values in peaks for both E and B modes for the worst B mode fields. The black points show the fraction of each field which contains peaks in the E mode data, and the red point shows the fraction of each field which contains peaks in the B mode data. The five different pairs of points are for each of the 5 fields which have greater than 18% of peaks in B mode maps.

using the B mode cuts. I have run the same lensing analysis on the remaining 114 clusters, fitting NFW profiles at the luminosity-weighted centre of each cluster. Of the 114 clusters, I found non-zero mass estimates for 73 clusters, and upper limits for the remaining clusters.

Table 5.2. Cluster Weak Lensing Masses and Optical Measurements.

ID	R.A.	Dec.	$z_{\rm photo}$	L_{200}	$M_{L_{200}}$	M_{200}^{Lens}
	Centre of NFW fit			$(10^{12}L_\odot)$	$(10^{14}M_\odot)$	$(10^{14}M_\odot)$
SCSO 5.79408−54.313119	5:54:40.3	−54:18:47.2	0.11 ±0.02	5.39	6.05	< 0.25
SCSO 5.42075−55.211905	5:18:40.5	−55:12:42.9	0.12 ±0.04	5.13	6.93	$0.35^{+0.72}_{-0.35}$
SCSO 5.56148−54.696801	5:25:19.9	−54:41:48.5	0.12 ±0.02	2.48	3.64	< 0.07
SCSO 5.78627−51.201457	5:47:38.4	−51:12:05.2	0.18 ±0.05	5.95	5.39	$2.81^{+1.64}_{-1.26}$
SCSO 5.27704−54.500423	5:09:20.3	−54:30:01.5	0.23 ±0.03	10.1	28.4	$6.74^{+6.71}_{-4.71}$
SCSO 5.53191−55.341975	5:58:42.9	−55:20:31.1	0.23 ±0.04	5.27	9.54	$1.02^{+1.21}_{-0.82}$
SCSO 5.30725−56.013879	5:36:31.4	−56:00:50.0	0.24 ±0.04	2.37	3.66	$1.02^{+1.11}_{-0.78}$
SCSO 5.73378−51.215049	5:00:24.0	−51:12:54.2	0.26 ±0.03	2.40	4.37	< 0.54
SCSO 5.14211−51.187198	5:07:54.1	−51:11:13.9	0.37 ±0.04	1.22	1.86	$1.17^{+1.64}_{-1.06}$
SCSO 5.15594−53.703430	5:20:20.7	−53:42:12.3	0.39 ±0.04	2.57	4.38	$2.13^{+2.32}_{-1.57}$
SCSO 5.66455−56.239806	5:58:05.9	−56:14:23.3	0.39 ±0.04	6.12	13.3	< 1.23
SCSO 5.23456−51.717131	5:31:06.1	−51:43:01.7	0.50 ±0.03	1.86	3.36	$2.56^{+1.89}_{-1.39}$
SCSO 5.16431−51.698040	5:27:52.7	−51:41:52.9	0.55 ±0.03	3.26	6.77	< 0.51
SCSO 5.21829−53.890210	5:16:27.5	−53:53:24.7	0.58 ±0.05	2.95	6.40	$11.72^{+7.73}_{-5.57}$
SCSO 5.19628−51.893060	5:56:39.1	−51:53:35.0	0.61 ±0.05	5.32	9.78	$5.61^{+4.14}_{-3.16}$
SCSO 5.26881−54.637087	5:01:55.7	−54:38:13.5	0.65 ±0.04	4.40	9.89	< 3.08
SCSO 5.23682−51.667981	5:33:08.2	−51:40:04.7	0.68 ±0.04	7.43	13.4	$1.29^{+3.17}_{-1.28}$
SCSO 5.23336−51.443118	5:30:01.3	−51:26:35.2	0.71 ±0.05	8.82	21.7	$1.29^{+4.07}_{-1.28}$
SCSO 5.47937−54.513092	5:11:26.1	−54:30:47.1	0.12 ±0.03	3.24	4.10	$0.54^{+1.50}_{-0.54}$
SCSO 5.47971−51.329888	5:11:44.1	−51:19:47.6	0.12 ±0.02	2.96	2.94	$0.85^{+1.38}_{-0.81}$
SCSO 5.40736−54.764124	5:06:37.2	−54:45:50.8	0.12 ±0.02	4.93	6.11	< 1.12
SCSO 5.58475−52.506189	5:46:16.4	−52:30:22.3	0.14 ±0.02	1.45	1.43	$0.01^{+0.41}_{-0.01}$
SCSO 5.32110−51.812181	5:48:59.4	−51:48:43.9	0.14 ±0.03	0.96	0.79	$0.03^{+0.51}_{-0.03}$
SCSO 5.68083−54.607608	5:12:45.1	−54:36:27.4	0.14 ±0.02	1.12	0.82	$0.16^{+0.77}_{-0.16}$
SCSO 5.66015−51.502122	5:54:08.2	−51:30:07.6	0.14 ±0.02	1.77	1.29	< 0.12
SCSO 5.56148−54.696802	5:25:19.9	−54:41:48.5	0.14 ±0.03	2.96	4.71	< 0.07
SCSO 5.33784−53.781080	5:04:03.3	−53:46:51.9	0.16 ±0.03	2.71	3.11	< 0.43
SCSO 5.44098−51.934567	5:36:52.9	−51:56:04.4	0.17 ±0.04	2.01	1.31	$0.54^{+0.81}_{-0.46}$
SCSO 5.41659−51.586599	5:14:55.9	−51:35:11.8	0.18 ±0.03	2.87	2.91	< 0.09
SCSO 5.64863−53.409923	5:43:45.8	−53:24:35.7	0.20 ±0.04	2.14	2.09	$0.64^{+1.05}_{-0.64}$
SCSO 5.41222−53.669029	5:10:59.7	−53:40:08.5	0.21 ±0.03	1.71	2.21	$0.43^{+0.98}_{-0.43}$
SCSO 5.40584−51.008930	5:05:15.1	−51:00:32.1	0.22 ±0.03	2.11	1.60	$1.48^{+1.47}_{-1.09}$
SCSO 5.59611−51.137349	5:56:30.0	−51:08:14.5	0.22 ±0.05	0.67	0.61	$0.15^{+0.70}_{-0.15}$
SCSO 5.47450−51.003845	5:07:02.8	−51:00:13.8	0.23 ±0.04	1.57	1.77	$2.68^{+1.98}_{-1.40}$
SCSO 5.47793−52.074607	5:10:08.0	−52:04:28.6	0.23 ±0.03	1.89	2.00	$3.08^{+1.80}_{-1.39}$
SCSO 5.56688−54.312038	5:30:11.7	−54:18:43.3	0.23 ±0.04	6.54	12.5	< 0.64
SCSO 5.38321−51.905919	5:44:53.3	−51:54:21.3	0.23 ±0.03	1.45	2.29	$1.41^{+1.28}_{-0.85}$
SCSO 5.32175−54.690498	5:49:34.3	−54:41:25.8	0.25 ±0.03	2.15	4.09	< 0.29
SCSO 5.32615−54.908179	5:53:32.0	−54:54:29.4	0.25 ±0.04	0.64	0.75	$0.09^{+1.19}_{-0.09}$
SCSO 5.51112−52.160131	5:40:00.7	−52:09:36.5	0.25 ±0.04	2.32	3.81	$0.74^{+1.60}_{-0.74}$
SCSO 5.61134−51.658790	5:10:12.6	−51:39:31.6	0.25 ±0.04	1.30	2.41	$2.13^{+1.75}_{-1.20}$
SCSO 5.60040−53.886716	5:00:21.7	−53:53:12.2	0.26 ±0.03	1.70	2.77	$0.62^{+1.33}_{-0.61}$
SCSO 5.55756−54.337919	5:21:48.3	−54:20:16.5	0.27 ±0.03	5.67	12.2	$0.39^{+0.96}_{-0.39}$
SCSO 5.57451−51.827985	5:37:03.4	−51:49:40.7	0.27 ±0.04	0.68	1.08	< 0.27
SCSO 5.67844−54.800629	5:10:35.8	−54:48:02.3	0.27 ±0.03	1.06	1.50	$0.67^{+1.46}_{-0.67}$
SCSO 5.34490−54.788507	5:10:24.3	−54:47:18.6	0.28 ±0.05	1.71	2.32	< 0.15
SCSO 5.70413−54.956560	5:33:43.1	−54:57:23.6	0.28 ±0.04	1.65	3.08	$3.88^{+5.87}_{-3.80}$
SCSO 5.55298−53.504251	5:17:41.1	−53:30:15.3	0.29 ±0.04	1.56	2.46	$0.49^{+1.29}_{-0.49}$
SCSO 5.33336−54.802593	5:00:01.7	−54:48:09.3	0.29 ±0.05	2.43	3.73	$0.41^{+1.54}_{-0.41}$
SCSO 5.56085−53.888077	5:24:45.7	−53:53:17.1	0.30 ±0.05	1.74	3.80	< 0.51
SCSO 5.31030−53.924774	5:39:16.1	−53:55:29.2	0.30 ±0.05	0.49	0.66	< 0.56
SCSO 5.69293−54.387918	5:23:38.4	−54:23:16.5	0.31 ±0.04	2.03	3.81	< 0.54
SCSO 5.54358−52.883424	5:09:13.4	−52:53:00.3	0.35 ±0.03	0.92	1.38	$2.81^{+1.85}_{-1.53}$
SCSO 5.51500−54.803674	5:43:29.8	−54:48:13.2	0.36 ±0.04	4.74	7.64	< 0.89
SCSO 5.53558−54.845750	5:02:01.2	−54:50:44.7	0.36 ±0.03	1.84	3.46	$0.47^{+1.67}_{-0.47}$
SCSO 5.66082−50.937646	5:54:44.4	−50:56:15.5	0.36 ±0.03	1.86	3.27	$0.89^{+1.56}_{-0.89}$
SCSO 5.37465−54.765968	5:37:11.2	−54:45:57.5	0.37 ±0.03	0.54	0.81	$1.35^{+4.01}_{-1.34}$
SCSO 5.39414−51.290383	5:54:43.5	−51:17:25.4	0.38 ±0.03	0.99	1.48	$3.88^{+3.18}_{-2.33}$
SCSO 5.64698−53.766337	5:42:16.9	−53:45:58.8	0.39 ±0.04	3.70	7.55	< 0.25

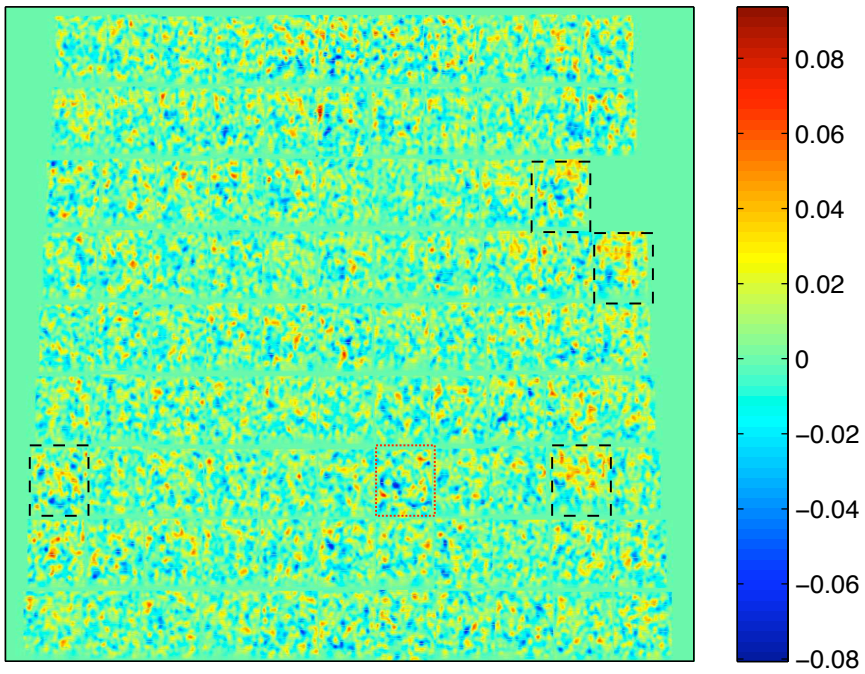

Figure 5.6: B mode mass reconstructions (as shown in Figure 5.3), showing fields to be removed. The fields outlined in black dashed rectangles have been removed because of the high levels of B modes. The field marked with the red dotted rectangle had a high B mode peak fraction, but a higher E mode, and has been left in the analysis (see Figure 5.5).

In Table 5.2 I present the lensing mass measurements for these 114 clusters. It also contains properties of these optically selected clusters, including the co-ordinates of the luminosity-weighted centre, the photometric redshifts of the BCG with $\pm 1\sigma$ limits, and the optical mass estimate $M_{L_{200}}$, where the uncertainty in this is estimated to be a factor of two (Menanteau et al., 2009).

A histogram of best fit lensing mass is shown in Figure 5.7, where N is the number of clusters in each mass bin of $\log_{10}(M_{200}^{Lens}/M_{\odot})$. Plots comparing mass estimates follow in the next section.

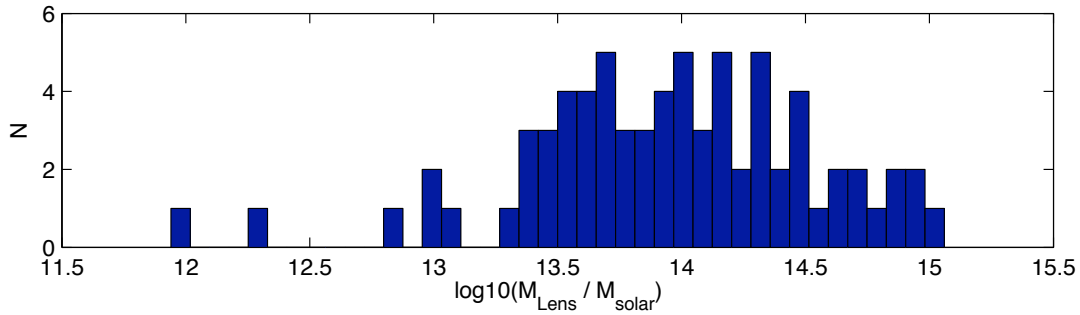

Figure 5.7: Histogram of cluster lensing masses. N is the number of clusters in each mass bin, of $\log_{10}(M_{200}^{Lens}/M_{\odot})$.

5.3 Scaling Relations

Finding and testing relationships between observables and the physical properties of galaxy clusters, such as mass, is an important area of research. If we are able to understand the relations between, for example, luminosity of a galaxy cluster, and its mass, then we can build up a large cluster catalogue of galaxy cluster masses and use this to test $N(m,z)$. It is not possible to do this with only the optical measurements, as mass estimates obtained in this way are based on only the optical tracers, not the true total mass. Nor is it practical using only weak lensing observations - as it is difficult to get deep enough lensing data for such a large sample of clusters. However, if we understand the relationship between these measurements, then we can construct a scaling relation which relates the two, which is much more powerful. In this section I compare lensing masses to optical quantities and observables and test the scaling relation found by Reyes et al. (2008).

5.3.1 Comparing with $M_{L_{200}}$ Results

As with the SPT clusters, and the 23^{hr} field clusters, I compared my measurement of M_{200}^{Lens} with the optical mass estimate $M_{L_{200}}$ with these 5^{hr} field clusters. The resulting comparison of M_{200}^{Lens} with $M_{L_{200}}$ for the 31 clusters with solid detections is shown in the left hand plot of Figure 5.8. The red dashed line shows a one-to-one correspondence. The comparison of the full cluster list is shown in the right hand plot of Figure 5.8, where the black points are those that are in the left hand plot, and the blue points are the clusters where the lower error bars on M_{200}^{Lens} reach zero, or the measurement of

Table 5.2 (cont'd)

ID	R.A.	Dec.	$z_{\rm photo}$	L_{200}	$M_{L_{200}}$	M_{200}^{Lens}
	Centre of NFW fit			$(10^{12}L_\odot)$	$(10^{14}M_\odot)$	$(10^{14}M_\odot)$
SCSO 5.58801−51.810569	5:49:12.6	−51:48:38.0	0.42 ±0.05	0.89	1.98	$0.45^{+1.79}_{-0.45}$
SCSO 5.60241−51.963961	5:02:10.4	−51:57:50.3	0.44 ±0.06	0.44	0.60	$0^{+1.48}_{-0}$
SCSO 5.53631−51.186942	5:02:40.9	−51:11:13.0	0.48 ±0.03	0.79	1.29	$1.54^{+3.57}_{-1.54}$
SCSO 5.53480−52.283599	5:01:19.1	−52:17:01.0	0.48 ±0.03	1.38	2.41	$0.89^{+2.82}_{-0.89}$
SCSO 5.47823−54.351517	5:10:24.4	−54:21:05.5	0.49 ±0.03	1.43	2.88	$2.68^{+2.67}_{-1.87}$
SCSO 5.45877−53.301486	5:52:53.5	−53:18:05.4	0.49 ±0.04	3.57	7.44	< 0.97
SCSO 5.34155−54.831654	5:07:23.9	−54:49:54.0	0.50 ±0.03	0.97	1.67	$0.27^{+3.11}_{-0.27}$
SCSO 5.67516−54.245699	5:07:38.8	−54:14:44.5	0.52 ±0.03	6.45	13.2	$2.23^{+4.51}_{-2.23}$
SCSO 5.53580−51.041202	5:02:13.4	−51:02:28.3	0.52 ±0.04	3.04	5.89	$4.25^{+5.49}_{-3.58}$
SCSO 5.67908−51.787696	5:11:10.6	−51:47:15.7	0.52 ±0.04	2.95	4.89	$1.69^{+3.42}_{-1.69}$
SCSO 5.39513−51.651059	5:55:37.1	−51:39:03.8	0.53 ±0.04	0.71	0.91	< 1.41
SCSO 5.57852−52.517800	5:40:40.0	−52:31:04.1	0.54 ±0.04	3.27	6.10	$0.37^{+1.97}_{-0.37}$
SCSO 5.51122−51.606258	5:40:05.9	−51:36:22.5	0.55 ±0.03	0.64	1.06	< 1.86
SCSO 5.62580−54.422674	5:23:13.2	−54:25:21.6	0.55 ±0.04	4.33	9.63	< 3.54
SCSO 5.56196−53.067017	5:25:45.9	−53:04:01.3	0.56 ±0.05	0.99	1.63	< 1.77
SCSO 5.52130−53.616634	5:49:10.3	−53:36:59.9	0.56 ±0.05	0.86	1.36	$0.93^{+2.77}_{-0.93}$
SCSO 5.61055−52.999801	5:09:29.9	−52:59:59.3	0.58 ±0.04	2.61	6.55	$6.15^{+5.57}_{-4.11}$
SCSO 5.35404−51.071826	5:18:38.1	−51:04:18.6	0.58 ±0.04	10.5	24.6	$3.54^{+4.20}_{-2.73}$
SCSO 5.61355−53.840517	5:12:11.9	−53:50:25.9	0.59 ±0.04	2.00	3.72	$1.48^{+4.13}_{-1.47}$
SCSO 5.58338−53.338503	5:45:02.5	−53:20:18.6	0.59 ±0.05	9.82	29.9	$0.74^{+5.41}_{-0.74}$
SCSO 5.33784−53.929009	5:04:03.3	−53:55:44.4	0.60 ±0.04	1.35	1.97	$5.11^{+7.73}_{-4.91}$
SCSO 5.68383−52.899995	5:15:27.1	−52:53:60.0	0.60 ±0.03	4.86	9.65	$1.94^{+3.66}_{-1.94}$
SCSO 5.30923−53.730483	5:38:18.2	−53:43:49.7	0.60 ±0.04	4.24	8.39	< 1.62
SCSO 5.49115−53.412739	5:22:02.3	−53:24:45.9	0.61 ±0.04	3.30	6.28	$0.37^{+2.71}_{-0.37}$
SCSO 5.47486−54.551823	5:07:22.6	−54:33:06.6	0.61±0.04	3.12	4.92	$2.45^{+5.29}_{-2.45}$
SCSO 5.55571−51.938321	5:20:08.5	−51:56:18.0	0.62 ±0.03	0.54	0.73	< 1.54
SCSO 5.30108−53.928304	5:30:58.1	−53:55:41.9	0.62 ±0.04	3.14	6.13	< 1.69
SCSO 5.52937−54.277693	5:56:25.9	−54:16:39.7	0.62 ±0.04	2.54	4.18	$8.89^{+8.85}_{-6.32}$
SCSO 5.61962−53.291656	5:17:39.6	−53:17:30.0	0.63 ±0.05	2.64	5.74	$1.62^{+6.12}_{-1.62}$
SCSO 5.46962−51.811015	5:02:39.3	−51:48:39.7	0.64 ±0.04	3.60	7.27	< 0.51
SCSO 5.67717−51.554748	5:09:27.3	−51:33:17.1	0.64 ±0.05	5.02	9.70	$1.69^{+5.37}_{-1.69}$
SCSO 5.68588−51.566150	5:17:17.7	−51:33:58.1	0.64 ±0.05	6.38	12.5	< 3.23
SCSO 5.60854−53.555948	5:07:41.4	−53:33:21.4	0.65 ±0.05	2.79	6.49	< 1.86
SCSO 5.48411−54.655126	5:15:41.9	−54:39:18.5	0.65 ±0.05	0.77	1.13	$2.04^{+6.85}_{-2.04}$
SCSO 5.50829−53.669244	5:37:27.7	−53:40:09.3	0.65 ±0.04	1.42	1.97	$0.14^{+2.95}_{-0.13}$
SCSO 5.48354−53.976010	5:15:11.0	−53:58:33.6	0.66 ±0.04	10.7	28.8	$10.68^{+6.25}_{-4.81}$
SCSO 5.54420−53.016685	5:09:46.7	−53:01:00.1	0.67 ±0.04	3.06	6.75	$1.29^{+4.59}_{-1.28}$
SCSO 5.46814−52.998004	5:01:19.5	−52:59:52.8	0.67 ±0.04	8.92	18.7	$3.38^{+4.73}_{-2.87}$
SCSO 5.40807−52.355486	5:07:15.9	−52:21:19.8	0.67 ±0.05	1.42	3.21	< 0.93
SCSO 5.55460−51.708026	5:19:08.4	−51:42:28.9	0.68 ±0.04	3.35	6.00	$3.88^{+7.31}_{-3.79}$
SCSO 5.37310−52.262399	5:35:47.4	−52:15:44.6	0.69 ±0.04	0.97	1.14	< 7.39
SCSO 5.40967−51.831526	5:08:42.1	−51:49:53.5	0.70 ±0.04	1.94	3.13	$16.17^{+13.26}_{-8.78}$
SCSO 5.40573−52.237086	5:05:09.5	−52:14:13.5	0.71 ±0.04	3.14	6.11	< 1.86
SCSO 5.53477−54.630952	5:01:17.5	−54:37:51.4	0.71 ±0.04	1.97	2.87	< 1.86
SCSO 5.61957−55.039264	5:17:36.9	−55:02:21.3	0.72 ±0.04	7.67	17.8	< 2.13
SCSO 5.35299−53.293044	5:17:41.5	−53:17:35.0	0.72 ±0.04	4.50	7.71	$7.74^{+15.64}_{-7.74}$
SCSO 5.35600−54.121130	5:20:24.2	−54:07:16.1	0.72 ±0.04	2.64	5.15	< 2.68
SCSO 5.55619−53.463564	5:20:34.0	−53:27:48.8	0.72 ±0.05	4.90	10.4	$12.27^{+13.36}_{-8.39}$
SCSO 5.41645−52.916606	5:14:48.1	−52:54:59.8	0.73 ±0.04	8.06	19.0	< 2.44
SCSO 5.49094−54.499432	5:21:50.7	−54:29:58.00	0.73 ±0.04	2.14	3.40	$10.20^{+19.22}_{-10.0}$
SCSO 5.43386−53.006494	5:30:28.6	−53:00:23.4	0.74 ±0.04	3.04	6.09	< 4.88
SCSO 5.67362−51.388119	5:06:15.4	−51:23:17.2	0.75 ±0.04	0.92	1.13	$0.47^{+5.68}_{-0.47}$
SCSO 5.32158−52.368485	5:49:25.5	−52:22:06.5	0.76 ±0.04	4.84	8.53	$0.71^{+6.69}_{-0.71}$
SCSO 5.45809−51.510663	5:52:16.6	−51:30:38.4	0.76 ±0.04	1.66	3.05	$0.59^{+4.77}_{-0.59}$
SCSO 5.32662−53.718748	5:53:57.4	−53:43:07.5	0.76 ±0.04	0.15	0.19	< 1.35

Note. — Physical properties of optically selected clusters in the SCS 5^{hr} region. Redshifts are the photometric redshift of the BCG, with $\pm 1\sigma$ limits. The ID is based on the position of the BCG. The NFW fit is centred at the luminosity-weighted centre. Cluster list with positions, z, L_{200} and $M_{L_{200}}$ provided by Felipe Menanteau. The uncertainty in $M_{L_{200}}$ is estimated to be a factor of two (Menanteau et al., 2009).

	M_L^0	α_L	γ_L
$0.10 < z < 0.23$	1.81 ± 0.15	1.27 ± 0.17	0.40 ± 0.23
$0.23 < z < 0.30$	1.76 ± 0.22	1.30 ± 0.29	0.26 ± 0.41

Table 5.3: Extract from Table 2 of Reyes et al. (2008). Best-fitting coefficients of the power laws in Eqs. 5.1 and 5.2.

M_{200}^{Lens} is zero. Again, the red line denotes $M_{200}^{Lens} = M_{L_{200}}$ and is there solely as a guide. Because of the asymmetric error bars, and that many of the mass estimates are zero but with upper limits, it is difficult to test the correlation between these. Instead, in the following section I compare M_{200}^{Lens} directly to the luminosity measurements, L_{200}. Looking at the plots in Figure 5.8, it is not clear that there is any correlation between M_{200}^{Lens} and $M_{L_{200}}$. It appears as though if one only considered the non-zero masses, a flat line would be as good a fit as the equality line. As a rough test, I have repeated the χ^2 fit that I carried out on the corresponding plot of the 23^{hr} field. Note again that this assumes symmetric error bars, and that I have used the larger lower errors for this. The flat line $M_{200}^{Lens} =< M_{200}^{Lens} >$ fits the data slightly better than the line $M_{200}^{lens} = M_{L_{200}}$. The reduced χ^2 values were ~ 7 and ~ 9 respectively. The data appears to be better fitted by a flat line. This could suggest a problem with either the lensing results or the original optically-selected cluster catalogue and optical masses. I believe that some of the clusters candidates which have zero mass estimates from the lensing analysis, may not be clusters. These may have been added to the catalogue in error through incorrect optical cluster selection. However, for the most part I believe the problem lies in the quality of the lensing data. Many of these clusters may be at too high a redshift to be detected by these lensing data, or may be in areas where the noise is so high, and hence the number density of background sources is so low, that the clusters are not detectable. For these reasons I believe that many M_{200}^{Lens} values are zero. Where we are able to detect the clusters, I hold more belief in the value of the lensing mass because it is a measure of the mass from the whole cluster, not just from the optical tracers, and is dependent on an NFW fit rather than a scaling relation extrapolated from low redshift clusters, which I believe is more accurate. However, where we have been unable to detect the cluster with lensing, I believe that most (but not all) of these clusters are correct cluster candidates, and that we have not detected them because of the poor data quality. Another factor could be the scaling relation used by Menanteau et al. (2009) to calculate $M_{L_{200}}$ from L_{200} and for this reason, I compare these quantities directly in the section to follow.

With this larger cluster list gained from the 5^{hr} field, I compare the results from luminosity-weighted centering and BCG centering. Figure 5.9 shows the comparison of lensing mass estimates made using these two different centres. The blue dashed line has a gradient equal to one. It can be seen on the left-hand side of this plot that there are 12 clusters which have a mass estimate of zero when centred on the BCG, but which have non-zero mass estimates when centred using the luminosity-weighted centre. The other points show that there seems to be a slight bias towards higher mass estimate when the luminosity-weighted centre is used.

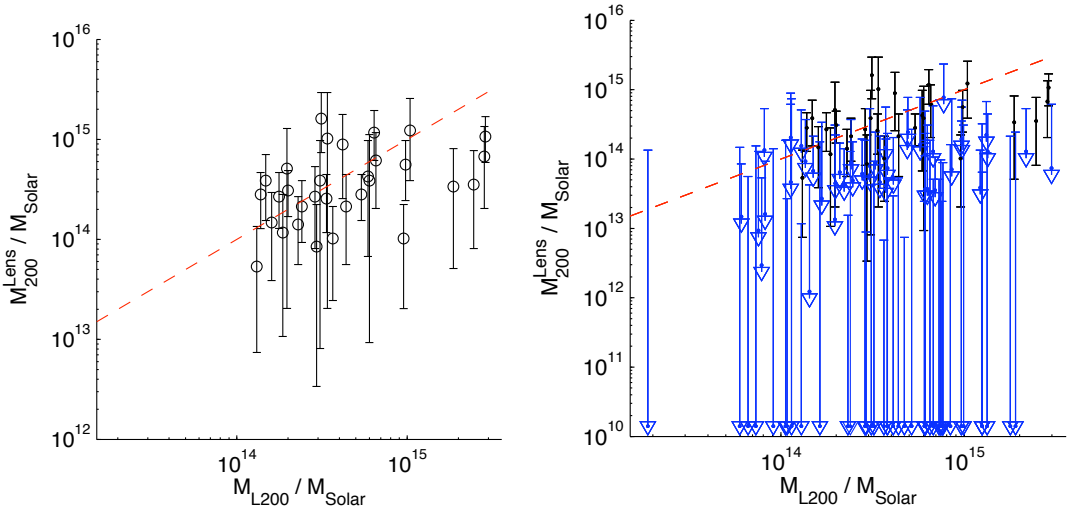

Figure 5.8: *Left:* M^{Lens}_{200} against $M_{L_{200}}$ for clusters with solid detections and *Right:* M^{Lens}_{200} against $M_{L_{200}}$ for all 114 clusters. The black points are the same in both plots, and are those that have solid detections, and the blue points are the clusters where the lower error bars on M^{Lens}_{200} reach zero, or the measurement of M^{Lens}_{200} is zero. In both plots, the red line shows M^{Lens}_{200} = $M_{L_{200}}$.

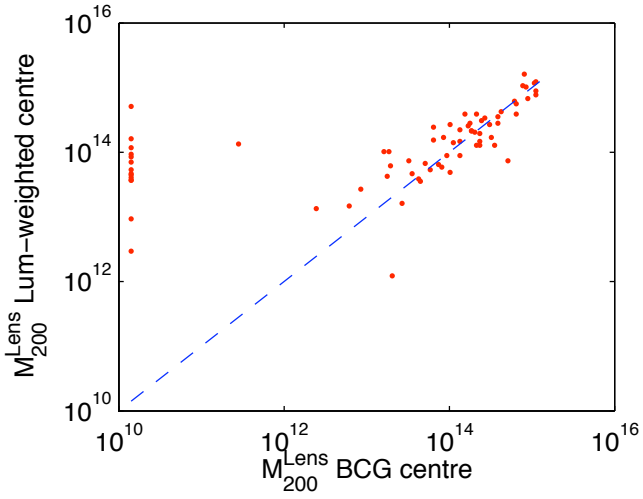

Figure 5.9: Comparison of lensing mass using luminosity-weighted centre and BCG. The blue line has a gradient equal to one. The line of points on the left-hand side are 12 clusters which have a mass estimate of zero when centred on the BCG, but which have non-zero mass estimates when centred using the luminosity-weighted centre. It seems that using the luminosity-weighted centre slightly raises the mass estimate on average, compared to using the BCG centre, implying that it is a better proxy for the dark matter centre.

5.3.2 Scaling Relation Results

The next stage of this project, was to compare my lensing mass measurements, M^{Lens}_{200}, directly to the luminosity measurements, L_{200} (Section 4.3.2 and Section 5.1.2). The reason I chose to do this is because Reyes et al. (2008) provide their relation out to redshift $z = 0.3$, and that Menanteau's $M_{L_{200}}$ values are based on an extrapolation to

higher redshift (see Menanteau et al. (2009)). So rather than compare to mass estimates which are based on an extrapolation to a scaling relation from luminosity, I wanted to compare directly to the luminosity measurements. In this section, I show comparison with luminosity measurements, and test the fit found by Reyes et al. (2008). I started this work by plotting lensing masses against L_{200}, and this is shown in Figure 5.10. This plot uses the same colours and symbols as 5.8, where the black points are those that have solid detections, and the blue points are the clusters where the lower error bars on M_{200}^{Lens} reach zero, or the measurement of M_{200}^{Lens} is zero. Reyes et al. (2008) looked at $\sim 13,000$ galaxy clusters with redshift less than 0.3, and so I also show M_{200}^{Lens} and L_{200} comparisons split into two redshift ranges, $z = 0 - 0.3$ and $z = 0.3 - 0.8$. These are shown in Figure 5.11. The left hand plot shows clusters in the range $z = 0 - 0.3$, and the right hand plot shows cluster in the range $z = 0.3 - 0.8$. From this figure, we can see that the average mass of the detected clusters increases with the higher redshift sample. We would expect this with a sample of clusters which has been optically selected because at higher redshifts it will preferentially pick more massive galaxies. This is because there are less background sources and higher noise, and so only the most massive clusters will be detected.

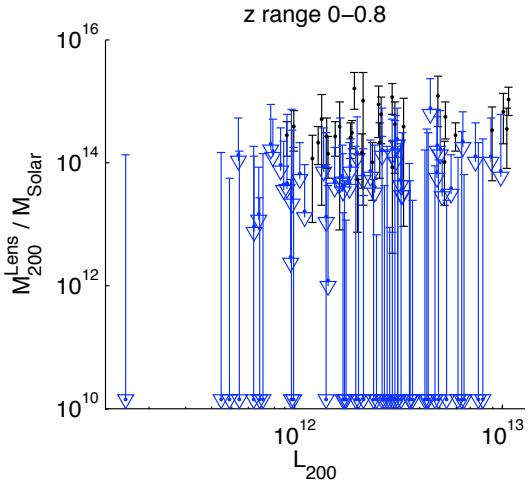

Figure 5.10: M_{200}^{Lens} against L_{200} for 114 clusters in full redshift range. The black points are those that have solid detections, and the blue points are the clusters where the lower error bars on M_{200}^{Lens} reach zero, or the measurement of M_{200}^{Lens} is zero.

Having compared lensing masses to luminosity measurements, I then used the parametrization of Reyes et al. (2008) to calculate the best-fit values of the coefficients for this new cluster sample.

To do this, I adapted the NFW-fitting code to write out the values of the χ^2 goodness-of-fit for each cluster, for each possible model mass. I then had 300 χ^2 values, and the 300 corresponding possible mass values for each cluster.[1] The likelihood of each of these masses for each cluster was calculated. Clusters which had $\chi^2 > 11$ were cut from this sample. The reason for cutting the sample in this way was to remove those clusters which were least well fit by an NFW. Without these cuts, the results produced were unphysical, and so a cut removing the worst fitting clusters was applied. A cut

[1]The mass corresponding to the lowest χ^2 is the one which is quoted in Table 5.2.

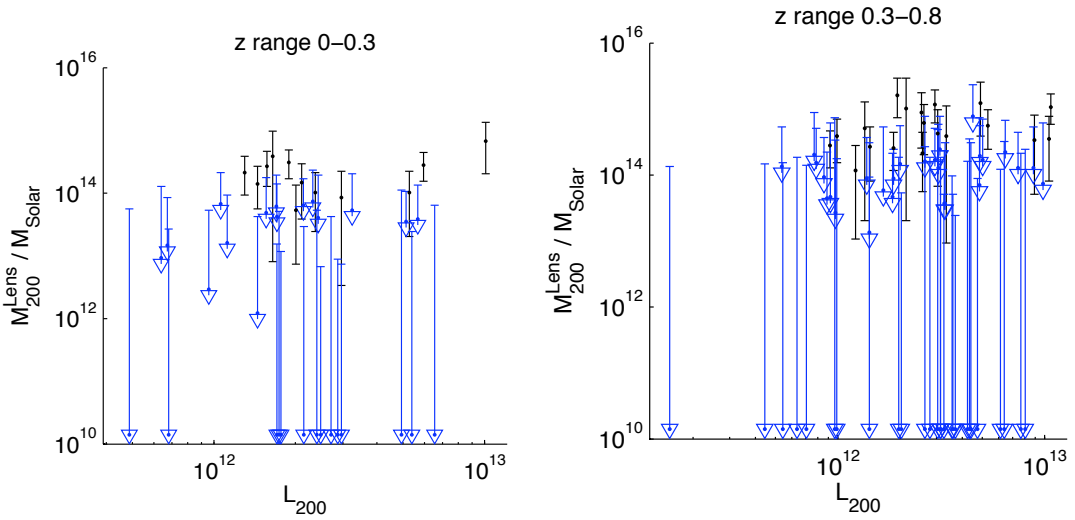

Figure 5.11: M_{200}^{Lens} against L_{200} for 114 clusters, as in Figure 5.10, but split into two redshift bins, *Left:* $z = 0 - 0.3$ and *Right:* $z = 0.3 - 0.8$.

at $\chi^2 > 11$ was chosen (for $\nu = 8$ degrees of freedom), as a good fit would be $\chi^2 \sim 8$. This cut removed 40 clusters from the sample, leaving 74 clusters: 28 in the redshift range $z = 0 - 0.3$ and 46 in the range $z = 0.3 - 0.8$.

By following Eq. 5.1, I fitted free parameters c,α_L and γ_L such that

$$\log_{10} M_{14} = c + \alpha_L \log_{10} \frac{L_{200}}{40} + \gamma_L \log_{10} L_{\rm BCG} - \gamma_L \log_{10} \bar{L}_{\rm BCG}^{(L)} \tag{5.3}$$

here $c = \log_{10} M_L^0$ (where M_L^0 is given in Eq. 5.1).
By using four nested loops and calculating the model value of $\log_{10} M_{14}$ for each cluster, for varying c, α_L and γ_L, I formed a four-dimensional array of $\log_{10} M_{14}$, the fourth dimension being the 74 clusters. I then located the closest value of $\log_{10} M_{14}^{Lens}$ for each cluster, and took the value of the likelihood for this cluster for this mass, and these formed a second 4-D array. By marginalising over the fourth dimension in this new array, I was given a three-dimensional array which contained the probability of the three coefficients, given the data, P(α_L, c, γ_L | data).

Figure 5.12 shows the likelihood marginalised over each one of these three parameters in turn. The contours are regions of highest likelihood which enclose 68.3% and 95% of the marginalised likelihood. Note that the probabilities are not very localised, so the contours reflect to a certain extent the hard prior boundaries on the parameters which are at the figure boundaries. It is the 74 best-fit clusters with $\chi^2 < 11$ which appear in this plot. The reason for this is that the whole low-redshift sample peaks at an unnatural $\gamma_L < 0$. With only the best fitting clusters used, there is a peak at $\alpha_L \sim 2, \gamma_L \sim 0.2$.

In the lower redshift sample, $z = 0 - 0.3$ we find $-2 < \alpha_L < 1$, and $c < -5$, inconsistent with the the coefficient values calculated by Reyes et al. (2008). This is surprising, as a negative value of α is non physical (see Eq. 5.3). Our measurement of γ_L in this low redshift range has two peaks, and it is conceivable that the higher peak is correct, as it is in closer agreement to that found by Reyes et al. (2008). In

the higher redshift range, $z = 0.3 - 0.8$, we find that $\alpha_L = 0.5 \pm 1.5$, $\gamma_L = 1.5 \pm 1.5$, $c > -1$. In this high redshift range, where there is no measurement by Reyes et al. (2008), we have assumed no evolution of parameters and compare to the low redshift result of Reyes et al. (2008). Our measurements here are in good agreement with the Reyes et al. (2008) findings.

The results here for the lower redshift clusters are not fully understood, but due to time constraints, it is beyond the scope of this thesis to further investigate this. It is hard to know what is going on in this lower redshift range and pin down the problem. We conclude that the problem arises because the low redshift sample is much smaller, with only 28 clusters. This may be why our results are non physical in this range, whereas the higher redshift sample —with nearly twice as many clusters — is better constrained. It is also important to note that Reyes et al. (2008) had $\sim 13,000$ clusters in their sample.

5.4 Stacking Clusters from the SCS 5hr Field

In order to test the shape of the tangential shear profile of this sample of galaxy clusters, I stacked together their profiles. Stacking cluster profiles leads to an increased signal-to-noise of the tangential shear profile, compared to a single cluster's profile. Stacking the weak lensing shear measurements of similar objects to boost signal-to-noise was first suggested by Kaiser & Squires (1993), and this method has since been used in many investigations, including work by Dahle et al. (2003), Mandelbaum et al. (2006), Mandelbaum et al. (2008) and Okabe et al. (2009).

Stacking also has the advantage that it can reduce the noise caused by:

- shape measurement noise on individual clusters
- PSF systematics
- uncorrelated structure along the line-of-sight or
- individual shape variations of cluster halos including substructure and non-spericity of mass distribution.

As shown in Section 2.8.2, the shear of an NFW profile can be expressed as $\gamma(x) = \kappa_k j(x)$ (Equation 2.84). The scaled gamma, $j(x) = \frac{\gamma(x)}{\kappa_k}$, is that given by Equation 2.85.

In order to stack the cluster profiles, it was first necessary to re-scale the tangential shears, both their amplitude and the position of the radii from the cluster centres. For each cluster, the position of the radial bins in which the tangential shear was calculated, was re-scaled by the factor r_s. To do this I used ΛCDM angular diameter distances with WMAP parameters to compute r from the angular size. Using the mass measurement of each cluster, the shears were re-scaled by the function of their mass, giving an estimate of $j(x)$ for each cluster. Similarly the scaled error was also calculated.

5.4.1 Stacking Results

I then stacked the scaled radial tangential shear profiles for the 73 clusters with non-zero mass estimates. The stacking was done in order to test the shape of the tangential

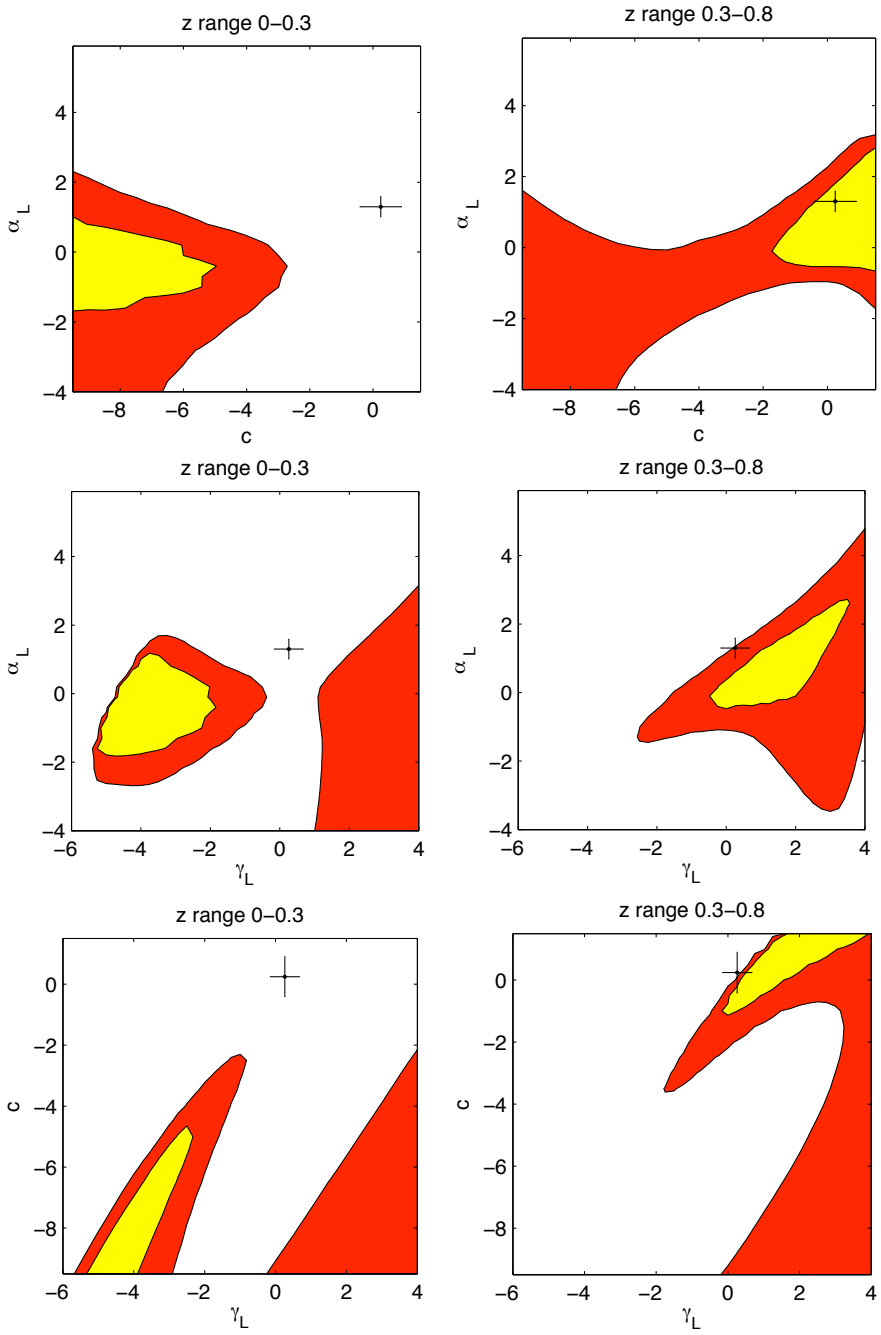

Figure 5.12: Contour plots showing 68% (red) and 95% (yellow) confidence levels for the coefficients c, α_L and γ_L of the Reyes et al. (2008) fit from 74 best-fit clusters with $\chi^2 < 10$. *Left:* redshift range $z = 0 - 0.3$ and *Right:* redshift range $z = 0 - 0.3$. The black crosses show the values found by Reyes et al. (2008), but note that these values were for the redshift range $z = 0.23 - 0.3$.

shear profile of this sample of galaxy clusters. The result of this is shown in Figure 5.13, where the the scaled gamma is the scaled tangential shear (which is $j(x)$ described in Eq. 2.85), and r/r_s is the scaled radii from the cluster centre.

Then I calculated the average scaled tangential shear in bins, and used inverse variance weighting to calculate the errors. Figure 5.14 shows the result of this. The

stacked radial profiles of Figure 5.14 suggests that these clusters in fact have lower concentrations, or higher shears than the NFW model fit, because most points lie above the model. Figure 5.15 contains a histogram of the number of data points going into each radial bin in Figure 5.14. By stacking these estimates of $j(x)$ it has allowed me to recover $j(x)$ for the NFW profile. The red dashed line shows the theoretical value of the function $j(x)$ from Eq. 2.85. The χ^2 value of this model to the data is 25 for 13 degrees of freedom. From this value we can say that the NFW is a reasonable, but not excellent, fit to this data.

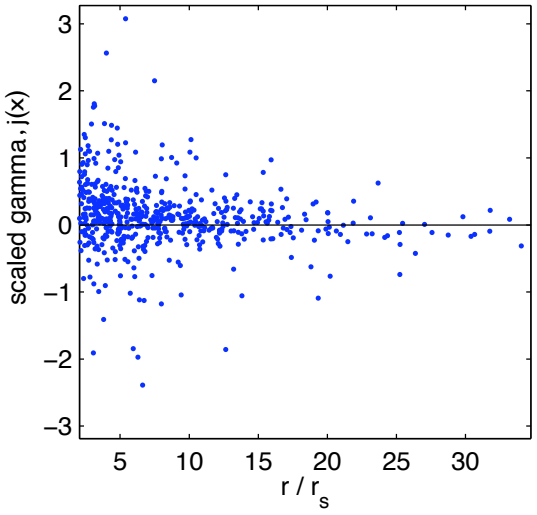

Figure 5.13: Scaled tangential shear data for 73 clusters.

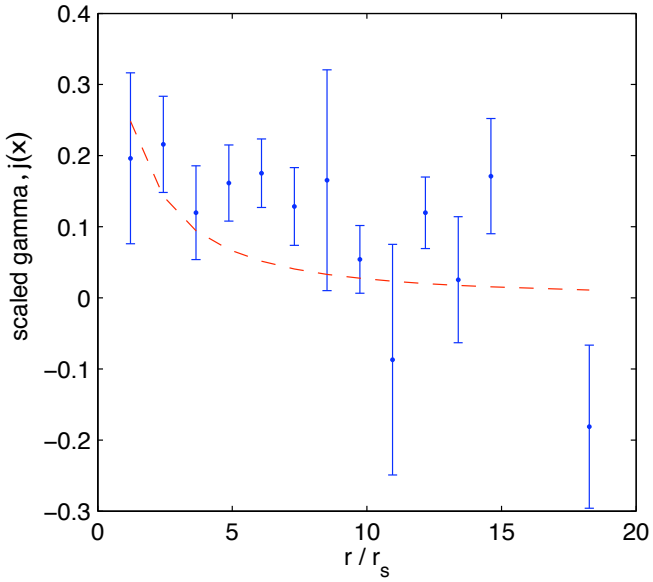

Figure 5.14: The resulting tangential shear profile from stacking 73 clusters. The red dashed line is the theoretical value of the function j(x) from Eq. 2.85.

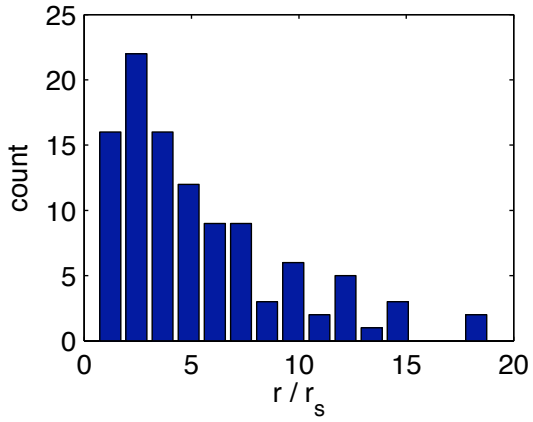

Figure 5.15: Histogram of the number of data points in each radial bin of r/r_s for the scaled tangential shear result of Figure 5.14.

5.4.2 Testing the NFW fit

I generalised the NFW model to seek a better fit to observations. The motivation for this was that a χ^2 value of 25 for 13 degrees of freedom is not an excellent fit[2]. So I used an NFW as a starting point for the model, but allowed it to stretch in radial direction and in amplitude. The best model in this case (which is no longer an NFW) has $\chi^2 = 10.4$ for 11 degrees of freedom. The new fit has a higher overall amplitude, and lower concentration, with the best-fitting value of $\langle\gamma_t\rangle/\langle\gamma_{t\ NFW}\rangle = 0.51$ and a re-scaled concentration of $c'/c_{\rm Dolag} = 0.2$. A contour plot showing $\log_{10}\chi^2$ values for the different values of $\langle\gamma_t\rangle/\langle\gamma_{t\ NFW}\rangle$ and $c'/c_{\rm Dolag}$ is shown in Figure 5.16. The white contours show $\Delta\chi^2 = 2.3$, giving the 68.3% of the likelihood for 2 parameters, and at $\Delta\chi^2 = 6.7$ showing 95.4% confidence levels for the parameters given the data. The magenta contour lines show the values which have appropriate goodness-of-fit given the data and the model for $\nu = 11$ degrees of freedom, calculated using $< \chi^2 >= \nu + \sqrt{2\nu}$ giving 68.3% and $< \chi^2 >= \nu + 2\sqrt{2\nu}$ giving 95.4%. The black lines (which both lie very close together) show the Dolag et al. (2004) relation between concentration and mass for two typical cluster concentration values of $c = 5$ and $c = 10$. It can be seen that the black lines do not cross through the best-fit regions of the χ^2 distribution and so we can again conclude that the NFW model is not the best fit to these data.

The best-fitting re-scaled model is shown in black in Figure 5.17, along with the stacked cluster data. The original NFW fit is shown as a red dashed line. It can be seen that the preferred model favours a lower concentration and a higher shear amplitude (which is proportional to mass). This supports the findings of Mandelbaum et al. (2008) who show that massive clusters (the clusters used in this investigation are all classed as massive clusters) tend to have lower concentrations than expected from simulations. However, our results also prefer a higher shear normalisation suggesting that there may be additional effects in our analysis that need to be considered before we could recommend a more general profile than NFW.

[2] we expect $\chi^2 = \nu \pm \sqrt{2\nu}$, for ν degrees of freedom.

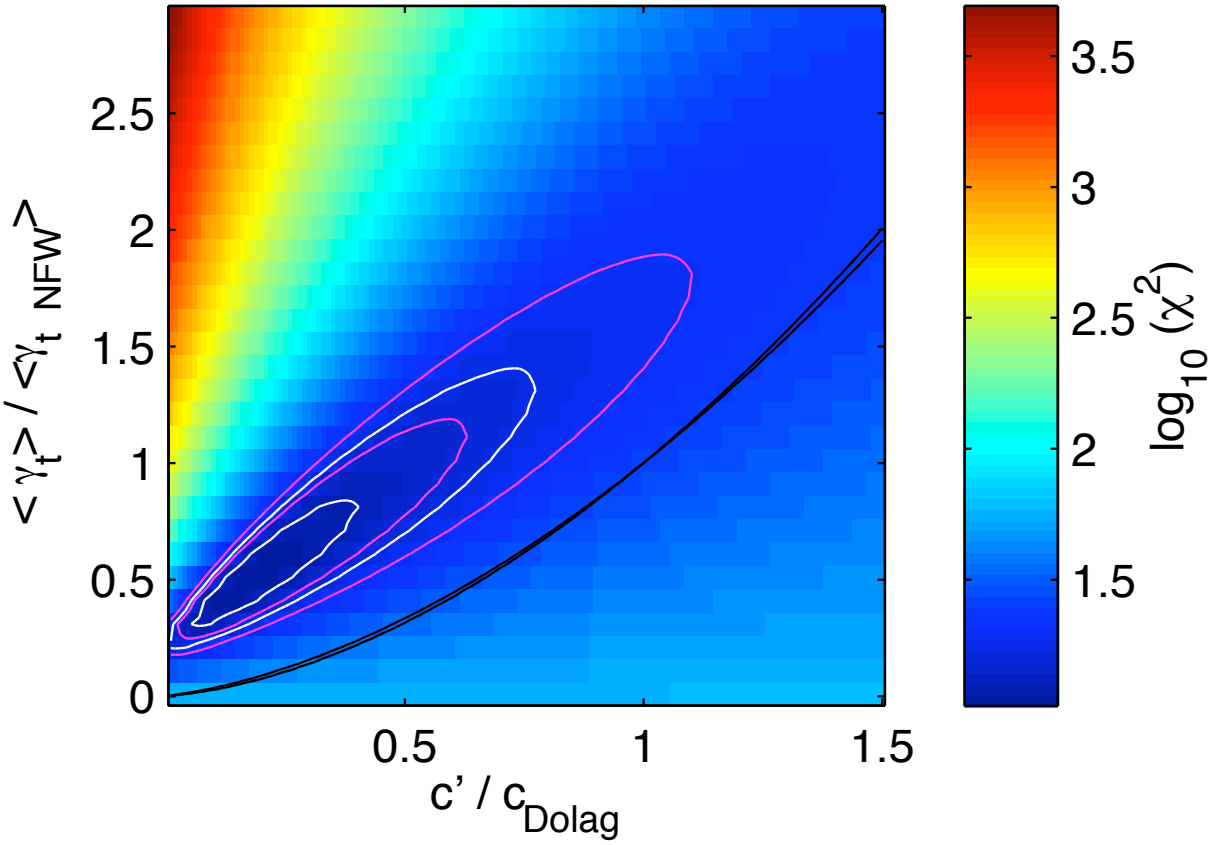

Figure 5.16: Likelihood surface for the different values of $\langle\gamma_t\rangle/\langle\gamma_{t\ NFW}\rangle$ and $c'/c_{\rm Dolag}$. The white contours enclose the 68.3% and 95.4% confidence levels for the parameters given the data. These were calculated using $\Delta\chi^2 = 2.3$, giving the 68.3% confidence levels for 2 parameters, and at $\Delta\chi^2 = 6.7$ giving 95.4%. The magenta contour lines show the values which have appropriate goodness-of-fit given the data and the model for $\nu = 11$ degrees of freedom, calculated using $< \chi^2 >= \nu + \sqrt{2\nu}$ giving 68.3% and $< \chi^2 >= \nu + 2\sqrt{2\nu}$ giving 95.4%. The black lines show the expected relation for an NFW model, for values of concentration $c = 10$ and $c = 5$ as expected to span low to high mass clusters according to the mass-concentration scalings observed in simulations by Dolag et al. (2004).

5.5 Conclusions

As the B modes we find are significant compared to the noise, we conclude that the results that follow should be more appropriately flagged as a proof of concept.

In this comparison of lensing data and optical data, I have measured the lensing mass, M_{200}^{Lens} for 38 clusters in the SCS 23^{hr} field and 114 clusters in the SCS 5^{hr} field. For the clusters in the 23^{hr} field I have also provided predictions of the expected temperature decrement in the Rayleigh-Jeans limit $\Delta T_{RJ} = 2T_{CMB}\langle y\rangle$, averaged within r_{200}. I have compared the lensing masses of the 5^{hr} clusters to measurements of their optical luminosity, and have tested the scaling relation of Reyes et al. (2008). In the higher redshift range of $z = 0.3 - 0.8$, my results are $\alpha_L = 0.5 \pm 1.5$, $\gamma_L = 1.5 \pm 1.5$, $c > -1$. If we assume no evolution of parameters to this higher redshift range (which was not looked at by Reyes et al. (2008)) then we see that our results are in good agreement with the findings of Reyes et al. (2008). The low redshift constraints are puzzling, but

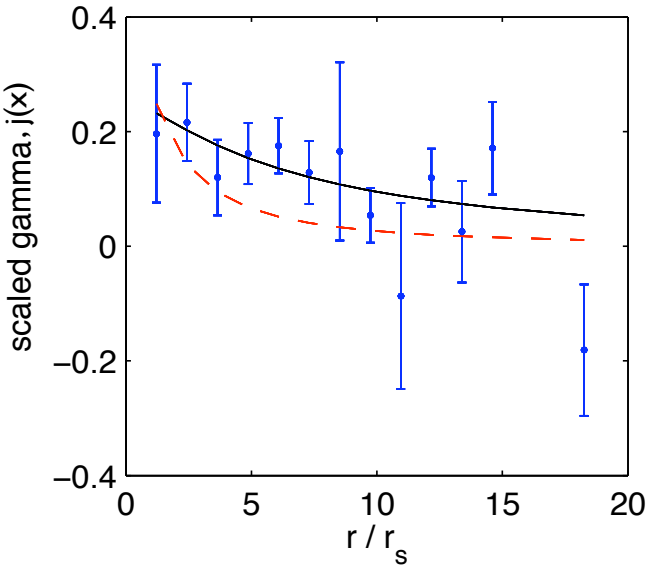

Figure 5.17: The tangential shear profile of the stacked clusters. The best-fit model is shown in black and the red dashed line is the theoretical value of the function j(x) from Eq. 2.85.

the sample size is half of the high redshift cluster, at only 28 clusters. There is something not fully understood here and further investigation is needed. This would be an interesting project for the future, but sadly there was not sufficient time to continue it as part of this thesis.

I then stacked the 73 non-zero lensing mass clusters from the 5^{hr} field to test their shear profile. I have shown that an NFW fits sufficiently well to these data with the fit having $\chi^2 = 25$ (for 11 degrees of freedom). By allowing two more things to vary a better fit can be found, which has a much lower χ^2, showing that a very good agreement to the data has been found. This best fit is found when the normalisation of the shears is re-scaled by a factor of $\langle\gamma_t\rangle/\langle\gamma_{t\ NFW}\rangle = 0.51$ and the concentration by a factor $c'/c_{\rm Dolag} = 0.2$ and has $\chi^2 = 10$. This fit has a lower concentration, which supports the findings of Mandelbaum et al. (2008) that massive halos have a lower concentration than expected. From this we can say that further study of profiles might be productive.

Chapter 6

Conclusions and Future Work

In this final chapter, the main conclusions of this thesis are summarised. A description of possible future work which could naturally follow on from the results is also presented here.

6.1 Overview and Conclusions

This thesis illustrates the power of combining SZ surveys and gravitational lensing. Using these methods together with future large-area sky surveys will mean that a huge sample of galaxy clusters, with accurate measurements of their total mass, can be constructed. I have written an automated pipeline for a lensing analysis of ground-based data, and applied it to the Southern Cosmology Survey (SCS), which has a median depth of $z = 0.65$ and galaxy density of $n = 9$ galaxies per square arcminute and mean seeing of $0.89''$. I have determined the masses of galaxy clusters, and made predictions of the SZ Y parameter. I presented weak lensing masses for three clusters selected by their SZ emission in the South Pole Telescope survey (SPT). By doing so, I have confirmed that the SZ selection procedure is successful in detecting mass concentrations.

The next generation of weak lensing surveys, such as Pan-STARRS-1, DES, VST-KIDS, EUCLID, will be orders of magnitude larger in size than the surveys which have come before. For a gravitational lensing analysis to be carried out on these, pipelines will need to be fully automated, requiring little or no manual intervention. I have used the publicly available data from the 100 square degrees SCS dataset as a testbed for these large future surveys. It is already larger than previous surveys, which were only a few degrees in size, and it has similar characteristics to the large-area sky surveys which are planned to follow it. For this reason, it is the ideal dataset on which to develop and test an automated pipeline, highlighting the problems which will be faced by larger, future surveys.

I have developed an automated lensing pipeline, and rigorously tested it using STEP simulations. Like the pipeline it is based on (Bacon et al., 2000; Brown et al., 2003), it consistently underestimates shear by a factor 0.82 ± 0.05. The pipeline takes co-added r or i band images and outputs object catalogues with shear measurements as well as producing a 2-D mass reconstruction for each field. I have shown that this pipeline is successful not only on simulations, but also on real data (McInnes et al., 2009). While producing consistent results, the pipeline is considerably faster than the

manual version. I have also tested the SCS dataset for correlations between the galaxy shear and stellar ellipticity, x and y position, magnitude, signal-to-noise, size and seeing, and see no large residuals. This dataset has a complicated PSF arising from the alignment of CCD chips, and co-addition of the images from the Mosaic II camera. I have minimised this by modelling the PSF variation as a sum of fourth-order polynomials and trigonometric functions up to eighth order. These choices give a small r.m.s. residual $|e|$ of 0.0092.

It has been long thought that SZ surveys would provide a favourable way of detecting galaxy clusters for cosmological studies. Simulations show that the SZ detection is independent of redshift and that the threshold corresponds very closely to a threshold in mass. It was, however, not guaranteed that the first blind SZ experiments would detect mass. To demonstrate this I have, for the first time, measured weak lensing masses of clusters detected by their SZ signature. Four clusters were detected by the SPT survey (Staniszewski et al., 2008), and I have detected three of them using the SCS data. The fourth cluster is too distant ($z = 0.88$) to be detected with these optical data. I fitted Navarro, Frenk and White (NFW) profiles and found that the SZ clusters have large masses, as high as $15 \times 10^{14} M_{\odot}$. By doing this I have established that the published SZ peaks correspond to mass regions. Consequently I can confirm that the first installment of SZ selected clusters do indeed trace the most massive clusters. Using the best fit masses for all the clusters, I analytically calculated the expected SZ integrated Y parameter which was consistent with the SPT observations.

I have also presented weak lensing mass estimates, M_{200}^{Lens}, for other clusters detected optically in the SCS: 38 clusters in the SCS 23^{hr} field and 114 clusters in the SCS 5^{hr} field. As one might expect the published SZ clusters have amongst the highest masses in this sample. For the clusters in the 23^{hr} field I have also provided predictions of the integrated Compton Y parameter. These predictions will be invaluable as they can be compared to the new SZ measurements when they are made for these clusters.

As the B modes we find are significant compared to the noise, we conclude that the results that follow should be more appropriately flagged as a proof of concept.

I have compared M_{200}^{Lens} of the 5^{hr} clusters to measurements of their optical luminosity, and have tested the scaling relation of Reyes et al. (2008). We find our data is inconclusive in the lower-redshift range of $z = 0 - 0.3$, probably due to the small sample size of 28 clusters. In the higher redshift range $z = 0.3 - 0.8$, we find agreement with the lower-redshift results of Reyes et al. (2008) if we assume no evolution in the scaling relations.

Finally, by scaling and stacking the 73 non-zero lensing mass clusters from the 5^{hr} field, I have measured their average shear profile. The NFW model fits poorly ($\chi^2 = 25$ for 11 degrees of freedom), but by moving away from an NFW fit a much better fit can be found. This fit has a lower concentration, but a higher shear normalisation (which is proportional to mass). This study supports that of Mandelbaum et al. (2008) who find that that massive halos have a lower concentration than expected. These results seem to disagree with the expected consequence of Adiabatic Contraction in clusters, where by the collapse of gas into the dark matter halo is expected to increase the concentration. However, it may be evidence that supernova feedback mechanisms proposed for galaxies may operate on cluster scales as well. Further study of cluster profiles will be required to resolve this.

6.2 Future Work

There are limitations to using the SCS data set for lensing, largely because its depth means that it has a low number density of $n = 9$ galaxies per square arcminute, and a median magnitude of i~23. This corresponds to a median photometric redshift of $z = 0.65$. These parameters mean that the results of a lensing analysis have a low signal-to-noise ratio.

The motivation for using this data set, however, is that it is very much like the large sky surveys which are being carried out now, for example Pan-STARRS-1 (PS1). These large area surveys are also not very deep, so it is important to be able to understand not only how to analyse this sort of dataset, but also the sort of results one could expect to get out of them. It is currently thought that the PS1 3π survey will have a number density of $n \sim 6$ galaxies per square arcminute, so this dataset is likely to have very similar properties, and problems, that have been encountered with this SCS dataset. However, it is important to note that although the data from this survey is unlikely to be deep enough to carry out a full 3D lensing reconstruction on cluster scales (which requires many galaxies in each redshift bin), I have shown with this analysis that 2D mass reconstructions can be done on data of this quality, and successfully reconstruct large galaxy clusters. A Wiener-filter method is preferable to better handle this type of data (which has a low signal-to-noise across much of the field).

I have shown with this analysis however, that with a number density of $n \sim 9$ it is possible to detect the most massive clusters with lensing, but it is difficult. With the lower number density of $n \sim 6$ or lower expected from PS1 it will prove very difficult to detect individual clusters. The PS1 3π survey is unlikely to be deep enough and have a high enough number density of galaxies to constrain the cluster mass function and therefore to constrain cosmological parameters using lensing as had been initially hoped. However, PS1 will survey a massive area, and so the stacking analysis should work extremely well, and it should be possible to further test the shape of the cluster profiles with stacking as I demonstrated here with the smaller SCS dataset.

A natural progression of this project would be to carry out the same analysis on the Medium Deep Survey (MDS) of PS1. The medium deep survey looks particularly promising as it is predicted to have a number density of $n \sim 20$ galaxies per square arcminute, and covers 10 areas of 7 square degrees. With data of this quality the mass reconstructions would have a much higher signal-to-noise, and higher significance determinations of galaxy cluster masses would possible. Further testing of the shape of cluster profiles could be carried out with this large sample of deeper data by stacking tangential shears as was carried out in this project. It would also be interesting to carry out a 3D mass reconstruction of some of the clusters detailed in this thesis, to see if substructure could be seen.

Once the full ACT SZ dataset is published, I would be keen to see the result of the comparison of my lensing mass maps and the SZ. I feel that this is a promising area, to calculate the correlation between SZ decrement and surface mass density.

Finally, I would like to see a future survey test the scaling relation of Reyes et al. (2008) at low redshift with a larger sample, and confirm my findings that the scaling relation holds at higher redshifts with no evolution.

Bibliography

Abate A., Wittman D., Margoniner V. E., Bridle S. L., Gee P., Tyson J. A., Dell'Antonio I. P., 2009, ApJ, 702, 603

Abell G. O., 1958, ApJS, 3, 211

Abell G. O., Corwin Jr. H. G., Olowin R. P., 1989, ApJS, 70, 1

Allen S. W., Schmidt R. W., Ebeling H., Fabian A. C., van Speybroeck L., 2004, MNRAS, 353, 457

Atrio-Barandela F., Kashlinsky A., Kocevski D., Ebeling H., 2008, ApJL, 675, L57

Bacon D. J., Refregier A., Clowe D., Ellis R. S., 2001, MNRAS, 325, 1065

Bacon D. J., Refregier A. R., Ellis R. S., 2000, MNRAS, 318, 625

Bardeau S., Soucail G., Kneib J., Czoske O., Ebeling H., Hudelot P., Smail I., Smith G. P., 2007, A&A, 470, 449

Bartelmann M., 1996, A&A, 313, 697

Bartelmann M., 2006, Gravitational Lensing Lecture Notes, http://www.oact.inaf.it/gl/lectures.html

Bartelmann M., Schneider P., 2001, Phys. Rep., 340, 291

Benítez N., 2000, ApJ, 536, 571

Benjamin J., Heymans C., Semboloni E., van Waerbeke L., Hoekstra H., Erben T., Gladders M. D., Hetterscheidt M., Mellier Y., Yee H. K. C., 2007, MNRAS, 381, 702

Bennett C. L., et al., 2003, ApJS, 148, 97

Benson B. A., Church S. E., Ade P. A. R., Bock J. J., Ganga K. M., Henson C. N., Thompson K. L., 2004, ApJ, 617, 829

Bernardeau F., van Waerbeke L., Mellier Y., 1997, A&A, 322, 1

Bertin E., 2006, SWarp Resample and Coadd Software, http://terapix.iap.fr/cplt/oldSite/soft/swarp/index.html

Bertin E., Arnouts S., 1996, A&AS, 117, 393

Binney J., Tremaine S., 1987, Galactic dynamics. Princeton, NJ, Princeton University Press, 1987, 747 p.

Birkinshaw M., 1999, Phys. Rep., 310, 97

Blanton M. R., Brinkmann J., Csabai I., Doi M., Eisenstein D., Fukugita M., Gunn J. E., Hogg D. W., Schlegel D. J., 2003, AJ, 125, 2348

Bradač M., Allen S. W., Treu T., Ebeling H., Massey R., Morris R. G., von der Linden A., Applegate D., 2008, ApJ, 687, 959

Bradač M., Lombardi M., Schneider P., 2004, A&A, 424, 13

Bridle S., Abdalla F. B., 2007, ApJL, 655, L1

Bridle S., King L., 2007, New Journal of Physics, 9, 444

Broadhurst T., Takada M., Umetsu K., Kong X., Arimoto N., Chiba M., Futamase T., 2005, ApJL, 619, L143

Brown M. L., Taylor A. N., Bacon D. J., Gray M. E., Dye S., Meisenheimer K., Wolf C., 2003, MNRAS, 341, 100

Bullock J. S., Kolatt T. S., Sigad Y., Somerville R. S., Kravtsov A. V., Klypin A. A., Primack J. R., Dekel A., 2001, MNRAS, 321, 559

Carlstrom J. E., Holder G. P., Reese E. D., 2002, ARA&A, 40, 643

Catelan P., Kamionkowski M., Blandford R. D., 2001, MNRAS, 320, L7

Clowe D., Bradač M., Gonzalez A. H., Markevitch M., Randall S. W., Jones C., Zaritsky D., 2006, ApJL, 648, L109

Clowe D., Luppino G. A., Kaiser N., Gioia I. M., 2000, ApJ, 539, 540

Corless V. L., King L. J., 2007, MNRAS, 380, 149

Crittenden R. G., Natarajan P., Pen U., Theuns T., 2001, ApJ, 559, 552

Croft R. A. C., Metzler C. A., 2000, ApJ, 545, 561

Dahle H., Hannestad S., Sommer-Larsen J., 2003, ApJL, 588, L73

Dahle H., Kaiser N., Irgens R. J., Lilje P. B., Maddox S. J., 2002, ApJS, 139, 313

Dawson K. S., Holzapfel W. L., Carlstrom J. E., Joy M., LaRoque S. J., 2006, ApJ, 647, 13

Dietrich J. P., Schneider P., Clowe D., Romano-Díaz E., Kerp J., 2005, A&A, 440, 453

Dolag K., Bartelmann M., Perrotta F., Baccigalupi C., Moscardini L., Meneghetti M., Tormen G., 2004, A&A, 416, 853

Erben T., et al., 2005, Astronomische Nachrichten, 326, 432

Ettori S., Fabian A. C., Allen S. W., Johnstone R. M., 2002, MNRAS, 331, 635

Evrard A. E., 1989, ApJL, 341, L71

Fontanot F., De Lucia G., Monaco P., Somerville R. S., Santini P., 2009, MNRAS, 397, 1776

Freedman W. L., Madore B. F., Gibson B. K., Ferrarese L., Kelson D. D., Sakai S., Mould J. R., Kennicutt Jr. R. C., Ford H. C., Graham J. A., Huchra J. P., Hughes S. M. G., Illingworth G. D., Macri L. M., Stetson P. B., 2001, ApJ, 553, 47

Fu L., et al., 2008, A&A, 479, 9

Gray M. E., et al., 2009, MNRAS, 393, 1275

Gray M. E., Taylor A. N., Meisenheimer K., Dye S., Wolf C., Thommes E., 2002, ApJ, 568, 141

Haiman Z., Mohr J. J., Holder G. P., 2001, ApJ, 553, 545

Hansen S. M., McKay T. A., Wechsler R. H., Annis J., Sheldon E. S., Kimball A., 2005, ApJ, 633, 122

Heavens A., Refregier A., Heymans C., 2000, MNRAS, 319, 649

Heymans C., et al., 2006, MNRAS, 368, 1323

Heymans C., Heavens A., 2003, MNRAS, 339, 711

Hincks A. D., et al., 2009, ArXiv e-prints

Hirata C. M., Mandelbaum R., Ishak M., Seljak U., Nichol R., Pimbblet K. A., Ross N. P., Wake D., 2007, MNRAS, 381, 1197

Hirata C. M., Seljak U., 2004, PhRvD, 70, 063526

Hoekstra H., 2007, MNRAS, 379, 317

Hoekstra H., Jain B., 2008, Annual Review of Nuclear and Particle Science, 58, 99

Hoekstra H., Mellier Y., van Waerbeke L., Semboloni E., Fu L., Hudson M. J., Parker L. C., Tereno I., Benabed K., 2006, ApJ, 647, 116

Hoekstra H., Yee H. K. C., Gladders M. D., 2002, ApJ, 577, 595

Host O., Hansen S. H., 2009, ArXiv e-prints

Hu W., Keeton C. R., 2002, PhRvD, 66, 063506

Ilbert O., et al., 2006, A&A, 457, 841

Jain B., Seljak U., White S., 2000, ApJ, 530, 547

Jing Y. P., 2000, ApJ, 535, 30

Jing Y. P., Suto Y., Mo H. J., 2007, ApJ, 657, 664

Joachimi B., Bridle S. L., 2009, ArXiv e-prints

Johnston D. E., Sheldon E. S., Wechsler R. H., Rozo E., Koester B. P., Frieman J. A., McKay T. A., Evrard A. E., Becker M. R., Annis J., 2007, ArXiv e-prints

Kaiser N., 1992, ApJ, 388, 272

Kaiser N., Squires G., 1993, ApJ, 404, 441

Kaiser N., Squires G., Broadhurst T., 1995, ApJ, 449, 460

Kilbinger M., Benabed K., Guy J., Astier P., Tereno I., Fu L., Wraith D., Coupon J., Mellier Y., Balland C., Bouchet F. R., Hamana T., Hardin D., McCracken H. J., Pain R., Regnault N., Schultheis M., Yahagi H., 2009, A&A, 497, 677

King L., Schneider P., 2002, A&A, 396, 411

King L. J., Schneider P., 2003, A&A, 398, 23

King L. J., Schneider P., Springel V., 2001, A&A, 378, 748

Kitching T. D., Miller L., Heymans C. E., van Waerbeke L., Heavens A. F., 2008, MNRAS, 390, 149

Kneib J., Ellis R. S., Santos M. R., Richard J., 2004, ApJ, 607, 697

Kneib J., Ellis R. S., Smail I., Couch W. J., Sharples R. M., 1996, ApJ, 471, 643

Kochanek C. S., 2004, ArXiv Astrophysics e-prints

Koester B. P., et al., 2007, ApJ, 660, 239

Komatsu E., Dunkley J., Nolta M. R., Bennett C. L., Gold B., Hinshaw G., Jarosik N., Larson D., Limon M., Page L., Spergel D. N., Halpern M., Hill R. S., Kogut A., Meyer S. S., Tucker G. S., Weiland J. L., Wollack E., Wright E. L., 2009, ApJS, 180, 330

Komatsu E., et al., 2010, ArXiv e-prints

Kubo J. M., Stebbins A., Annis J., Dell'Antonio I. P., Lin H., Khiabanian H., Frieman J. A., 2007, ApJ, 671, 1466

Lewis A., King L., 2006, PhRvD, 73, 063006

Lewis A. D., Buote D. A., Stocke J. T., 2003, ApJ, 586, 135

Limousin M., Richard J., Kneib J., Brink H., Pelló R., Jullo E., Tu H., Sommer-Larsen J., Egami E., Michałowski M. J., Cabanac R., Stark D. P., 2008, A&A, 489, 23

Luppino G. A., Kaiser N., 1997, ApJ, 475, 20

Mandelbaum R., Hirata C. M., Ishak M., Seljak U., 2006, in Bulletin of the American Astronomical Society Vol. 38 of Bulletin of the American Astronomical Society, A Detection of Large-scale Intrinsic Alignments and Implications for Cosmic Shear. p. 1001

Mandelbaum R., Seljak U., Cool R. J., Blanton M., Hirata C. M., Brinkmann J., 2006, MNRAS, 372, 758

Mandelbaum R., Seljak U., Hirata C. M., 2008, Journal of Cosmology and Astro-Particle Physics, 8, 6

Markevitch M., Gonzalez A. H., David L., Vikhlinin A., Murray S., Forman W., Jones C., Tucker W., 2002, ApJL, 567, L27

Massey R., et al., 2007a, Nat, 445, 286

Massey R., et al., 2007b, MNRAS, 376, 13

Mather J. C., et al., 1990, ApJL, 354, L37

McInnes R. N., Menanteau F., Heavens A. F., Hughes J. P., Jimenez R., Massey R., Simon P., Taylor A., 2009, MNRAS, 399, L84

Menanteau F., Hughes J. P., 2009, ApJL, 694, L136

Menanteau F., Hughes J. P., Jimenez R., Hernandez-Monteagudo C., Verde L., Kosowsky A., Moodley K., Infante L., Roche N., 2009, ApJ, 698, 1221

Milkeraitis M., van Waerbeke L., Heymans C., Hildebrandt H., Dietrich J. P., Erben T., 2010, MNRAS, p. 701

Miller L., Kitching T. D., Heymans C., Heavens A. F., van Waerbeke L., 2007, MNRAS, 382, 315

Mohr J. J., 2005, in S. C. Wolff & T. R. Lauer ed., Observing Dark Energy Vol. 339 of Astronomical Society of the Pacific Conference Series, Cluster Survey Studies of the Dark Energy. pp 140–+

Moore B., Governato F., Quinn T., Stadel J., Lake G., 1998, ApJL, 499, L5+

Motl P. M., Hallman E. J., Burns J. O., Norman M. L., 2005, ApJL, 623, L63

Munshi D., Valageas P., van Waerbeke L., Heavens A., 2008, Phys. Rep., 462, 67

Nagai D., 2006, ApJ, 650, 538

Narayan R., Bartelmann M., 1996, ArXiv Astrophysics e-prints

Navarro J. F., Frenk C. S., White S. D. M., 1996, ApJ, 462, 563

Neistein E., van den Bosch F. C., Dekel A., 2006, MNRAS, 372, 933

Oaxaca Wright C., Brainerd T. G., 1999, ArXiv Astrophysics e-prints

Okabe N., Takada M., Umetsu K., Futamase T., Smith G. P., 2009, ArXiv e-prints

Olsen L. F., Benoist C., Cappi A., Maurogordato S., Mazure A., Slezak E., Adami C., Ferrari C., Martel F., 2007, A&A, 461, 81

Peacock J., 1999, Cosmological Physics. C.U.P.

Pedersen K., Dahle H., 2007, ApJ, 667, 26

Perlmutter S., et al., 1999, ApJ, 517, 565

Plagge T., et al., 2009, ArXiv e-prints

Rasia E., Tormen G., Moscardini L., 2004, MNRAS, 351, 237

Refregier A., 2003, MNRAS, 338, 35

Refregier A., Amara A., Kitching T. D., Rassat A., Scaramella R., Weller J., Euclid Imaging Consortium f. t., 2010, ArXiv e-prints

Reid B. A., Spergel D. N., 2006, ApJ, 651, 643

Reiprich T. H., Böhringer H., 2002, ApJ, 567, 716

Reyes R., Mandelbaum R., Hirata C., Bahcall N., Seljak U., 2008, MNRAS, 390, 1157

Richard J., Pei L., Limousin M., Jullo E., Kneib J. P., 2009, A&A, 498, 37

Riess A. G., et al., 1998, AJ, 116, 1009

Riess A. G., et al., 2004, ApJ, 607, 665

Saha P., Read J. I., 2009, ApJ, 690, 154

Sand D. J., Treu T., Ellis R. S., Smith G. P., Kneib J., 2008, ApJ, 674, 711

Sand D. J., Treu T., Smith G. P., Ellis R. S., 2004, ApJ, 604, 88

Santos M. R., Ellis R. S., Kneib J., Richard J., Kuijken K., 2004, ApJ, 606, 683

Schneider P., 2006a, in Meylan G., Jetzer P., North P., Schneider P., Kochanek C. S., Wambsganss J., eds, Saas-Fee Advanced Course 33: Gravitational Lensing: Strong, Weak and Micro Part 1: Introduction to gravitational lensing and cosmology. pp 1–89

Schneider P., 2006b, in Meylan G., Jetzer P., North P., Schneider P., Kochanek C. S., Wambsganss J., eds, Saas-Fee Advanced Course 33: Gravitational Lensing: Strong, Weak and Micro Part 3: Weak gravitational lensing. pp 269–451

Schrabback T., et al., 2009, ArXiv e-prints

Sealfon C., Verde L., Jimenez R., 2006, ApJ, 649, 118

Seitz C., Schneider P., 1997, A&A, 318, 687

Semboloni E., Mellier Y., van Waerbeke L., Hoekstra H., Tereno I., Benabed K., Gwyn S. D. J., Fu L., Hudson M. J., Maoli R., Parker L. C., 2006, A&A, 452, 51

Simon P., Taylor A. N., Hartlap J., 2009, MNRAS, 399, 48

Spergel D. N., et al., 2007, ApJS, 170, 377

Spergel D. N., Verde L., Peiris H. V., Komatsu E., Nolta M. R., Bennett C. L., Halpern M., Hinshaw G., Jarosik N., Kogut A., Limon M., Meyer S. S., Page L., Tucker G. S., Weiland J. L., Wollack E., Wright E. L., 2003, ApJS, 148, 175

Springel V., White S. D. M., Jenkins A., Frenk C. S., Yoshida N., Gao L., Navarro J., Thacker R., Croton D., Helly J., Peacock J. A., Cole S., Thomas P., Couchman H., Evrard A., Colberg J., Pearce F., 2005, Nat, 435, 629

Staniszewski Z., et al., 2008, ArXiv e-prints

Sunyaev R. A., Zel'dovich I. B., 1981, Astrophysics and Space Physics Reviews, 1, 1

Takada M., White M., 2004, ApJL, 601, L1

Van Waerbeke L., Mellier Y., 2003, ArXiv Astrophysics e-prints

Voit G. M., 2005, Reviews of Modern Physics, 77, 207

Wambsganss J., 2006, in Meylan G., Jetzer P., North P., Schneider P., Kochanek C. S., Wambsganss J., eds, Saas-Fee Advanced Course 33: Gravitational Lensing: Strong, Weak and Micro Part 4: Gravitational microlensing. pp 453–540

Wittman D., Dell'Antonio I. P., Hughes J. P., Margoniner V. E., Tyson J. A., Cohen J. G., Norman D., 2006, ApJ, 643, 128

Zappacosta L., Buote D. A., Gastaldello F., Humphrey P. J., Bullock J., Brighenti F., Mathews W., 2006, ApJ, 650, 777

Zhang Y., Finoguenov A., Böhringer H., Kneib J., Smith G. P., Kneissl R., Okabe N., Dahle H., 2008, A&A, 482, 451

Zhang Y.-Y., Böhringer H., Finoguenov A., Ikebe Y., Matsushita K., Schuecker P., Guzzo L., Collins C. A., 2006, A&A, 456, 55

Appendix A

Derivation of Y

The SZ Compton y parameter is defined as

$$y = \frac{\sigma_T}{m_e c^2} \int \mathrm{d}l \, n_e k T_e = \frac{\sigma_T}{m_e c^2} \int \mathrm{d}l \, p_e \tag{A.1}$$

and the integrated Y parameter is

$$Y = \int \mathrm{d}\Omega y(\Omega) = \int_0^\infty \frac{2\pi R \mathrm{d}R}{D_A^2} y(R). \tag{A.2}$$

If we assume hydrostatic equilibrium we know that the total pressure is related by

$$-\frac{\mathrm{d}p}{\mathrm{d}r} = \frac{GM(<r)\rho_g(r)}{r^2} \tag{A.3}$$

where we $M(<r)$ is the mass contained within radius r and $\rho(r)$ is the density at r, ρ_g is the gas density, and $p = \alpha p_e$.

Now we want to integrate to give an expressions for Y in terms of concentration, redshift and mass. To do this we must first integrate our expression for pressure (Eq. A.3) giving us y, then integrate this expression to give the desired expression for Y.

From Eq. A.3 we can write

$$p_e(r) = \frac{G}{\alpha} \int_r^\infty \frac{M(<r')\rho_g(r')}{r'^2} \tag{A.4}$$

and we can now express Eq. A.1 as the integral along the line of sight

$$y(R) = \frac{2\sigma_T}{\alpha m_e c^2} \int_{l=0}^\infty \mathrm{d}l \, p_e(r) \, . \tag{A.5}$$

We can now replace the integral over l with an integral over r by considering the fact that $r^2 = l^2 + R^2$ (and remembering that R is a constant),

$$2l\mathrm{d}l = 2r\mathrm{d}r \tag{A.6}$$

and

$$\mathrm{d}l = \frac{2r\mathrm{d}r}{2l} \tag{A.7}$$

thus

$$\mathrm{d}l = \frac{r\mathrm{d}r}{\sqrt{r^2 - R^2}} \tag{A.8}$$

which leads us to our new expression for y:

$$y(R) = \frac{2\sigma_T}{\alpha m_e c^2} \int_R^\infty \frac{r\mathrm{d}r}{\sqrt{r^2 - R^2}} p_e(r) \, . \tag{A.9}$$

Substituting $p(r)$ from the Eq. A.4 we now have

$$y(R) = \frac{2\sigma_T}{\alpha m_e c^2} \int_R^\infty \frac{\mathrm{d}r \, r}{\sqrt{r^2 - R^2}} \int_{r'=r}^\infty \frac{\mathrm{d}r' \, GM(< r')\rho_g(r')}{r'^2} \, . \tag{A.10}$$

By reversing the order of integration we get

$$y(R) = \frac{2\sigma_T G}{\alpha m_e c^2} \int_{r'=R}^\infty \frac{\mathrm{d}r' \, M(< r')\rho_g(r')}{r'^2} \int_{r=R}^{r'} \frac{\mathrm{d}r \, r}{\sqrt{r^2 - R^2}} \tag{A.11}$$

which if we do the second integration gives

$$y(R) = \frac{2\sigma_T G}{\alpha m_e c^2} \int_{r'=R}^\infty \frac{\mathrm{d}r' \, M(< r')\rho_g(r')}{r'^2} \left[\left(r^2 - R^2 \right)^{\frac{1}{2}} \right]_R^{r'} \tag{A.12}$$

$$y(R) = \frac{2\sigma_T}{\alpha m_e c^2} \int_{r'=R}^\infty \frac{\mathrm{d}r' \, GM(< r')\rho_g(r')}{r'^2} \left(r'^2 - R^2 \right)^{\frac{1}{2}} \, . \tag{A.13}$$

We can write the following expression for the mass:

$$M(< r') = \int_0^{r'} 4\pi r''^2 \mathrm{d}r'' \rho(r''). \tag{A.14}$$

Recalling Eq A.2 we can write the following expression for Y:

$$Y = \int \mathrm{d}\Omega y(\Omega) = \int_0^\infty \frac{2\pi R\mathrm{d}R}{D_A^2} y(R). \tag{A.15}$$

$$= \int_0^\infty \frac{2\pi R\mathrm{d}R}{D_A^2} \frac{2\sigma_T}{\alpha m_e c^2} \int_{r'=R}^\infty \frac{\mathrm{d}r' \, GM(< r')\rho_g(r')}{r'^2} \left(r'^2 - R^2 \right)^{\frac{1}{2}} \tag{A.16}$$

$$= \frac{4\pi G}{D_A^2} \frac{\sigma_T}{\alpha m_e c^2} \int_{R=0}^{R=\infty} R \int_{r'=R}^\infty \frac{M(< r')\rho_g(r') \left(r'^2 - R^2 \right)^{\frac{1}{2}}}{r'^2} \, \mathrm{d}r' \, \mathrm{d}R \, . \tag{A.17}$$

Once again we change the order of integration:

$$= \frac{4\pi G}{\alpha D_A^2} \frac{\sigma_T}{m_e c^2} \int_{r'=0}^{r'=\infty} \frac{M(< r')\rho_g(r')}{r'^2} \int_{R=0}^{R=r'} R \left(r'^2 - R^2 \right)^{\frac{1}{2}} \, \mathrm{d}R \, \mathrm{d}r' \, , \tag{A.18}$$

and use the substitution $u = r'^2 - R^2$, $\mathrm{d}u = -2R\mathrm{d}R$, which gives:

$$= \frac{4\pi G}{\alpha D_A^2}\frac{\sigma_T}{m_e c^2}\int_{r'=0}^{r'=\infty}\frac{M(<r')\rho_g(r')}{r'^2}\int_{u=r'^2}^{u=0}-\frac{1}{2}u^{\frac{1}{2}}\,\mathrm{d}u \tag{A.19}$$

$$= \frac{4\pi G}{\alpha D_A^2}\frac{\sigma_T}{m_e c^2}\int_{r'=0}^{r'=\infty}\frac{M(<r')\rho_g(r')}{r'^2}\left[-\frac{1}{2}\frac{u^{3/2}}{\frac{3}{2}}\right]_{r'^2}^{0} \tag{A.20}$$

$$= \frac{4\pi G}{\alpha D_A^2}\frac{\sigma_T}{m_e c^2}\int_{r'=0}^{r'=\infty}\frac{M(<r')\rho_g(r')}{r'^2}\left(\frac{1}{3}r'^3\right) \tag{A.21}$$

which can be tidied to

$$Y = \frac{4\pi G}{3\alpha D_A^2}\frac{\sigma_T}{m_e c^2}\int_{r'=0}^{r'=\infty}M(<r')\rho_g(r')r'\,\mathrm{d}r' \tag{A.22}$$

$$= \frac{4\pi G}{3\alpha D_A^2}\frac{\sigma_T}{m_e c^2}\int_{r'=0}^{r'=\infty}\rho(r')r'\int_0^{r'}4\pi r''^2\rho(r'')\,\mathrm{d}r''\,\mathrm{d}r'\,. \tag{A.23}$$

If we now substitute $\rho(r'')$ for the equation for an NFW (from Eq. 1.33) we get:

$$= \frac{16\pi^2 G}{3\alpha D_A^2}\frac{\sigma_T}{m_e c^2}\int_{r'=0}^{r'=\infty}\rho(r')r'\int_0^{r'}\frac{\bar{\rho}r''^2}{(r''/r_s)\,(1+r''/r_s)^2}\,\mathrm{d}r''\,\mathrm{d}r' \tag{A.24}$$

$$= \frac{16\pi^2 G\bar{\rho}_c}{3\alpha D_A^2 r_s}\frac{\sigma_T}{m_e c^2}\int_{r'=0}^{r'=\infty}\rho(r')r'\int_{r''=0}^{r''=r'}\frac{r''}{(1+r''/r_s)^2}\,\mathrm{d}r''\,\mathrm{d}r' \tag{A.25}$$

$$= \frac{16\pi^2 G\bar{\rho}}{3\alpha D_A^2 r_s}\frac{\sigma_T}{m_e c^2}\int_{r'=0}^{r'=\infty}\rho(r')r'r_s^3\left[\log(1+r''/r_s)-\frac{r''}{r''+r_s}\right]_0^{r'}\mathrm{d}r' \tag{A.26}$$

$$= \frac{16\pi^2 G\bar{\rho}r_s^3}{3\alpha D_A^2}\frac{\sigma_T}{m_e c^2}\int_{r'=0}^{r'=\infty}\rho(r')r'\left(\log(1+r'/r_s)-\frac{r'}{r'+r_s}\right)\mathrm{d}r'\,. \tag{A.27}$$

Substituting again for $\rho(r'')$ as before,

$$= \frac{16\pi^2 G\bar{\rho}^2 r_s^3}{3\alpha D_A^2}\frac{\sigma_T}{m_e c^2}\int_{r'=0}^{r'=\infty}\frac{r'}{(r'/r_s)\,(1+r'/r_s)^2}\left(\log(1+r'/r_s)-\frac{r'}{r'+r_s}\right)\mathrm{d}r' \tag{A.28}$$

and dividing through by r'/r_s:

$$= \frac{16\pi^2 G\bar{\rho}^2 r_s^3}{3\alpha D_A^2}\frac{\sigma_T}{m_e c^2}\int_{r'=0}^{r'=\infty}\frac{\left(\log(1+r'/r_s)-\frac{r'/r_s}{r'/r_s+1}\right)}{(1+r'/r_s)^2}\,\mathrm{d}r' \tag{A.29}$$

$$= \frac{16\pi^2 G\bar{\rho}^2 r_s^5}{3\alpha D_A^2}\frac{\sigma_T}{m_e c^2}\int_{u=0}^{u=\infty}\frac{\left(\log(1+u)-\frac{u}{u+1}\right)}{(1+u)^2}\,\mathrm{d}u \tag{A.30}$$

where $u = r'/r_s$, and $\mathrm{d}u = 1/r_s \mathrm{d}r$. The integral on the right can be looked up and it is equal to one half. We now have the following much simpler expression for Y,

$$Y = \frac{16\pi^2 G\bar{\rho}^2 r_s^5}{3\alpha D_A^2}\frac{\sigma_T}{m_e c^2}\frac{1}{2} = \frac{8\pi^2 G\bar{\rho}^2 r_s^5}{3\alpha D_A^2}\frac{\sigma_T}{m_e c^2}. \tag{A.31}$$

We want this expressed in terms of M_{200} and concentration index, c_s. As in Eq. A.28, mass at $r_{200} \equiv c_s r_s$ is

$$M(< r_{200}) = 4\pi\bar{\rho} r_s^3 \left(\log(1+c_s) - \frac{c_s}{1+c_s}\right) \equiv M_{200} \tag{A.32}$$

$$\Rightarrow Y = \frac{G\sigma_T M_{200}^2 c_s}{6\alpha m_e c^2 D_A^2 r_{200}\left(\log(1+c_s) - \frac{c_s}{1+c_s}\right)^2} \tag{A.33}$$

There is still a dependence on r_{200}, and so we use

$$r_{200} = \frac{GM_{200}}{VH_0^2(1+z)^3}, \tag{A.34}$$

where, for an NFW, $V \simeq 200$. Using this expression we can now write Y as

$$Y = \frac{G^{2/3}\sigma_T M_{200}^{5/3} c_s (200)^{1/3} H_0^{2/3}(1+z)}{6\alpha m_e c^2 D_A^2 r_{200}\left(\log(1+c_s) - \frac{c_s}{1+c_s}\right)^2} \tag{A.35}$$

and we use the concentration index from Dolag et al. (2004)[1]:

$$c_s(M_{200}) = 9.59(1+z)^{-1}(M_{200}/10^{14}h^{-1}M_\odot)^{-0.102}\ . \tag{A.36}$$

[1] but note that this is for a $\sigma_8 = 0.9$ cosmology, higher than current estimates (Komatsu et al., 2009).

Appendix B

Derivation of the Deflection Angle from the Geodesic Equation

The geodesic equation from General Relativity governs the wordline x^λ ($\lambda = 0, 1, 2, 3$) of a particle. It is written as follows:

$$\frac{d^2x^\mu}{dp^2} + \Gamma^\mu_{\nu\sigma}\frac{dx^\nu}{dp}\frac{dx^\sigma}{dp} = 0\,, \tag{B.1}$$

where p is an affine parameter. $\Gamma^\mu_{\nu\sigma}$ is the *affine connection*, which can be written in terms of the metric tensor $g_{\mu\nu}$ as

$$\Gamma^\mu_{\nu\sigma} = \frac{1}{2}g^{\mu\rho}\left\{\frac{\partial g_{\nu\rho}}{\partial x^\sigma} + \frac{\partial g_{\rho\sigma}}{\partial x^\nu} - \frac{\partial g_{\nu\sigma}}{\partial x^\rho}\right\}\,. \tag{B.2}$$

Or, equivalently, in alternative notation:

$$\ddot{x}^\mu + \Gamma^\mu_{\nu\sigma}\dot{x}^\nu\dot{x}^\sigma = 0\,. \tag{B.3}$$

$$\Gamma^\mu_{\nu\sigma} = \frac{1}{2}g^{\mu\rho}\left\{g_{\nu\rho,\sigma} + g_{\rho\sigma,\nu} - g_{\nu\sigma,\rho}\right\}\,. \tag{B.4}$$

Note that a dot denotes d/dp throughout this section.

For weak fields we use Eq. (2.2) as our metric and define *conformal time*, in place of the usual time coordinate. Conformal time is defined by

$$d\eta = \frac{cdt}{R(t)}\,. \tag{B.5}$$

This allows us to re-write Eq. (2.2) more simply:

$$ds^2 = R^2(t)\left\{\left(1 + \frac{2\Phi}{c^2}\right)d\eta^2 - \left(1 - \frac{2\Phi}{c^2}\right)\left[dr^2 + S_k^2(r)\left(d\theta_x^2 + d\theta_y^2\right)\right]\right\}\,. \tag{B.6}$$

We can now write the metric tensor for the weakly perturbed flat FLRW metric as

$$R^2(t)\begin{pmatrix} 1+2\Phi/c^2 & 0 & 0 & 0 \\ 0 & -(1-2\Phi/c^2) & 0 & 0 \\ 0 & 0 & -r^2(1-2\Phi/c^2) & 0 \\ 0 & 0 & 0 & -r^2(1-2\Phi/c^2) \end{pmatrix} . \tag{B.7}$$

What we want to find out is how the angles (θ_x, θ_y) of the ray change, as the photon travels along its path, when the varying gravitational potential is present. The path of the unperturbed, radial ray is set by $0 = ds^2 \simeq d\eta^2 - dr^2$, therefore for the radial incoming ray

$$\frac{dr}{d\eta} = -1 . \tag{B.8}$$

$g^{\mu\nu}$ is defined such that $g_{\mu\nu}g^{\nu\alpha} = \delta^\alpha_\mu$ and so we now compute the affine connections.

We want to find $d^2\eta/dp^2$ so we set $\mu = 0$ in Eq. (B.3) so we write:

$$\ddot{x}^0 + \Gamma^0_{\nu\sigma}\dot{x}^\nu\dot{x}^\sigma = 0 , \tag{B.9}$$

non-zero affine connections have $\mu = \rho = 0$:

$$\Gamma^0_{\nu\sigma} = \frac{1}{2}g^{0\,0}\left\{g_{\nu\,0,\sigma} + g_{0\,\sigma,\nu} - g_{\nu\sigma,0}\right\} . \tag{B.10}$$

We can read off the value of g_{00} from Eq. (B.7)

$$g^{00} = \frac{1}{g_{00}} = \frac{1}{R^2\left(1+2\Phi/c^2\right)} \tag{B.11}$$

We will now compute only $\Gamma^0_{00}, \Gamma^0_{01}, \Gamma^0_{02}, \Gamma^0_{03}, \Gamma^0_{11}, \Gamma^0_{22}, \Gamma^0_{33}$, because we know that all others must be zero. We keep this to zero order in Φ.

Γ^0_{00}

$$\Gamma^0_{00} = \frac{1}{2R^2}\left(1-\frac{2\Phi}{c^2}\right)\left\{g_{00,0} + g_{00,0} - g_{00,0}\right\} \tag{B.12}$$

$$\Rightarrow \Gamma^0_{00} = \frac{1}{2R^2}\left(1-\frac{2\Phi}{c^2}\right)\left\{\frac{\partial}{\partial\eta}\left(R^2\left(1+2\Phi/c^2\right)\right)\right\} \tag{B.13}$$

$$\Rightarrow \Gamma^0_{00} = \frac{1}{2R^2}\frac{\partial\left(R^2\right)}{\partial\eta} = \frac{1}{2R^2}2R\frac{\partial R}{\partial\eta} = \frac{1}{R}\frac{\partial R}{\partial\eta} \tag{B.14}$$

Γ^0_{01}

$$\Gamma^0_{01} = \frac{1}{2R^2}\left(1-\frac{2\Phi}{c^2}\right)\left\{g_{00,1} + g_{01,0} - g_{01,0}\right\} \tag{B.15}$$

$$\Rightarrow \Gamma^0_{01} = \frac{1}{2R^2}\left(1-\frac{2\Phi}{c^2}\right)\left\{\frac{\partial}{\partial r}\left(R^2\left(1+2\Phi/c^2\right)\right)\right\} \tag{B.16}$$

$$\Rightarrow \Gamma^0_{01} = \frac{1}{2R^2}\left(1 - \frac{2\Phi}{c^2}\right)\left\{\frac{\partial}{\partial r}\left(R^2\right)\right\} = \frac{R^2}{2R^2}\left\{\frac{\partial}{\partial r}(1)\right\} = 0 \tag{B.17}$$

Γ^0_{02}

$$\Gamma^0_{02} = \frac{1}{2R^2}\left(1 - \frac{2\Phi}{c^2}\right)\{g_{00,2} + g_{02,0} - g_{02,0}\} \tag{B.18}$$

$$\Rightarrow \Gamma^0_{02} = \frac{1}{2R^2}\left(1 - \frac{2\Phi}{c^2}\right)\left\{\frac{\partial}{\partial \theta_x}\left(R^2(1)\right)\right\} = 0 \tag{B.19}$$

Γ^0_{03}

$$\Gamma^0_{03} = \frac{1}{2R^2}\left(1 - \frac{2\Phi}{c^2}\right)\{g_{00,3}\} = \frac{1}{2R^2}\left\{\frac{\partial}{\partial \theta_y}\left(R^2(1)\right)\right\} = 0 \tag{B.20}$$

Γ^0_{11}

$$\Gamma^0_{11} = \frac{1}{2R^2}\{-g_{11,0}\} = \frac{-1}{2R^2}\left\{\frac{\partial}{\partial \eta}\left(-R^2\right)\right\} \tag{B.21}$$

$$\Rightarrow \Gamma^0_{11} = \frac{1}{2R^2}\frac{\partial\left(R^2\right)}{\partial \eta} = \frac{1}{2R^2}2R\frac{\partial R}{\partial \eta} = \frac{1}{R}\frac{\partial R}{\partial \eta} \tag{B.22}$$

Γ^0_{22}

$$\Gamma^0_{22} = \frac{1}{2R^2}\{-g_{22,0}\} = \frac{-1}{2R^2}\left\{\frac{\partial}{\partial \eta}\left(-R^2r^2\right)\right\} \tag{B.23}$$

$$\Rightarrow \Gamma^0_{22} = \frac{r^2}{2R^2}\frac{\partial\left(R^2\right)}{\partial \eta} = \frac{r^2}{R}\frac{\partial R}{\partial \eta} \tag{B.24}$$

Γ^0_{33}

$$\Gamma^0_{33} = \frac{1}{2R^2}\{-g_{33,0}\} = \frac{-1}{2R^2}\left\{\frac{\partial}{\partial \eta}\left(-R^2r^2\right)\right\} \tag{B.25}$$

$$\Rightarrow \Gamma^0_{33} = \frac{r^2}{2R^2}\frac{\partial\left(R^2\right)}{\partial \eta} = \frac{r^2}{R}\frac{\partial R}{\partial \eta} \tag{B.26}$$

So we return to Eq. (B.9) which can now be written as

$$\ddot{x}^0 + \Gamma^0_{\nu\sigma}\dot{x}^\nu\dot{x}^\sigma = \ddot{x}^0 + \Gamma^0_{00}\dot{x}^0\dot{x}^0 + \Gamma^0_{11}\dot{x}^1\dot{x}^1 + \Gamma^0_{22}\dot{x}^2\dot{x}^2 + \Gamma^0_{33}\dot{x}^3\dot{x}^3 = 0 \tag{B.27}$$

$$\Rightarrow \ddot{x}^0 + \frac{1}{R}\frac{\partial R}{\partial \eta}\dot{x}^0\dot{x}^0 + \frac{1}{R}\frac{\partial R}{\partial \eta}\dot{x}^1\dot{x}^1 + \frac{r^2}{R}\frac{\partial R}{\partial \eta}\dot{x}^2\dot{x}^2 + \frac{r^2}{R}\frac{\partial R}{\partial \eta}\dot{x}^3\dot{x}^3 = 0 \tag{B.28}$$

$$\Rightarrow \frac{d^2\eta}{dp^2} + \frac{1}{R}\frac{\partial R}{\partial \eta}\left(\frac{d\eta}{dp}\right)^2 + \frac{1}{R}\frac{\partial R}{\partial \eta}\left(\frac{dr}{dp}\right)^2 + \frac{r^2}{R}\frac{\partial R}{\partial \eta}\left(\frac{d\theta_x}{dp}\right)^2 + \frac{r^2}{R}\frac{\partial R}{\partial \eta}\left(\frac{d\theta_y}{dp}\right)^2 = 0 \tag{B.29}$$

$$\Rightarrow \frac{d^2\eta}{dp^2} = -\frac{1}{R}\frac{\partial R}{\partial \eta}\left\{\left(\frac{d\eta}{dp}\right)^2 + \left(\frac{dr}{dp}\right)^2 + r^2\left(\frac{d\theta_x}{dp}\right)^2 + r^2\left(\frac{d\theta_y}{dp}\right)^2\right\} \tag{B.30}$$

Now, from Eq. (B.8) we see that

$$\frac{dr}{dp} = \frac{dr}{d\eta}\frac{d\eta}{dp} = (-1)\frac{d\eta}{dp}\,, \tag{B.31}$$

so to first order we have

$$\frac{d^2\eta}{dp^2} = -\frac{1}{R}\frac{\partial R}{\partial \eta}\left\{\left(\frac{d\eta}{dp}\right)^2 + \left(\frac{d\eta}{dp}\right)^2\right\} = -\frac{2}{R}\frac{\partial R}{\partial \eta}\left(\frac{d\eta}{dp}\right)^2 = -\frac{2}{R}\frac{dR}{dp}\frac{d\eta}{dp}\,. \tag{B.32}$$

Therefore by choosing units of p appropriately, we find that

$$\boxed{\frac{d\eta}{dp} = -\frac{1}{R^2}\,.} \tag{B.33}$$

Now we will look at the $\mu = 2$ cases in Eq. (B.3):

$$\ddot{x}^2 + \Gamma^2_{\nu\sigma}\dot{x}^\nu\dot{x}^\sigma = 0\,, \tag{B.34}$$

non-zero affine connections have $\mu = \rho = 2$:

$$\Gamma^2_{\nu\sigma} = \frac{1}{2}g^{2\,2}\left\{g_{\nu\,2,\sigma} + g_{2\,\sigma,\nu} - g_{\nu\sigma,2}\right\}\,. \tag{B.35}$$

We can read off the value of g_{22} from Eq. (B.7)

$$g^{22} = \frac{1}{g_{22}} = \frac{-1}{R^2r^2\left(1 - 2\Phi/c^2\right)} \tag{B.36}$$

We will now compute $\Gamma^2_{00}, \Gamma^2_{02}, \Gamma^2_{22}, \Gamma^2_{23}, \Gamma^2_{21}, \Gamma^2_{11}, \Gamma^2_{33}$, (we know that all others must be zero) to first order[1].

Γ^2_{00}

$$\Gamma^2_{00} = \left\{\frac{-1}{2R^2r^2\left(1 - 2\Phi/c^2\right)}\right\}\left\{-R^2\frac{2}{c^2}\frac{\partial\Phi}{\partial\theta_x}\right\} = \frac{1}{r^2c^2}\frac{\partial\Phi}{\partial\theta_x} \tag{B.37}$$

Γ^2_{02}

[1] To zero order in Φ as before

$$\Gamma^2_{02} = \left\{\frac{-1}{2R^2r^2\left(1-2\Phi/c^2\right)}\right\}\left\{\frac{d\left(R^2\right)}{d\eta}\left(-r^2\left(1-\frac{2\Phi}{c^2}\right)\right)\right\} \tag{B.38}$$

$$\Rightarrow \Gamma^2_{02} = \left\{\frac{-1}{2R^2r^2}\right\}\left\{-2Rr^2\frac{dR}{d\eta}\right\} = \frac{1}{R}\frac{dR}{d\eta} \tag{B.39}$$

Γ^2_{22}

$$\Gamma^2_{22} = \left\{\frac{-1}{2R^2r^2\left(1-2\Phi/c^2\right)}\right\}\left\{-R^2r^2\left(-\frac{2}{c^2}\frac{d\Phi}{d\theta_x}\right)\right\} = -\frac{\partial\Phi}{\partial\theta_x}\frac{1}{c^2} \tag{B.40}$$

Γ^2_{23}

$$\Gamma^2_{23} = \left\{\frac{-1}{2R^2r^2\left(1-2\Phi/c^2\right)}\right\}\left\{R^2r^2\frac{2}{c^2}\frac{d\Phi}{d\theta_y}\right\} = -\frac{\partial\Phi}{\partial\theta_x}\frac{1}{c^2} \tag{B.41}$$

Γ^2_{21}

$$\Gamma^2_{21} = \left\{\frac{-1}{2R^2r^2\left(1-2\Phi/c^2\right)}\right\}\left\{\frac{\partial}{\partial r}\left(-R^2r^2\left(1-\frac{2\Phi}{c^2}\right)\right)\right\} \tag{B.42}$$

$$\Rightarrow \Gamma^2_{21} = \left\{\frac{-1}{2R^2r^2}\right\}\left\{-2R^2r\left(1-2\Phi/c^2\right) - R^2r^2\left(-\frac{2}{c^2}\right)\frac{\partial\Phi}{\partial r})\right\} \tag{B.43}$$

$$\Rightarrow \Gamma^2_{21} = \frac{1}{r}\left(1-2\Phi/c^2\right) - \frac{1}{c^2}\frac{\partial\Phi}{\partial r} \tag{B.44}$$

Γ^2_{11}

$$\Gamma^2_{11} = \left\{\frac{-1}{2R^2r^2\left(1-2\Phi/c^2\right)}\right\}\left\{-\frac{2R^2}{c^2}\frac{\partial\Phi}{\partial\theta_x}\right\} = \frac{1}{c^2r^2}\frac{\partial\Phi}{\partial\theta_x} \tag{B.45}$$

Γ^2_{33}

$$\Gamma^2_{33} = \left\{\frac{-1}{2R^2r^2\left(1-2\Phi/c^2\right)}\right\}\left\{\frac{2R^2}{c^2r^2}\frac{\partial\Phi}{\partial\theta_x}\right\} = -\frac{1}{c^2}\frac{\partial\Phi}{\partial\theta_x} \tag{B.46}$$

So we return to Eq. (B.34) which can now be written as

$$\ddot{x}^2 + \Gamma^2_{00}\dot{x}^0\dot{x}^0 + 2\Gamma^2_{02}\dot{x}^0\dot{x}^2 + \Gamma^2_{22}\dot{x}^2\dot{x}^2 + 2\Gamma^2_{23}\dot{x}^2\dot{x}^3 + 2\Gamma^2_{21}\dot{x}^2\dot{x}^1 + \Gamma^2_{11}\dot{x}^1\dot{x}^1 + \Gamma^2_{33}\dot{x}^3\dot{x}^3 = 0 \tag{B.47}$$

$$\begin{aligned}\Rightarrow \ddot{\theta}_x &+ \tfrac{1}{r^2c^2}\tfrac{\partial\Phi}{\partial\theta_x}\left(\tfrac{d\eta}{dp}\right)^2 + \tfrac{2}{R}\tfrac{dR}{d\eta}\tfrac{d\eta}{dp}\tfrac{d\theta_x}{dp} - \tfrac{\partial\Phi}{\partial\theta_y}\tfrac{1}{c^2}\left(\tfrac{d\theta_x}{dp}\right)^2 - \tfrac{\partial\Phi}{\partial\theta_x}\tfrac{2}{c^2}\tfrac{d\theta_x}{dp}\tfrac{d\theta_y}{dp} \\ &+ \left(\tfrac{2}{r}\left(1-\tfrac{2\Phi}{c^2}\right) - \tfrac{1}{c^2}\tfrac{\partial\Phi}{\partial r}\right)\tfrac{dr}{dp}\tfrac{d\theta_x}{dp} + \tfrac{1}{c^2r^2}\tfrac{\partial\Phi}{\partial\theta_x}\left(\tfrac{dr}{dp}\right)^2 - \tfrac{1}{c^2}\tfrac{\partial\Phi}{\partial\theta_x}\left(\tfrac{d\theta_y}{dp}\right)^2 = 0\end{aligned} \tag{B.48}$$

Note that the factor of 2 arises in front of Γ^2_{02}, Γ^2_{23} and Γ^2_{21} due to the fact that we must

include e.g. Γ^2_{02} *and* Γ^2_{20}. Keeping to first order in Φ, this reduces to

$$\ddot{\theta}_x + \frac{1}{r^2c^2}\frac{\partial\Phi}{\partial\theta_x}\left(\frac{d\eta}{dp}\right)^2 + \frac{2}{R}\frac{dR}{d\eta}\frac{d\eta}{dp}\frac{d\theta_x}{dp} + \frac{2}{r}\frac{dr}{dp}\frac{d\theta_x}{dp} + \frac{1}{c^2r^2}\frac{\partial\Phi}{\partial\theta_x}\left(\frac{dr}{dp}\right)^2 = 0 \tag{B.49}$$

$$\Rightarrow \ddot{\theta}_x + \frac{1}{r^2c^2}\frac{\partial\Phi}{\partial\theta_x}\left(\frac{1}{R^2}\right)^2 + \frac{2}{R}\frac{dR}{d\eta}\frac{d\eta}{dp}\frac{d\theta_x}{dp} + \frac{2}{r}\frac{dr}{dp}\frac{d\theta_x}{dp} + \frac{1}{c^2r^2}\frac{\partial\Phi}{\partial\theta_x}\left(-\frac{1}{R^2}\right)^2 = 0 \tag{B.50}$$

$$\Rightarrow \ddot{\theta}_x + \frac{2}{r^2c^2R^4}\frac{\partial\Phi}{\partial\theta_x} + \frac{2}{R}\frac{dR}{dp}\frac{d\theta_x}{dp} + \frac{2}{r}\frac{dr}{dp}\frac{d\theta_x}{dp} = 0 \tag{B.51}$$

Now we want to change from $\ddot{\theta}_x$ to $\frac{d^2\theta_x}{d\eta^2}$:

$$\frac{d^2\theta_x}{d\eta^2} = \frac{d}{d\eta}\left(\frac{d\theta_x}{d\eta}\right) = \frac{dp}{d\eta}\frac{d}{dp}\left(\frac{dp}{d\eta}\frac{d\theta_x}{dp}\right) = \left(\frac{dp}{d\eta}\right)^2\frac{d^2\theta_x}{dp^2} + \frac{dp}{d\eta}\frac{d\theta_x}{dp}\frac{d}{dp}\left(\frac{dp}{d\eta}\right) \tag{B.52}$$

and we can use the fact that

$$\frac{dr}{dp} = \frac{dr}{d\eta}\frac{d\eta}{dp} = -\frac{d\eta}{dp} \tag{B.53}$$

to give

$$\frac{d^2\theta_x}{d\eta^2} = R^4\frac{d^2\theta_x}{dp^2} + R^2\frac{d\theta_x}{dp}2R\frac{dR}{dp} \tag{B.54}$$

So substituting from Eq. (B.51) gives

$$\frac{d^2\theta_x}{d\eta^2} = R^4\left(-\frac{2}{r^2c^2R^4}\frac{\partial\Phi}{\partial\theta_x} - \frac{2}{R}\frac{dR}{dp}\frac{d\theta_x}{dp} - \frac{2}{r}\frac{dr}{dp}\frac{d\theta_x}{dp}\right) + 2R^3\frac{d\theta_x}{dp}\frac{dR}{dp} \tag{B.55}$$

$$\Rightarrow \frac{d^2\theta_x}{d\eta^2} = -\frac{2}{r^2c^2}\frac{\partial\Phi}{\partial\theta_x} - 2R^3\frac{dR}{dp}\frac{d\theta_x}{dp} - \frac{2R^4}{r}\frac{dr}{dp}\frac{d\theta_x}{dp} + 2R^3\frac{d\theta_x}{dp}\frac{dR}{dp} \tag{B.56}$$

$$\Rightarrow \frac{d^2\theta_x}{d\eta^2} = -\frac{2}{r^2c^2}\frac{\partial\Phi}{\partial\theta_x} - \frac{2R^4}{r}\frac{dr}{dp}\frac{d\theta_x}{dp} \tag{B.57}$$

$$\Rightarrow \frac{d^2\theta_x}{d\eta^2} + \frac{2R^4}{r}\frac{dr}{d\eta}\frac{d\eta}{dp}\frac{d\theta_x}{d\eta}\frac{d\eta}{dp} = -\frac{2}{r^2c^2}\frac{\partial\Phi}{\partial\theta_x} \tag{B.58}$$

$$\Rightarrow \frac{d^2\theta_x}{d\eta^2} + \frac{2R^4}{r}(-1)\frac{1}{R^2}\frac{d\theta_x}{d\eta}\frac{1}{R^2} = -\frac{2}{r^2c^2}\frac{\partial\Phi}{\partial\theta_x} \tag{B.59}$$

$$\frac{d^2\theta_x}{d\eta^2} - \frac{2}{r}\frac{d\theta_x}{d\eta} = -\frac{2}{r^2c^2}\frac{\partial\Phi}{\partial\theta_x} \tag{B.60}$$

You will often see this result expressed in terms of the comoving transverse distance, $X = S_k\theta_x$. We start by expressing $\dot{X}$ and $\ddot{X}$:

$$\dot{X} = \dot{S}_k\theta_x + S_k\dot{\theta}_x \tag{B.61}$$

$$\ddot{X} = \ddot{S}_k\theta_x + \dot{S}_k\dot{\theta}_x + \dot{S}_k\dot{\theta}_x + S_k\ddot{\theta}_x = \ddot{S}_k\theta_x + 2\dot{S}_k\dot{\theta}_x + S_k\ddot{\theta}_x \tag{B.62}$$

Recall the definition of S_k,

$$S_k(r) = \begin{cases} \sin r & (k=1) \\ \sinh r & (k=-1) \\ r & (k=0)\,. \end{cases} \tag{B.63}$$

Flat Case

We will now consider the flat case. In this case $S_k = r$ and so $\dot{S}_k = \dot{r} = -1/R^2$, and

$$\ddot{S}_k = \ddot{r} = \frac{d\eta}{dp}\frac{d}{d\eta}(\dot{r}) = \frac{1}{R^2}\frac{d}{d\eta}\left(-\frac{1}{R^2}\right) = \frac{1}{R^2}\left(2R^{-3}\frac{dr}{d\eta}\right) = \frac{2}{R^5}\frac{dR}{d\eta}\,. \tag{B.64}$$

In this case we can write $\dot{X}$ and $\ddot{X}$ as:

$$\dot{X} = \dot{S}_k\theta_x + S_k\dot{\theta}_x = -\frac{\theta_x}{R^2} + r\dot{\theta}_x = -\frac{X}{rR^2} + r\dot{\theta}_x \tag{B.65}$$

$$\Rightarrow \dot{\theta}_x = \frac{\dot{X}}{r} + \frac{X}{r^2R^2} \tag{B.66}$$

$$\ddot{X} = \ddot{S}_k\theta_x + 2\dot{S}_k\dot{\theta}_x + S_k\ddot{\theta}_x = \frac{2}{R^5}\frac{dR}{d\eta}\theta_x - \frac{2}{R^2}\dot{\theta}_x + r\ddot{\theta}_x = \frac{2}{R^5}\frac{dR}{d\eta}\frac{X}{r} - \frac{2}{R^2}\dot{\theta}_x + r\ddot{\theta}_x \tag{B.67}$$

$$\Rightarrow \ddot{\theta}_x = \frac{\ddot{X}}{r} + \frac{2}{rR^2}\dot{\theta}_x - \frac{2}{r^2R^5}\frac{dR}{d\eta}X \tag{B.68}$$

Now we substitute for $\dot{\theta}_x$ from Eq. (B.66):

$$\Rightarrow \ddot{\theta}_x = \frac{\ddot{X}}{r} + \frac{2}{rR^2}\left(\frac{\dot{X}}{r} + \frac{X}{r^2R^2}\right) - \frac{2}{r^2R^5}\frac{dR}{d\eta}X \tag{B.69}$$

$$\Rightarrow \ddot{\theta}_x = \frac{\ddot{X}}{r} + \frac{2\dot{X}}{r^2R^2} + \frac{2X}{r^3R^4} - \frac{2}{r^2R^5}\frac{dR}{d\eta}X \tag{B.70}$$

Now returning to Eq. (B.51), we can use Eq. (B.66) and Eq. (B.70) to re-write it as:

$$\frac{\ddot{X}}{r} + \frac{2\dot{X}}{r^2R^2} + \frac{2X}{r^3R^4} - \frac{2}{r^2R^5}\frac{dR}{d\eta}X + \frac{2}{r^2c^2R^4}\frac{\partial\Phi}{\partial\theta_x} + \frac{2}{R}\dot{R}\left(\frac{\dot{X}}{r} + \frac{X}{r^2R^2}\right) + \frac{2}{r}\dot{r}\left(\frac{\dot{X}}{r} + \frac{X}{r^2R^2}\right) = 0 \tag{B.71}$$

$$\Rightarrow \frac{\ddot{X}}{r} + \left(\frac{2}{r^2R^2} + \frac{2}{rR}\dot{R} + \frac{2}{r^2}\dot{r}\right)\dot{X} + \left(-\frac{2}{r^2R^5}\frac{dR}{d\eta} + \frac{2}{r^3R^4} + \frac{2}{r^2R^3}\dot{R} + \frac{2}{r^3R^2}\dot{r}\right)X = -\frac{2}{r^2c^2R^4}\frac{\partial\Phi}{\partial\theta_x} \tag{B.72}$$

$$= \frac{\ddot{X}}{r} + \left(\frac{2}{r^2R^2} + \frac{2}{rR}\frac{dR}{d\eta}\frac{1}{R^2} + \frac{2}{r^2}\left(-\frac{1}{R^2}\right)\right)\dot{X} + \left(-\frac{2}{r^2R^5}\frac{dR}{d\eta} + \frac{2}{r^3R^4} + \frac{2}{r^2R^3}\frac{dR}{d\eta}\frac{1}{R^2} + \frac{2}{r^3R^2}\left(-\frac{1}{R^2}\right)\right)X \tag{B.73}$$

$$\Rightarrow \ddot{X} + \frac{2}{R}\frac{dR}{d\eta}\frac{1}{R^2}\dot{X} = -\frac{2}{rc^2R^4}\frac{\partial\Phi}{\partial\theta_x} \tag{B.74}$$

Now we use the fact that:

$$\frac{d^2X}{dp^2} = \frac{d}{dp}\frac{dX}{dp} = \frac{d\eta}{dp}\frac{d}{d\eta}\left(\frac{dX}{d\eta}\frac{d\eta}{dp}\right) = \frac{1}{R^2}\frac{d}{d\eta}\left(\frac{dX}{d\eta}\frac{1}{R^2}\right) \tag{B.75}$$

$$\Rightarrow \frac{d^2X}{dp^2} = \frac{1}{R^2}\left(\frac{d^2X}{d\eta^2}\frac{1}{R^2} + \frac{dX}{d\eta}\frac{d}{d\eta}\left(\frac{1}{R^2}\right)\right) = \frac{1}{R^4}\frac{d^2X}{d\eta^2} + \frac{1}{R^2}\frac{dX}{d\eta}\left(-2R^{-3}\frac{dR}{d\eta}\right) \tag{B.76}$$

Lastly, we return to Eq. (B.74), substituting $\ddot{\theta}_x$

$$\frac{1}{R^4}\frac{d^2X}{d\eta^2} - \frac{2}{R^5}\frac{dX}{d\eta}\frac{dR}{d\eta} + \frac{2}{R^3}\frac{dR}{d\eta}\frac{1}{R^2}\frac{dX}{d\eta} = -\frac{2}{rc^2R^4}\frac{\partial\Phi}{\partial\theta_x} \tag{B.77}$$

$$\Rightarrow \frac{d^2X}{d\eta^2} = -\frac{2}{c^2r}\frac{\partial\Phi}{\partial\theta_x} \tag{B.78}$$

Finally this allows us to write the result for the flat case:

$$\boxed{\frac{d^2\boldsymbol{X}}{d\eta^2} = -\frac{2}{c^2}\boldsymbol{\nabla}_\perp\Phi\,.} \tag{B.79}$$

where $\boldsymbol{\nabla}_\perp = \left(\frac{d}{dX}, \frac{d}{dY}\right)$.

Appendix C

Derivation of the Deflection Angle from the Euler-Lagrange Equation

A more compact way to derive the deflection angle is to use the Euler-Lagrange equation (again a dot denotes d/dp):

$$\frac{\partial L^2}{\partial x^\mu} - \frac{d}{dp}\left(\frac{\partial L^2}{\partial \dot{x}^\mu}\right) = 0 \tag{C.1}$$

We are free to choose L^2 in the Euler-Lagrange equation and we set it to be equal to $(ds/dp)^2$,

$$L^2 = R^2(\eta)\left\{\left(1+\frac{2\Phi}{c^2}\right)\dot{\eta}^2 - \left(1-\frac{2\Phi}{c^2}\right)\left[\dot{r}^2 + S_k^2\left(\dot{\theta}_x^2+\dot{\theta}_y^2\right)\right]\right\}\,, \tag{C.2}$$

and where we define $x^\mu = (\eta, r, \theta_x, \theta_y)$. We now calculate Eq. (C.1) for the different values of μ. These are calculated to zero order in Φ.

$\mu = 0$

$$\frac{\partial L^2}{\partial \eta} - \frac{d}{dp}\left(\frac{\partial L^2}{\partial \dot{\eta}}\right) = 0 \tag{C.3}$$

$$\Rightarrow 2R\frac{dR}{d\eta}\left\{\left(1+\frac{2\Phi}{c^2}\right)\dot{\eta}^2 - \left(1-\frac{2\Phi}{c^2}\right)\left[\dot{r}^2 + S_k^2\left(\dot{\theta}_x^2+\dot{\theta}_y^2\right)\right]\right\} - \frac{d}{dp}\left[R^2 2\dot{\eta}\right] = 0 \tag{C.4}$$

For photons we know that $ds^2 = 0$ therefore $L^2 = 0$ and so the term

$$\left\{\left(1+\frac{2\Phi}{c^2}\right)\dot{\eta}^2 - \left(1-\frac{2\Phi}{c^2}\right)\left[\dot{r}^2 + S_k^2\left(\dot{\theta}_x^2+\dot{\theta}_y^2\right)\right]\right\} = 0\,. \tag{C.5}$$

Therefore we can write

$$-\frac{d}{dp}\left[R^2 2\dot{\eta}\right] = 0 \tag{C.6}$$

$$\Rightarrow R^2\dot{\eta} = \text{constant} \tag{C.7}$$

$$\Rightarrow \frac{d\eta}{dp} = \frac{1}{R^2} \text{ by choice of suitable units of p.} \tag{C.8}$$

$\mu = 1$

$$\frac{\partial L^2}{\partial r} - \frac{d}{dp}\left(\frac{\partial L^2}{\partial \dot{r}}\right) = 0 \tag{C.9}$$

To zeroth order, for an incoming, radial ray we need only use the fact that $ds^2 = 0$ to give straightforwardly

$$0 = R^2\left[d\eta^2 - dr^2\right], \tag{C.10}$$

$$\Rightarrow \frac{dr}{d\eta} = -1, \tag{C.11}$$

$$\Rightarrow \dot{r} = \frac{dr}{dp} = \frac{dr}{d\eta}\frac{d\eta}{dp} = \frac{(-1)}{R^2}. \tag{C.12}$$

$\mu = 2$

$$\frac{\partial L^2}{\partial \theta_x} - \frac{d}{dp}\left(\frac{\partial L^2}{\partial \dot{\theta}_x}\right) = 0 \tag{C.13}$$

$$\Rightarrow R^2\dot{\eta}^2\frac{2}{c^2}\frac{\partial \Phi}{\partial \theta_x} + \frac{2R^2}{c^2}\frac{\partial \Phi}{\partial \theta_x}\left[\dot{r}^2 + S_k^2(r)\left({\dot{\theta}_x}^2 + {\dot{\theta}_y}^2\right)\right] - \frac{d}{dp}\left(-R^2S_k^2 2\dot{\theta}_x\left(1 - \frac{2\Phi}{c^2}\right)\right) = 0 \tag{C.14}$$

Ignoring terms $\frac{\partial \Phi}{\partial \theta_x}\left({\dot{\theta}_x}^2 + {\dot{\theta}_y}^2\right)$ and $\dot{\theta}_x\left(-\frac{2\Phi}{c^2}\right)$ as they are 2nd order, we now write

$$\Rightarrow R^2\dot{\eta}^2\frac{2}{c^2}\frac{\partial \Phi}{\partial \theta_x} + \frac{2R^2}{c^2}\frac{\partial \Phi}{\partial \theta_x}\dot{r}^2 - \frac{d}{dp}\left(-R^2S_k^2 2\dot{\theta}_x\right) = 0 \tag{C.15}$$

Substituting in from Eq. (C.8) and Eq. (C.12) we get

$$R^2\frac{1}{R^4}\frac{2}{c^2}\frac{\partial \Phi}{\partial \theta_x} + \frac{2R^2}{c^2}\frac{\partial \Phi}{\partial \theta_x}\frac{1}{R^4} + \frac{d}{dp}\left(2R^2S_k^2\dot{\theta}_x\right) = 0 \tag{C.16}$$

$$\Rightarrow \frac{2}{c^2R^2}\frac{\partial \Phi}{\partial \theta_x} + \frac{2}{c^2R^2}\frac{\partial \Phi}{\partial \theta_x} + 2\frac{d}{dp}\left(R^2S_k^2\dot{\theta}_x\right) = 0 \tag{C.17}$$

$$\Rightarrow \frac{4}{c^2R^2}\frac{\partial \Phi}{\partial \theta_x} = -2\frac{d}{dp}\left(R^2S_k^2\dot{\theta}_x\right) \tag{C.18}$$

$$\Rightarrow R^2\frac{d}{dp}\left(R^2S_k^2\dot{\theta}_x\right) = -\frac{2}{c^2}\frac{\partial \Phi}{\partial \theta_x} \tag{C.19}$$

We now want an expression for $d^2X/d\eta^2$, where $X = S_k\theta_x$ is the comoving transverse distance. We start by expressing $\dot{X}$:

$$\dot{X} = \dot{S}_k\theta_x + S_k\dot{\theta}_x \tag{C.20}$$

Recall the definition of S_k,

$$S_k(r) = \begin{cases} \sin r & (k=1) \\ \sinh r & (k=-1) \\ r & (k=0)\,. \end{cases} \tag{C.21}$$

Flat Case

Firstly we will consider the flat case. In this case $S_k = r$ and so $\dot{S_k} = \dot{r} = -1/R^2$. Therefore Eq. (C.20) becomes

$$\dot{X} = \frac{\theta_x}{R^2} + r\dot{\theta_x} = \frac{-X}{rR^2} + r\dot{\theta_x} \tag{C.22}$$

Now we can substitute for $\dot{\theta_x}$ in Eq. (C.19):

$$R^2 \frac{d}{dp}\left(R^2 r^2 \left[\frac{\dot{X}}{r} + \frac{X}{r^2R^2}\right]\right) = -\frac{2}{c^2}\frac{\partial\Phi}{\partial\theta_x} \tag{C.23}$$

Now we want an expression for d/dp:

$$\frac{d}{dp} = \frac{d\eta}{dp}\frac{d}{d\eta} = \frac{1}{R^2}\frac{d}{d\eta} \tag{C.24}$$

$$\Rightarrow \frac{R^2}{R^2}\frac{d}{d\eta}\left(R^2 r^2 \left[\frac{1}{r}\frac{1}{R^2}\frac{dX}{d\eta} + \frac{X}{r^2R^2}\right]\right) = -\frac{2}{c^2}\frac{\partial\Phi}{\partial\theta_x} \tag{C.25}$$

$$\Rightarrow \frac{d}{d\eta}\left(r\frac{dX}{d\eta} + X\right) = -\frac{2}{c^2}\frac{\partial\Phi}{\partial\theta_x} \tag{C.26}$$

$$\Rightarrow \frac{dr}{d\eta}\frac{dx}{d\eta} + r\frac{d^2X}{d\eta^2} + \frac{dX}{d\eta} = -\frac{2}{c^2}\frac{\partial\Phi}{\partial\theta_x} \tag{C.27}$$

Recall that we learnt in Eq. (C.11) that $\frac{dr}{d\eta} = -1$, therefore

$$\frac{d^2X}{d\eta^2} = -\frac{2}{c^2 r}\frac{\partial\Phi}{\partial\theta_x} \tag{C.28}$$

Finally this allows us to write the result for the flat case:

$$\boxed{\frac{d^2\boldsymbol{X}}{d\eta^2} = -\frac{2}{c^2}\boldsymbol{\nabla}_\perp\Phi\,.} \tag{C.29}$$

where $\boldsymbol{\nabla}_\perp = \left(\frac{d}{dX}, \frac{d}{dY}\right)$.

General Case

Now we will look at the General case, firstly by finding an expression for $\dot{S}_k$:

$$S_k(r) = \begin{cases} \sin r \\ \sinh r \\ r\,, \end{cases} \tag{C.30}$$

$$\Rightarrow \dot{S}_k(r) = \begin{cases} \cos r\,\dot{r} \\ \cosh r\,\dot{r} \\ \dot{r} \end{cases} = \begin{cases} \left(1-\sin^2 r\right)^{\frac{1}{2}}\dot{r} \\ \left(1+\sinh^2 r\right)^{\frac{1}{2}}\dot{r} \\ \dot{r} \end{cases} = \begin{cases} \left(1-s_k^2\right)^{\frac{1}{2}}\dot{r} \\ \left(1+s_k^2\right)^{\frac{1}{2}}\dot{r} \\ \dot{r} \end{cases} = \left(1-kS_k^2\right)^{\frac{1}{2}}\dot{r} \tag{C.31}$$

$$\Rightarrow \dot{S}_k(r) = -\frac{\left(1-kS_k^2\right)^{\frac{1}{2}}}{R^2}\,. \tag{C.32}$$

We will substitute into Eq. (C.19) and then in to Eq. (C.20).

$$\dot{X} = \dot{S}_k\theta_x + S_k\dot{\theta}_x \tag{C.33}$$

$$\Rightarrow \dot{X} = -\frac{\left(1-kS_k^2\right)^{\frac{1}{2}}}{R^2}\theta_x + S_k\dot{\theta}_x \tag{C.34}$$

$$\Rightarrow \dot{X} = -\frac{X}{S_k R^2}\left(1-kS_k^2\right)^{\frac{1}{2}} + S_k\dot{\theta}_x \tag{C.35}$$

$$\Rightarrow \dot{\theta}_x = \frac{\dot{X}}{S_k} + \left(1-kS_k^2\right)^{\frac{1}{2}}\frac{X}{R^2S_k^2} \tag{C.36}$$

Now we substitute this expression for $\dot{\theta}_x$, and that for d/dp from Eq. (C.24) into Eq. (C.19):

$$\frac{d}{d\eta}\left(R^2S_k^2\left[\frac{dX}{dp}\frac{1}{S_k} + \left(1-kS_k^2\right)^{\frac{1}{2}}\frac{X}{R^2S_k^2}\right]\right) = -\frac{2}{c^2}\frac{\partial\Phi}{\partial\theta_x} \tag{C.37}$$

$$\Rightarrow \frac{d}{d\eta}\left(S_k\frac{dX}{d\eta} + X\left(1-kS_k^2\right)^{\frac{1}{2}}\right) = -\frac{2}{c^2}\frac{\partial\Phi}{\partial\theta_x} \tag{C.38}$$

$$\Rightarrow \frac{dS_k}{d\eta}\frac{dX}{d\eta} + S_k\frac{d^2X}{d\eta^2} + \left(1-kS_k^2\right)^{\frac{1}{2}}\frac{dX}{d\eta} + \frac{1}{2}X\left(1-kS_k^2\right)^{-\frac{1}{2}}\left(-2kS_k\frac{dS_k}{d\eta}\right) = -\frac{2}{c^2}\frac{\partial\Phi}{\partial\theta_x} \tag{C.39}$$

$$\Rightarrow \frac{dp}{d\eta}\frac{dS_k}{dp}\frac{dX}{d\eta} + S_k\frac{d^2X}{d\eta^2} + \left(1-kS_k^2\right)^{\frac{1}{2}}\frac{dX}{d\eta} - \frac{kS_kX}{\left(1-kS_k^2\right)^{\frac{1}{2}}}\frac{dp}{d\eta}\frac{dS_k}{dp} = -\frac{2}{c^2}\frac{\partial\Phi}{\partial\theta_x} \tag{C.40}$$

Now substituting in for $\frac{dS_k}{dp}$ from Eq. (C.32)

$$R^2\left(-\frac{\left(1-kS_k^2\right)^{\frac{1}{2}}}{R^2}\right)\frac{dX}{d\eta} + S_k\frac{d^2X}{d\eta^2} + \left(1-kS_k^2\right)^{\frac{1}{2}}\frac{dX}{d\eta} - \frac{kS_kX}{\left(1-kS_k^2\right)^{\frac{1}{2}}}R^2\left(-\frac{\left(1-kS_k^2\right)^{\frac{1}{2}}}{R^2}\right) = -\frac{2}{c^2}\frac{\partial\Phi}{\partial\theta_x} \tag{C.41}$$

$$\Rightarrow -\left(1-kS_k^2\right)^{\frac{1}{2}}\frac{dX}{d\eta}+S_k\frac{d^2X}{d\eta^2}+\left(1-kS_k^2\right)^{\frac{1}{2}}\frac{dX}{d\eta}+\frac{kS_kX\left(1-kS_k^2\right)^{\frac{1}{2}}}{\left(1-kS_k^2\right)^{\frac{1}{2}}}=-\frac{2}{c^2}\frac{\partial\Phi}{\partial\theta_x} \quad \text{(C.42)}$$

$$\Rightarrow S_k\frac{d^2X}{d\eta^2}+kS_kX=-\frac{2}{c^2}\frac{\partial\Phi}{\partial\theta_x} \quad \text{(C.43)}$$

which leads us to the result for the general case:

$$\frac{d^2\boldsymbol{X}}{d\eta^2}+k\boldsymbol{X}=-\frac{2}{c^2}\boldsymbol{\nabla}_\perp\Phi\,, \quad \text{(C.44)}$$

where $\boldsymbol{\nabla}_\perp=\left(\frac{d}{dX},\frac{d}{dY}\right)$.